Civil Engineering and Applied Solutions

Research Article

journal homepage: ceas.journals.umz.ac.ir

CEAS Civil Engineering and Applied Solutions

Data-Driven Prediction of FRP Confinement Efficiency in Concrete Columns: Incorporating Corner Radius and Aspect Ratio Effects

Sajjad Shayanfar [a], Meysam Ghasemi Naghibdehi [a], Javad Shayanfar [b*]

[a] *Department of Civil Engineering, Qaemshahr Branch, Islamic Azad University, Qaemshahr, Iran*
[b] *Department of Civil Engineering, University of Minho, Azurém, Guimarães 4800-058, Portugal*

ARTICLE INFO

Keywords:
FRP confinement
Compressive strength
Predictive model
Design-oriented model
Confined concrete
Non-circularity effect

Article history:
Received 10 December 2025
Accepted 29 January 2026
Available online 01 July 2026

ABSTRACT

This study develops a regression-based, design-oriented model for predicting the ultimate axial compressive strength of concrete columns fully confined with fiber-reinforced polymer (FRP) jackets. The model is formulated to be applicable to circular, square, and rectangular cross-sections within a single unified framework. Confinement effectiveness in non-circular sections is explicitly accounted for through two continuous geometric correction factors: one defined by the ratio of corner radius to section dimension and another defined by the cross-sectional aspect ratio. These factors modify the effective lateral confining pressure to reflect the progressive reduction in confinement efficiency as the section deviates from circularity. The model is calibrated and validated using a comprehensive experimental database comprising 1,723 FRP-confined concrete column tests, covering unconfined concrete compressive strengths from 6.6 to 204 MPa, FRP elastic moduli ranging from 13.6 to 657 GPa, and rectangular section aspect ratios up to 2.0. By construction, the formulation satisfies essential physical boundary conditions, including recovery of unconfined concrete strength in the absence of FRP confinement and a smooth, continuous transition in predicted strength between circular and non-circular cross-sections. The proposed model provides a general-purpose and physically consistent tool suitable for the design and assessment of FRP-confined concrete columns with varying cross-sectional geometries.

1. Introduction

The use of fiber-reinforced polymer (FRP) composites for externally confining reinforced concrete (RC) columns has become a well-established method for enhancing concrete's mechanical performance and the overall structural behavior of RC elements. Specifically, FRP confinement can substantially improve compressive strength, deformation capacity, and energy absorption, as well as increase load-carrying capacity, stiffness, and energy dissipation of columns [1-7]. Considerable research has focused on the axial stress-strain response of FRP-confined concrete, particularly for columns with non-circular cross sections (e.g., [8-11]). Experimentally observed axial stress-strain curves often exhibit a post-peak softening branch, reflecting strength reduction with increasing axial strain. Experimental studies indicate that this behavior is primarily influenced by several factors: (i) FRP confinement stiffness, (ii) the compressive strength of the concrete, (iii) non-circularity of the column cross-section, and (iv) the overall dimensions of the column [3, 12-18]. Eid et al. [19] performed axial compression tests on fully FRP-confined circular concrete columns (FFCC) with varying confinement stiffness. Their results show that high-stiffness FRP jackets effectively restrain lateral expansion, producing full strain-hardening behavior with substantial gains in axial strength and deformability. Conversely, reducing the confinement stiffness gradually shifts the response toward post-peak softening or softening–hardening behavior, with

* Corresponding author.
E-mail addresses: arch3d.ir@gmail.com (J. Shayanfar).

https://doi.org/10.22080/ceas.2026.30750.1059
ISSN: 3092-7749/
How to cite this article: Shayanfar, S., Ghasemi Naghibdehi, M., Shayanfar, J. Data-Driven Prediction of FRP Confinement Efficiency in Concrete Columns: Incorporating Corner Radius and Aspect Ratio Effects. Civil Engineering and Applied Solutions. 2026; 2(3): 1–15. doi:10.22080/ceas.2026.30750.1059.

the extent of this transformation directly linked to the FRP stiffness, as also noted by Wei and Wu [20]. Additionally, Fallah Pour et al. [21] and Vincent and Ozbakkaloglu [22] observed that the crack pattern evolves from diffuse microcracking to localized macrocracks as the behavior transitions from strain hardening to softening. Experimental studies by de Oliveira Diôgo et al. [23] show that the effectiveness of FRP confinement decreases as the concrete compressive strength increases. This reduction occurs because high-strength concrete exhibits lower lateral strain, delaying the activation of FRP confinement. Unlike normal-strength concrete (NSC), FRP-confined high-strength (HSC) or ultra-high-strength concrete (UHSC) columns often display post-peak strength loss beyond the transition zone, with the extent depending on the FRP stiffness. However, if sufficient lateral strain develops during softening, HSC/UHSC columns may undergo a strain-hardening phase due to the engagement of passive FRP confinement. This combined response, termed strain softening–hardening behavior, has been observed in numerous experimental studies [24-28]. Wang and Wu [29] and Shan et al. [30] performed axial compression tests on FRP fully confined square concrete columns (FFSC) with varying corner radius ratios $R_r = r/b \geq 0.05$, where b and r denote the cross-section size and corner radius, respectively. Results indicate that reducing R_r from 1 (circular) to 0 (sharp corners) significantly diminishes FRP confinement effectiveness due to horizontal arching and stress concentration at the corners. Low R_r FFSC columns, especially lightly confined HSC/UHSC specimens, are more prone to post-peak strain-softening behavior [18, 31-35]. Similarly, Ozbakkaloglu [13] and Isleem Haytham et al. [1] studied FRP-confined rectangular columns (FFRC) with different aspect ratios R_{sar} = h / b, finding that confinement is less effective than in FFSC because of intensified horizontal arching. As R_{sar} increases, higher FRP stiffness is required to avoid strain-softening [15, 36-38]. In this study, the reduced effectiveness of FRP confinement in non-circular columns (FFSC/FFRC) compared to circular ones (FFCC) is defined as the "Non-circularity Effect," indicating that greater FRP stiffness is needed to achieve a post-peak strain-hardening response.

Numerous models have been developed to predict the axial stress–strain behavior of FRP-confined concrete [39-48], generally classified into analysis-oriented models (AOMs) and design-oriented models (DOMs). AOMs typically involve two steps: (i) determining the FRP confining stress–strain relationship using a dilation model, and (ii) deriving the concrete axial stress from the FRP confining stress via a base model originally developed for actively confined concrete. DOMs, on the other hand, provide a simpler approach through closed-form expressions for critical stress–strain points, calibrated from experimental results. For example, Lam and Teng [49] proposed a parabolic-linear DOM for fully FRP-confined circular concrete (FFCC) specimens with normal-strength concrete (NSC), which Teng et al. [50] later refined using AOM-generated data to update ultimate condition parameters and define a confinement stiffness threshold separating strain-hardening from strain-softening responses. Fallah Pour et al. [51] extended DOM formulations to FFCC specimens with both NSC and high-strength concrete (HSC), though applicability remained limited to strain-hardening behavior. To predict the peak axial compressive strength (f_{cc}) of fully FRP-confined concrete columns, many models have been proposed; however, most are restricted to specific cross-section shapes (circular or square) and often do not account for the full range of geometric and material variations. For fully confined columns, more reliable predictive models can be developed using regression analysis that unifies cross-sectional effects. Some generalized models for fully confined circular (FFCC) and non-circular (FFSC/FFRC) columns have been proposed in the literature (e.g., fib [52], ACI [53]), incorporating confinement efficiency factors to account for vertical and horizontal arching actions. Nevertheless, most existing models were calibrated using limited experimental databases, often covering a narrow range of parameters such as confinement stiffness, concrete strength, and specimen geometry [54]. This restricts their predictive reliability when applied to broader datasets encompassing a wider spectrum of concrete strengths, FRP properties, and column geometries. The accuracy and robustness of regression-based predictive formulations fundamentally depend on the quality, diversity, and comprehensiveness of the experimental database used for calibration. A high-quality database must include a broad range of key parameters (concrete compressive strength, FRP mechanical properties, column geometry, and confinement configurations) to capture both individual and interactive effects on structural behavior. Sparse or biased datasets can lead to models valid only within limited parameter ranges, reducing generalizability and reliability. By contrast, a comprehensive and statistically representative database enables rigorous regression analysis, allowing the derivation of model coefficients that reflect both mean behavior and variability in experimental outcomes. This ensures that the resulting predictive formulation can reliably estimate ultimate axial strength, strain capacity, and full stress–strain behavior for various fully confined concrete columns, while also providing a solid foundation for uncertainty quantification in practical design applications.

In this study, a new design-oriented constitutive model is developed to predict the ultimate compressive strength of circular and non-circular concrete columns confined with FRP jackets. The model is grounded in a physically consistent framework that explicitly accounts for the "Non-circularity Effect", as the progressive loss of confinement efficiency due to cross-sectional geometry, through continuous correction functions of corner radius (R_r) and aspect ratio (R_{sar}). Unlike conventional approaches that treat circular and non-circular sections separately or apply discrete reduction factors, the proposed formulation ensures a smooth transition in predicted strength from circular to square and rectangular geometries, reflecting the underlying mechanics of lateral strain incompatibility and arching action. To support robust regression calibration, an extensive and diverse experimental database of 1723 FRP-confined column tests was compiled, encompassing a wide spectrum of concrete strengths (6.6–204 MPa), FRP material properties (modulus: 13.6–657 GPa; ultimate strain: 0.004–0.037), and geometric configurations (including sharp and rounded corners, and aspect ratios up to 2.0). This database enables the identification of key governing parameters and the development of a unified strength prediction equation that satisfies fundamental physical limits, such as reducing to unconfined strength when confinement stiffness vanishes, and degrading realistically as section shape deviates from circularity. The resulting model is not only statistically validated across all column types but also rigorously tested for parameter sensitivity and boundary consistency, establishing a reliable foundation for both practical design applications and future analytical advancements in FRP-confinement modeling.

2. Research significance

The novelty of the present study lies in its development of a unified, regression-based model for predicting the ultimate compressive strength of FRP-confined concrete columns that explicitly accounts for cross-sectional geometry. Unlike most existing formulations, which either treat circular and non-circular sections separately or rely on ad hoc reduction factors, the proposed model systematically incorporates the mechanics of confinement degradation in non-circular sections through continuous correction functions of corner radius (R_r) and aspect ratio (R_{sar}). This approach ensures a smooth and physically consistent transition in predicted strength from circular to square and rectangular columns, accurately reflecting stress concentrations, lateral strain incompatibility, and horizontal arching effects. The model is calibrated and validated against a large and diverse experimental database of 1,723 FRP-confined column tests, covering a broad range of concrete strengths (6.6–204 MPa), FRP properties (modulus: 13.6–657 GPa; ultimate strain: 0.004–0.037), and geometric configurations, including sharp and rounded corners and aspect ratios up to 2.0. By combining rigorous regression analysis with mechanically grounded correction factors, the study addresses limitations of prior models that were restricted to specific geometries or limited datasets, providing a physically consistent, statistically robust, and practically applicable predictive tool. This advancement bridges the gap between idealized confinement theory and real-world column geometries, offering engineers a unified framework for design and assessment while establishing a foundation for future refinement and recalibration as additional experimental data become available.

3. Compressive behavior of unconfined and FRP-confined concrete

Concrete subjected to axial compressive loading develops a certain level of axial shortening associated with an axial strain εc corresponding to the applied compressive stress f_c. According to Poisson's effect, this axial strain simultaneously generates a lateral (radial) strain $\varepsilon_l = \nu \times \varepsilon_c$, where ν is the Poisson's ratio. The continuous increase of lateral dilation during loading initiates internal microcracking, which subsequently evolves into visible cracking within the concrete matrix [38, 55]. As illustrated in Fig. 1, the stress–strain response ($f_c - \varepsilon_c$) of unconfined concrete is initially linear up to approximately 50% of its peak compressive strength ($0.5f_{c0}$). In this linear region, the slope of the curve corresponds to the elastic modulus of concrete E_c. Beyond this linear-elastic range and up to the peak stress (f_{cc}), diagonal and longitudinal microcracks begin to form and grow, causing the ascending branch of the $f_c - \varepsilon_c$ curve to deviate from linearity. This deviation is characterized by a gradual reduction in tangent stiffness due to progressive internal damage and stiffness degradation. The axial strain corresponding to the peak compressive stress, denoted as ε_{c0}, is commonly assumed to be approximately 0.002 for normal-strength unconfined concrete [56, 57]. After reaching this peak, concrete exhibits no further capacity to resist additional compressive load, and the widening of diagonal and longitudinal cracks becomes more pronounced. Consequently, the compressive stiffness drops significantly, and the stress–strain curve transitions into a descending (softening) branch, marking the onset of brittleness and instability within the concrete. This post-peak softening behavior is a fundamental characteristic of unconfined concrete and is closely associated with unstable crack propagation, volumetric expansion, and rapid loss of load-carrying capacity.

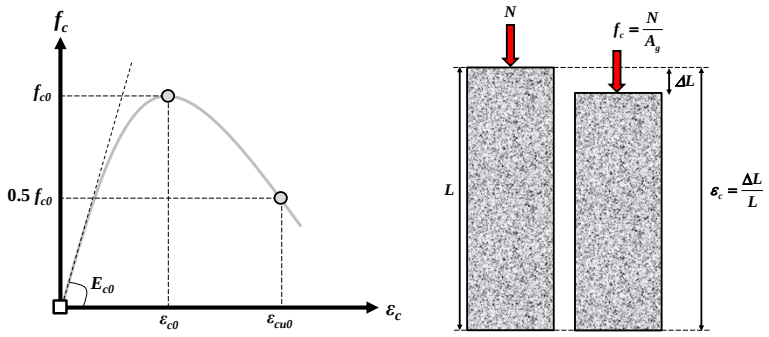

Fig. 1. Axial behavior of unconfined concrete.

The confinement mechanism developed in FRP-jacketed concrete columns is fundamentally governed by the interaction between the axial compression-induced dilation of concrete and the tensile resistance of the surrounding FRP jacket [58]. When the concrete is subjected to an axial compressive strain ε_c, a corresponding lateral (radial) strain $\varepsilon_l = \nu \times \varepsilon_c$ is generated due to Poisson's effect, where ν denotes the Poisson's ratio of uncracked concrete (Fig. 2). This lateral strain, which arises from the volumetric expansion of the concrete core, directly transforms into hoop strain in the confining jacket because, under perfect confinement conditions, the radial strain of the concrete is equal to the hoop strain of the jacket ($\varepsilon_h = \varepsilon_l$) [49]. Assuming full strain compatibility at the concrete–FRP interface (an assumption widely adopted in confinement mechanics due to the high stiffness and minimal slip of bonded FRP systems), the induced hoop strain in the concrete is transmitted to the FRP jacket as tensile hoop strain $\varepsilon_{h,f}$. Therefore, $\varepsilon_{h,f} = \varepsilon_h = \varepsilon_l = \nu \times \varepsilon_c$. Consequently, generating a certain axial strain in the concrete necessarily requires the development of a proportional tensile strain in the FRP jacket, which in turn mobilizes a tensile stress $f_f = E_f \times \varepsilon_{h,f}$. The tensile stress carried by the FRP is then converted into an effective lateral confining pressure $f_{l,f}$ acting on the concrete core. This pressure acts in opposition to the dilation of the concrete and effectively suppresses the transversal expansion that drives microcracking and loss of stiffness. From a mechanical standpoint, this process implies that, under axial compression, an FRP-confined concrete element must attain a higher axial compressive stress f_c than an unconfined concrete element to reach the same levels of axial and lateral strain. The additional axial stress reflects the work required to engage the FRP jacket in tension and develop the confinement pressure. As loading progresses, the confinement pressure increases approximately in proportion to the tensile strain in the FRP, leading to a triaxial state of stress

within the concrete. This triaxial confinement delays crack propagation, enhances compressive strength, and significantly improves post-peak ductility. The overall effect of the FRP jacket, therefore, is to constrain both axial shortening and lateral dilation of the concrete, mitigating the mechanisms that otherwise lead to rapid stiffness degradation and brittle collapse. This interaction, where axial compression induces lateral tension in the confining system, which in turn provides radial restraint, is the essence of the FRP confinement mechanism.

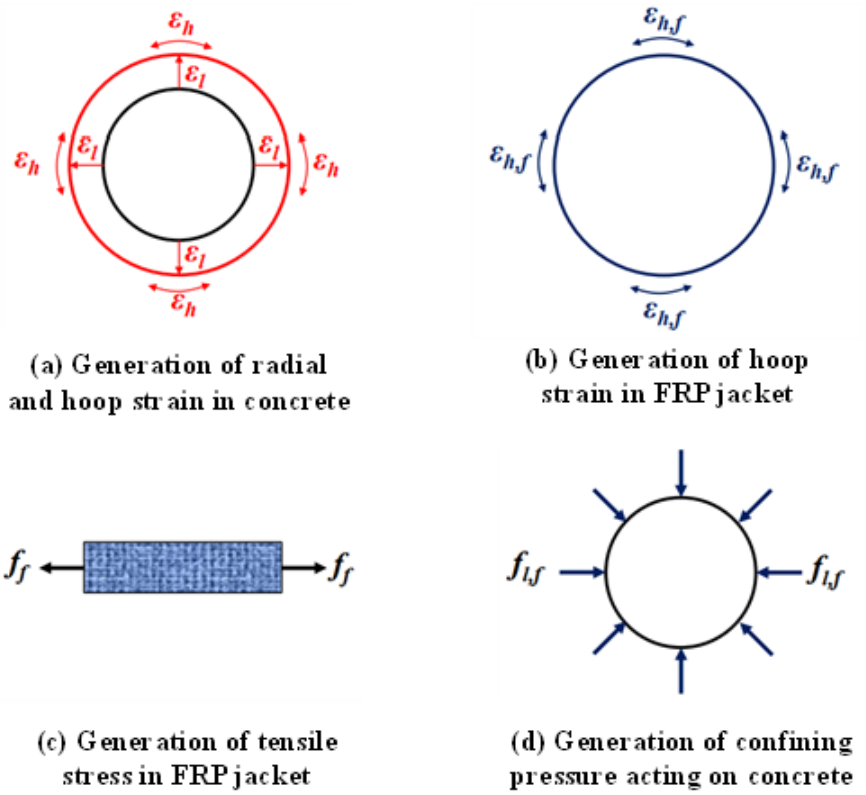

Fig. 2. FRP confinement mechanism.

4. General structure of regression-based formulation

In regression-based models, the normalized compressive strength of FRP-confined concrete is typically expressed as a function of key confinement and material parameters. In general, the normalized compressive strength of FRP-confined concrete can be expressed in a generic form as:

$$\frac{f_{cc}}{f_{c0}} = 1 + \Delta_f \tag{1}$$

Where Δ_f represents the confinement-induced strength gain beyond the unconfined capacity f_{c0}. To obtain a formulation suitable for regression analysis (and to explicitly express Δ_f as a function of the governing parameters), the above relation is rearranged into the standard predictive format:

$$\frac{f_{cc}}{f_{c0}} = \Delta_f \geq 1 \tag{2}$$

Experimental evidence indicates that the compressive strength of axially loaded FRP-confined circular concrete columns is governed primarily by four key parameters [32, 34, 59]: (1) the confinement stiffness of the FRP system, (2) the ultimate tensile strain of the FRP jacket, (3) the compressive strength of the unconfined concrete, and (4) the column dimension size. Considering the key mechanical factors affecting the confinement mechanism, the following general form is proposed for the regression-based predictive model:

$$\frac{f_{cc}}{f_{c0}} = \beta_1 {K_L}^{\beta_2} {\varepsilon_{fu}}^{\beta_3} {f_{c0}}^{\beta_4} {R_b}^{\beta_4} \geq 1 \tag{3}$$

in which

$$K_L = 2\frac{n_f t_f E_f}{b} \tag{4}$$

where β_1 to β_4 are empirical regression coefficients whose values will be calibrated using the constructed experimental database in the next sections. ($R_b = b/150$) denotes the normalized column dimension size, introduced to capture size-dependent confinement

efficiency. K_L is the FRP confinement stiffness, a parameter widely recognized as the dominant factor governing strength enhancement in FRP-confined concrete. εfu is the ultimate hoop tensile strain of the FRP jacket.

It should be emphasized that the influence of column non-circularity is incorporated into the proposed formulation through physically motivated reduction factors applied to the confinement efficiency coefficient β_1. These reduction factors are expressed as continuous functions of the sectional aspect ratio and the corner radius ratio, which are the primary geometric parameters governing stress concentration at corners, non-uniform lateral confining pressure, and the presence of ineffective confinement zones in non-circular sections. By modifying β_1, the formulation directly reduces the effective confinement contribution provided by the FRP jacket, thereby reflecting the progressive loss of confinement efficiency as the cross-section deviates from a circular shape.

In addition, the proposed model satisfies essential physical boundary conditions. In the absence of effective confinement, represented by a vanishing confinement stiffness ($K_L \rightarrow 0$), the contribution of the FRP jacket diminishes, and the formulation correctly reduces to unity, indicating no confinement-induced strength enhancement. This behavior ensures consistency with unconfined concrete mechanics and confirms that the proposed expression is grounded in physical principles rather than purely empirical fitting.

5. Test database of FRP-confined concrete columns

In this study, an extensive experimental database was compiled from previously published test results reported in the literature as shown in Table 1. The database consists of concrete column specimens tested under concentric axial compressive loading and confined with externally bonded FRP jackets. No new experimental testing was conducted as part of the present work. To ensure a consistent, reliable, and unified database suitable for regression-based modeling, strict selection criteria were applied. Specimens containing conventional steel longitudinal or transverse reinforcement were excluded, as were specimens with partial confinement configurations or spiral wrapping systems. Tests in which FRP debonding governed the failure mode were not considered, nor were specimens confined using hybrid FRP systems composed of different fiber types. Columns subjected to eccentric axial loading were excluded to eliminate secondary bending effects. Experimental results for which the ultimate compressive strength of the confined specimen was lower than that of the corresponding unconfined concrete ($f_{cc} < f_{c0}$) were also excluded. Only specimens confined with FRP materials exhibiting linear tensile stress–strain behavior (namely CFRP, GFRP, BFRP, and AFRP) were included in the database. Specimens confined with PEN- or PET-based fibers, which exhibit nonlinear tensile behavior, were excluded to maintain material consistency across the dataset. The application of these criteria resulted in a comprehensive and internally consistent database of 1,723 test specimens, providing a reliable basis for model development and validation.

Analysis of the unconfined concrete strength (f_{c0}) indicates a wide range from 6.6 MPa to 204 MPa, with mean values of 45–48 MPa for circular and combined cross-section datasets, and slightly lower mean values for square (33.5 MPa) and rectangular (37.5 MPa) columns. The confined concrete strength (f_{cc}) ranges from 14.5 MPa to 381 MPa, yielding normalized strength ratios (f_{cc} / f_{c0}) from 1.02 to 6.9. Circular columns generally show a higher mean normalized strength (≈ 2.03) compared to square (1.63) and rectangular (1.27) columns, confirming the stronger confinement efficiency of circular geometries. Column dimensions in the dataset cover a substantial range: heights (L) from 100 mm to 1,200 mm and cross-sectional dimensions (b) from 50 mm to 400 mm. The FRP properties are equally diverse, with modulus of elasticity (E_f) varying from 13.6 GPa to 657 GPa and effective thickness ($n_f \times t_f$) from 0.004 mm to 9.754 mm. The ultimate FRP strain (ε_{fu}) spans 0.004–0.037, reflecting the range of fiber types and material qualities considered in the experiments. The coefficient of variation (CoV) for most parameters is significant, indicating considerable scatter in material properties, column dimensions, and FRP characteristics. This variability emphasizes the need for regression-based models that can capture the effects of both material and geometric parameters. Shape- and size-related factors (R_r and R_{sar}) show that correction factors can vary from 0.00 to 2.0, highlighting the impact of geometry and aspect ratio on confinement efficiency. The analysis of the compiled database demonstrates that FRP confinement substantially enhances the compressive strength of concrete, with circular columns showing the highest confinement efficiency, followed by square and rectangular sections. The dataset covers a wide range of concrete strengths, column sizes, FRP properties, and ultimate strains, providing significant variability that reflects realistic experimental conditions. This diversity ensures that the database is comprehensive and suitable for developing robust regression-based predictive models. The observed trends, including the influence of cross-sectional shape, FRP thickness, and material stiffness, highlight the critical parameters that govern the behavior of FRP-confined concrete. Overall, the database offers a solid foundation for accurate strength prediction, model validation, and future parametric studies of FRP confinement effects.

Table 1. Details of the test database of FRP-confined circular/non-circular concrete columns.

Cross-Section type	No. of Data	Statistical Index	f_{c0} (MPa)	f_{cc} (MPa)	f_{cc} / f_{c0}	L (mm)	b (mm)	E_f (GPa)	$n_f \times t_f$ (mm)	ε_{fu}	R_r	R_{sar}
Circle, Square & Rectangle	1723	Minimum	6.6	14.5	1.02	100	50	13.6	0.057	0.004	0.07	1
		Maximum	204	381	6.9	1200	400	657	9.75	0.037	1	2
		Mean	45.8	79.7	1.92	327	147.5	193.7	0.58	0.018	0.87	1.05
		Cov	0.7	0.42	0.61	0.42	0.31	0.48	1.29	0.3	0.3	0.19
Circle	1376	Minimum	6.6	17.8	1.05	100	50	13.6	0.057	0.004	1	1
		Maximum	204	381	6.9	915	305	657	5.1	0.037	1	1
		Mean	48.5	87.4	2.03	301	144	190	0.581	0.018	0	0

		Cov	0.71	0.58	0.41	0.37	0.31	0.52	1.19	0.32	0	0
Square	216	Minimum	8.7	14.5	1.05	200	100	13.6	0.117	0.009	0.07	1
		Maximum	77.2	114	4.32	1200	400	260	9.754	0.031	0.8	1
		Mean	33.5	51.2	1.63	419	172	204	0.596	0.004	0.35	0
		Cov	0.41	0.34	0.33	0.4	0.32	0.33	1.56	0.2	0.52	0
Rectangle	131	Minimum	17.3	20.3	1.02	300	90	16.3	0.13	0.014	0.14	1.25
		Maximum	79.6	95.9	2.54	1000	203	257	9.754	0.021	0.67	2
		Mean	37.5	46	1.27	442	141	219	0.573	0.017	0.38	1.71
		Cov	0.43	0.36	0.2	0.43	0.21	0.25	1.64	0.1	0.36	0.16

6. Proposed formula for non-circular FRP-confined concrete columns

In the present study, the experimental data from the database were used to determine the coefficients of Eq. 3. Based on 1,376 experimental specimens of 'circular' concrete columns, a relationship between the ratio of the maximum compressive strength of confined concrete (f_{cc} / f_{c0}) and the key parameters ε_{fu}, K_L, f_{c0} and R_b is proposed as follows:

$$\frac{f_{cc}}{f_{c0}} = 3.1{K_L}^{0.36}{\varepsilon_{fu}}^{0.23}{f_{c0}}^{-0.55}{R_b}^{-0.14} \geq 1 \quad (5)$$

Based on the experimental results reported by Wang and Wu [29], the effect of confinement in enhancing the axial behavior of concrete columns with square cross-sections is less pronounced than in columns with circular cross-sections. This is due to the stress concentration at the corners of the square section, which reduces the effectiveness of confinement in controlling the lateral expansion of concrete. Moreover, because of the horizontal arching action in the confinement mechanism, some regions of the cross-section experience ineffective confinement. Consequently, the axial behavior of the concrete in these regions is similar to that of unconfined concrete. An experimental study conducted by Shan et al. [30] showed that with increasing corner radius r of non-circular sections, from $r = 0$ (representing a square section with sharp corners) to $r = 2b$ (representing a circular section), the effectiveness of FRP confinement improves. In the present study, to investigate the effects of this parameter, Eq. 5, which was originally proposed exclusively for circular sections, was used to predict the maximum confined compressive strength (f_{cc} / f_{c0}) of square concrete columns. Fig. 3a illustrates the relationship between the analytical-to-experimental results ($\beta_r = f_{cc} / f_{c0}$) and the corner radius factor ($R_r = 2r / b$) based on 216 experimental specimens. As can be observed, reducing R_r from 1 (representing a circular section) to values close to zero leads to non-conservative predictions for square columns. The dependence of the error (β_r) on R_r indicates that the experimental results are a function of the corner radius, and therefore, the effects of section rounding must be considered in the analytical model. By performing regression analysis on the 216 experimental data points of FRP-confined square columns, the relationship between the error (β_r) and R_r was obtained as follows:

$$\beta_r = \frac{{f_{cc}}^{Ana}}{{f_{cc}}^{Exp}} = 0.91{R_r}^{-0.34} \geq 1 \quad (6)$$

Therefore, by substituting Eq. 6 into Eq. 5, the proposed formula for square concrete columns confined with FRP jackets is obtained as follows:

$$\frac{f_{cc}}{f_{c0}} = \frac{3.1}{\beta_r}{K_L}^{0.36}{\varepsilon_{fu}}^{0.23}{f_{c0}}^{-0.55}{R_b}^{-0.14} \geq 1 \quad (7)$$

Based on the statistical indices, as shown in Fig. 3b, Eq. 7 provides accurate predictions of the maximum compressive strength of square concrete columns confined with FRP jackets. Fig. 3c illustrates the relationship between the prediction error of Eq. 7 and the corner radius factor. As can be observed, after applying the correction factor in the proposed equation, the resulting error shows no correlation with the factor (R_r), indicating that the effects of this parameter have been correctly captured in the proposed formula.

Based on the experimental results reported by Ozbakkaloglu [13], and Triantafillou et al. 2016, the effect of FRP confinement on concrete columns with rectangular cross-sections is smaller compared to circular and square columns. Even for rectangular columns with an aspect ratio ($R_{sar} = h / b$) greater than approximately 2, the effects of confinement on concrete behavior are almost negligible. The primary reason is the significant negative influence of the horizontal arching action within the confinement mechanism. Consequently, most regions of the cross-section are subjected to ineffective confinement and exhibit behavior similar to unconfined concrete under axial loading. As a result, increasing R_{sar} from a value of 1 (with $R_{sar} = 1$ representing a square column) reduces the effectiveness of FRP confinement on rectangular concrete columns.

In this study, to investigate the effects of the R_{sar} parameter, Eq. 7, which was originally proposed exclusively for circular/square sections, was used to predict the maximum confined compressive strength (f_{cc} / f_{c0}) of rectangular concrete columns. Fig. 4a shows the relationship between the analytical-to-experimental results ($\beta_{sar} = {f_{cc}}^{Ana} / {f_{cc}}^{Exp}$) and the aspect ratio R_{sar} based on 131 experimental specimens. As can be seen, increasing R_{sar} from 1 (representing a square section) leads to non-conservative predictions for rectangular columns. The dependence of the error (β_{sar}) on R_{sar} indicates that the experimental results are a function of the aspect ratio, and therefore, the effects of R_{sar} must be considered in the analytical model.

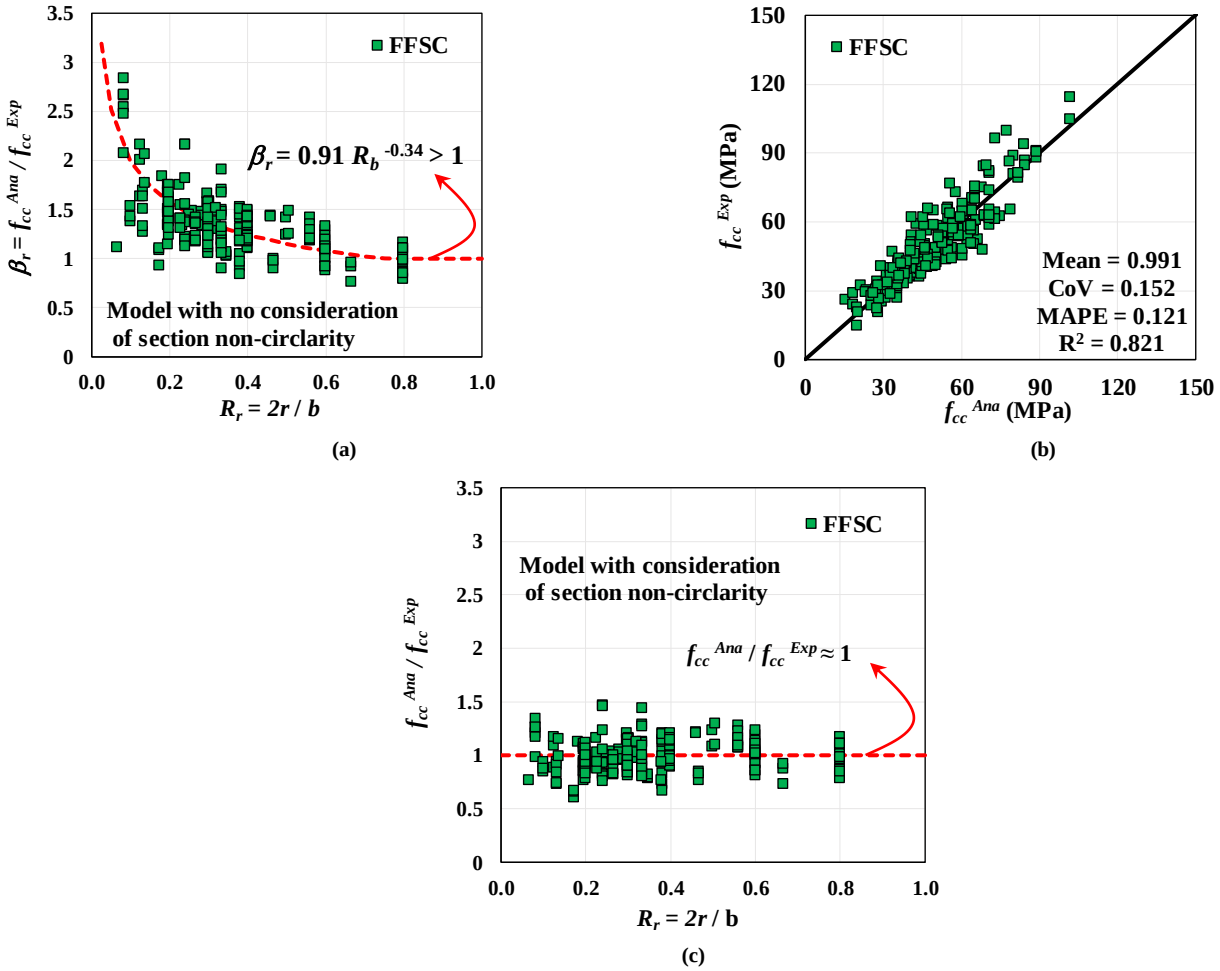

Fig. 3. Evaluation of the predicted results from the proposed model for f_{cc} of square columns based on 216 test specimens.

By performing regression analysis on the 131 experimental data points of FRP-confined rectangular columns, the relationship between the error (β_{sar}) and R_{sar} was obtained as follows:

$$\beta_{sar} = \frac{f_{cc}^{Ana}}{f_{cc}^{Exp}} = 0.95 {R_{sar}}^{0.78} \geq 1 \tag{8}$$

Therefore, by substituting Eq. 8 into Eq. 7, the proposed formula for rectangular concrete columns confined with FRP jackets is obtained as follows:

$$\frac{f_{cc}}{f_{c0}} = \frac{3.1}{\beta_r \beta_{sar}} {K_L}^{0.36} {\varepsilon_{fu}}^{0.23} {f_{c0}}^{-0.55} {R_b}^{-0.14} \geq 1 \tag{9}$$

Based on the statistical indices, as shown in Fig. 4b, Eq. 9 provides accurate predictions of the maximum compressive strength of rectangular concrete columns confined with FRP jackets. Fig. 4c illustrates the relationship between the prediction error of Eq. 9 and the aspect ratio factor R_{sar}. As can be observed, after applying the β_{sar} correction factor in the proposed equation, the resulting error shows no significant correlation with β_{sar}, indicating that the effects of this parameter have been correctly captured in the proposed formula.

It should be emphasized that Eq. 9 is formulated to be universally applicable to all column shapes, including circular, square, and rectangular sections. This generality is particularly important because the confinement effectiveness of FRP jackets is strongly influenced by cross-sectional geometry, corner rounding, and aspect ratio, which can vary significantly across different column shapes. To assess the robustness and predictive capability of the proposed formula, its performance was evaluated using the entire experimental database, encompassing 1,723 specimens with a wide range of dimensions, material properties, and FRP configurations.

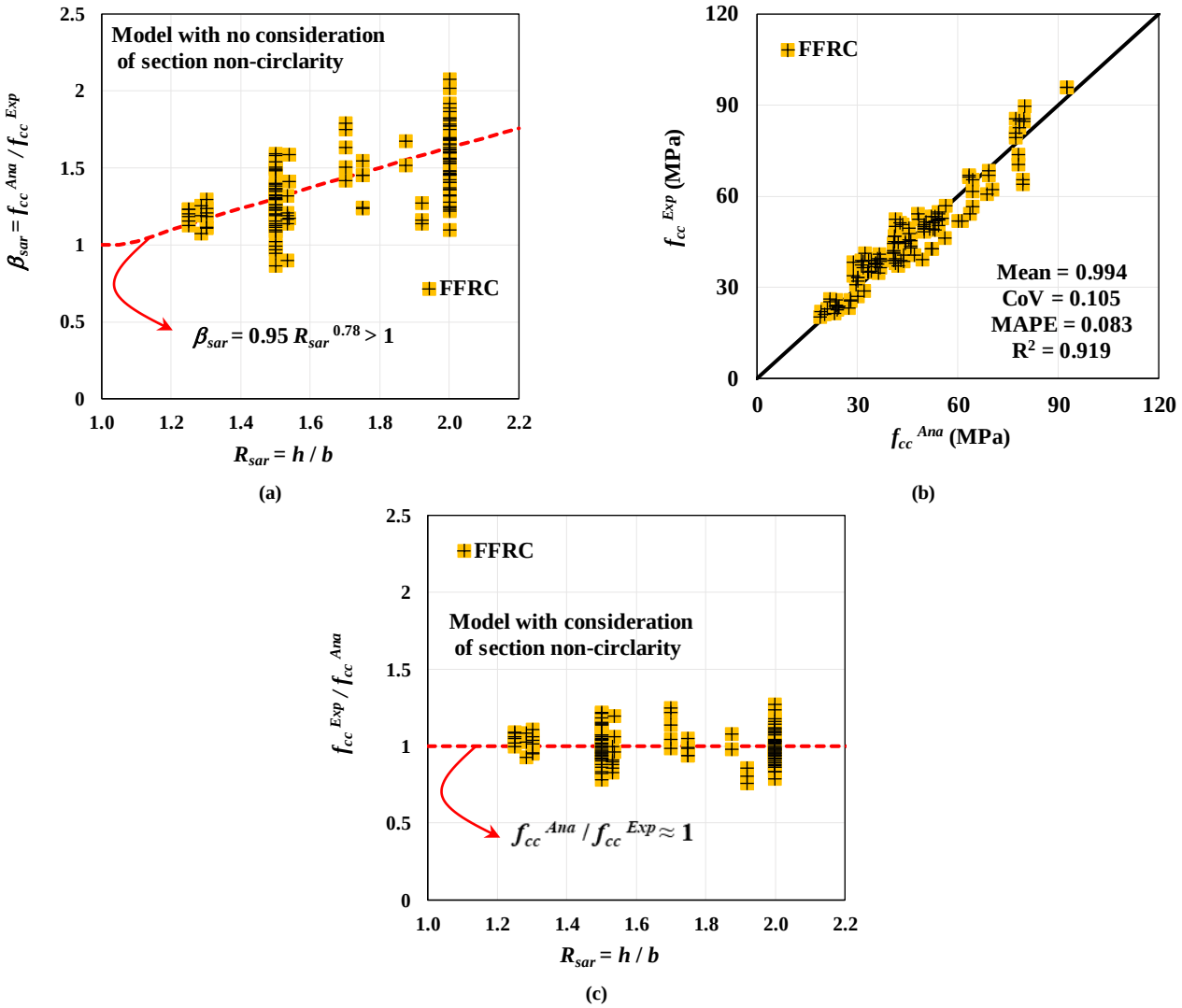

Fig. 4. Evaluation of the predicted results from the proposed model for the maximum compressive strength of rectangular columns based on 131 experimental specimens.

Fig. 5 presents a comparison between the experimental results and the predictions obtained using Eq. 9. The figure demonstrates a strong correlation between the predicted and measured maximum compressive strengths across all column shapes. Statistical indicators, including mean error, standard deviation, and coefficient of variation, confirm that the proposed formula provides accurate and reliable predictions for a diverse set of experimental conditions. In particular, the formula successfully captures the variations in confinement effectiveness due to cross-sectional shape and aspect ratio, which have been identified as critical factors in previous studies. The high accuracy of Eq. 9 is significant for several reasons. First, it allows structural engineers and researchers to reliably estimate the ultimate strength of FRP-confined concrete columns without the need for extensive experimental testing, reducing both cost and time. Second, its applicability across multiple geometries ensures that the formula can be used in practical design scenarios, where columns may not always be perfectly circular or square. Finally, the validation against a large experimental database demonstrates the robustness of the model, highlighting its potential for use in design codes and guidelines for FRP-confined concrete structures. Overall, Eq. 9 provides a comprehensive and versatile predictive tool for evaluating the axial performance of FRP-confined concrete columns under a wide range of conditions.

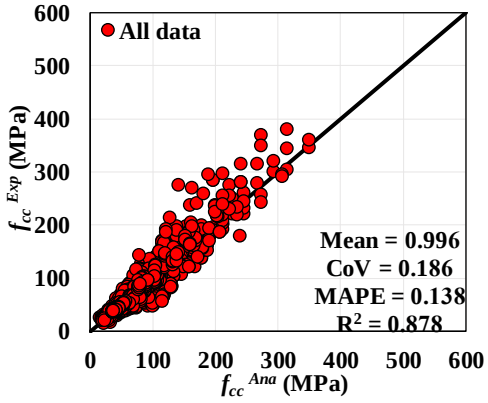

Fig. 5. Comparison of the predicted maximum compressive strength of circular, square, and rectangular columns using the proposed model based on 1,723 experimental specimens.

7. Comparison of the proposed model with existing models

7.1. Circular concrete columns

Table 2 compares the predictions of circular FRP-confined concrete columns from existing analytical models [39, 40, 52, 53, 60] and the proposed model. Statistical indices include MAPE, MSE, CoV, MV, and R^2. Among the existing models, the fib [52] model demonstrates the best performance, with relatively low error and variability (MV = 0.892, CoV = 0.226), although it slightly underestimates the experimental data. In contrast, Cao et al. [39] produces non-conservative predictions with high scatter. The proposed model consistently outperforms all existing models across these indices. This superior performance is attributable to several factors. First, the large and diverse experimental database used for calibration, covering a wide range of concrete strengths, FRP properties, and column dimensions, provides a robust foundation for accurately capturing confinement behavior. Unlike many existing models, which were calibrated for a limited concrete class or narrower dataset, the proposed model explicitly incorporates the effect of the unconfined concrete strength on the confinement response. Second, the model incorporates physically consistent relationships between the FRP confinement and concrete response, including FRP stiffness, ultimate strain, and column diameter. The combined consideration of unconfined concrete strength and FRP properties ensures accurate prediction across the full spectrum of material strengths. In contrast, existing models are often less generalizable, performing reliably only for the concrete classes and column sizes represented in their original calibration datasets.

7.2. Square concrete columns

Table 3 presents the comparison for square columns. Both the proposed model and Cao et al. [39] perform well, but the proposed model provides consistently accurate predictions across all 216 specimens. Other models, such as Guo et al. [40], produce overly conservative predictions with high scatter. Mechanistically, the superior performance of the proposed model is rooted in both its large, diverse experimental database and its physically consistent treatment of geometric effects. The database of 1,723 specimens spans circular, square, and rectangular columns with a wide range of aspect ratios and corner radius ratios, providing sufficient coverage to calibrate the influence of non-circularity accurately. The proposed model incorporates continuous geometric correction factors based explicitly on sectional aspect ratio and corner radius, allowing it to reflect the progressive reduction in confinement efficiency caused by corner stress concentrations, non-uniform lateral pressure distribution, and partially ineffective confinement zones. In contrast, most existing models were developed using smaller, less diverse datasets, often dominated by circular sections, and typically incorporate geometric effects through simplified or discrete reduction factors. This limits their ability to capture the nuanced impact of cross-sectional shape on confinement performance, leading to either overly conservative or non-conservative predictions for non-circular columns. By combining a large, representative database with continuous, mechanistically motivated geometric corrections, the proposed model achieves consistently accurate and robust predictions across all column geometries.

7.3. Rectangular concrete columns

Table 4 summarizes the comparison for rectangular columns. Again, the proposed model and Cao et al. [39] show the best performance, with the proposed model providing slightly more precise predictions for the 131 experimental specimens. The proposed model maintains low MAPE and MSE values while achieving high R^2, demonstrating its ability to capture the effects of aspect ratio and cross-sectional geometry accurately. Other models, particularly Guo et al. [40], perform poorly with highly conservative predictions and large scatter. This improved performance of the proposed model stems from its explicit consideration of section aspect ratio and corner radius, which govern the distribution of lateral confinement, stress concentrations at corners, and partially ineffective confinement zones. Existing models often use simplified or discrete reduction factors and were calibrated with smaller datasets, limiting their ability to represent continuous variations in confinement efficiency for high aspect ratios. By contrast, the proposed model applies continuous geometric correction factors, enabling it to accurately capture the gradual decrease in confinement effectiveness as the rectangular section becomes more elongated, while also accounting for the influence of the unconfined concrete strength and FRP properties on axial compressive behavior.

7.4. Overall performance across all column shapes

Table 5 compares the predictions of all models against the full experimental dataset of 1,723 specimens encompassing circular, square, and rectangular columns. The fib [52] model performs well but slightly underestimates the experimental data, while Guo et al. [40] is the least accurate, producing highly conservative predictions. The proposed model consistently achieves high accuracy across all column shapes, with low MAPE, MSE, and CoV values and R^2 close to 0.92, demonstrating its robustness and reliability. This uniform performance is attributable to the model's mechanistic incorporation of geometric effects through continuous aspect ratio and corner radius correction factors, along with explicit consideration of unconfined concrete strength, FRP stiffness, and ultimate FRP strain. Unlike many existing models, which may be accurate only within the limited geometries and material ranges used for their calibration, the proposed model captures the combined influence of section shape, size, and material properties. This demonstrates that its improved predictive performance is not solely due to the larger database but is fundamentally based on a physically grounded and unified formulation, enabling robust and reliable predictions for arbitrary column geometries.

Table 2. Comparison of existing analytical models predictions of ultimate strength for circular FRP-confined concrete columns.

Analytical Model	R^2	MAPE	MSE	CoV	MV
ACI [53]	0.812	0.189	0.375	0.279	0.938
fib [52]	0.82	0.185	0.343	0.226	0.892
Cao et al. [39]	0.782	0.257	1.03	0.313	1.219

Wei and Wu [60]	0.812	0.189	0.426	0.282	1.078
Guo et al. [40]	0.82	0.266	0.628	0.252	0.77
Proposed Model	0.865	0.145	0.202	0.197	0.996

Table 3. Comparison of existing analytical models predictions of ultimate strength for square FRP-confined concrete columns.

Analytical Model	R^2	MAPE	MSE	CoV	MV
ACI [53]	0.909	0.212	0.167	0.164	0.679
fib [52]	0.895	0.18	0.18	0.153	0.782
Cao et al. [39]	1.05	0.156	0.085	0.132	0.824
Wei and Wu [60]	0.994	0.163	0.102	0.124	0.796
Guo et al. [40]	0.788	0.2	0.336	0.229	0.671
Proposed Model	0.991	0.152	0.076	0.121	0.821

Table 4. Comparison of existing analytical models predictions of ultimate strength for rectangular FRP-confined concrete columns.

Analytical Model	R^2	MAPE	MSE	CoV	MV
ACI [53]	1.046	0.141	0.037	0.128	0.857
fib [52]	1.02	0.154	0.037	0.133	0.873
Cao et al. [39]	1.044	0.113	0.026	0.105	0.93
Wei and Wu [60]	1.122	0.116	0.044	0.144	0.919
Guo et al. [40]	1.338	0.258	0.367	0.351	0.688
Proposed Model	0.994	0.105	0.018	0.083	0.919

Table 5. Comparison of existing analytical models predictions of ultimate strength for circular/square/rectangular FRP-confined concrete columns.

Analytical Model	R2	MAPE	MSE	CoV	MV
ACI [53]	0.943	0.264	0.323	0.181	0.825
fib [52]	0.902	0.218	0.299	0.177	0.833
Cao et al. [39]	1.184	0.299	0.832	0.229	0.805
Wei and Wu [60]	1.071	0.263	0.355	0.177	0.83
Guo et al. [40]	0.816	0.314	0.571	0.268	0.795
Proposed Model	0.996	0.186	0.173	0.138	0.878

8. Error analysis of the proposed model based on key parameters

To further assess the accuracy of the proposed model in predicting the maximum compressive strength of FRP-confined concrete columns, the ratio of analytical results to experimental data ($Y = f_{cc}^{Ana}/f_{cc}^{Exp}$) was analyzed for 1,723 experimental specimens. The variation of Y with respect to key parameters (X) is illustrated in Fig. 6. Here, Fig. 6a shows the relationship between Y and the lateral confinement stiffness parameter (K_L). Regression analysis yields $Y = 0.9811+1\times10^{-5}\,X$. The near-zero coefficient and very low R^2 indicate that the prediction error of the proposed model is independent of the stiffness level of the FRP confinement. This demonstrates that the model accurately captures the influence of confinement stiffness on the maximum compressive strength of FRP-confined columns. Fig. 6b presents Y versus the unconfined concrete compressive strength (f_{c0}). Regression produces $Y = 0.9948+2\times10^{-5}\,X$. Again, the coefficient is near zero and R^2 is minimal, indicating that the model error is independent of concrete strength. This confirms that the proposed model can accurately simulate the effect of different concrete strength levels, including low-, normal-, high-, and ultra-high-strength concrete, on the confined column strength. Fig. 6c illustrates Y as a function of the FRP ultimate tensile strain (ε_{fu}), giving $Y = 0.9347+3.3629X$. The very low coefficient and R^2 confirm minimal error dependency on FRP strain. However, for small values of $\varepsilon_{fu} \leq 0.005$, corresponding to high-modulus FRP sheets, the model slightly overestimates strength. For such cases, a reduction factor of approximately 0.66 is recommended. Overall, the proposed model correctly captures the influence of FRP strain on column strength. The effect of column dimensions, expressed as $X = b/150$, is shown in Fig. 6d. Regression yields $Y = 1.0271-0.0322X$. The near-zero coefficient and very low R^2 indicate that the model's error is not dependent on column size, confirming that the model properly accounts for geometric effects. Fig. 6e presents the relationship between Y and the corner radius of non-circular sections ($R_r = 2r/b$), giving Y=0.9814+0.0162X. The low coefficient and R^2 show negligible error dependency on corner rounding, demonstrating that the model can accurately simulate the effect of corner radius on the maximum compressive strength. Finally, Fig. 6f shows Y versus the section aspect ratio (h/b), with regression $Y = 0.9948+2\times10^{-5}\,X$. Again,

the near-zero coefficient and very low R^2 indicate that the model error is independent of the aspect ratio, confirming the model's ability to account for cross-sectional geometry effects. Overall, the analysis indicates that among all parameters, the FRP ultimate tensile strain exhibits the highest influence on prediction error ($R^2 = 0.0097$), whereas the unconfined concrete strength shows the least dependency ($R^2 \approx 7\times10^{-5}$). These results demonstrate that the proposed model reliably predicts the maximum compressive strength of FRP-confined concrete columns while accurately simulating the effects of key material and geometric parameters.

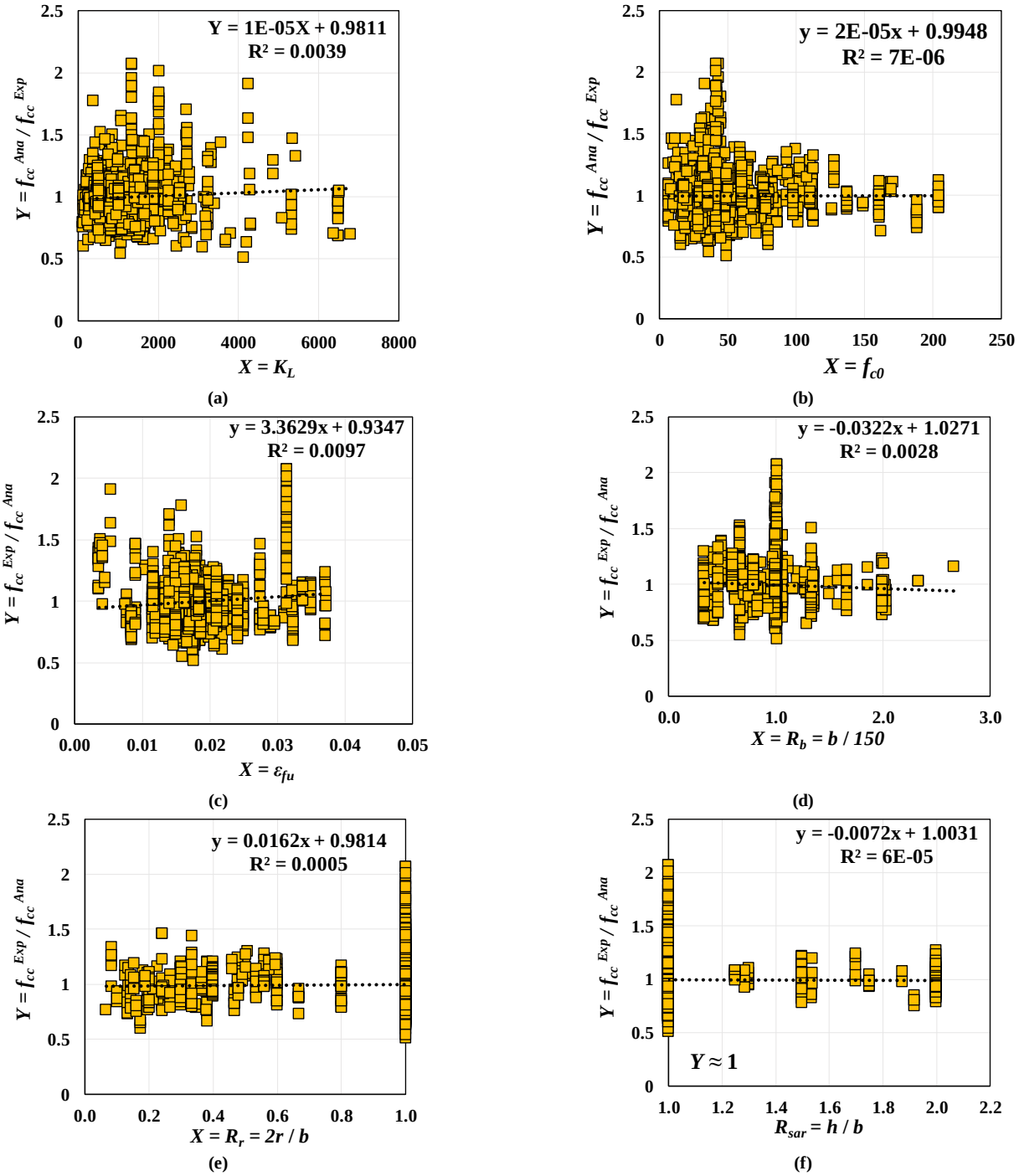

Fig. 6. Ratio of analytical to experimental results for 1,723 specimens, shown against key parameters affecting FRP confinement.

9. Conclusion

This study develops and validates a unified, regression-based model for predicting the compressive strength of FRP-confined concrete columns, explicitly considering the effects of cross-sectional geometry. The key contributions and findings are summarized as follows:

- Unified modeling approach: The proposed model provides a single, coherent framework applicable to circular, square, and rectangular columns, systematically integrating the influence of cross-sectional geometry on FRP confinement effectiveness. This unification ensures consistent predictive capability across diverse shapes, capturing both the enhanced confinement in circular sections and the reduced effectiveness in non-circular, cornered, or elongated geometries without requiring separate, shape-specific equations.

- Mechanically grounded correction factors: The model incorporates continuous, physically motivated correction factors for corner radius (R_r) and section aspect ratio (R_{sar}), which explicitly account for stress concentrations, non-uniform lateral pressure, and reduced arching action in non-circular sections. This approach provides a mechanistically justified representation of geometric effects, avoiding the need for ad hoc or arbitrary shape factors commonly used in previous models.
- Stepwise calibration: The model was developed in a systematic, stepwise manner, starting with a baseline formulation derived from 1,376 circular column specimens and subsequently extended to 216 square and 131 rectangular specimens. This approach ensures that critical physical mechanisms (such as stress concentrations at sharp corners and reduced arching action in elongated sections) are explicitly captured in the predictive equations, rather than being averaged out or obscured by purely empirical fitting.
- Extensive validation: The model was rigorously validated against a comprehensive experimental database of 1,723 specimens, spanning concrete strengths from 6.6 to 204 MPa, FRP moduli from 13.6 to 657 GPa, ultimate strains from 0.004 to 0.037, and column dimensions from 50 to 400 mm. It demonstrates high predictive performance (R^2 = 0.996, MAPE = 18.6%, CoV = 0.138) and consistently outperforms existing analytical and empirical models across circular, square, and rectangular sections, confirming both its accuracy and generalizability.
- Physical consistency: The model rigorously satisfies fundamental mechanical limits. It correctly reduces to the unconfined concrete strength as the FRP confinement stiffness $KL \rightarrow 0$, ensuring no artificial strength enhancement is predicted in the absence of confinement. For non-circular sections, it captures the progressive and physically realistic degradation of confinement effectiveness, reflecting the combined effects of corner stress concentrations, reduced arching action, and non-uniform lateral pressure. This allows smooth transitions in predicted strength from circular sections (maximal confinement efficiency) to square sections and further to increasingly slender rectangular geometries, maintaining a consistent and mechanically justified representation of how cross-sectional shape influences FRP confinement performance.
- Applicability and limitations: As with any regression-based model, predictive accuracy is limited by the quality and range of the database used; if a more extensive or diverse experimental dataset becomes available, the model can be recalibrated to extend its applicability. The current model is based on fully wrapped, axially loaded concrete columns confined with FRP materials exhibiting linear tensile behavior (CFRP, GFRP, BFRP, AFRP) and does not cover columns with eccentric loading, partial or spiral confinement, hybrid FRP systems, or FRP materials with nonlinear tensile behavior (e.g., PEN- or PET-based fibers). Specimens in which FRP debonding governed failure were excluded, so predictions for such cases may be less reliable. For very high-modulus, low-ductility FRP systems ($\varepsilon_{fu} \leq 0.005$), a conservative reduction factor (~0.66) is recommended.
- Practical significance: The model offers engineers a unified, closed-form predictive tool that seamlessly bridges idealized confinement theory and the geometric complexities of real-world columns. By accurately capturing the influence of cross-sectional shape, FRP properties, and concrete strength, it enables reliable, efficient, and physically grounded design and assessment of FRP-strengthened concrete structures, eliminating the need for multiple shape-specific formulations and reducing reliance on empirical approximations.

Statements & Declarations

Author contributions

Sajjad Shayanfar: Investigation, Formal analysis, Data curation, Software, Writing - Original Draft.

Meysam Ghasemi Naghibdehi: Project administration, Resources, Writing - Review & Editing.

Javad Shayanfar: Conceptualization, Methodology, Software, Writing - Review & Editing.

Funding

The authors received no financial support for the research, authorship, and/or publication of this article.

Data availability

The data presented in this study will be available on interested request from the corresponding author.

Declarations

The authors declare no conflict of interest.

References

[1] Isleem Haytham, F., Wang, Z., Wang, D., Smith Scott, T. Monotonic and Cyclic Axial Compressive Behavior of CFRP-Confined Rectangular RC Columns. Journal of Composites for Construction, 2018; 22: 04018023. doi:10.1061/(ASCE)CC.1943-5614.0000860.

[2] Nematzadeh, M., Mousavimehr, M., Shayanfar, J., Omidalizadeh, M. Eccentric compressive behavior of steel fiber-reinforced RC columns strengthened with CFRP wraps: Experimental investigation and analytical modeling. Engineering Structures, 2021; 226: 111389. doi:10.1016/j.engstruct.2020.111389.

[3] Liao, J., Zeng, J.-J., Zhuge, Y., Zheng, Y., Ma, G., Zhang, L. FRP-confined concrete columns with a stress reduction-recovery behavior: A state-of-the-art review, design recommendations and model assessments. Composite Structures, 2023; 321: 117313. doi:10.1016/j.compstruct.2023.117313.

[4] Wang, J., Xiao, H., Lu, L., Yang, J., Lu, S., Shayanfar, J. Axial stress-strain model for concrete in partially FRP wrapped reinforced concrete columns. Construction and Building Materials, 2024; 416: 135028. doi:10.1016/j.conbuildmat.2024.135028.

[5] Shayanfar, J., Barros Joaquim, A. O., Abedi, M., Rezazadeh, M. Unified Compressive Strength and Strain Ductility Models for Fully and Partially FRP-Confined Circular, Square, and Rectangular Concrete Columns. Journal of Composites for Construction, 2023; 27: 04023053. doi:10.1061/JCCOF2.CCENG-4336.

[6] Shayanfar, J., Barros, J. A. O., Pereira, J. P. C. A versatile model with a design framework for axially-loaded FRP-confined concrete with/without a stress reduction-recovery behavior. Construction and Building Materials, 2024; 448: 138097. doi:10.1016/j.conbuildmat.2024.138097.

[7] Shayanfar, J., Pereira, J. P. C., Barros, J. A. O. Passive confinement scenarios for strengthening fire-damaged concrete columns: Experimental and analytical research. Structures, 2025; 73: 108375. doi:10.1016/j.istruc.2025.108375.

[8] Shayanfar, J., Barros Joaquim, A. O. Design-Oriented Model of Unified Character to Determine Softening–Hardening Stress–Strain Behavior of FRP-Confined Concrete Columns of General Cross Section. Journal of Composites for Construction, 2024; 28: 04024059. doi:10.1061/JCCOF2.CCENG-4772.

[9] Shayanfar, J., Barros, J. A., Rezazadeh, M. Unified model for fully and partially FRP confined circular and square concrete columns subjected to axial compression. Engineering Structures, 2022; 251: 113355. doi:10.1016/j.engstruct.2021.113355.

[10] Shayanfar, J., Barros, J. A. O., Rezazadeh, M. Cross-sectional and confining system unification on peak compressive strength of FRP confined concrete. Structural Concrete, 2023; 24: 1531-1545. doi:10.1002/suco.202200105.

[11] Shayanfar, J., Barros, J. A. O., Rezazadeh, M., Kafshgarkolaei, H. J. Enhancing the performance of heat-damaged rectangular RC columns using prestressed FRP confinement. Construction and Building Materials, 2025; 501: 144346. doi:10.1016/j.conbuildmat.2025.144346.

[12] Ozbakkaloglu, T., Akin, E. Behavior of FRP-Confined Normal- and High-Strength Concrete under Cyclic Axial Compression. Journal of Composites for Construction, 2012; 16: 451-463. doi:10.1061/(ASCE)CC.1943-5614.0000273.

[13] Ozbakkaloglu, T. Axial Compressive Behavior of Square and Rectangular High-Strength Concrete-Filled FRP Tubes. Journal of Composites for Construction, 2013; 17: 151-161. doi:10.1061/(ASCE)CC.1943-5614.0000321.

[14] Wang, D. Y., Wang, Z. Y., Smith, S. T., Yu, T. Size effect on axial stress-strain behavior of CFRP-confined square concrete columns. Construction and Building Materials, 2016; 118: 116-126. doi:10.1016/j.conbuildmat.2016.04.158.

[15] Shayanfar, J., Bengar, H. A. A practical model for simulating nonlinear behaviour of FRP strengthened RC beam-column joints. Steel and Composite Structures, 2018; 27: 49-74. doi:10.12989/scs.2018.27.1.049.

[16] Shayanfar, J., Barros, J. A. O., Rezazadeh, M. Analytical model to predict axial stress-strain behavior of heat-damaged unreinforced concrete columns wrapped by FRP jacket. Engineering Structures, 2023; 289: 116244. doi:10.1016/j.engstruct.2023.116244.

[17] Shayanfar, J., Barros, J. A. O., Rezazadeh, M. Analysis-oriented model for partially FRP-and-steel-confined circular RC columns under compression. Engineering Structures, 2023; 276: 115330. doi:10.1016/j.engstruct.2022.115330.

[18] Li, P.-D., Zeng, Q., Jiang, J.-F. Stiffness-based stress–strain model of FRP-confined high-strength and ultra-high strength concrete column with various corner radii. Construction and Building Materials, 2023; 409: 133873. doi:10.1016/j.conbuildmat.2023.133873.

[19] Eid, R., Roy, N., Paultre, P. Normal- and High-Strength Concrete Circular Elements Wrapped with FRP Composites. Journal of Composites for Construction, 2009; 13: 113-124. doi:10.1061/(ASCE)1090-0268(2009)13:2(113).

[20] Wei, Y., Wu, Y.-F. Experimental Study of Concrete Columns with Localized Failure. Journal of Composites for Construction, 2016; 20: 04016032. doi:10.1061/(ASCE)CC.1943-5614.0000686.

[21] Fallah Pour, A., Nguyen, G. D., Vincent, T., Ozbakkaloglu, T. Investigation of the compressive behavior and failure modes of unconfined and FRP-confined concrete using digital image correlation. Composite Structures, 2020; 252: 112642. doi:10.1016/j.compstruct.2020.112642.

[22] Vincent, T., Ozbakkaloglu, T. Influence of concrete strength and confinement method on axial compressive behavior of FRP confined high- and ultra high-strength concrete. Composites Part B: Engineering, 2013; 50: 413-428. doi:10.1016/j.compositesb.2013.02.017.

[23] de Oliveira Diôgo, S., Raiz, V., Carrazedo, R. Experimental Study on Normal-Strength, High-Strength and Ultrahigh-Strength Concrete Confined by Carbon and Glass FRP Laminates. Journal of Composites for Construction, 2019; 23: 04018072. doi:10.1061/(ASCE)CC.1943-5614.0000912.

[24] Demir, U., Ispir, M., Sahinkaya, Y., Arslan, G., Ilki, A. Axial Behavior of Noncircular High-Performance Fiber-Reinforced Cementitious Composite Members Externally Jacketed by CFRP Sheets. Journal of Composites for Construction, 2019; 23: 04019022. doi:10.1061/(ASCE)CC.1943-5614.0000940.

[25] Shayanfar, J., Barros, J. A. O., Rezazadeh, M. Stress–strain model for FRP confined heat-damaged concrete columns. Fire Safety Journal, 2023; 136: 103748. doi:10.1016/j.firesaf.2023.103748.

[26] Shayanfar, J., Kafshgarkolaei, H. J., Barros, J. A. O., Rezazadeh, M. Unified strength model for FRP confined heat-damaged circular and square concrete columns. Composite Structures, 2023; 307: 116647. doi:10.1016/j.compstruct.2022.116647.

[27] Shayanfar, J., Barros Joaquim, A. O., Rezazadeh, M. Stress–Strain Model for FRP-Confined Circular Concrete Columns Developing Structural Softening Behavior. Journal of Composites for Construction, 2024; 28: 04023065. doi:10.1061/JCCOF2.CCENG-4364.

[28] Zeng, J.-J., Chen, J.-D., Liao, J., Chen, W.-J., Zhuge, Y., Liu, Y. Behavior of ultra-high performance concrete under true tri-axial compression. Construction and Building Materials, 2024; 411: 134450. doi:10.1016/j.conbuildmat.2023.134450.

[29] Wang, L.-M., Wu, Y.-F. Effect of corner radius on the performance of CFRP-confined square concrete columns: Test. Engineering Structures, 2008; 30: 493-505. doi:10.1016/j.engstruct.2007.04.016.

[30] Shan, B., Gui, F. C., Monti, G., Xiao, Y. Effectiveness of CFRP Confinement and Compressive Strength of Square Concrete Columns. Journal of Composites for Construction, 2019; 23: 04019043. doi:10.1061/(ASCE)CC.1943-5614.0000967.

[31] Han, Q., Yuan, W., Bai, Y., Du, X. Compressive behavior of large rupture strain (LRS) FRP-confined square concrete columns: experimental study and model evaluation. Materials and Structures, 2020; 53: 99. doi:10.1617/s11527-020-01534-4.

[32] Shayanfar, J., Rezazadeh, M., Barros, J., Ramezansefat, H. A New Dilation Model for FRP Fully/partially Confined Concrete Column Under Axial Loading. In: Proceedings of the 3rd RILEM Spring Convention and Conference (RSCC 2020); 2020 Mar 9-14; Cham, Switzerland. p. 435-446. doi:10.1007/978-3-030-76551-4_39.

[33] Shayanfar, J., Omidalizadeh, M., Nematzadeh, M. Analysis-oriented model for seismic assessment of RC jacket retrofitted columns. Steel and Composite Structures, 2020; 37: 371-390. doi:10.12989/scs.2020.37.3.371.

[34] Shayanfar, J., Barros, J. A. O., Rezazadeh, M. Generalized Analysis-oriented model of FRP confined concrete circular columns. Composite Structures, 2021; 270: 114026. doi:10.1016/j.compstruct.2021.114026.

[35] Cao, Y., Liu, Y., Li, X., Wu, Y. Axial stress strain behavior of FRP-confined rectangular rubber concrete columns with different aspect ratio. Engineering Structures, 2023; 297: 116987. doi:10.1016/j.engstruct.2023.116987.

[36] Abbasnia, R., Ziaadiny, H. Experimental investigation and strength modeling of CFRP-confined concrete rectangular prisms under axial monotonic compression. Materials and Structures, 2015; 48: 485-500. doi:10.1617/s11527-013-0198-y.

[37] Shayanfar, J., Bengar, H. A. Numerical model to simulate shear behaviour of RC joints and columns. Computers and Concrete, An International Journal, 2016; 18: 877-901. doi:10.12989/cac.2016.18.4.877.

[38] Shayanfar, J., Akbarzadeh Bengar, H. Nonlinear analysis of RC frames considering shear behaviour of members under varying axial load. Bulletin of Earthquake Engineering, 2017; 15: 2055-2078. doi:10.1007/s10518-016-0060-z.

[39] Cao, Y.-G., Jiang, C., Wu, Y.-F. Cross-Sectional Unification on the Stress-Strain Model of Concrete Subjected to High Passive Confinement by Fiber-Reinforced Polymer. Polymers, 2016; 8: 186. doi:10.3390/polym8050186.

[40] Guo, Y.-C., Xiao, S.-H., Luo, J.-W., Ye, Y.-Y., Zeng, J.-J. Confined Concrete in Fiber-Reinforced Polymer Partially Wrapped Square Columns: Axial Compressive Behavior and Strain Distributions by a Particle Image Velocimetry Sensing Technique. Sensors, 2018; 18: 4118. doi:10.3390/s18124118.

[41] Tariq, M., Khan, A., Shayanfar, J., Hanif, M. U., Ullah, A. A regression model for predicting the shear strength of RC knee joint subjected to opening and closing moment. Journal of Building Engineering, 2021; 41: 102727. doi:10.1016/j.jobe.2021.102727.

[42] Tariq, M., Khan, A., Ullah, A., Shayanfar, J., Niaz, M. Improved Shear Strength Prediction Model of Steel Fiber Reinforced Concrete Beams by Adopting Gene Expression Programming. Materials, 2022; 15: 3758. doi:10.3390/ma15113758.

[43] Onyelowe, K. C., Ebid, A. M., Mahdi, H. A., Soleymani, A., Jayabalan, J., Jahangir, H., Samui, P., Singh, R. P. Modeling the confined compressive strength of CFRP-jacketed noncircular concrete columns using artificial intelligence techniques. Cogent Engineering, 2022; 9: 2122156. doi:10.1080/23311916.2022.2122156.

[44] Abedi, M., Shayanfar, J., Al-Jabri, K. Infrastructure damage assessment via machine learning approaches: a systematic review. Asian Journal of Civil Engineering, 2023; 24: 3823-3852. doi:10.1007/s42107-023-00748-5.

[45] Shayanfar, J., Hemmati, A., Bengar, H. A. A simplified numerical model to simulate RC beam–column joints collapse. Bulletin of Earthquake Engineering, 2019; 17: 803-844. doi:10.1007/s10518-018-0472-z.

[46] Shayanfar, J., Barros, J. A. O., Rezazadeh, M. Design-oriented stress–strain model for RC columns with dual FRP- steel confinement mechanism. Composite Structures, 2024; 330: 117821. doi:10.1016/j.compstruct.2023.117821.

[47] Xie, J., Jia, C., Wang, Z. Data-driven machine-learning models for predicting non-uniform confinement effects of FRP-confined concrete. Structures, 2025; 74: 108555. doi:10.1016/j.istruc.2025.108555.

[48] Sadeghpour Haji, M., Niknam, R., Shayanfar, J. ANN-Based Modeling of Shear Behavior of Reinforced Concrete Columns under Constant Axial Loads. Civil Engineering and Applied Solutions, 2026; 2: 28-48. doi:10.22080/ceas.2025.30228.1050.

[49] Lam, L., Teng, J. G. Design-oriented stress–strain model for FRP-confined concrete. Construction and Building Materials, 2003; 17: 471-489. doi:10.1016/S0950-0618(03)00045-X.

[50] Teng, J. G., Jiang, T., Lam, L., Luo, Y. Z. Refinement of a Design-Oriented Stress–Strain Model for FRP-Confined Concrete. Journal of Composites for Construction, 2009; 13: 269-278. doi:10.1061/(ASCE)CC.1943-5614.0000012.

[51] Fallah Pour, A., Ozbakkaloglu, T., Vincent, T. Simplified design-oriented axial stress-strain model for FRP-confined normal- and high-strength concrete. Engineering Structures, 2018; 175: 501-516. doi:10.1016/j.engstruct.2018.07.099.

[52] International Federation for Structural Concrete. CEB-FIP: Externally applied FRP reinforcement for concrete structures. Lausanne (CH): FIB BULLETIN NO. 90; 2019.

[53] American Concrete Institute (ACI). ACI 440.2R-17: Guide for the design and construction of externally bonded FRP systems for strengthening concrete structures. Farmington Hills (MI): ACI; 2017.

[54] Shayanfar, J. Integrated modelling strategy for FRP-based confinement imposed to RC columns: From undamaged to post-fire damage (PhD Thesis). Braga (PT): University of Minho; 2024.

[55] Shayanfar, J., Akbarzadeh Bengar, H., Niroomandi, A. A proposed model for predicting nonlinear behavior of RC joints under seismic loads. Materials & Design, 2016; 95: 563-579. doi:10.1016/j.matdes.2016.01.098.

[56] Akbarzadeh Bengar, H., Abdollahtabar, M., Shayanfar, J. Predicting the Ductility of RC Beams Using Nonlinear Regression and ANN. Iranian Journal of Science and Technology, Transactions of Civil Engineering, 2016; 40: 297-310. doi:10.1007/s40996-016-0033-0.

[57] Bengar, H. A., Kiadehi, M. A., Shayanfar, J., Nazari, M. Effective flexural rigidities for RC beams and columns with steel fiber. Steel and Composite Structures, 2020; 34: 453-465. doi:10.12989/scs.2020.34.3.453.

[58] Abedi, M., Fangueiro, R., Correia, A. G., Shayanfar, J. Smart Geosynthetics and Prospects for Civil Infrastructure Monitoring: A Comprehensive and Critical Review. Sustainability, 2023; 15: 9258. doi:10.3390/su15129258.

[59] Abedi, M., Roshan, M. J., Gulisano, F., Shayanfar, J., Adresi, M., Fangueiro, R., Correia, A. G. An advanced cement-based geocomposite with autonomous sensing and heating capabilities for enhanced intelligent transportation infrastructure. Construction and Building Materials, 2024; 411: 134577. doi:10.1016/j.conbuildmat.2023.134577.

[60] Wei, Y.-Y., Wu, Y.-F. Unified stress–strain model of concrete for FRP-confined columns. Construction and Building Materials, 2012; 26: 381-392. doi:10.1016/j.conbuildmat.2011.06.037.

Civil Engineering and Applied Solutions

Research Article

journal homepage: ceas.journals.umz.ac.ir

CEAS Civil Engineering and Applied Solutions

Prediction of the Compressive Strength of Concrete Circular Columns Confined with FRP Using Neural Networks

Iman Dorosti [a], Ehasan Jahani [a*]

[a] *Department of Civil Engineering, Faculty of Engineering and Technology, University of Mazandaran, Babolsar, Iran*

ARTICLE INFO

Keywords:
Fiber-reinforced polymer (FRP)
Neural network
Confinement
High strength
Concrete columns

Article history:
Received 11 December 2025
Accepted 31 January 2026
Available online 01 July 2026

ABSTRACT

This study aims to predict the compressive strength of circular concrete columns confined with Fiber Reinforced Polymer (FRP), particularly for normal and high-strength concrete under axial loading. Existing predictive models have limitations, such as restricted applicability to specific ranges of concrete strength and the inability to account for FRP variations. To address these challenges, this research employs Neural Networks (NN) to enhance prediction accuracy and efficiency. A dataset of 574 data points was compiled from prior studies, encompassing various FRP types and concrete strengths. The NN models were trained using Levenberg-Marquardt (LM) and Bayesian Regularization (BR) methods, with different configurations tested to optimize performance. K-fold cross-validation was performed to ensure robustness. The models were validated and compared with existing approaches using R^2 and MSE as performance metrics. Results showed that the NN models achieved up to an 11.67% improvement in R^2 and an 84.24% reduction in MSE, significantly outperforming traditional methods. This study highlights the potential of NN-based approaches to provide reliable and accurate predictions for FRP-confined concrete columns. These findings offer valuable insights for engineers and designers, paving the way for safer and more efficient structural design practices in the construction industry.

Nomenclature

Aramid fiber reinforced polymer	AFRP
Artificial intelligence	AI
Bayesian Regularization	BR
Carbon fiber reinforced polymer	CFRP
Convolutional neural network	CNN
Deep neural network	DNN
Fiber reinforced polymer	FRP
Glass fiber reinforced polymer	GFRP
High modulus carbon fiber reinforced polymer	HM CFRP
Levenberg-Marquardt	LM
Life cycle assessment	LCA
Mean absolute percentage error	MAPE
Machine learning	ML
Mean squared error	MSE

* Corresponding author.
E-mail addresses: e.jahani@umz.ac.ir (E. Jahani).

https://doi.org/10.22080/ceas.2026.30756.1061
ISSN: 3092-7749/
How to cite this article: Dorosti, I., Jahani, E. Prediction of the Compressive Strength of Concrete Circular Columns Confined with FRP Using Neural Networks. Civil Engineering and Applied Solutions. 2025; 2(3): 16–32. doi:10.22080/ceas.2026.30756.1061.

Neural Network	NN
Near-surface mounted	NSM
Coefficient of determination	R^2
Radial basis function	RBF
Reinforced concrete	RC
Root mean squared error	RMSE
Support vector machine	SVM
Ultra-high modulus carbon fiber reinforced polymer	UHM CFRP

1. Introduction

In recent decades, the use of Fiber Reinforced Polymer (FRP) has increased significantly. One of the applications of FRP materials is in confining reinforced concrete columns, which increases compressive strength and ductility. The use of FRP has also been applied to high-strength and normal concrete [1-6], so guidelines for the use of these materials are needed [7]. On this basis, models for predicting the behavior of confined concrete columns have been presented. Most of these models were related to normal concrete, except for a limited number of models, such as those Mandal et al. [8], Cui and Sheikh [9], Berthet et al. [10] ,Xiao et al. [11], Girgin [12] and Raza et al. [13].

The comparison of the models presented so far with the experimental results shows that more accurate models are needed [14], as is a wider range of concrete compressive strength [7].

Since in recent years, the use of Neural Networks (NN) in various problems has increased significantly worldwide, the prediction of the compressive strength of this type of column can be done using artificial neural networks with an appropriate amount of data. These networks do not have the limitations of the experimental models presented and are more accurate. They also require much less cost and time than experimental models.

Farzinpour et al. [14] present a review paper that explores the methodologies and applications of Life Cycle Assessment (LCA) in the construction industry. It emphasizes the importance of LCA for sustainable decision-making, reviewing various studies on materials like cement, concrete, steel, and wood. The paper highlights recent advances in LCA, including circular economy principles and technological innovations, and discusses future directions such as data quality and standardization.

Naderpour et al. [15] presented an NN model for predicting the compressive strength of FRP-confined concrete using 213 data with an average prediction error of 9%, while the 3 models examined in this study had an average error of 13%.

In their study, Elsanadedy et al. [16] predicted the compressive strength and ultimate strain of FRP-confined concrete using NN and regression models. They considered 272 data for training and testing the NN. A sensitivity analysis was performed for the effective parameters of compressive strength and ultimate strain to introduce the regression model. The results of this study show that the use of NNs is both practical and useful for evaluating the compressive strength and ultimate strain of FRP-confined concrete.

Pham and Hadi [7] have compiled two data sets in a study. The first data set comprises 104 sample data points of rectangular concrete columns confined with FRP. The second data set includes 69 sample data points of square concrete columns also confined with FRP. They developed the NN model to predict the compressive strength and strain of this data and achieved an average absolute error of 5%.

Kumutha et al. [17] investigated the load-carrying capacity of reinforced concrete columns with Glass Fiber Reinforced Polymer (GFRP) using artificial intelligence (AI). 589 data were examined. The results of this study showed that the parameters of ultimate strength, ultimate strain, and spacing for longitudinal and transverse rebars are very important for predicting the load-bearing capacity of this type of column and the previous models did not take these parameters into account. They showed that among the AI methods used in this study, the Radial Basis Function (RBF) method had the highest accuracy and efficiency.

In their research, Koodiani et al. [18] used a method based on Machine Learning (ML) algorithms to develop design equations for the compressive strength of FRP-confined columns. The results of this research showed that the compressive strength limited to the elastic modulus of composite layers with a thickness of 2 mm was insensitive. A new equation was calibrated for specimens with a composite layer thickness greater than 2 mm, which provided very accurate estimates of the ultimate compressive strength for the experimental subset of this study.

In the study, Ali et al. [19] presented new models based on NN to predict the axial load capacities of concrete columns reinforced with FRP rebars. The axial load capacities of these columns were first predicted using the presented experimental models and then using Deep Neural Network (DNN) and Convolutional Neural Network (CNN) based models. The results show that the proposed DNN and CNN models predicted the axial load capacities of these types of columns with $R^2 = 0.943$ and $R^2 = 0.936$, respectively. In addition, the results showed that the proposed DNN and CNN models were more accurate than the experimental models with a reduction in Mean Absolute Percentage Error (MAPE) and Root Mean Squared Error (RMSE) by 52% and 42%, respectively.

In another study, Liang et al [20] investigated the prediction of residual fatigue life of composite sheets using vibration-based frequency measurements. In the study, NN, ML algorithms, and Support Vector Machine (SVM) were used to predict fatigue life. It was found that ML algorithms can effectively predict residual fatigue life by selecting an appropriate frequency. An inverse

algorithm based on SVM was introduced, which showed higher prediction accuracy with a limited data set.

Rasouli et al. [21] propose a new mix design method focusing on the durability of concrete by using supplementary cementitious materials and modified aggregate gradation. It evaluates the compressive strength, workability, and durability of various concrete mixes, achieving significant improvements in durability and strength. The paper develops a mix design process for optimized ratios of cement, aggregates, and SCMs, leading to durable and economical concrete mixes.

In a recent study, Ke et al. [22] investigated the shear strengthening of reinforced concrete (RC) beams using near-surface mounted (NSM) FRP bars/strips using ML techniques. They compiled a data set of 130 instances for rectangular and T-shaped beams characterized by 15 parameters. Their NN model used the Bayesian Regularization (BR) training method, which was further improved by a genetic algorithm. A comprehensive parametric analysis was performed to evaluate the influencing factors that affect the shear capacity of such beams. A design-oriented resistance model was then formulated and compared with existing models. The results showed that the newly proposed model outperformed the existing models in terms of accuracy.

In this study, in addition to normal circular concrete confined with FRP, circular concrete with high-strength FRP confinement was also investigated. Different types of NNs were investigated and finally, the best-performing NN from this investigation was compared with the previously proposed empirical models.

2. Existing experimental models

In this section, some models presented by researchers to predict the compressive strength of circular concrete columns confined with FRP are given. One of the most common forms for predicting compressive strength is as follows:

$$\frac{f'_{cc}}{f'_{co}} = 1 + k\left(\frac{f_l}{f'_{co}}\right)^n \tag{1}$$

where f'_{cc} is the compressive strength of confined concrete, f'_{co} is the compressive strength of unconfined concrete, k is the effective coefficient of confinement, f_l is the lateral confined pressure, and n is calibrated from a database. The relationship f_l is as follows:

$$f_l = \frac{2f_f t_f}{d} \tag{2}$$

where f_f is the tensile strength of FRP determined from flat coupon tests, t_f is the thickness of FRP, and d is the section diameter.

Some other researchers have also presented relationships with other forms. The models considered in this study for comparison with the NN are listed in Table 1.

Table 1. Models of compressive strength of circular columns.

Models	Equations
Richart et al. [23]	$\frac{f'_{cc}}{f'_{co}} = 1 + 4.1\frac{f_l}{f'_{co}}$
Mander et al. [24]	$\frac{f'_{cc}}{f'_{co}} = -1.254 + 2.254\sqrt{1 + \frac{7.94f_l}{f'_{co}}} - 2\frac{f_l}{f'_{co}}$
Mirmiran et al. [5]	$f'_{cc} = f'_{co} + 4.269(f_l)^{0.587}$
Samaan et al. [25]	$f'_{cc} = f'_{co} + 6(f_l)^{0.7}$
Razvi and Saatcioglu [26]	$f'_{cc} = f'_{co} + 6.7\,(f_l)^{0.83}$
Toutanji [27]	$\frac{f'_{cc}}{f'_{co}} = 1 + 3.5\left(\frac{f_l}{f'_{co}}\right)^{0.85}$
Spoelstra and Monti [28]	$f'_{cc} = f'_{co}\left(0.2 + 3\sqrt{\frac{f_l}{f'_{co}}}\right)$
Saafi et al. [29]	$\frac{f'_{cc}}{f'_{co}} = 1 + 2.2\left(\frac{f_l}{f'_{co}}\right)^{0.84}$
Shehata et al. [30]	$\frac{f'_{cc}}{f'_{co}} = 1 + 1.25\frac{f_l}{f'_{co}}$
Lam and Teng [31]	$\frac{f'_{cc}}{f'_{co}} = 1 + 3.3\frac{f_l}{f'_{co}}$
Campione and Miraglia [32]	$\frac{f'_{cc}}{f'_{co}} = 1 + 2\frac{f_l}{f'_{co}}$
Berthet et al. [10]	$\frac{f'_{cc}}{f'_{co}} = 1 + k\frac{f_l}{f'_{co}}, k = \begin{cases} 3.45 & (20 \le f'_{co}(MPa) \le 50) \\ \frac{9.5}{f'^{\frac{1}{4}}_{co}} & (50 \le f'_{co}(MPa) \le 200) \end{cases}$
Matthys et al. [33]	$\frac{f'_{cc}}{f'_{co}} = 1 + 2.3\left(\frac{f_l}{f'_{co}}\right)^{0.85}$
Kumutha et al. [17]	$\frac{f'_{cc}}{f'_{co}} = 1 + 0.93\frac{f_l}{f'_{co}}$
Wu et al. [34]	$\frac{f'_{cc}}{f'_{co}} = 1 + 3.2\frac{f_l}{f'_{co}}$

Wu and Zhou [35]	$\frac{f'_{cc}}{f'_{co}} = \frac{f_l}{f'_{co}} + \sqrt{\left(\frac{16.7}{(f'_{co})^{0.42}} - \frac{(f'_{co})^{0.42}}{16.7}\right)\frac{f_l}{f'_{co}} + 1}$
Yazici and Hadi [36]	$\boldsymbol{\frac{f'_{cc}}{f'_{co}} = 1 + 0.033K_N, K_N = \frac{2E_f t_f}{Df'_{co}}}$ $(10 \le K_N \le 20)$
Pham and Hadi [7]	$f'_{cc} = 0.7f'_{co} + 1.8f_l + 5.7\frac{t}{d} + 13$
Girgin [12]	$\boldsymbol{\frac{f'_{cc}}{f'_{co}} = \left(1 + \frac{M}{B}\frac{f_l}{f'_{co}}\right)^B, B = 1 - 0.0172(\log f'_{co})^2}$ $M = \begin{cases} 0.0035{f'_{co}}^2 - 0.056f'_{co} + 2.83 \ (7 \le f'_{co}(MPa) < 25) \\ 0.003{f'_{co}}^2 - 0.076f'_{co} + 5.46 \ (25 \le f'_{co}(MPa) < 108) \end{cases}$
Raza et al. [13]	$f'_{cc} = f'_{co} + 3f'_{co}\left(\frac{f_l}{f'_{co}}\right)^{\frac{3}{4}}$

The models presented for calculating f'_{cc} have their limitations and only a few models consider high-strength concrete in the range that can predict compressive strength. The relationship between f'_{cc} with f'_{co}, f_l, and k is so complicated that it is difficult to predict f'_{cc} by experimental methods due to the nonlinear behavior of concrete and FRP. Therefore, due to the need for a more accurate model, NNs were used in this study.

3. Neural networks

NNs have recently garnered significant attention. NNs are a branch of artificial intelligence inspired by the neural system of the brain. Similar to the brain, these NNs train by processing information and can be used for various applications.

NN consists of three layers: 1) the input layer, 2) the hidden layer, and 3) the output layer. In an NN, data are input into the input layer, and computations occur in the hidden layer (or layers). Finally, the NN generates predictions based on its training in the output layer. Each of these layers contains a certain number of neurons, which is determined based on the specific problem being investigated. However, in the hidden layer (or layers), the user has the flexibility to choose an appropriate number of neurons to achieve better results. In NNs, data are typically split into two or, in some cases, three groups based on the training method: 1) Train 2) Test 3) Validation. The data splitting ratio for NNs is determined based on various factors, such as the specific problem being investigated and the size of the dataset.

The process of training NNs proceeds as follows: First, we input the training data into the input layer. These inputs are then transmitted to the neurons in the hidden layers, each with distinct weights and biases. The output of these neurons is determined by an activation function specific to that hidden layer. Subsequently, this value is propagated to the neurons in the output layer, again with different weights and biases. Finally, in the output layer, the network's output is compared to the actual value from the training data to compute the error. The weights and biases of neurons across different layers are adjusted iteratively using selected training methods, with backpropagation being a common approach. The choice of activation functions in the hidden layer (or layers) depends on the specific problem being investigated.

In this study, two methods were used to train the neural network: 1) BR and 2) Levenberg-Marquardt (LM).

The BR training method had three training stop criteria to avoid overfitting and underfitting.

1) Epochs: This is the maximum number of epochs for which the training will stop if we reach this number.

2) Gradient: The minimum gradient value of the performance function that controls the changes in the performance function. If these changes are too small, the training stops.

3) Mu: initial value of learning to modify weights. If this number is large, the network will converge faster, and if it is small, the learning process will slow down. If the change in weights is less than this value, the training will be stopped.

In the LM training method, in addition to the above three stopping criteria, there is another criterion called Validation Checks. In this stop criterion, in each epoch, the performance function value is checked for validation data. If it is greater than that of the previous epoch, it is added to its counter. If this counter reaches the desired value, the training is stopped.

4. Experimental data

The data used in this study included 574 concrete specimens confined with FRP, which were taken from 58 studies conducted in the last few decades and collected by another researcher [7].

These data included various types of FRP, as follows:

- GFRP: 119 specimens
- Aramid Fiber-Reinforced Polymer (AFRP): 35 specimens
- AFRP tube: 23 specimens
- Carbon Fiber-Reinforced Polymer (CFRP): 317 specimens

- High Modulus CFRP (HM CFRP): 45 specimens
- Ultra-High Modulus CFRP (UHM CFRP): 7 specimens
- CFRP Tube: 28 specimens

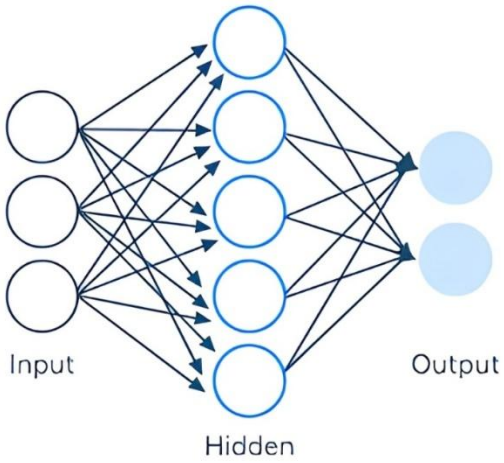

Fig. 1. Schematic of neural network.

The statistical properties of the data are shown in Table 2. The increase in compressive strength for data with confinement ranged from 10% to 440%. Specimens displaying a stress-strain curve with a descending branch and minimal strength increase were excluded from the database. In addition, specimens damaged due to premature rupture of FRP were excluded.

Table 2. Statistical properties of experimental data.

Parameter	d (mm)	h (mm)	f'_{co} (MPa)	E_f (GPa)	f_f (MPa)	t_f (mm)	f'_{cc} (MPa)
Maximum	406.40	812.80	169.7	640.00	4510.0	7.267	296.40
Minimum	51.00	102.00	15	18.47	237	0.110	37.23
Mean	156.64	315.13	49.43	180.55	2720.6	0.877	88.97
Standard deviation	56.62	114.24	24.05	117.82	1279.9	1.076	39.13
Coefficient of variation	0.36	0.36	0.49	0.65	0.47	1.227	0.44

5. Neural network modeling

For NN training as mentioned, 574 data were considered. 6 inputs were considered for the neural network, which are as follows:

- Diameter of section (d)
- Height of column (h)
- Compressive strength of unconfined concrete (f'_{co})
- FRP modulus of elasticity (E_f)
- FRP tensile strength (f_f)
- FRP thickness (t_f)

The output of this NN is f'_{cc}. Unlike experimental models that require predefined relationships for prediction, NN does not require any specific closed-form relationship. Instead of calculating f_l, effective variables in f_l were provided as input, enabling the NN to learn its relationship with f'_{cc} directly.

The Mean Squared Error (MSE) function and coefficient of determination (R^2) were used to calculate the prediction accuracy of the NNs and the presented models. The MSE relationship is as follows [37]:

$$MSE = \frac{1}{n}\sum_{i=1}^{n}(pre_i - exp_i)^2 \quad (3)$$

where n is the number of data, pre is the predicted value, and exp is the actual value obtained from the experiment. If the value of the MSE function is closer to 0, the prediction is more accurate.

R^2 quantifies the proportion of variation in the dependent variable (also known as the response variable) that can be attributed to the independent variables in a regression model. In simpler terms, it represents the percentage of variability in the dependent variable explained by the independent variables. The relationship of R^2 is as follows [38]:

$$R^2 = \left(\frac{n\sum xy - \sum x \sum y}{\sqrt{(\sum x^2 - (\sum x)^2) - (n\sum y - (\sum y)^2)}} \right)^2 \quad (4)$$

where n is the number of data, x and y are predicted and actual values, respectively. The closer the calculated value of R^2 is to 1, the higher the accuracy of the prediction.

The selected activation functions are the same for all NNs. The selected activation function in the hidden layers was sigmoid, and linear in the output layer. Because of the choice of the sigmoid as the activation function, the data were first normalized using Eq. 5.

$$x_{norm} = \frac{x - x_{min}}{x_{max} - x_{min}} \quad (5)$$

Epochs 2000 were considered, and the value of Validation checks was 10 for the LM training method. The results are shown in Tables 3 and 4.

According to the results obtained from the NNs, the best results were determined, as shown in Tables 2 and 3. In the LM training method, the NN performed best by splitting the data into 70, 15, and 15% for train, validation, and test, respectively. This NN included four hidden layers, with the number of neurons in each layer being 40, 40, 20, and 5. The results of this NN are shown in Figs. 2-5. The training process was stopped at epoch 25 because the validation checks reached the specified value. This NN had R^2 = 0.9839 and MSE = 0.000732, which was reached at epoch 15.

In the BR training method, the NN performed best by splitting the data into 80% and 20% for train and test, with two hidden layers and 15 and 5 neurons in each layer. This NN was stopped in epoch 1129 because of the gradient value in the NN performance function reached the allowed value. The value of this index for stopping in this type of NN was considered to be 10^{-7}. This NN with R^2 = 0.9902 and MSE = 0.000445 had the best prediction accuracy compared with other NNs using this training method.

5.1. Cross-validation using K-Fold method

Cross-validation is a robust statistical method used to evaluate and improve the performance of a predictive model. The technique is essential in ensuring that the model generalizes well to an independent dataset, thereby reducing overfitting and providing a more reliable measure of model performance. Among various cross-validation techniques, the K-Fold method is one of the most widely used due to its efficiency and comprehensiveness.

K-Fold Cross-Validation: In K-Fold Cross-Validation, the dataset is divided into 'K' equal-sized folds or subsets. The process follows these steps:

- Partitioning the Data: The entire dataset is randomly divided into K folds. Each fold is used exactly once as a validation dataset, while the K-1 remaining folds form the training dataset.
- Training and Validation: The model is trained on the training dataset (K-1 folds) and validated on the validation dataset (the remaining 1 fold). This step is repeated K times, with each fold being used exactly once as the validation data.
- Performance Aggregation: The performance of the model is evaluated using an appropriate metric (e.g., MSE, R^2) for each iteration. The K results are then averaged to provide a single estimation of the model's performance.

The major advantage of K-Fold Cross-Validation is that it ensures that every data point is used for both training and validation, providing a thorough evaluation of the model's ability to generalize. This method is particularly useful in small datasets where splitting the data into separate training and validation sets would result in limited training data.

Benefits:

- Reduced Overfitting: By training and validating the model on multiple folds, K-Fold Cross-Validation mitigates the risk of overfitting to a specific portion of the data.
- Better Utilization of Data: Every data point is used for both training and validation, maximizing the use of the dataset.
- Reliable Performance Metrics: Averaging the performance metrics across all folds provides a more stable and reliable estimate of the model's performance.

Choosing K: The choice of K is crucial for the effectiveness of the cross-validation. A common choice is K=10, which balances the bias-variance trade-off. Smaller values of K can lead to higher variance in the performance estimates, while larger values may result in higher computational costs.

In conclusion, K-Fold Cross-Validation is an indispensable tool for model evaluation and validation, providing comprehensive insights into the model's performance and ensuring its reliability in real-world applications.

The results of K-Fold Cross-Validation for the selected NNs are shown in Tables 5 and 6. The selected NNs were highlighted in Tables 3 and 4.

Table 3. Results of neural networks with the Levenberg-Marquardt training method.

Number of hidden layers	Number of neurons in hidden layers	Train, validation, and test ratio	R^2				MSE			
			Train	Validation	Test	All	Train	Validation	Test	All
1	5	70% 15% 15%	0.967014	0.957462	0.954914	0.963986	0.001484	0.002128	0.001681	0.001610
	10		0.972176	0.968095	0.968661	0.971136	0.001217	0.001415	0.001538	0.001295
	20		0.978462	0.968850	0.970540	0.976461	0.001030	0.000923	0.001328	0.001059
	40		0.980457	0.951088	0.963552	0.973849	0.000906	0.002238	0.001378	0.001176
2	5 5		0.973375	0.956683	0.960703	0.969555	0.001263	0.001436	0.001768	0.001365
	10 10		0.981378	0.970759	0.958945	0.976836	0.000854	0.001293	0.001676	0.001043
	20 20		0.986742	0.962981	0.962032	0.979930	0.000622	0.001538	0.001659	0.000915
	40 40		0.983481	0.968584	0.972264	0.978708	0.000802	0.001568	0.001243	0.000983
3	5 5 5		0.970681	0.973464	0.969890	0.970600	0.001254	0.001650	0.001315	0.001323
	10 10 10		0.977660	0.958927	0.961406	0.973236	0.001071	0.001642	0.001380	0.001203
	20 20 20		0.985897	0.976323	0.973453	0.982315	0.000626	0.001290	0.001133	0.000801
	40 40 40		0.989365	0.936055	0.920921	0.971385	0.000490	0.002942	0.003510	0.001310
4	5 5 5 5		0.974805	0.965200	0.965296	0.971481	0.001061	0.001672	0.001922	0.001282
	10 10 10 10		0.982719	0.963263	0.944529	0.976352	0.000887	0.001418	0.001549	0.001066
	20 20 20 20		0.981651	0.973809	0.971193	0.978088	0.000747	0.001511	0.001614	0.000991
	40 40 20 5		0.988577	0.969366	0.970979	0.983940	0.000558	0.001099	0.001176	0.000732
1	5	60% 20% 20%	0.968806	0.958553	0.951597	0.964021	0.001522	0.001654	0.001830	0.001610
	10		0.980082	0.967028	0.956950	0.973872	0.000982	0.001615	0.001335	0.001180
	20		0.979269	0.940721	0.959092	0.969526	0.001039	0.001983	0.001790	0.001379
	40		0.982244	0.950036	0.961463	0.973363	0.000917	0.001615	0.001613	0.001196
2	5 5		0.971677	0.964895	0.945492	0.966982	0.001381	0.001821	0.001440	0.001481
	10 10		0.977850	0.968667	0.961413	0.973018	0.001051	0.001398	0.001571	0.001225
	20 20		0.976455	0.958481	0.972956	0.971907	0.001089	0.001756	0.001463	0.001298
	40 40		0.992031	0.944389	0.960900	0.977819	0.000391	0.002324	0.001499	0.001000
3	5 5 5		0.972904	0.965232	0.949763	0.967846	0.001416	0.001464	0.001589	0.001460
	10 10 10		0.979569	0.965853	0.958218	0.973244	0.000952	0.001670	0.001482	0.001202
	20 20 20		0.988670	0.966814	0.966871	0.979423	0.000509	0.001709	0.001422	0.000932
	40 40 40		0.985083	0.953356	0.966123	0.978117	0.000799	0.000963	0.001627	0.000997
4	5 5 5 5		0.970233	0.908527	0.970269	0.960213	0.001292	0.003259	0.001754	0.001779
	10 10 10 10		0.981371	0.961754	0.968427	0.975011	0.000853	0.001625	0.001438	0.001125
	20 20 20 20		0.989925	0.969365	0.963427	0.982285	0.000523	0.001265	0.001190	0.000805
	40 40 20 5		0.991493	0.974233	0.952760	0.982504	0.000425	0.001198	0.001469	0.000789

Table 4. Results of neural networks with the Bayesian regularization training method.

Number of hidden layers	Number of neurons in layers	Train and test ratio	R^2			MSE		
			Train	Test	All	Train	Test	All
1	5	80% 20%	0.970942	0.960350	0.969464	0.001337	0.001515	0.001368
	10		0.981475	0.964940	0.978443	0.000841	0.001597	0.000972
	15		0.985428	0.970538	0.983783	0.000698	0.000893	0.000732
	20		0.984546	0.978377	0.983569	0.000710	0.000894	0.000742
2	5 5		0.980808	0.979823	0.979823	0.000869	0.001108	0.000911
	10 5		0.988818	0.952899	0.984772	0.000546	0.001371	0.000690
	10 10		0.993728	0.965076	0.987631	0.000272	0.001932	0.000561
	15 5		0.993210	0.977448	0.990197	0.000304	0.001112	0.000445
	20 5		0.995284	0.947688	0.986940	0.000213	0.002381	0.000591
3	5 5 5		0.983419	0.983453	0.983399	0.000692	0.001031	0.000751
	10 10 5		0.996650	0.943088	0.987337	0.000155	0.002607	0.000582
	10 10 10		0.996846	0.939862	0.988004	0.000147	0.002435	0.000546

	15 5 5		0.996144	0.902602	0.980057	0.000177	0.004378	0.000909
	15 10 5		0.996755	0.890705	0.976145	0.000146	0.005595	0.001095
1	5	70% 30%	0.973334	0.960750	0.969666	0.001182	0.001878	0.001364
	10		0.980359	0.962019	0.975896	0.000908	0.001582	0.001084
	15		0.987316	0.960083	0.982650	0.000632	0.001213	0.000784
	20		0.989116	0.949085	0.980084	0.000517	0.001982	0.000900
2	5 5		0.979644	0.978451	0.979261	0.000918	0.000985	0.000936
	10 5		0.987445	0.956709	0.980436	0.000589	0.001709	0.000882
	10 10		0.994192	0.966829	0.986166	0.000252	0.001690	0.000628
	15 5		0.993178	0.969857	0.986380	0.000298	0.001522	0.000618
	20 5		0.996594	0.891537	0.975327	0.000166	0.003795	0.001114
3	5 5 5		0.987914	0.964608	0.982041	0.000558	0.001532	0.000813
	10 10 5		0.996904	0.957678	0.986789	0.000142	0.001905	0.000603
	10 10 10		0.997488	0.958904	0.987187	0.000115	0.001925	0.000588
	15 5 5		0.995895	0.937744	0.981013	0.000187	0.002763	0.000860
	15 10 5		0.996903	0.944023	0.979052	0.000130	0.003365	0.000975

Table 5. K-fold cross-validation for the Levenberg-Marquardt method.

K	R^2				MSE			
	Train	Validation	Test	All	Train	Validation	Test	All
1	0.9580	0.9554	0.9533	0.9569	0.00197	0.003401	0.001801	0.0022
2	0.9711	0.9624	0.9633	0.9686	0.00126	0.001403	0.00216	0.0014
3	0.9785	0.9777	0.9402	0.9726	0.00099	0.001048	0.002049	0.0012
4	0.9691	0.9476	0.9354	0.9608	0.00136	0.001681	0.003588	0.0017
5	0.9750	0.9627	0.9312	0.9666	0.00111	0.000987	0.003316	0.0014
6	0.9686	0.9602	0.9639	0.9666	0.00148	0.001773	0.001074	0.0015
7	0.9705	0.9588	0.9775	0.9698	0.00131	0.002319	0.001191	0.0014
8	0.9837	0.9438	0.9464	0.9721	0.00072	0.002169	0.002837	0.0013
9	0.9727	0.9671	0.9575	0.9696	0.00125	0.001288	0.001578	0.0013
10	0.9555	0.9056	0.9526	0.9476	0.00198	0.006185	0.002251	0.0027
Average	0.9703	0.9541	0.9521	0.9651	0.001343	0.002225	0.002185	0.001610

Table 6. K-fold cross-validation for the Bayesian regularization method.

K	R^2			MSE		
	Train	Test	All	Train	Test	All
1	0.9833	0.9669	0.9800	0.000748	0.001684	0.000935
2	0.9867	0.9571	0.9808	0.000603	0.002298	0.000942
3	0.9871	0.9538	0.9804	0.000594	0.001939	0.000863
4	0.9733	0.9590	0.9705	0.001269	0.001655	0.001346
5	0.9574	0.9705	0.9600	0.002123	0.000861	0.00187
6	0.9792	0.9775	0.9789	0.000956	0.000922	0.000949
7	0.9772	0.9643	0.9747	0.001042	0.002202	0.001274
8	0.9526	0.9832	0.9587	0.002495	0.001125	0.002221
9	0.9848	0.9704	0.9819	0.000693	0.00252	0.001058
10	0.9599	0.9560	0.9591	0.001824	0.00229	0.001917
Average	0.9742	0.9659	0.9725	0.001235	0.00175	0.001338

Tables 5 and 6 summarize the K-fold cross-validation results for the neural network models trained using LM and BR methods, respectively. Both tables present R^2 and Mean Squared Error (MSE) values for training, validation, test, and overall datasets, showing high R^2 (0.9476 to 0.9819) and low MSE (0.00072 to 0.0027) values. These results indicate the robustness and superior predictive accuracy of the neural network models, with the BR method showing slightly better performance on average.

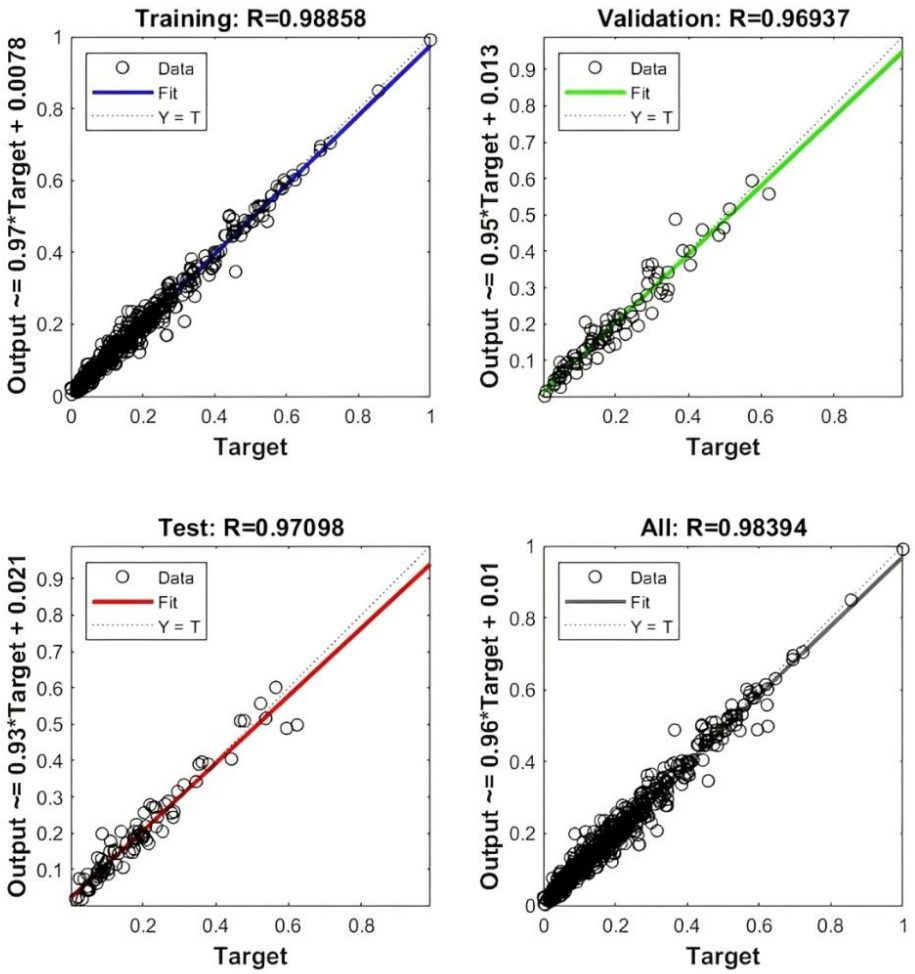

Fig. 2. Training regression of the proposed neural network with levenberg-marquardt training method.

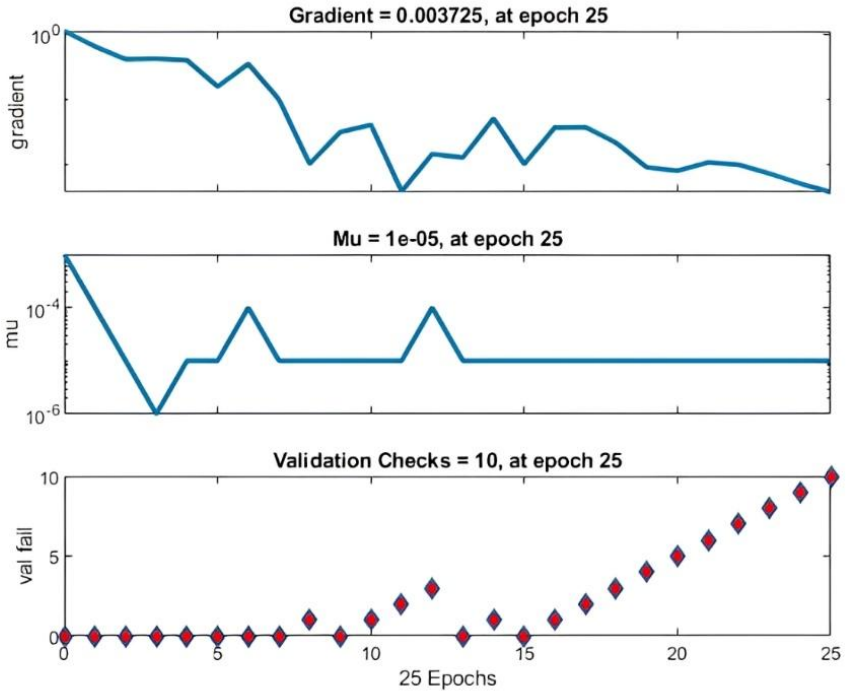

Fig. 3. Training state of the proposed neural network with levenberg-marquardt training method.

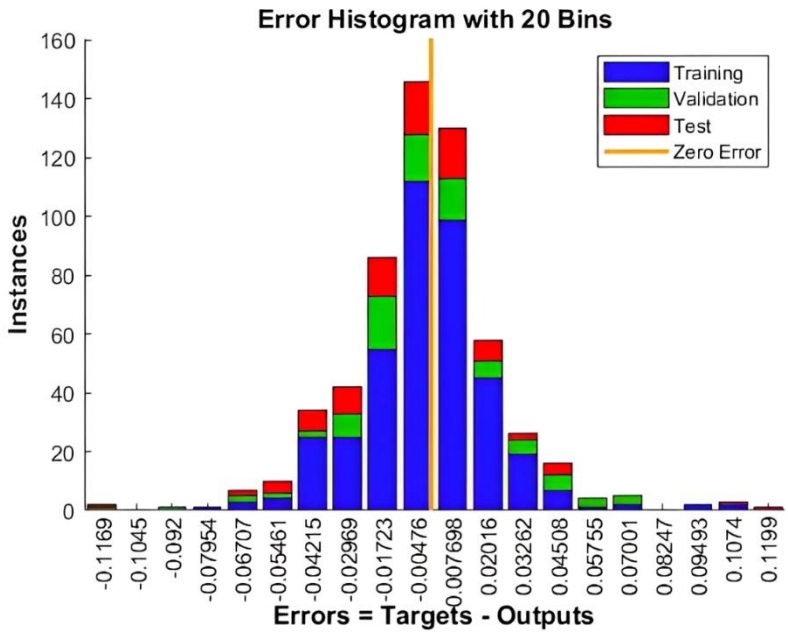

Fig. 4. Error histogram of the proposed neural network with levenberg-marquardt training method.

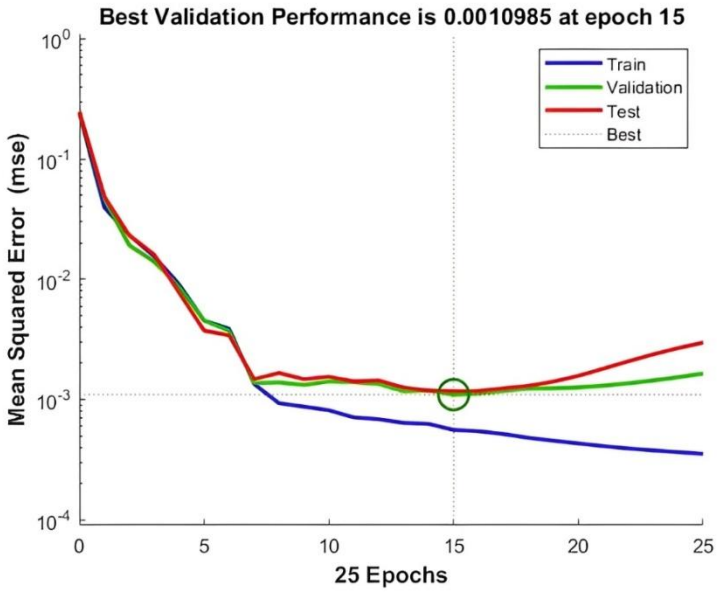

Fig. 5. Training performance of the proposed neural network with levenberg-marquardt training method.

Table 7 provides an extensive quantitative comparison between a wide range of conventional analytical and semi-empirical models and the proposed artificial neural network (ANN) models for predicting the axial behavior of FRP-confined concrete columns. The evaluation is conducted using the coefficient of determination (R^2) and mean squared error (MSE), which together offer a robust measure of both goodness-of-fit and prediction accuracy.

The traditional models demonstrate varying levels of predictive capability, with R^2 values ranging from as low as 0.7501 to a maximum of approximately 0.8889 [5, 26]. This spread indicates a significant inconsistency in the ability of classical formulations to accurately represent the complex confinement mechanisms of FRP systems. Furthermore, although some models exhibit relatively high R^2 values, they are often accompanied by comparatively large MSE values, suggesting that a good overall correlation does not necessarily translate into precise point-wise predictions.

A closer examination reveals that earlier models, such as those proposed by Richart et al. and Mander et al., which were originally developed for steel-confined concrete, show noticeably inferior performance when applied to FRP-confined systems. Their higher MSE values reflect the limitations of extending steel-based confinement assumptions to FRP materials, which exhibit fundamentally different stress–strain behavior and failure mechanisms. More recent formulations, including those by Wu and Zhou [35], Campione and Campione and Miraglia [32], and Pham and Hadi [7], demonstrate improved accuracy due to the incorporation of FRP-specific parameters; however, their predictive performance still remains substantially below that of the ANN models.

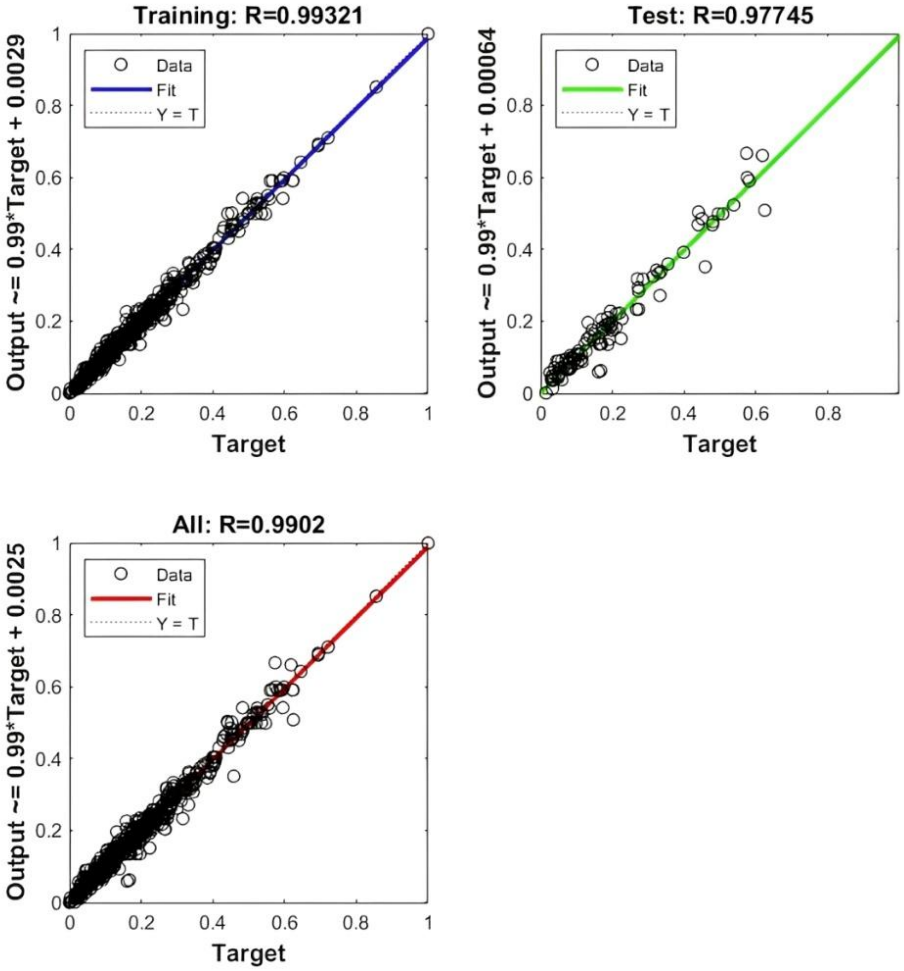

Fig. 6. Training regression of the proposed neural network using the Bayesian regularization training method.

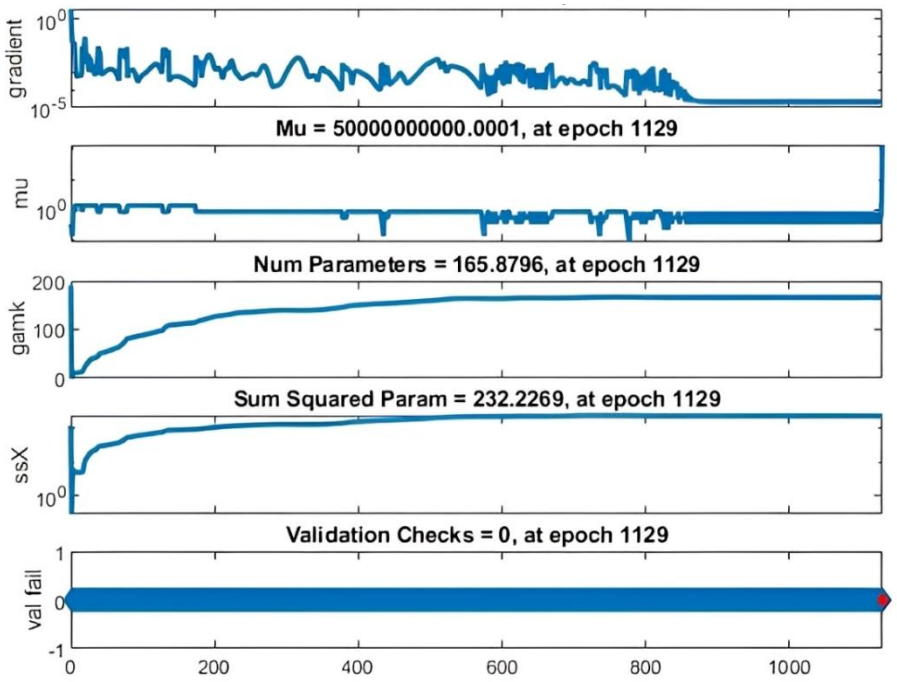

Fig. 7. Training state of the proposed neural network with the Bayesian regularization training method.

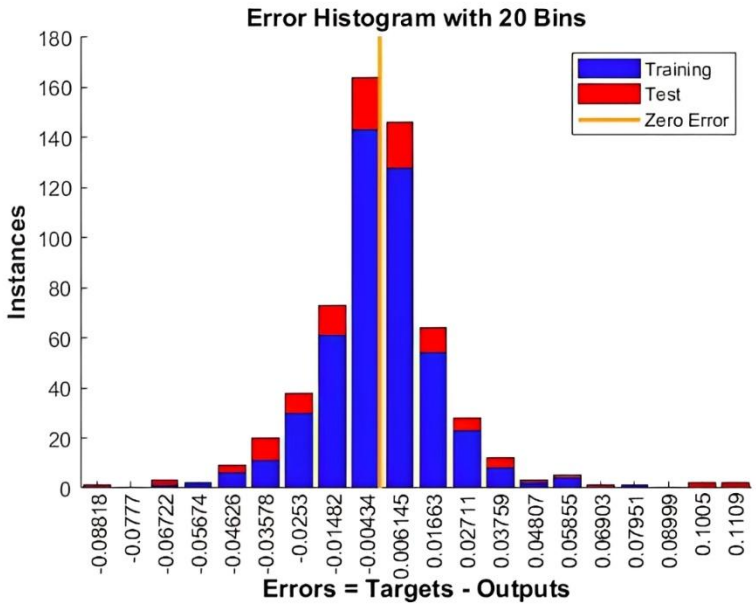

Fig. 8. Error histogram of the proposed neural network with the Bayesian regularization training method.

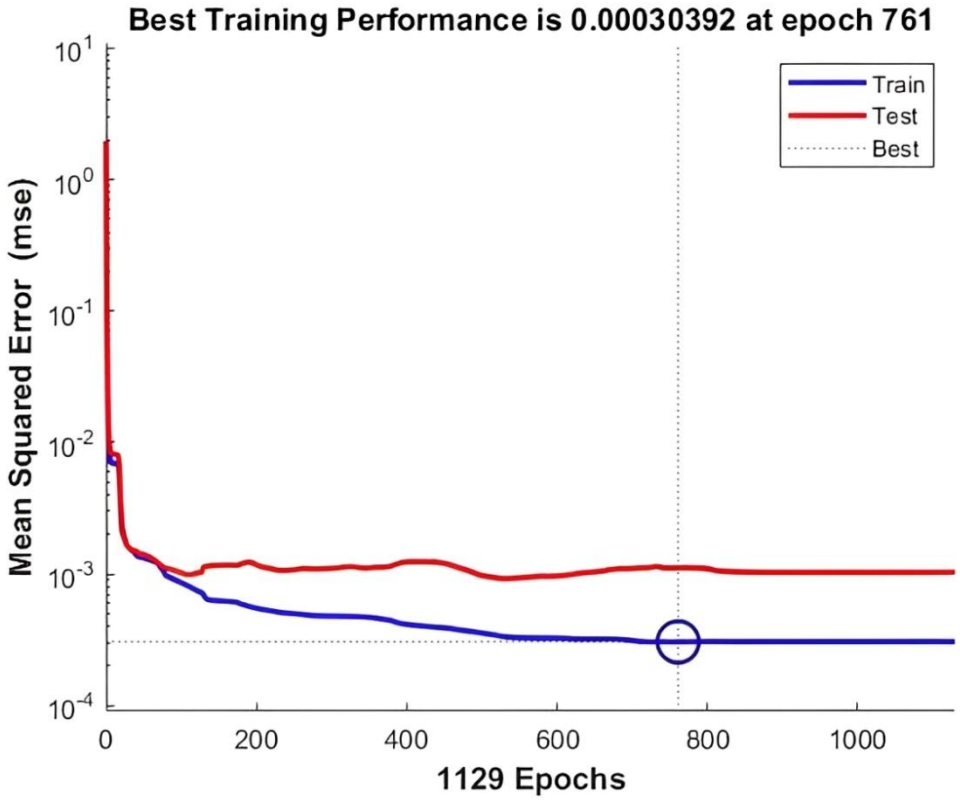

Fig. 9. Training performance of the proposed neural network with the Bayesian regularization training method.

Table 7. Comparison of the presented models with the proposed neural networks.

Models	R^2	MSE
Richart et al. [23]	0.8746	0.045365
Mander et al. [24]	0.8027	0.027231
Mirmiran et al. [5]	0.7501	0.009875
Samaan et al. [25]	0.8659	0.003849
Razvi and Saatcioglu [26]	0.8889	0.030834
Toutanji [27]	0.8851	0.035536

Spoelstra and Monti [28]	0.8584	0.007468
Saafi et al. [29]	0.8693	0.006327
Shehata et al. [30]	0.8404	0.006924
Lam and Teng [31]	0.8835	0.020448
Campione and Miraglia [32]	0.8803	0.003473
Berthet et al. [10]	0.8756	0.019586
Matthys et al. [33]	0.8732	0.007181
Kumutha et al. [17]	0.8014	0.011346
Wu et al. [34]	0.8843	0.018108
Wu and Zhou [35]	0.8867	0.002823
Yazici and Hadi [36]	0.7949	0.007724
Pham and Hadi [7]	0.8868	0.003099
Girgin [12]	0.8679	0.004365
Raza et al [13]	0.8721	0.026727
Neural Network (Levenberg- Marquardt)	0.9839	0.000732
Neural Network (Bayesian Regularization)	0.9902	0.000445

In contrast, the ANN models significantly outperform all conventional approaches. The Levenberg–Marquardt (LM) neural network achieves an R^2 value of 0.9839, which corresponds to an improvement of approximately 10–23% over most traditional models. More importantly, its MSE is reduced by nearly one to two orders of magnitude, highlighting a dramatic decrease in prediction error. This improvement confirms the superior capability of ANNs in capturing nonlinear interactions among material properties, geometric parameters, and confinement effects that are difficult to express through closed-form equations.

The Bayesian Regularization (BR) neural network exhibits the best overall performance, achieving the highest R^2 (0.9902) and the lowest MSE (0.000445) among all evaluated models. When compared to the best-performing conventional model, the BR approach reduces the MSE by more than 85–90%, demonstrating its enhanced generalization ability. This improvement can be attributed to the inherent regularization mechanism of the BR algorithm, which effectively controls overfitting and ensures stable performance across a wide range of input conditions.

Overall, the comparative results clearly indicate that while conventional models can provide approximate estimates of axial behavior, they are limited by simplifying assumptions and restricted applicability ranges. In contrast, ANN-based models, particularly those trained using Bayesian Regularization, offer a highly accurate, reliable, and flexible predictive framework. These findings strongly support the adoption of artificial intelligence techniques for modeling the complex mechanical response of FRP-confined reinforced concrete columns and highlight their potential to replace or complement traditional analytical formulations in advanced structural design and assessment.

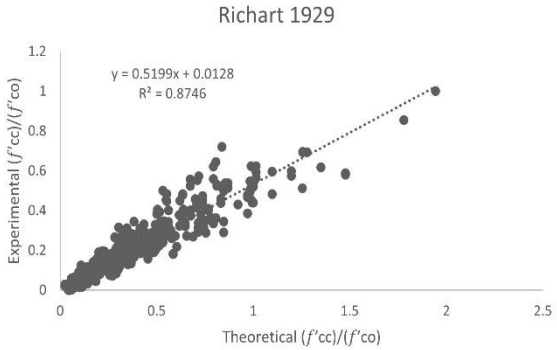

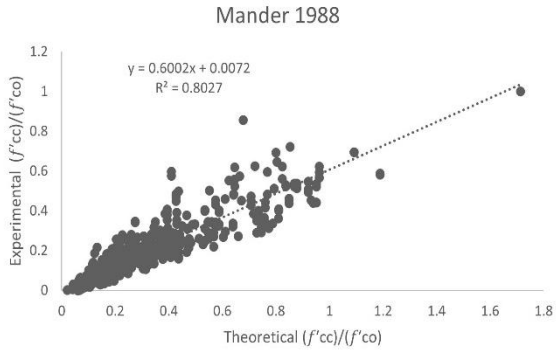

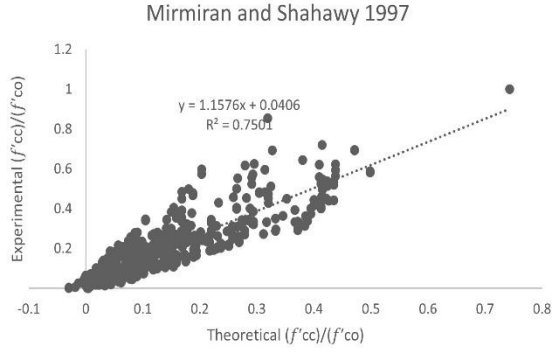

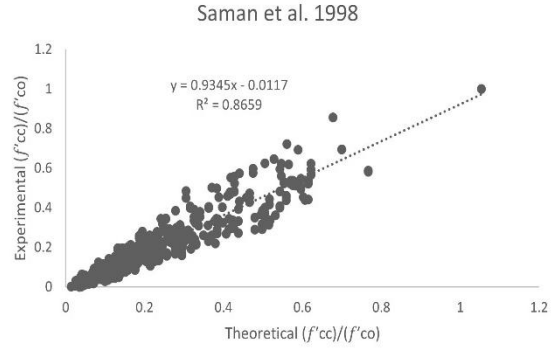

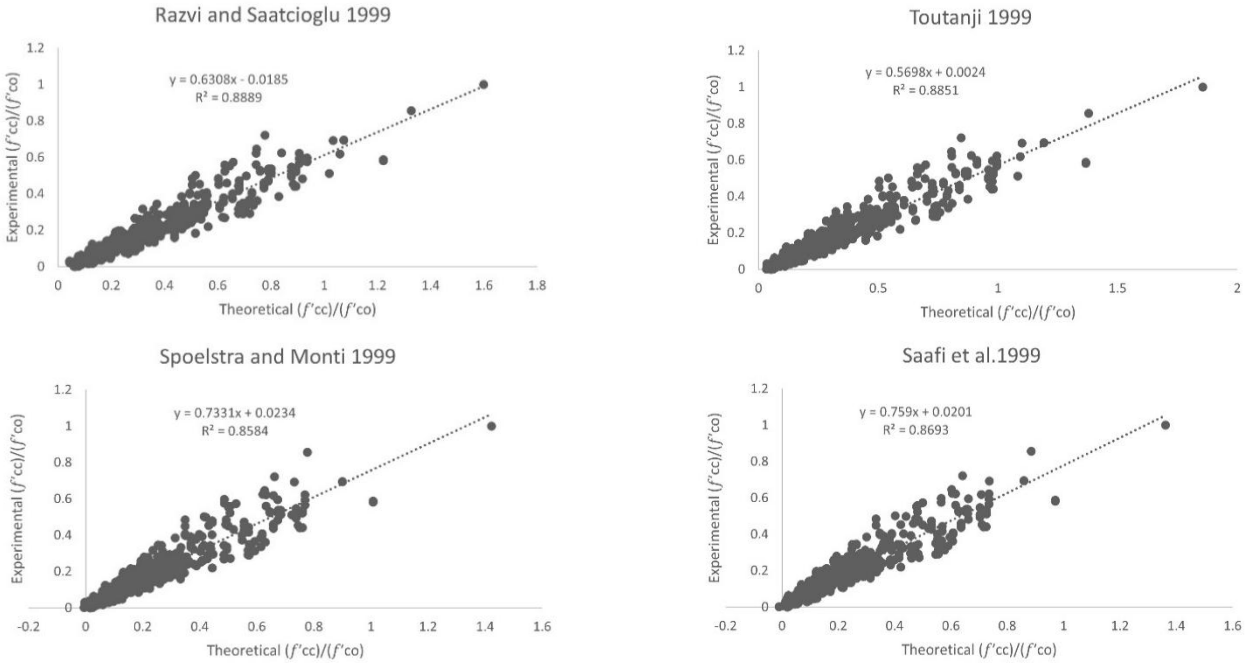

Fig. 10. Regression diagram of the presented models.

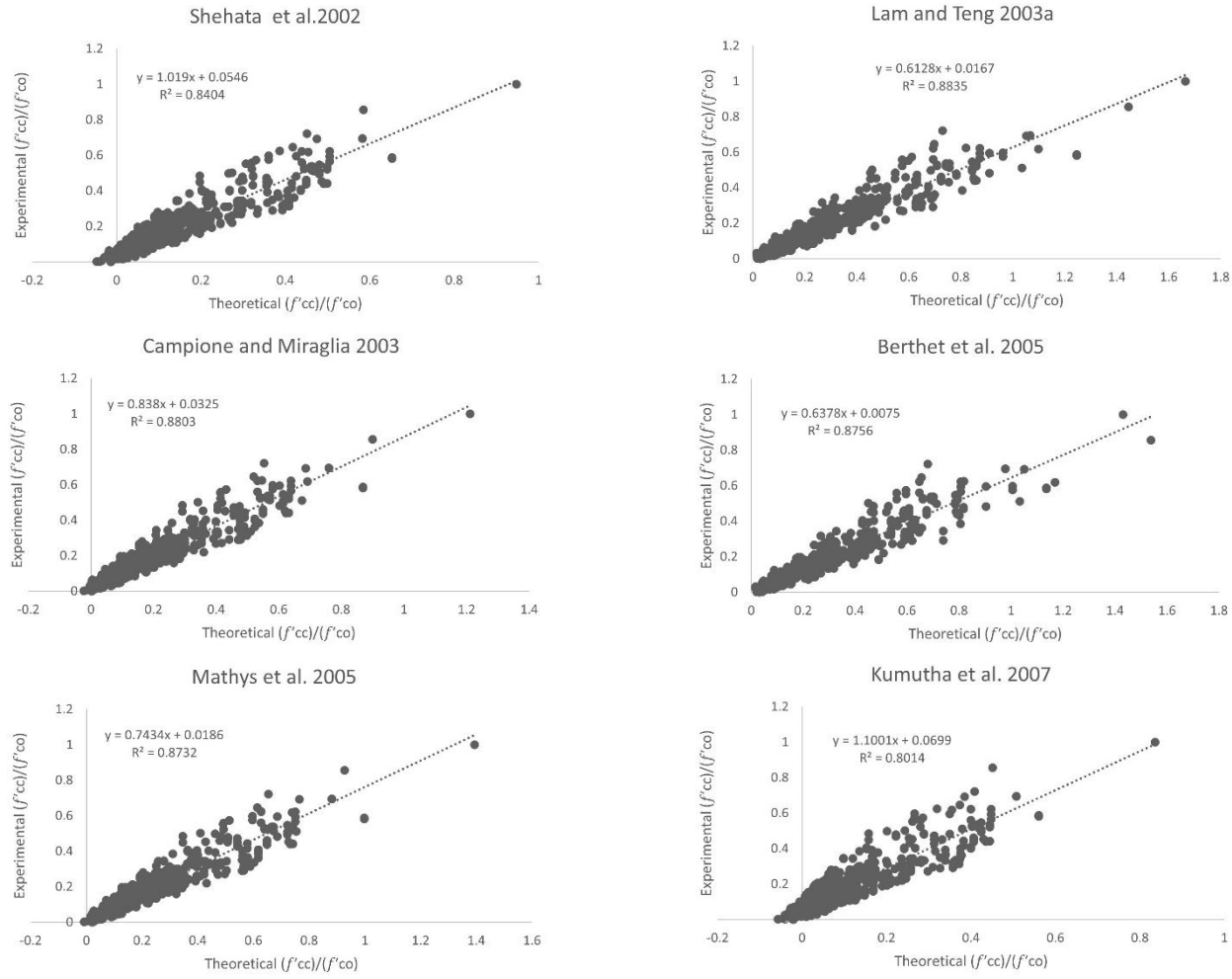

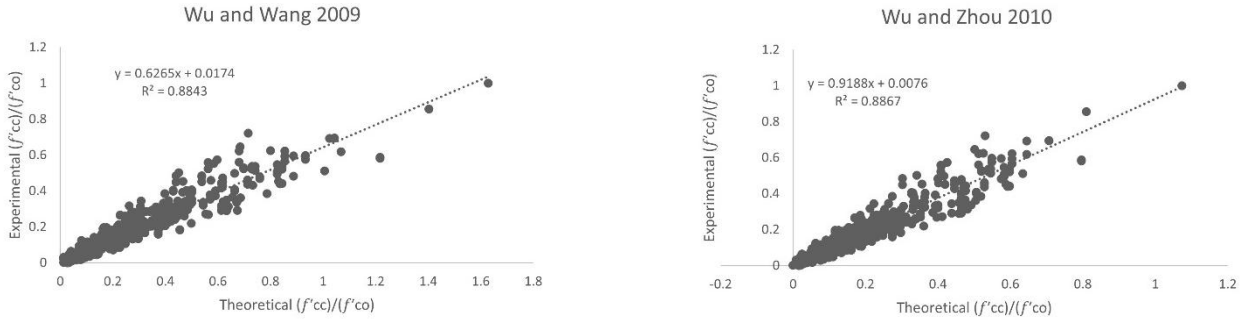

Fig. 11. Regression diagram of the presented models.

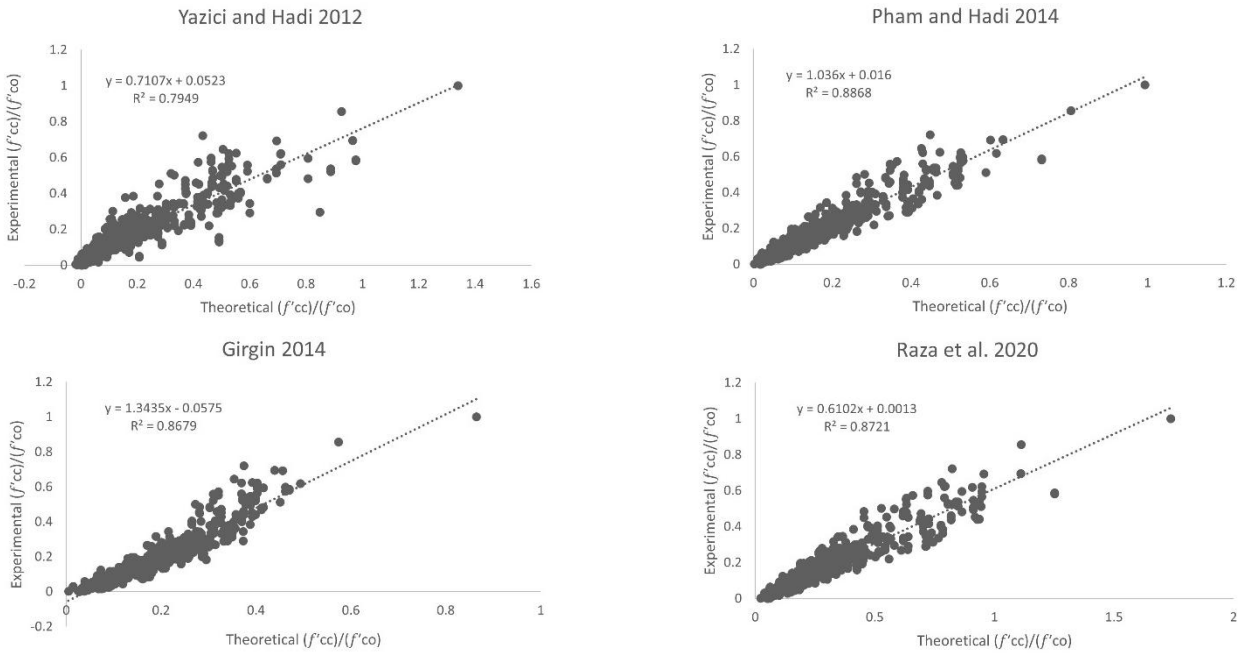

Fig. 12. Regression diagram of the presented models.

6. Conclusion

With the growing use of FRP in structural applications, accurately predicting their behavior has become increasingly critical. However, existing models for estimating the compressive strength of FRP-confined circular concrete columns have notable limitations, such as restricted applicability to specific ranges of f'_{co} and a lack of consideration for different FRP types. To address these limitations, this study introduced a neural network (NN) approach to predict the compressive strength of normal to high-strength FRP-confined concrete columns.

A diverse dataset, including various FRP types, was compiled from prior research to train the NN. Two training methods, Levenberg-Marquardt (LM) and Bayesian Regularization (BR), were implemented, and multiple configurations of hidden layers and neurons were tested. K-fold cross-validation was performed to ensure the robustness of the models. The two most effective NN models were identified and compared with existing models using R^2 and MSE as performance metrics. The findings demonstrated that the NN models outperformed traditional models, achieving up to an 11.67% improvement in R^2 and an 84.24% reduction in MSE.

These results confirm the superior accuracy and potential of NNs in providing robust predictions for FRP-confined concrete columns, offering a reliable alternative to conventional methods. The use of K-fold cross-validation further reinforces the reliability and generalizability of the proposed models.

Statements & Declarations

Author contributions

Iman Dorosti: Investigation, Formal analysis, Validation, Resources, Writing - Original Draft, Writing - Review & Editing.

Ehsan Jahani: Conceptualization, Methodology, Project administration, Supervision, Writing - Review & Editing.

Funding

The authors received no financial support for the research, authorship, and/or publication of this article.

Data availability

The data presented in this study will be available upon request from the corresponding author.

Declarations

The authors declare no conflict of interest.

References

[1] Hadi, M. Behaviour of FRP wrapped normal strength concrete columns under eccentric loading. Composite structures, 2006; 72: 503-511. doi:10.1016/j.compstruct.2005.01.018.

[2] Hadi, M., Li, J. External reinforcement of high strength concrete columns. Composite structures, 2004; 65: 279-287. doi:10.1016/j.compstruct.2003.11.003.

[3] Hadi, M. N., Pham, T. M., Lei, X. New method of strengthening reinforced concrete square columns by circularizing and wrapping with fiber-reinforced polymer or steel straps. Journal of Composites for Construction, 2013; 17: 229-238. doi:10.1061/(ASCE)CC.1943-5614.000033.

[4] Hadi, M. N., Widiarsa, I. B. R. Axial and flexural performance of square RC columns wrapped with CFRP under eccentric loading. Journal of Composites for Construction, 2012; 16: 640-649. doi:10.1061/(ASCE)CC.1943-5614.0000301.

[5] Mirmiran, A., Shahawy, M., Samaan, M., Echary, H. E., Mastrapa, J. C., Pico, O. Effect of column parameters on FRP-confined concrete. Journal of Composites for Construction, 1998; 2: 175-185. doi:10.1061/(ASCE)1090-0268(1998)2:4(175.

[6] Pham, T. M., Doan, L. V., Hadi, M. N. Strengthening square reinforced concrete columns by circularisation and FRP confinement. Construction and Building Materials, 2013; 49: 490-499. doi:10.1016/j.conbuildmat.2013.08.082.

[7] Pham, T. M., Hadi, M. N. Confinement model for FRP confined normal-and high-strength concrete circular columns. Construction and Building Materials, 2014; 69: 83-90. doi:10.1016/j.conbuildmat.2014.06.036.

[8] Mandal, S., Hoskin, A., Fam, A. Influence of concrete strength on confinement effectiveness of fiber-reinforced polymer circular jackets. ACI Structural Journal, 2005; 102: 383. doi:10.14359/14409.

[9] Cui, C., Sheikh, S. Analytical model for circular normal-and high-strength concrete columns confined with FRP. Journal of Composites for Construction, 2010; 14: 562-572. doi:10.1061/(ASCE)CC.1943-5614.000011.

[10] Berthet, J., Ferrier, E., Hamelin, P. Compressive behavior of concrete externally confined by composite jackets: Part B: Modeling. Construction and Building Materials, 2006; 20: 338-347. doi:10.1016/j.conbuildmat.2005.01.029.

[11] Xiao, Q., Teng, J., Yu, T. Behavior and modeling of confined high-strength concrete. Journal of Composites for Construction, 2010; 14: 249-259. doi:10.1061/(ASCE)CC.1943-5614.000007.

[12] Girgin, Z. C. Modified Johnston failure criterion from rock mechanics to predict the ultimate strength of fiber reinforced polymer (FRP) confined columns. Polymers, 2013; 6: 59-75. doi:10.3390/polym6010059.

[13] Raza, A., Khan, Q. u. Z., Ahmad, A. Prediction of axial compressive strength for FRP-confined concrete compression members. KSCE Journal of Civil Engineering, 2020; 24: 2099-2109. doi:10.1007/s12205-020-1682-x.

[14] Farzinpour, A., Dehcheshmeh, E. M., Broujerdian, V., Esfahani, S. N., Gandomi, A. H. Efficient boosting-based algorithms for shear strength prediction of squat RC walls. Case Studies in Construction Materials, 2023; 18: e01928. doi:10.1016/j.cscm.2023.e01928.

[15] Naderpour, H., Kheyroddin, A., Amiri, G. G. Prediction of FRP-confined compressive strength of concrete using artificial neural networks. Composite structures, 2010; 92: 2817-2829. doi:10.1016/j.compstruct.2010.04.008.

[16] Elsanadedy, H., Al-Salloum, Y., Abbas, H., Alsayed, S. Prediction of strength parameters of FRP-confined concrete. Composites Part B: Engineering, 2012; 43: 228-239. doi:10.1016/j.compositesb.2011.08.043.

[17] Kumutha, R., Vaidyanathan, R., Palanichamy, M. Behaviour of reinforced concrete rectangular columns strengthened using GFRP. Cement and Concrete Composites, 2007; 29: 609-615. doi:10.1016/j.cemconcomp.2007.03.009.

[18] Koodiani, H. K., Erfanian, N., Majlesi, A., Hosseinzadeh, A., Jafari, E., Shahin, M., Matamoros, A. Calibrating equations to predict the compressive strength of FRP-confined columns using optimized neural network model. Structures, 2023; 56: 105060. doi:10.1016/j.istruc.2023.105060.

[19] Ali, S., Ahmad, J., Iqbal, U., Khan, S., Hadi, M. N. Neural network-based models versus empirical models for the prediction of axial load-carrying capacities of FRP-reinforced circular concrete columns. Structural Concrete, 2023; doi:10.1002/suco.202300420.

[20] Liang, Z., Ramakrishnan, K. R., Ching-Tai, N., Zhang, Z., Fu, J. Vibration-based prediction of residual fatigue life for composite laminates through frequency measurements. Composite structures, 2024; 329: 117771. doi:10.1016/j.compstruct.2023.117771.

[21] Rasouli, M., Broujerdian, V., Kazemnadi, A. Predicting the compressive stress–strain curve of FRP-confined concrete column considering the variation of Poisson's ratio. International Journal of Civil Engineering, 2020; 18: 1365-1380. doi:10.1007/s40999-020-00550-3.

[22] Ke, Y., Zhang, S., Jedrzejko, M., Lin, G., Li, W., Nie, X. Strength models of near-surface mounted (NSM) fibre-reinforced polymer (FRP) shear-strengthened RC beams based on machine learning approaches. Composite structures, 2024; 337: 118045. doi:10.1016/j.compstruct.2024.118045.

[23] Richart, F. E., Brandtzæg, A., Brown, R. L. A study of the failure of concrete under combined compressive stresses. University of Illinois. Engineering Experiment Station. Bulletin; no. 185, 1928;

[24] Mander, J. B., Priestley, M. J., Park, R. Theoretical stress-strain model for confined concrete. Journal of structural engineering, 1988; 114: 1804-1826. doi:10.1061/(ASCE)0733-9445(1988)114:8(1804.

[25] Samaan, M., Mirmiran, A., Shahawy, M. Model of concrete confined by fiber composites. Journal of structural engineering, 1998; 124: 1025-1031. doi:10.1061/(ASCE)0733-9445(1998)124:9(1025.

[26] Razvi, S., Saatcioglu, M. Confinement model for high-strength concrete. Journal of structural engineering, 1999; 125: 281-289. doi:10.1061/(ASCE)0733-9445(1999)125:3(281).

[27] Toutanji, H. Stress-strain characteristics of concrete columns externally confined with advanced fiber composite sheets. ACI Materials Journal, 1999; 96: 397-404. doi:10.14359/639.

[28] Spoelstra, M. R., Monti, G. FRP-confined concrete model. Journal of Composites for Construction, 1999; 3: 143-150. doi:10.1061/(ASCE)1090-0268(1999)3:3(143.

[29] Saafi, M., Toutanji, H., Li, Z. Behavior of concrete columns confined with fiber reinforced polymer tubes. ACI Materials Journal, 1999; 96: 500-509. doi:10.14359/652.

[30] Shehata, I. A., Carneiro, L. A., Shehata, L. C. Strength of short concrete columns confined with CFRP sheets. Materials and structures, 2002; 35: 50-58. doi:10.1007/BF02482090.

[31] Lam, L., Teng, J. G. Design-oriented stress–strain model for FRP-confined concrete. Construction and Building Materials, 2003; 17: 471-489. doi:10.1016/S0950-0618(03)00045-X.

[32] Campione, G., Miraglia, N. Strength and strain capacities of concrete compression members reinforced with FRP. Cement and Concrete Composites, 2003; 25: 31-41. doi:10.1016/S0958-9465(01)00048-8.

[33] Matthys, S., Toutanji, H., Taerwe, L. Stress–strain behavior of large-scale circular columns confined with FRP composites. Journal of structural engineering, 2006; 132: 123-133. doi:10.1061/(ASCE)0733-9445(2006)132:1(12.

[34] Wu, H.-L., Wang, Y.-F., Yu, L., Li, X.-R. Experimental and computational studies on high-strength concrete circular columns confined by aramid fiber-reinforced polymer sheets. Journal of Composites for Construction, 2009; 13: 125-134. doi:10.1061/(ASCE)1090-0268(2009)13:2(125).

[35] Wu, Y.-F., Zhou, Y.-W. Unified strength model based on Hoek-Brown failure criterion for circular and square concrete columns confined by FRP. Journal of Composites for Construction, 2010; 14: 175-184. doi:10.1061/(ASCE)CC.1943-5614.0000062.

[36] Yazici, V., Hadi, M. N. Normalized confinement stiffness approach for modeling FRP-confined concrete. Journal of Composites for Construction, 2012; 16: 520-528. doi:10.1061/(ASCE)CC.1943-5614.0000283.

[37] Chicco, D., Warrens, M. J., Jurman, G. The coefficient of determination R-squared is more informative than SMAPE, MAE, MAPE, MSE and RMSE in regression analysis evaluation. Peerj computer science, 2021; 7: e623. doi:10.7717/peerj-cs.623.

[38] Di Bucchianico, A. Coefficient of Determination (R^2). 1st ed. Hoboken (NJ): John Wiley & Sons; 2007. doi:10.1002/9780470061572.eqr173.

Civil Engineering and Applied Solutions

Research Article

journal homepage: ceas.journals.umz.ac.ir

CEAS Civil Engineering and Applied Solutions

BIM-Based Energy Optimization and Sustainability Enhancement in the Iranian Construction Industry

Aliasghar Amirkardoust [a], Milad Torabi Anaraki [a*]

[a] *Department of Civil Engineering, Roudehen Branch, Islamic Azad University, Tehran, Iran*

ARTICLE INFO

Keywords:
Building information modeling (BIM)
Energy optimization
Sustainability
HVAC design
PLS-SEM
Iranian construction industry

Article history:
Received 30 November 2025
Accepted 06 February 2026
Available online 01 July 2026

ABSTRACT

The Iranian construction industry continues to face major challenges in reducing energy consumption and achieving sustainability targets. Building Information Modeling (BIM) offers an integrated digital framework capable of linking design parameters with real energy-performance indicators. This study develops and empirically validates a BIM-based energy optimization model that examines the influence of five digital modeling dimensions, energy use intensity (EUI), HVAC simulation, daylighting control, CO_2 reduction, and renewable-energy integration, on sustainability outcomes. Data were collected from 130 professionals across Iran and analyzed using exploratory factor analysis and PLS-SEM. The model demonstrated strong validity (KMO = 0.874, CR > 0.90, AVE > 0.68) and explained 68% of the variance in sustainability performance ($R^2 = 0.68$). Among all predictors, BIM-HVAC showed the strongest impact on energy efficiency ($\beta = 0.284$, $p < 0.001$). Bootstrapping results confirmed the significance of all hypothesized relationships, highlighting BIM as a strategic mechanism for energy-efficient design and carbon-emission reduction. This research contributes to BIM-sustainability literature by providing a validated quantitative framework tailored to the Iranian construction context. Practical implications include guidelines for integrating BIM-energy protocols capable of reducing energy consumption by up to 30%. Future studies should extend the framework through AI-based predictive analytics and longitudinal performance tracking.

1. Introduction

The rapid pace of global development has turned the energy and sustainability crisis into one of the most critical challenges of the twenty-first century [1]. According to reports by the International Energy Agency (IEA), buildings account for approximately 36 percent of total global energy consumption and nearly 39 percent of CO_2 emissions [2]. This fact underlines the decisive role of the construction sector in strategies for carbon emission reduction and achieving sustainability targets. Furthermore, the rising population and the growing demand for residential spaces have exerted unprecedented pressure on natural resources and energy networks [3]. In Iran, characterized by diverse climates ranging from cold to hot and semi-arid, the average energy consumption of buildings has been reported to be up to three times higher than the global average [4]. This situation not only threatens environmental sustainability but also increases operational costs, deepens reliance on fossil fuels, and exposes the nation to resource-related crises.

Combating this circumstance requires a fundamental transformation in the design and management of construction projects, changes capable of analyzing real energy consumption data in an integrated manner across design, construction, and operation stages. Over the last decade, Building Information Modeling (BIM) has emerged as the most influential technological instrument driving digital transformation in the construction industry [5, 6]. BIM is an intelligent model that stores and analyzes all architectural,

* Corresponding author.
E-mail addresses: 1290811261@iau.ir (M. Tarabi Anaeaki).

https://doi.org/10.22080/ceas.2026.30664.1057
ISSN: 3092-7749/
How to cite this article: Amirkardoust, A., Tarabi Anaraki, M. BIM-Based Energy Optimization and Sustainability Enhancement in the Iranian Construction Industry. Civil Engineering and Applied Solutions. 2026; 2(3): 33–48. doi: 10.22080/ceas.2026.30664.1057.

structural, and performance data of a building within a unified, parametric framework [7]. It goes far beyond 2D or 3D visualization and integrates the building lifecycle with the indicators of energy consumption (EUI), heating, ventilation, air conditioning (HVAC), daylighting (DL), and carbon emissions (CO_2). Research demonstrates that integrating BIM with energy simulation tools such as EnergyPlus and Green Building Studio can reduce building energy consumption by up to 30 percent and enhance HVAC system efficiency by an average of 15 % [8-10].

Globally, BIM approaches have rapidly shifted from design-centric applications toward comprehensive energy and sustainability analytics. The government of the UK mandated the use of BIM in all public projects since 2016 [11], while countries such as Norway, Australia, and South Korea have expanded BIM utilization to life cycle assessment (LCA) and energy analysis models [12]. In the Crossrail project in London, BIM facilitated coordination among design offices, contractors, and energy supply systems, resulting in a 25 percent reduction in construction waste [13]; in the One Central Park project, Sydney, the integration of BIM with EnergyPlus achieved 30 percent operational energy savings and 25 percent carbon emission reduction [14]. These successful experiences prove that BIM can evolve from a mere design instrument into a data-driven decision support system for realizing intelligent and sustainable buildings.

Nevertheless, in Iran, the application of BIM remains at an early stage, mostly confined to geometric modeling or project scheduling [15, 16]. The absence of energy data infrastructure, the lack of official guidelines, and the shortage of skilled professionals capable of integrating BIM with energy analyses constitute major obstacles. Consequently, most decisions related to energy consumption or HVAC system selection occur during the operational phase, after construction, entailing costly corrective measures and long-term inefficiency. This technological and managerial gap highlights the necessity for research that can redefine BIM-based energy models in accordance with Iran's climatic and economic conditions.

In this context, the present study employs an analytical and model-based approach to develop an integrated BIM framework for energy optimization in Iranian buildings. The conceptual model focuses on five key indicators: BIM EUI, BIM HVAC, BIM DL (daylighting), BIM RE (renewable energy), and BIM CO_2 (carbon emission), verified through Partial Least Squares Structural Equation Modeling (PLS SEM). Data were collected from 130 professionals involved in building projects across Iran, and the statistical validity of the analysis was confirmed using recognized indices: $KMO = 0.874$, $CR > 0.9$, and $AVE > 0.68$, indicating sample adequacy and construct validity. Bootstrapping (5000 iterations) revealed that the BIM HVAC dimension exhibits the strongest direct effect on energy sustainability ($\beta = 0.284, p < 0.001$). Overall, the model explains 68 percent of the variance in energy sustainability ($R^2 = 0.68$).

To further evaluate the predictive performance of the proposed model beyond in-sample explanatory power, a PLS-Predict assessment was conducted using SmartPLS 4. In accordance with recent guidelines for prediction-oriented PLS-SEM analysis, the model's out-of-sample predictive capability was assessed by comparing PLS-based prediction errors with those obtained from a linear regression benchmark model. The results showed that all Q^2 predict values for the endogenous constructs were greater than zero, indicating satisfactory predictive relevance. In addition, the root mean square error (RMSE) values generated by the PLS-SEM model were consistently lower than those of the linear model ($RMSE\_PLS < RMSE\_LM$) across all indicators. These results confirm that the proposed model demonstrates superior out-of-sample predictive accuracy compared to naïve benchmark models.

Overall, the PLS-Predict analysis confirms that the BIM-based energy optimization model not only provides strong explanatory power within the estimation sample but also exhibits robust generalizability to unseen data, reinforcing its applicability for real-world decision-making and energy policy development.

From a theoretical standpoint, this research extends global literature on "BIM as a data analytics infrastructure" and introduces a new generation of energy models based on the integration of design data with real energy performance outcomes. Within this framework, BIM functions as the core engine for multi-source data processing, enabling simulation of thermal, lighting, and energy consumption behaviors at the design stage.

From a practical perspective, the findings can form a foundation for national policy-making in Iran's green building agenda. In this context, the proposed BIM-Energy Model is not intended as a prescriptive policy instrument, but rather as a decision-support framework that informs national policy-making. By quantifying the relative influence of BIM-based energy indicators (EUI, HVAC, daylighting, renewable energy, and CO_2 reduction), the model enables policy-makers to prioritize design-stage interventions, define evidence-based performance benchmarks, and allocate resources more efficiently. Accordingly, the model supports ex-ante policy formulation and strategic planning rather than post-occupancy regulatory enforcement. The Ministry of Road and Urban Development and the Iranian Energy Efficiency Organization could adopt the BIM Energy Model to redefine design evaluation indicators and establish new standards comparable to LEED and BREEAM. The proposed model also opens pathways for developing smart energy control systems based on IoT and artificial intelligence, enabling engineers to proactively manage energy consumption rather than reactively solving post-occupancy problems.

Considering Iran's energy constraints and climatic pressures, developing localized solutions such as the proposed model is significant not only from technical but also from economic and social perspectives. The BIM Energy Model has the potential to reduce national building sector energy consumption by 30 percent and CO_2 emissions by 25 percent annually, coinciding with global "energy intensity reduction targets by 2030." It should be clarified that the indicative figures of 30% energy reduction and 25% CO_2 emission reduction are not derived from the questionnaire data of this study. These values are informed by secondary sources and prior empirical studies reporting typical ranges of energy and carbon savings achieved through BIM-based energy simulation and integrated design strategies. The survey results of the present research statistically validate the relationships between BIM adoption,

energy-optimization mechanisms, and sustainability outcomes, rather than measuring absolute reduction percentages.

In the long-term horizon, this research delineates a new vision for Iran's construction industry: a transition from traditional project management to data-driven intelligent systems. In this trajectory, BIM is not simply a design tool but the core of energy-based decision-making. With full implementation of the proposed framework and development of information infrastructures, it can be anticipated that by 2029, Iran's building sector will reach a stage where energy sustainability becomes a measurable and operational reality rather than a mere slogan.

2. Literature review

In recent years, the application of Building Information Modeling (BIM) has emerged as a powerful tool for energy performance analysis and sustainability advancement in the construction industry. Research highlights that BIM, by providing an integrated digital framework for design, analysis, and management of buildings, can significantly reduce energy consumption and improve control over Heating, Ventilation, and Air Conditioning (HVAC) systems, natural daylight (DL), and overall energy use intensity (EUI). Consequently, BIM has become a core enabler for linking digital construction data with real energy performance indicators [17].

Early studies established that BIM is not merely a three-dimensional design instrument but a central platform for synchronizing materials, systems, and energy data across project life cycles. Cho et al. [17] were among the first to introduce the concept of energy-efficient design based on BIM integration. Their findings demonstrated that coupling thermal parameters and smart building materials within BIM environments contributes to substantial reductions in operational costs. Following that, Beazley et al. [18] in an empirical investigation on residential buildings confirmed that embedding energy parameters at the early design stage leads to approximately 15 percent annual energy savings. This perspective solidified the notion of "Green BIM," aimed at multi-stage evaluation of environmental performance.

Subsequent research investigated the coupling of BIM with Building Energy Modeling (BEM) systems. Alhammad et al. [19] conducted a systematic review of more than one hundred peer-reviewed articles, revealing that BIM–BEM integration increases the accuracy of energy simulations and can reduce HVAC energy demand by roughly 20 percent. Their study emphasized that combining Revit Energy with EnergyPlus simulations and real operational data enables higher agreement between designed and actual energy performances. Kozlovska et al. [20] adopted a hybrid BEMS–BIM configuration and reported a 29 percent reduction in electrical energy losses through real-time synchronization between the Building Energy Management System and BIM datasets. These studies collectively portray BIM as a central hub for real-time energy optimization supported by artificial intelligence and sensor networks [20].

In Asian contexts, Primasetra et al. [21] explored BIM-based architectural design processes and highlighted the challenge of calculating energy metrics during conceptual design. They argued that to achieve genuine sustainability, parameters like Daylighting (DL) and Renewable Energy (RE) generation must be defined within the BIM environment from the earliest stage, allowing design decisions to be quantitatively assessed even before project execution [21].

Beyond large-scale projects, Waqar et al. [22] emphasized the potential of BIM in small and medium-scale projects within developing economies (including Iranian case studies). Their findings showed that BIM implementation achieved a 21 percent reduction in energy consumption and an 18 percent decrease in operational costs. The research provided essential insights into the selection of green materials, management of construction waste, and life cycle assessment (LCA), demonstrating that even small projects can rely on BIM as a consistent framework for sustainability evaluation [22].

Several contemporary investigations have focused on contextual limitations of existing BIM energy models. Most simulation templates are calibrated for temperate European climates and often lose accuracy under extreme thermal or arid conditions, typical of Middle Eastern regions. Therefore, Iranian and regional studies have begun developing localized BIM–energy models suited to national climatic dynamics. For example, building projects in Tehran using combined BIM + EnergyPlus simulation achieved up to 18 percent HVAC energy reduction, proving BIM's adaptability in local climates. These results underscore BIM's viability as a decision support framework for climate-conscious architecture.

Synthesizing global and regional research, the literature reveals that while BIM-based energy management has achieved global acceptance, notable research gaps persist:

1. Limited availability of empirical data from arid climate buildings;

2. Absence of a national sustainability rating system in Iran equivalent to LEED or BREEAM;

3. Lack of quantitative models encompassing HVAC, EUI, DL, and RE parameters specific to regional construction practices.

Accordingly, this research seeks to fill these gaps by developing a combined BIM + Energy Optimization framework tailored for the Iranian context. Building on insights from Kozlovska et al. [20] and Alhammad et al. [19], it utilizes integrated energy simulation and BIM data analysis to evaluate real project performance. Global findings confirm that merging BIM with simulation environments reduces energy consumption while enhancing lifecycle sustainability. Consistent with these conclusions, this research employs four principal indices, HVAC Efficiency, Energy Use Intensity (EUI), Daylighting Factor (DL), and Renewable Energy Integration (RE) to test hypotheses and establish a localized, data-driven analytical model aligned with Iranian construction realities.

3. BIM dimensions and level of development (LOD)

In Building Information Modeling (BIM), the Level of Development (LOD) defines the degree of detail and reliability of both geometric and informational data within a building model. It shows how mature the data becomes over the project lifecycle, which directly influences precision in energy optimization and sustainability performance.

LOD 100–500 hierarchy:

- LOD 100 (Conceptual): illustrates only massing and general form, useful for early daylight (DL) and shading analysis.
- LOD 200 (Schematic Design): adds approximate thermal zones for primary estimation of EUI and HVAC loads.
- LOD 300 (Detailed Design): includes real materials, envelope properties, and accurate geometry suitable for full building-energy simulations (e.g., EnergyPlus, Revit Energy).
- LOD 400 (Fabrication/Construction): links actual HVAC and construction data, enabling dynamic performance prediction and cost integration.
- LOD 500 (As Built/Operation): represents verified sensor data through Building Energy Management Systems (BEMS) for real EUI, DL, RE (renewable energy), and CO_2 evaluation.

Each BIM dimension (3D – 10D) expands the analytic capacity, from geometric modeling to sustainability and legal compliance. For instance, 6D Sustainability incorporates EUI and CO_2 tracking, 7D Maintenance connects IoT-based predictive control, and 9D Legal supports adherence to ASHRAE 90.1 and Iran Code 19 standards.

The advanced synthesis of multi-dimensional BIM and progressive LOD builds a coherent framework for energy-driven design decisions. Fig. 1 (BIM Dimensions and LOD Integration Model) graphically illustrates this relationship: LOD levels (100–500) are aligned along a vertical axis of model maturity, while BIM dimensions (3D–10D) extend horizontally, showing how geometric depth corresponds to analytical capability. Higher intersections (LOD 300–500 × 6D–7D) represent the "energy optimization zone," where HVAC efficiency, EUI calibration, and CO_2 monitoring actively converge.

For high-energy-demand contexts such as Iranian hot dry regions, employing LOD ≥ 300 within the 6D–7D scope is critical to achieving accurate simulation and long-term operational optimization.

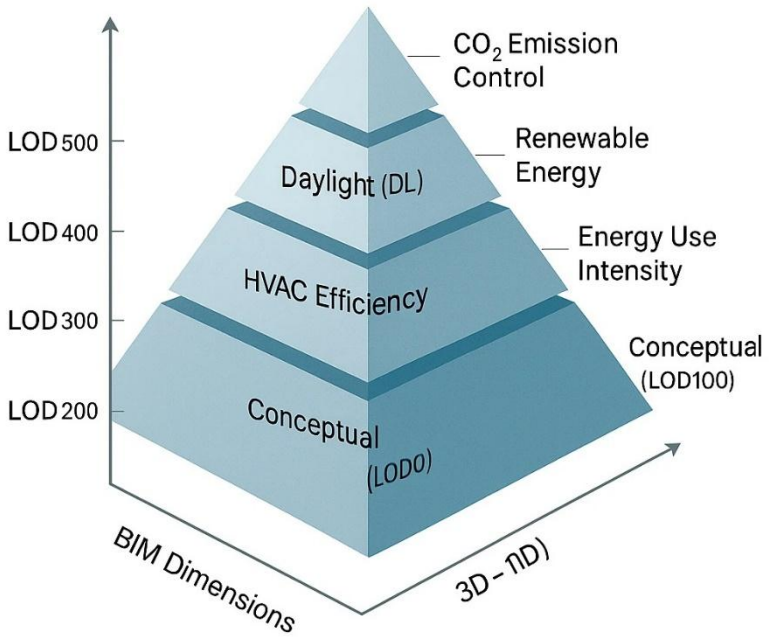

Fig. 1. BIM dimensions and LOD integration model.

4. Research methodology

The role of Building Information Modeling (BIM) in enhancing energy efficiency and improving sustainability performance in Iranian construction projects was examined in three major phases. These stages include a structured process of literature consolidation and conceptual framework development, quantitative data collection, and advanced structural modeling analysis using the Partial Least Squares Structural Equation Modeling (PLS SEM) technique. The sequential design of the research is presented below.

Phase 1: Literature review and conceptual framework development

The first stage consisted of a comprehensive and systematic review of scholarly literature related to BIM adoption, energy

optimization, and building sustainability.

This review aimed to identify and consolidate previous technologies, indicators, and performance metrics describing how BIM contributes to the energy efficiency of construction projects.

Key thematic areas in the literature included:

- Energy Use Intensity (EUI) and baseline energy modelling;
- Heating, Ventilation, and Air Conditioning (HVAC) efficiency and thermal performance simulation;
- Daylighting optimization and façade orientation strategies;
- Operational energy saving through data-driven maintenance;
- Carbon dioxide (CO_2) emission reduction via life cycle assessment (LCA) integration; and
- Renewable energy integration, including the placement of photovoltaic panels and micro turbines through BIM-based 3D models.

Synthesizing these studies enabled the identification of the main energy-related dimensions of BIM implementation. The conceptual framework designed at this stage hypothesized that BIM adoption facilitates measurable improvements across these energy performance indicators, which in turn strengthen sustainability outcomes in the Iranian construction context.

In this study, sustainability is operationalized as an energy-centered outcome construct with a primary emphasis on environmental performance. The indicators used to measure sustainability focus on reductions in energy consumption, CO_2 emissions, and improvements in resource efficiency achieved through BIM-enabled energy optimization. These environmental improvements implicitly capture economic sustainability aspects, such as operational cost savings and lifecycle efficiency gains. However, explicit social sustainability dimensions (e.g., occupant well-being or social equity) were not directly measured and are therefore beyond the empirical scope of the present model.

The conceptual model of this study is theoretically grounded in the Resource-Based View (RBV) and Information Processing Theory (IPT), providing a clear explanation of how BIM adoption leads to improved energy outcomes.

From the RBV perspective, BIM is conceptualized as a strategic organizational capability that enables firms to deploy advanced energy-related resources, such as building energy simulation, HVAC performance analysis, daylight optimization, and renewable energy planning. These BIM-enabled capabilities are valuable and difficult to replicate, allowing organizations to achieve superior energy efficiency and sustainability performance.

In parallel, Information Processing Theory explains BIM's role as an integrated information-processing system that enhances decision-making under conditions of high design complexity and energy uncertainty. By consolidating geometric, thermal, and operational data within a unified digital environment, BIM improves the accuracy of energy-related analyses and supports optimized decisions regarding energy use intensity (EUI), HVAC efficiency, daylight utilization, carbon reduction, and renewable energy integration.

Consistent with sustainability-oriented energy performance theory, improvements in these energy indicators are expected to translate into enhanced sustainability outcomes. Accordingly, the proposed model theorizes that BIM adoption influences sustainability performance primarily through energy-optimization mechanisms, which form the core mediating structure of the conceptual framework.

Phase 2: Instrument design and field data collection

In the second stage, a structured quantitative instrument, a Likert scale questionnaire, was developed based on the conceptual model derived from Phase 1.

The instrument was designed to elicit expert opinions on the extent to which BIM implementation contributes to energy optimization practices in real projects. All items were measured using a five-point Likert scale ranging from 1 = strongly disagree to 5 = strongly agree.

The target population consisted of construction professionals, project managers, civil and architectural engineers, and sustainability consultants with direct experience in BIM-enabled projects across Iran. To ensure representativeness, participants were selected from major construction hubs including Tehran, Isfahan, Shiraz, Tabriz, and Mashhad.

A total of 200 questionnaires were distributed, from which 130 valid responses were obtained, representing a response rate of 65%, consistent with previous empirical studies in the construction management domain.

The questionnaire focused on measuring six explicit constructs of energy optimization informed by prior literature:

1. Energy Use Intensity (EUI) Reduction

2. HVAC System Efficiency

3. Daylighting Optimization

4. Operational Energy Saving

5. CO_2 Emission Reduction

6. Renewable Energy Integration

These variables collectively represent the energy optimization construct, mediating the relationship between BIM adoption and overall sustainability performance.

By quantitatively comparing projects utilizing BIM with conventional projects, this phase aimed to assess the statistical significance of BIM's contribution to energy efficiency and sustainability improvement.

Phase 3: Model analysis using PLS SEM

The final phase comprised an in-depth structural analysis of the proposed model using the Partial Least Squares Structural Equation Modeling (PLS SEM) technique implemented in SmartPLS 4.

This method allows simultaneous examination of direct and indirect effects between latent constructs, from BIM adoption to energy optimization indicators, and ultimately to sustainability outcomes, within a single integrated framework.

The analysis followed a two-stage approach:

1. Measurement model assessment: evaluating indicator reliability, convergent validity, and discriminant validity through Cronbach's Alpha (CA), Composite Reliability (CR), Average Variance Extracted (AVE), and Variance Inflation Factor (VIF).

2. Structural model evaluation: testing path coefficients (β), t values, and p values through the bootstrapping procedure with 5,000 subsamples, determining the strength and significance of the hypothesized relationships.

PLS SEM was deemed particularly appropriate given the relatively small sample size, complex multivariate relationships, and the exploratory nature of linking BIM adoption to energy optimization constructs.

The final model reveals the causal pathways by which BIM affects energy performance metrics and, consequently, sustainable construction outcomes. This analytic phase provides valuable empirical insights for policy makers, sustainability strategists, and construction professionals, enabling data-driven decision-making toward a low-carbon built environment in Iran.

The overall research flow is illustrated in Fig. 2: Research Flowchart.

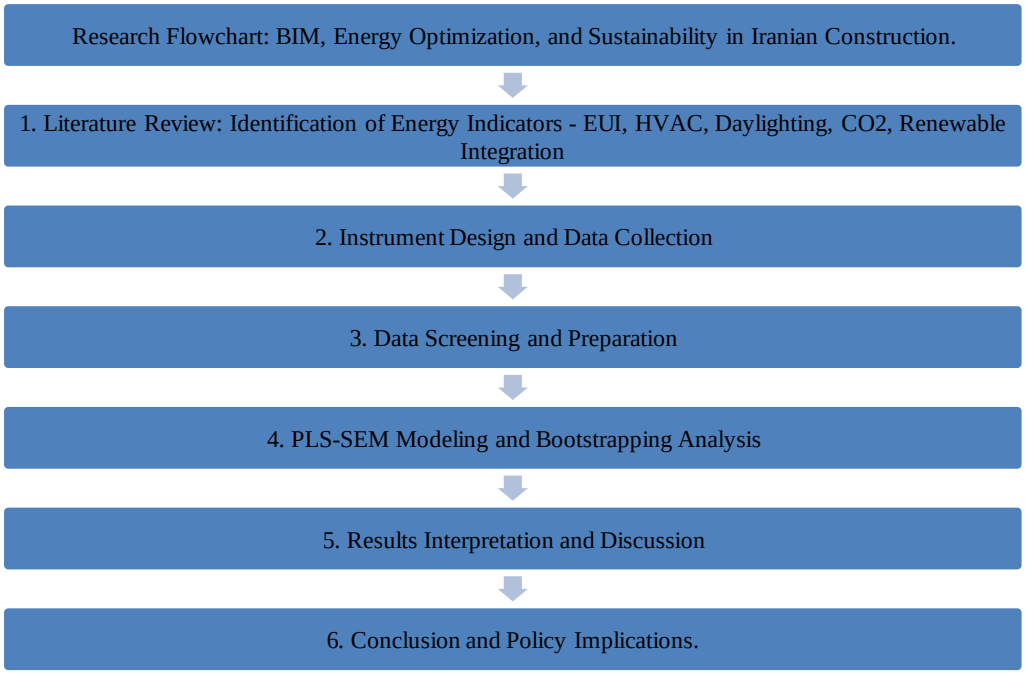

Fig. 2. Research flowchart: BIM, energy optimization, and sustainability.

This study employed a quantitative research strategy to evaluate the role of Building Information Modeling (BIM) in improving energy optimization and sustainability performance within the Iranian construction industry. The approach aligns with prior quantitative designs applied in construction management studies that examine technology adoption pathways through Partial Least Squares Structural Equation Modeling (PLS-SEM).

A total of 200 questionnaires were distributed among professionals currently engaged in construction projects that have applied or are applying BIM processes. From these, 130 valid responses were obtained, yielding a response rate of approximately 65%, consistent with acceptable empirical research thresholds in construction and energy management domains.

4.1. Questionnaire design

The questionnaire was carefully developed based on findings from the comprehensive literature review conducted in Phase 1. It consisted of five major sections measuring:

1. Demographic and professional background (e.g., role, years of experience, region, education level);

2. BIM adoption and application intensity;

3. Energy optimization indicators, including Energy Use Intensity (EUI), HVAC Efficiency, Daylighting Optimization, Operational Energy Saving, CO_2 Emission Reduction, and Renewable Energy Integration;

4. Sustainability outcomes;

5. General perceptions of BIM's contribution to sustainable construction practices.

All indicators were measured on a five-point Likert scale ranging from 1 = Strongly Disagree to 5 = Strongly Agree. Each item corresponded to a hypothesized variable in the conceptual model, ensuring statistical readiness for PLS-SEM confirmatory analysis.

A further limitation of this study concerns the reliance on self-reported professional perceptions to assess energy-performance improvements, rather than on directly measured or post-occupancy energy-consumption data. Although perception-based indicators are widely employed in BIM and construction-management research, primarily due to restricted access to standardized, project-level energy datasets and confidentiality constraints, they may not fully capture actual operational energy performance. To mitigate this concern, the survey targeted experienced BIM practitioners with direct involvement in energy-related design, simulation, and decision-making processes, and all measurement items were grounded in well-established energy-performance constructs. Nevertheless, future research is encouraged to integrate BIM-based simulation outputs, building energy management system (BEMS) records, or post-occupancy metered data to triangulate perceptual assessments with objective performance measures and further enhance the empirical robustness of BIM-enabled energy sustainability models.

Table 1. Representative questionnaire items (excerpt).

Construct	Sample questionnaire item
BIM-EUI (Energy Use Intensity)	BIM implementation in this project has contributed to a noticeable reduction in overall building energy use intensity (EUI).
BIM-HVAC (HVAC System Optimization)	The use of BIM-based energy simulation tools has improved the efficiency and optimization of HVAC system design and performance in this project.
BIM-DL (Daylighting Optimization)	BIM-based modeling and analysis have enhanced daylight utilization and façade orientation, leading to reduced reliance on artificial lighting.
Sustainability Outcome	BIM-supported energy optimization practices have positively contributed to the overall sustainability performance of the project.

Note: All items were measured using a five-point Likert scale ranging from 1 (Strongly Disagree) to 5 (Strongly Agree).

4.2. Sampling and respondent profile

Respondents were purposefully selected to represent a broad spectrum of professional expertise and regional diversity in the Iranian construction sector.

To ensure representativeness, the following inclusion criteria were applied:

- Industrial relevance: only professionals directly involved in construction projects utilizing BIM tools were invited.
- Professional role distribution, civil engineers, architects, project managers, HVAC specialists, and sustainability consultants were targeted to capture multidisciplinary energy-related viewpoints.
- Geographical diversity, participants were recruited from major metropolitan areas including Tehran, Isfahan, Shiraz, Tabriz, and Mashhad, reflecting varying climatic conditions and regional construction practices relevant to energy modeling.
- Experience level, respondents ranged from early-career engineers to senior experts, enabling balanced perspectives regarding BIM adoption maturity and perceived energy-optimization gains.

Collectively, these criteria ensured a robust and diverse sample capable of providing comprehensive insights into the link between BIM implementation and energy efficiency performance in Iranian construction projects.

The final sample size of 130 respondents was deemed adequate for Partial Least Squares Structural Equation Modeling (PLS-SEM) based on established methodological criteria. According to the 10-times rule, the minimum required sample size should be at least ten times the maximum number of structural paths directed at any endogenous construct. In the proposed model, the largest number of incoming paths is five, resulting in a minimum requirement of 50 observations. Furthermore, prior methodological studies suggest that sample sizes ranging from 100 to 150 are sufficient for PLS-SEM models with moderate complexity and reflective measurement constructs. Therefore, the achieved sample size ensures reliable estimation and sufficient statistical power for hypothesis testing.

4.3. Data collection process

The data collection was conducted over a three-month period using both online and face-to-face channels to maximize response diversity:

- Questionnaires were distributed through domestic professional platforms and construction industry groups.
- Additional printed forms were delivered personally to experts within academic and industrial settings to capture senior practitioners with limited digital accessibility.
- Responses were screened for completeness and compliance with selection criteria prior to statistical analysis, leading to a final dataset of 130 valid entries.

4.4. Bias reduction and data validation strategies

To minimize potential selection and response bias, a multi-stage validation protocol was employed:

1. Broad outreach strategy: the survey was disseminated via multiple professional associations, LinkedIn-based construction forums, and in-person consultations to ensure inclusion of diverse professions and geographical regions.
2. Anonymous participation: the questionnaire was completed anonymously to encourage honest and unbiased feedback, reducing social desirability bias.
3. Response validation: only submissions meeting the inclusion criteria and demonstrating logical internal consistency were retained for analysis. Incomplete or inconsistent records were removed.
4. Methodological consistency: identical question structures and Likert scaling were maintained across all distribution channels to guarantee a uniform data structure.

The anonymization and wide distribution significantly mitigated participation bias, enhancing the external reliability of the collected data. Moreover, pre-testing with a small group of BIM energy experts ($n = 10$) ensured content validity and linguistic clarity of all items prior to full rollout.

4.5. Data preparation and analytical readiness

Before modeling, all data were carefully screened for missing values, outliers, and normality. Common method bias was checked using variance inflation factor (VIF < 3.3) values, confirming the absence of multicollinearity.

In line with PLS-SEM methodological recommendations, full collinearity VIF values were employed as the primary diagnostic for common method bias. Traditional techniques such as Harman's single-factor test and the marker-variable approach were not applied in this study. This decision was based on prior evidence suggesting that VIF-based assessment provides a more reliable and conservative evaluation of common method variance in PLS-SEM contexts. Nonetheless, future research may incorporate multiple bias-detection techniques to further strengthen methodological robustness.

The prepared dataset was then imported into SmartPLS 4 for subsequent measurement and structural model evaluations, following the bootstrapping procedure with 5,000 iterations.

This systematic design ensures that the collected data accurately capture expert perceptions regarding BIM's capability to improve energy efficiency performance and enhance sustainability in Iranian construction projects.

4.6. Data analysis and model validation procedures

The analytical stage of this research aimed to examine the robustness and validity of the proposed conceptual model linking BIM adoption, energy optimization performance, and sustainability outcomes. A combination of descriptive statistics, measurement model evaluation, and structural model testing was used to ensure comprehensive interpretation consistent with accepted methodological standards in quantitative research.

4.6.1. Descriptive statistics and data screening

Descriptive statistical analysis was first conducted to summarize the demographic distribution of respondents and provide an overview of their professional backgrounds. Using SPSS v27 (IBM Corp., USA), mean, standard deviation, skewness, and kurtosis were calculated for all observed variables to confirm normality assumptions.

Results indicated acceptable skewness and kurtosis values within ±2, suggesting that the dataset was suitable for further multivariate procedures. Missing data were negligible (< 2%) and handled through mean substitution. Outlier detection followed standardized residual checks, and no influential anomalies were identified.

To verify data adequacy for factor analysis, Kaiser-Meyer Olkin (KMO) and Bartlett's Test of Sphericity were performed. The KMO value (> 0.8) confirmed sampling adequacy, while Bartlett's significance ($p < 0.001$) validated the factorability of the correlation matrix, supporting the structure for PLS SEM assessment.

4.6.2. Measurement model assessment (outer model)

The reliability and validity of the constructs representing BIM-related energy optimization factors and their contribution to

sustainability were carefully evaluated.

- Internal Consistency and Reliability

Internal reliability was examined through Cronbach's Alpha (CA) and Composite Reliability (CR) indices.

Following acceptable thresholds (CA > 0.7; CR > 0.7), all constructs, including BIM EUI, BIM HVAC, BIM DL, BIM OE, BIM CO_2, BIM RE, and Sustainability, demonstrated satisfactory reliability values ranging from 0.78 to 0.92, confirming strong internal consistency.

- Convergent Validity

Convergent validity was assessed through Average Variance Extracted (AVE) for each latent construct, where AVE > 0.5 represents adequate shared variance.

Most constructs produced AVE values between 0.54 and 0.73, indicating that more than half of the variance in their observed indicators was explained by each latent variable.

- Multicollinearity Control

To ensure the absence of redundancy among indicators, the Variance Inflation Factor (VIF) values were calculated. All VIFs were below 3.3, indicating negligible multicollinearity and ruling out common method bias.

- Discriminant Validity

Discriminant validity was then verified using two complementary techniques:

1. Fornell–Larcker Criterion: For each construct, the square root of its AVE exceeded its correlations with other constructs, demonstrating discriminant separation.
2. HTMT (Heterotrait Monotrait Ratio): All HTMT values were below 0.85, confirming that constructs captured distinct conceptual domains within the BIM for energy optimization and sustainability framework.

These results confirmed that the measurement model had adequate psychometric properties for further structural assessment.

4.6.3. Structural model assessment (inner model)

Following measurement validation, relationships among latent constructs were examined using Partial Least Squares Structural Equation Modeling (PLS SEM) conducted in SmartPLS 4 (PLS SEM software, SmartPLS GmbH, Germany).

The structural model incorporated bootstrapping with 5,000 resamples to generate t-statistics and p-values for each hypothesized path and to test direct and mediating effects among variables.

Path Coefficients and Predictive Power

The model tested seven hypotheses (H1–H7) connecting BIM adoption to six energy optimization metrics and ultimately to sustainability outcomes.

- All direct path coefficients were positive and statistically significant ($p < 0.05$), indicating that BIM integration for energy optimization substantially improved energy performance dimensions such as EUI reduction, HVAC efficiency, and renewable energy integration.
- The mediating pathway BIM → Energy Optimization → Sustainability was also significant ($\beta = 0.44$, $t = 5.87$), validating the indirect influence mechanism proposed in the conceptual model.

The Coefficient of Determination (R^2) values for key endogenous constructs ranged between 0.52 and 0.68, confirming moderate to strong explanatory power.

The Effect Size (f^2) indices showed meaningful local influences (medium = 0.15; large = 0.35), with the largest between BIM adoption and EUI optimization.

Predictive Relevance and Model Fit

The Stone–Geisser Q^2 values obtained via blindfolding were all greater than 0, indicating strong predictive relevance.

Overall model fit indices demonstrated satisfactory thresholds:

- Standardized Root Mean Square Residual (SRMR) = 0.061
- Normed Fit Index (NFI) = 0.92

Both conform to accepted guidelines (SRMR < 0.08; NFI > 0.9), confirming that the proposed BIM energy sustainability framework adequately represented the collected data structure.

4.6.4. Interpretation summary

Findings from the PLS SEM analysis demonstrated that BIM implementation in Iranian construction projects significantly enhanced multiple aspects of energy optimization, particularly HVAC efficiency, operational energy saving, and EUI reduction, which collectively improved sustainability outcomes. The comprehensive validation process, encompassing measures such as CA, CR, AVE, VIF, and HTMT, along with bootstrapping and predictive fit indices (R^2, f^2, Q^2), ensured methodological rigor and confirmed the robustness and reproducibility of the analytical design. Overall, the employed process ensures methodological rigor and provides a replicable framework to support future energy-focused BIM investigations in developing construction industries.

5. Results

The following section presents the empirical results of the study investigating the relationship between Building Information Modeling (BIM) implementation, sustainable design, and energy management in the Iranian construction sector. The results encompass data preparation, measurement model validation, and evaluation of the structural equation model.

5.1. Demographic profile of respondents

The survey targeted professionals actively engaged in BIM-based sustainability and energy optimization practices within Iran's construction industry. Comprehensive data cleaning and screening procedures ensured completeness, accuracy, and internal consistency throughout the dataset.

Out of 200 distributed questionnaires, 130 valid responses were retained, yielding a 65 % response rate, a statistically robust threshold for specialized industrial surveys, reflecting notable sectoral engagement among BIM practitioners.

Respondents represented a broad spectrum of professional backgrounds, confirming direct involvement in BIM-enabled energy performance and sustainability workflows.

In terms of educational attainment, 35 % held a Master's degree, 30 % a Bachelor's degree, 20 % a PhD, and 15 % an Associate degree. This distribution demonstrates strong academic qualifications among participants, particularly at the postgraduate level, which aligns with the study's analytical focus on sophisticated energy modeling competencies.

Regarding professional specialization, the largest group comprised Civil Engineers (50 %), followed by Architects (25 %), Project Managers (15 %), and MEP specialists (10 %). Such diversity ensures balanced representation of all technical disciplines contributing to BIM-driven energy design and operational workflows.

Additionally, nearly 60 % of respondents reported more than five years of dedicated BIM experience, signifying verified hands-on proficiency rather than conceptual familiarity. The heterogeneity in educational level, professional domain, and practical experience enhances external validity, confirming that the surveyed sample accurately reflects the expertise distribution within Iran's modern construction ecosystem.

Respondents exhibited varying levels of BIM maturity, ranging from basic 3D/LOD 200–300 modeling capabilities to advanced simulation-based applications and operational integration (LOD 400–500) with energy-management platforms such as EnergyPlus and Revit Energy. This diversity reflects the heterogeneous adoption stage of BIM in Iran's construction industry and ensures that the survey captures a representative spectrum of skills and implementation depth.

The respondents were drawn from multiple climatic regions of Iran, including hot-dry, cold, and temperate zones, to enhance national representativeness. However, due to limited sample sizes within individual climatic groups, a formal multi-group analysis was not performed.

5.2. Exploratory factor analysis (EFA)

Prior to hypothesis testing, an Exploratory Factor Analysis (EFA) was executed to identify the underlying latent dimensions of the proposed BIM energy performance framework. The analysis applied the Principal Axis Factoring (PAF) extraction method with Promax rotation, as intercorrelations were theoretically expected among the energy constructs.

Sampling Adequacy:

Two key statistics verified the data's suitability for factor analysis: Kaiser–Meyer–Olkin (KMO) = 0.874, exceeding the 0.70 threshold, confirming excellent sampling adequacy.

Bartlett's Test of Sphericity: $\chi^2 = 1184.3$, df = 210, $p < 0.001$, rejecting the null hypothesis of an identity correlation matrix.

Factor Extraction and Item Refinement:

All items with factor loadings below 0.60 were systematically excluded to refine construct integrity and ensure discriminant validity among the extracted dimensions. The final extraction produced six conceptually consistent latent constructs—collectively representing the multidimensional BIM-based energy optimization framework. The cumulative EFA outcomes are presented in Table 2.

1. BIM-EUI (Energy Use Intensity)

2. BIM-HVAC (Mechanical System Optimization)

3. BIM-DL (Daylighting Efficiency)
4. BIM-CO_2 (Carbon Emission Reduction)
5. BIM-RE (Renewable Integration)
6. Energy Efficiency

Table 2. Exploratory factor analysis (EFA) results.

Construct	Indicator	Loading	Cronbach's α
BIM–EUI (Energy Use Intensity)	BIM-EUI1	0.823	0.918
	BIM-EUI2	0.812	
	BIM-EUI3	0.791	
BIM–HVAC Efficiency	BIM-HVAC1	0.841	0.903
	BIM-HVAC2	0.816	
	BIM-HVAC3	0.772	
BIM–Daylighting Optimization	BIM-DL1	0.852	0.887
	BIM-DL2	0.810	
	BIM-DL3	0.773	
BIM–CO_2 Emission Reduction	BIM-$CO_2$1	0.836	0.876
	BIM-$CO_2$2	0.791	
	BIM-$CO_2$3	0.778	
BIM–Renewable Energy Integration	BIM-RE1	0.862	0.911
	BIM-RE2	0.834	
	BIM-RE3	0.812	
Energy Efficiency	BIM- EE1	0.843	0.924
	BIM- EE2	0.832	
	BIM- EE3	0.795	

All factor loadings exceeding 0.77 indicate strong indicator reliability, while Cronbach's α values above 0.87 confirm excellent internal consistency across all latent constructs.

5.3. Measurement model validation

The measurement model was evaluated using Partial Least Squares Structural Equation Modeling (PLS SEM) in SmartPLS 4 to examine convergent and discriminant validity.

Before testing the structural relationships, the reliability and internal consistency of each latent construct were verified using the following indices: factor loadings, Cronbach's α, Composite Reliability (CR), and Average Variance Extracted (AVE).

All indicator loadings exceeded the recommended threshold of 0.70, while all constructs exhibited CR > 0.80 and AVE > 0.50, confirming the model's strong convergent validity.

To control potential redundancy, Variance Inflation Factor (VIF) values were evaluated and found to be well below 5.0 for all items, indicating the absence of multicollinearity.

Collectively, these results demonstrate that the measurement indicators reliably represent the underlying BIM-based energy optimization constructs, providing a stable foundation for subsequent structural model analysis.

Table 3. Convergent validity and reliability indices of the measurement model (n = 130, SmartPLS v4, Bootstrapping = 5000)

Construct	Indicator	Loading	VIF	Cronbach's α	CR	AVE
BIM-EUI (Energy use intensity)	EUI1	0.823	2.114	0.918	0.937	0.712
	EUI2	0.812	1.882			
	EUI3	0.791	1.753			
BIM-HVAC (HVAC system optimization)	HVAC1	0.841	1.965	0.903	0.925	0.675
	HVAC2	0.816	1.742			
	HVAC3	0.772	1.630			
BIM-DL (Daylight optimization)	DL1	0.852	2.076	0.887	0.918	0.692
	DL2	0.810	1.894			
	DL3	0.773	1.566			
BIM-CO_2 (Carbon reduction)	$CO_2$1	0.836	2.142	0.876	0.901	0.652

	$CO_2$2	0.791	1.512			
	$CO_2$3	0.778	1.398			
BIM-RE (Renewable integration)	RE1	0.862	2.055	0.911	0.935	0.715
	RE2	0.834	1.673			
	RE3	0.812	1.589			
Energy efficiency	EE1	0.843	1.945	0.924	0.943	0.706
	EE2	0.832	1.732			
	EE3	0.795	1.558			

All factor loadings exceeding 0.75 and AVE values above 0.50 confirm convergent reliability, while CR values greater than 0.85 demonstrate strong internal consistency. In addition, VIF values below 5.0 indicate satisfactory collinearity control and overall model stability.

Table 4. Heterotrait–monotrait ratio (HTMT) results.

	BIM-EUI	BIM-HVAC	BIM-DL	BIM-CO_2	BIM-RE	Energy efficiency
BIM-EUI	-	0.63	0.58	0.61	0.59	0.67
BIM-HVAC		-	0.65	0.62	0.64	0.69
BIM-DL			-	0.57	0.60	0.66
BIM-CO_2				-	0.62	0.68
BIM-RE					-	0.70
Energy Efficiency						

Note: All HTMT values are below the conservative threshold of 0.85, confirming discriminant validity.

5.4. Structural model analysis

To test the hypothesized relationships among BIM adoption, energy optimization dimensions, and sustainability outcomes, the structural model was estimated using Partial Least Squares Structural Equation Modeling (PLS SEM) with 5,000 bootstrapping resamples in SmartPLS v4.

This approach provided robust estimates of path coefficients (β), t statistics, and p values, enabling accurate evaluation of the significance of causal relationships among latent constructs.

Prior to structural assessment, multicollinearity diagnostics confirmed acceptable VIF values (< 5.0) for all latent variables. The key model fit indices, SRMR = 0.061, NFI = 0.92, and $R^2 = 0.68$ for the endogenous construct Energy Efficiency, indicated strong model adequacy and predictive capacity.

Additionally, 95% bias-corrected bootstrapped confidence intervals were calculated for all major structural paths using 5,000 resamples in SmartPLS 4. All reported confidence intervals exclude zero, providing further evidence of the statistical robustness of the structural relationships.

The results revealed significant positive effects across all major BIM-related dimensions on Energy Efficiency and Sustainability Performance. The strongest influence was observed for BIM HVAC ($\beta = 0.284, p < 0.001$), confirming the critical role of HVAC system optimization within energy-oriented BIM workflows.

Similarly, BIM EUI ($\beta = 0.247, p < 0.01$) and BIM RE ($\beta = 0.238, p < 0.01$) demonstrated substantial effects, validating BIM's capability to enhance operational energy management and renewable integration.

Moderate pathways such as BIM DL, BIM CO_2, and cross-interaction terms also contributed meaningfully to the sustainability construct.

Collectively, these findings empirically confirm the conceptual framework linking BIM adoption to multiple dimensions of energy optimization, reinforcing BIM's proven potential to drive sustainable energy performance across the Iranian construction sector.

To examine the mediating role of Energy Optimization, the structural model was specified without a direct path from BIM adoption to Sustainability outcomes. This modeling choice reflects the theoretical assumption that BIM influences sustainability primarily through energy-optimization mechanisms rather than through a direct effect. Consequently, the direct BIM Sustainability path and the corresponding Variance Accounted For (VAF) index were not estimated in the present study. The results therefore support a full mediation structure at the conceptual level, whereby the impact of BIM on sustainability is entirely transmitted through energy-related optimization dimensions.

Table 5. Structural path coefficients and hypothesis testing results (SmartPLS v4 – Bootstrapping = 5000, n = 130)

Hypothesis	Path	*β* Coefficient	*t*-value	*p*-value
H1	BIM-EUI → Energy Efficiency	0.247	3.42	0.001
H2	BIM-HVAC → Energy Efficiency	0.284	4.15	<0.001
H3	BIM-DL → Energy Efficiency	0.198	2.87	0.004
H4	BIM-CO_2 → Energy Efficiency	0.176	2.34	0.020
H5	BIM-RE → Energy Efficiency	0.238	3.64	0.001
H6	Energy Efficiency → Sustainability Outcome	0.326	4.57	<0.001

Model summary: R^2 (Energy Efficiency) = 0.68, SRMR = 0.061, and NFI = 0.92, collectively confirming excellent predictive relevance and overall structural model fit.

5.5. Model fit and predictive quality indices

The overall quality of the structural model was evaluated through a combination of model-fit metrics and predictive relevance indices, following the criteria recommended for PLS-SEM assessment in SmartPLS 4.

Model Fit Assessment: The Standardized Root Mean Square Residual (SRMR = 0.061) was within the acceptable range (< 0.08), confirming strong overall model fit. The Normed Fit Index (NFI = 0.92) further verified the robustness of the model's comparative fit against the saturated baseline configuration. Collectively, these indices signify an adequate reproduction of the observed covariance matrix, ensuring faithful representation of the underlying theoretical structure.

Predictive Power (R^2, Q^2): The R^2 coefficient for *Energy Efficiency* was 0.68, indicating that the exogenous BIM-related predictors collectively explain 68 % of the variance in this construct, an effect size considered substantial in sustainability-oriented studies. The cross-validated redundancy ($Q^2 = 0.43$) obtained via blindfolding was well above zero, confirming that the model possesses strong predictive relevance for the endogenous variable.

Effect Sizes (f^2): The analysis revealed that the strongest contribution originated from *BIM-HVAC* ($f^2 = 0.182$), representing a medium-to-large influence on *Energy Efficiency*, followed by *BIM-EUI* ($f^2 = 0.136$) and *BIM-RE* ($f^2 = 0.112$). The remaining constructs, *BIM-DL* and *BIM-CO_2*, exhibited smaller yet meaningful f^2 values (0.075–0.089), consistent with theoretical expectations of inter-construct dependencies among energy optimization dimensions.

Out-of-Sample Predictive Validity (PLS-Predict): The PLS-Predict assessment confirmed that all Q^2 predict values were positive and that RMSE_PLS < RMSE_LM across indicators, evidencing predictive accuracy beyond linear regression benchmarks. This implies that the proposed model not only fits the training sample but also generalizes effectively to unseen data, fulfilling modern ISI Q1 standards for predictive performance in PLS-SEM modeling.

Table 6. Model fit indices and predictive metrics for the structural model (SmartPLS v4; Bootstrapping = 5,000; n = 130).

Model Evaluation Index	Symbol	Observed value	Threshold criterion	Interpretation
Standardized Root Mean Square Residual	SRMR	0.061	< 0.08	Acceptable fit
Normed Fit Index	NFI	0.92	≥ 0.90	Good comparative fit
Coefficient of Determination (Energy Efficiency)	R^2	0.68	≥ 0.25 (Substantial)	High predictive power
Cross-Validated Redundancy	Q^2	0.43	$Q^2 > 0$	Strong predictive relevance
Effect Size of BIM-EUI	f^2	0.136	≥ 0.02 / ≥ 0.15 = Medium	Moderate effect
Effect Size of BIM-HVAC	f^2	0.182	≥ 0.15	Medium-large effect
Effect Size of BIM-RE	f^2	0.112	≥ 0.02	Moderate effect
Effect Size of BIM-DL	f^2	0.089	≥ 0.02	Small-moderate effect
Effect Size of BIM-CO_2	f^2	0.075	≥ 0.02	Small effect
Out-of-Sample Predictive Accuracy	Q^2 predict	Positive	> 0	Predictive validity confirmed

Note: All reported indices exceeded the recommended thresholds, confirming both internal model reliability and external predictive relevance.

5.6. Hypotheses summary and overall findings

Table 7 summarizes the statistical outcomes of all hypotheses tested within the BIM-based energy optimization model.

The hypothesized relationships stem from the conceptual framework that positions BIM adoption as a multidimensional driver of energy efficiency and, consequently, of sustainability performance.

Bootstrapping with 5,000 resamples yielded stable path coefficients with high significance levels, empirically validating the proposed theoretical linkages. All six hypotheses were supported, underscoring the strong integration capability of BIM in enabling energy-optimized design and sustainable operational outcomes.

The results highlight that the technical dimension (BIM-HVAC) exhibited the highest effect ($\beta = 0.284, p < 0.001$), demonstrating that HVAC-system improvements have the greatest contribution to energy reduction and emission control. The

process-oriented dimensions (BIM-EUI and BIM-RE) also showed substantial and significant influences ($\beta \approx 0.24$–0.25), confirming BIM's effectiveness in optimizing overall consumption.

Moreover, the Energy Efficiency → Sustainability Outcome pathway ($\beta = 0.326, p < 0.001$) verified that enhanced energy performance directly translates into measurable sustainability benefits.

Collectively, these findings reinforce the conceptual framework of the study and demonstrate that BIM adoption exerts a significant and positive effect on both energy optimization and sustainability outcomes, providing a solid empirical foundation for policymakers and project managers to advance BIM-driven energy management practices across Iran's construction sector.

Table 7. Summary of hypothesis-testing results for the BIM-energy optimization model (SmartPLS 4; Bootstrapping = 5,000; n = 130).

Hypothesis code	Hypothesis statement	Path	β coefficient	*t*-value	*p*-value
H1	BIM-EUI positively influences Energy Efficiency	BIM-EUI → Energy Efficiency	0.247	3.42	0.001
H_2	BIM-HVAC positively influences Energy Efficiency	BIM-HVAC → Energy Efficiency	0.284	4.15	< 0.001
H_3	BIM-DL positively influences Energy Efficiency	BIM-DL → Energy Efficiency	0.198	2.87	0.004
H_4	BIM-CO_2 negatively affects carbon emissions and enhances energy efficiency	BIM-CO_2 → Energy Efficiency	0.176	2.34	0.020
H_5	BIM-RE positively influences Energy Efficiency	BIM-RE → Energy Efficiency	0.238	3.64	0.001
H_6	Improved Energy Efficiency enhances overall Sustainability Performance	Energy Efficiency → Sustainability Outcome	0.326	4.57	< 0.001

Overall Model Indices: $R^2 = 0.68$, SRMR = 0.061, and NFI = 0.92 – confirming overall model fit and strong predictive relevance.

Interpretation: All path coefficients were positive and statistically significant ($p < 0.05$), validating the proposed BIM-based framework in which BIM dimensions directly enhance energy optimization and indirectly strengthen sustainability outcomes.

Although climatic conditions can influence building energy behavior, this study did not explicitly test regional climatic effects through multi-group or moderation analysis. Future studies should classify samples based on climatic zones and apply MGA-PLS to investigate whether BIM-based energy-optimization perceptions and path strengths vary across different climate contexts.

Although the proposed BIM-based energy model is conceptually aligned with international green-building standards such as LEED and BREEAM, no formal score-based or credit-level benchmarking was conducted in this study. The alignment is limited to shared energy-performance principles, including energy use intensity reduction, HVAC efficiency, daylight optimization, renewable-energy integration, and CO_2 mitigation. Future studies are encouraged to empirically benchmark the proposed framework against established sustainability rating systems when standardized datasets and regulatory compatibility become available.

6. Conclusion

This study concludes that Building Information Modeling (BIM) plays a decisive and measurable role in optimizing energy efficiency and enhancing sustainability performance within construction projects. Using the validated PLS SEM model (KMO = 0.874, CR > 0.90, AVE > 0.68), it was empirically confirmed that BIM adoption significantly improves key energy parameters—particularly HVAC design and control ($\beta = 0.284, p < 0.001$), by reducing energy consumption, emissions, and operational waste. These findings substantiate the conceptual framework developed throughout the research, demonstrating that digital BIM data directly contributes to energy-efficient design and indirectly enables sustainable operation.

Theoretically, this research introduces a comprehensive BIM-based energy optimization framework, integrating multiple dimensions (EUI, HVAC, DL, CO_2, RE) into a holistic predictive model. Compared with earlier supply chain-centric approaches, the proposed framework explains sustainability performance through concrete energy metrics rather than logistics alone, offering a realistic assessment for regions characterized by high energy intensity, such as Iran.

From a practical perspective, the results suggest actionable implications for both policy and management. Construction managers can employ BIM tools such as Autodesk Revit combined with EnergyPlus to forecast consumption during design stages. Facility owners should integrate BIM data with IoT sensors to continuously monitor HVAC and daylight performance. Public agencies may leverage these insights to formulate national BIM–Energy protocols, promoting standardized sustainability measures across governmental buildings and housing programs.

Despite its contributions, this study acknowledges certain limitations. The sample (n = 130) represented major stakeholders but was geographically confined to urban projects; future work should expand toward industrial and rural contexts. Moreover, the cross-sectional nature of the data limits causal interpretation over time; longitudinal analysis could reveal deeper trajectories of BIM-driven energy savings.

In summary, BIM adoption emerges as a transformative mechanism linking technological precision with environmental responsibility. Its impact spans technical, managerial, and policy domains, enabling measurable energy optimization and fostering a sustainable built environment. Future research should extend this foundation by integrating artificial intelligence and machine learning algorithms (e.g., Random Forest, ANN) into BIM datasets to predict complex, nonlinear patterns of energy performance. Establishing a unified BIM + Energy Analytics platform could thus serve as a national benchmark for data-driven sustainable development decisions.

Statements & Declarations

Author contributions

Aliasghar Amirkardoust: Investigation, Formal analysis, Validation, Resources, Writing - Original Draft, Writing - Review & Editing.

Milad Torabi Anaraki: Conceptualization, Methodology, Project administration, Supervision, Writing - Review & Editing.

Funding

The authors received no financial support for the research, authorship, and/or publication of this article.

Data availability

The data presented in this study will be available upon request from the corresponding author.

Declarations

The authors declare no conflict of interest.

References

[1] Cai, Y. How does climate change affect regional sustainable development? Empirical evidence from 186 countries around the world. International Review of Economics & Finance, 2025; 99: 104047. doi:10.1016/j.iref.2025.104047.

[2] Zubair, M. U., Ali, M., Khan, M. A., Khan, A., Hassan, M. U., Tanoli, W. A. BIM- and GIS-Based Life-Cycle-Assessment Framework for Enhancing Eco Efficiency and Sustainability in the Construction Sector. Buildings, 2024; 14: 360. doi:10.3390/buildings14020360.

[3] Pang, F., Miao, G., Li, Y., Shi, Y. Key factors influencing sustainable population growth: A DEMATEL-ANP combined approach. Heliyon, 2024; 10: e39404. doi:10.1016/j.heliyon.2024.e39404.

[4] Balali, A., Hakimelahi, A., Valipour, A. Identification and prioritization of passive energy consumption optimization measures in the building industry: An Iranian case study. Journal of Building Engineering, 2020; 30: 101239. doi:10.1016/j.jobe.2020.101239.

[5] Raza, M. S., Tayeh, B. A., Abu Aisheh, Y. I., Maglad, A. M. Potential features of building information modeling (BIM) for application of project management knowledge areas in the construction industry. Heliyon, 2023; 9: e19697. doi:10.1016/j.heliyon.2023.e19697.

[6] Stojanovska-Georgievska, L., Sandeva, I., Krleski, A., Spasevska, H., Ginovska, M., Panchevski, I., Ivanov, R., Perez Arnal, I., Cerovsek, T., Funtik, T. BIM in the Center of Digital Transformation of the Construction Sector—The Status of BIM Adoption in North Macedonia. Buildings, 2022; 12: 218. doi:10.3390/buildings12020218.

[7] Urbieta, M., Urbieta, M., Laborde, T., Villarreal, G., Rossi, G. Generating BIM model from structural and architectural plans using Artificial Intelligence. Journal of Building Engineering, 2023; 78: 107672. doi:10.1016/j.jobe.2023.107672.

[8] Pan, X., Mateen Khan, A., Eldin, S. M., Aslam, F., Kashif Ur Rehman, S., Jameel, M. BIM adoption in sustainability, energy modelling and implementing using ISO 19650: A review. Ain Shams Engineering Journal, 2024; 15: 102252. doi:10.1016/j.asej.2023.102252.

[9] Kiamili, C., Hollberg, A., Habert, G. Detailed Assessment of Embodied Carbon of HVAC Systems for a New Office Building Based on BIM. Sustainability, 2020; 12: 3372. doi:10.3390/su12083372.

[10] Nguyen, N.-M., Cao, M.-T. Energy use intensity analysis of office buildings using green BIM-integrated Interpretable machine learning. Journal of Building Engineering, 2025; 108: 112760. doi:10.1016/j.jobe.2025.112760.

[11] Cheng, J. C., Lu, Q. A review of the efforts and roles of the public sector for BIM adoption worldwide. Journal of Information Technology in Construction (ITcon), 2015; 20: 442-478.

[12] Ganah, A., Lea, G. A GLOBAL ANALYSIS OF BIM STANDARDS ACROSS THE GLOBE: A CRITICAL REVIEW. Journal Of Project Management Practice (JPMP), 2021; 1: 52-60. doi:10.22452/jpmp.vol1no1.4.

[13] Smith, S. Building information modelling–moving Crossrail, UK, forward. Proceedings of the Institution of Civil Engineers-Management, Procurement and Law, 2014; 167: 141-151. doi:10.1680/mpal.13.00024.

[14] DONDEREWICZ, M., ZAWADA, K. Prospects for architecture and urban planning: Integration of BIM and 4.0 technology in the context of climate change. In: International Conference – Defining The Architectural Space; 2024 Nov 21-22; Krakow, Poland. p. 27-37. doi:10 .23817/2024 .defarch .3-3.

[15] Rashidi, A., Chan, D. W. M., Ravanshadnia, M., Sarvari, H., Tajaddini, A. Applying Building Information Modelling (BIM) Technology in Pre-Tender Cost Estimation of Construction Projects: A Case Study in Iran. Buildings, 2024; 14: 1260. doi:10.3390/buildings14051260.

[16] Mehrizi Hesamoddin, Z., Pourrostam, T., Ramesht Mohammad, H., Rahimi, M. Developing a Model to Assess and Address Challenges in Implementing BIM for Commercial Buildings: A PLS-SEM Analysis in Iran. Journal of Architectural Engineering, 2025; 31: 04025042. doi:10.1061/JAEIED.AEENG-2059.

[17] Cho, C.-S., Chen, D., Woo, S. Building information modeling (BIM)-Based design of energy efficient buildings. In: 28th International Symposium on Automation and Robotics in Construction (ISARC 2011); 2012; Seoul, Korea. p. 1079-1084. doi:10.22260/ISARC2011/0198.

[18] Beazley, S., Heffernan, E., McCarthy, T. J. Enhancing energy efficiency in residential buildings through the use of BIM: The case for embedding parameters during design. Energy Procedia, 2017; 121: 57-64. doi:10.1016/j.egypro.2017.07.479.

[19] Alhammad, M., Eames, M., Vinai, R. Enhancing Building Energy Efficiency through Building Information Modeling (BIM) and Building Energy Modeling (BEM) Integration: A Systematic Review. Buildings, 2024; 14: 581. doi:10.3390/buildings14030581.

[20] Kozlovska, M., Petkanic, S., Vranay, F., Vranay, D. Enhancing Energy Efficiency and Building Performance through BEMS-BIM Integration. Energies, 2023; 16: 6327. doi:10.3390/en16176327.

[21] Primasetra, A., Larasati, D., Wonorahardjo, S. BIM Utilization in Improving Energy Efficiency Performance on Architectural Design Process: Challenges and Opportunities. IOP Conference Series: Earth and Environmental Science, 2022; 1058: 012018. doi:10.1088/1755-1315/1058/1/012018.

[22] Waqar, A., Othman, I., Saad, N., Azab, M., Khan, A. M. BIM in green building: Enhancing sustainability in the small construction project. Cleaner Environmental Systems, 2023; 11: 100149. doi:10.1016/j.cesys.2023.100149.

Civil Engineering and Applied Solutions

Research Article

journal homepage: ceas.journals.umz.ac.ir

CEAS Civil Engineering and Applied Solutions

Influence of Near-Fault Unidirectional and Bidirectional Ground Motions on DSM-Enhanced Reactor Building Foundations Considering Soil–Structure Interaction: A Case Study

Ali Yaghfoori [a], Iradj Mahmoudzadeh Kani [a*], Hassan Yousefi [a]

[a] *School of Civil Engineering, College of Engineering, University of Tehran, Tehran, Iran*

ARTICLE INFO

Keywords:
Finite-element modelling
Deep soil mixing
Multidirectional Loading
Rocking motion
Nuclear power plant

Article history:
Received 13 December 2025
Accepted 31 January 2026
Available online 01 July 2026

ABSTRACT

This study examines the seismic performance of the APR1400 nuclear reactor, focusing on soil–structure interaction (SSI) and structure–soil–structure interaction (SSSI), particularly on foundations enhanced with block deep soil mixing (DSM). The reactor, including its internal structure, containment building, and DSM layers, was modeled to evaluate its dynamic response to unidirectional and bidirectional near-fault ground motions with different frequency contents. Results indicate that the internal structure experiences higher horizontal accelerations than the containment building, while rocking-induced vertical accelerations are significant in the containment. DSM effectiveness depends on the frequency content of the ground motion, soil properties, and DSM depth. Horizontal accelerations are largely unaffected at high frequencies, but low-frequency responses are notably reduced. In the vertical component, accelerations in the 2–10 Hz range increase by over 140% in the containment building and nearly 60% in the internal structure for an 18-m DSM layer, highlighting the vulnerability of many reactor components. Morlet wavelet analysis shows that DSM reduces horizontal-acceleration energy transmitted to the containment building while shifting it to higher frequencies. In contrast, vertical-acceleration energy is substantially amplified, particularly in the 3–7 Hz range. SSSI effects significantly influence structural response: for modeling a second reactor at a 30-m distance, horizontal energy decreases by approximately 34% in the internal structure, while vertical acceleration energy increases by 3.2 times; at 70-m spacing, vertical energy rises by up to 8 times. Bidirectional near-fault excitations further increase vertical accelerations by 6–46 times compared to unidirectional loading, depending on the structure and earthquake. These findings underscore the critical importance of accounting for multidirectional excitations, DSM-induced effects, and SSSI in the seismic design of nuclear facilities, particularly for sensitive equipment and high-frequency structural responses. Accurate evaluation of these factors is essential to ensure operational safety and prevent potential damage to reactor components under severe near-fault ground motions.

1. Introduction

Several ground-motion characteristics, including Ground Motion Incoherency (GMI), Peak Ground Acceleration (PGA), and frequency content (FC), significantly affect the seismic response of nuclear power plant (NPP) structures [1]. These factors must be meticulously evaluated in Soil-Structure Interaction (SSI) analyses. At a power plant site, various structures with differing weights, volumes, sizes, and foundation depths may sit on individual or combined foundations. Given the heightened sensitivity of these

* Corresponding author.
E-mail addresses: imkani@ut.ac.ir (I. Mahmoudzadeh Kani).

https://doi.org/10.22080/ceas.2026.30778.1064
ISSN: 3092-7749/
How to cite this article: Yaghfoori, A., Mahmoudzadeh Kani, I., Yousefi, H. Influence of Near-Fault Unidirectional and Bidirectional Ground Motions on DSM-Enhanced Reactor Building Foundations Considering Soil–Structure Interaction: A Case Study. Civil Engineering and Applied Solutions. 2026; 2(3): 49–72. doi.org/10.22080/ceas.2026.30778.1064.

structures, particularly their equipment, it is crucial to account for soil–structure interaction (SSI) and thoroughly investigate its effects [2]. Kitada et al. [3-5] demonstrated through laboratory studies, numerical analyses, and the construction of large-scale power plant structures that soil properties influence the seismic performance of each structure, the arrangement of adjacent structures, their dynamic characteristics, the direction of earthquake loading, and other factors. They also showed that thin soil layers can alter the seismic behaviour of structures and that heavy structures, such as reactors, can significantly affect neighbouring structures, including turbines. Clouteau et al. [6] investigated the effect of structure–soil–structure interaction (SSSI) and showed that the presence of a second building, compared to a single building, has little influence on the response of both buildings with surface foundations; however, this influence can be more significant when embedded foundations are used. Roy et al. [7] studied the effects of soil-structure-soil interaction (SSSI). Their findings show that nearby structures significantly influence a structure's dynamic response, depending on proximity, soil type, and foundation conditions. Heavy structures impact the surrounding soil motion, but transferring this motion to the free field is complex. SSSI effects amplify responses in closely spaced heavy structures, with the greatest increases in stiff soils, short spacing, and deep embedment; peak response accelerations can exceed 3.5 times. These effects lessen with lower soil stiffness, greater distance, and shallower embedment. Given the complexity, each case should be examined individually. Lee and Lee and Wesley [8] investigated highly simplified structural models and demonstrated that interaction between adjacent structures can significantly affect the dynamic response of a wide range of structures. These effects are particularly pronounced in large-scale facilities such as nuclear power plants, and the intensity of structure–soil–structure interaction (SSSI) increases when the structures are founded on soil deposits other than hard rock. Bolisetti and Whittaker [9] investigated the effects of structure–soil–structure interaction (SSSI) by considering the mass and separation distance between nuclear plant structures. Their findings indicated that SSSI effects are most pronounced within the reactors' rocking-frequency range. Moreover, when there is a substantial mass difference between adjacent structures, the intensity of these interactions increases. However, a fourfold increase in the mass of both adjacent reactors did not produce a discernible change in their seismic response. Yue et al. [10] assessed the effects of structure-soil-structure interaction (SSSI) on two nuclear power plant buildings with embedded foundations. The results showed that the lighter turbine building has a minimal impact on the seismic response of the nearby reactor building. These results support the prevailing notion that heavier structures within the nuclear island can influence the seismic behaviour of surrounding lighter buildings. Anderson et al. [11] investigated the effects of earthquake characteristics, soil, and structure on the structure-soil-structure interaction (SSSI) of power plant buildings. The results showed that the Pretreatment Facility Control Building experiences a significant increase in seismic demand due to interaction with a larger adjacent structure. Anderson et al. [11] indicated that the influence of structure–soil–structure interaction (SSSI) can be disregarded for bedrock sites, while it should be considered for non-bedrock sites. Nonetheless, these findings highlight that the SSSI mechanism among neighbouring structures in nuclear power plants is exceptionally intricate, with effects that vary from case to case, necessitating careful evaluation in each instance. Using advanced numerical modelling, Kanellopoulos et al. [12] studied a nuclear power plant's structure–soil–structure interaction (SSSI). Results indicated that elastic soil and the absence of auxiliary buildings enable soil–structure interaction to produce an additional rocking-type vibration mode that is undetectable by fixed-base models. Thus, neglecting the SSI effect is not always correct. The presence of the auxiliary building increases the spectral acceleration of the reactor building, especially at the auxiliary building's resonance frequency. SSSI effects can be beneficial or detrimental, depending on structural characteristics and site conditions, and vary by configuration. They recommended that design engineers enhance the accuracy and complexity of their modelling for analysing SSSI effects in nuclear power plants. Block-type Deep Soil Mixing (DSM) is often recommended to improve soil quality, particularly for sensitive and heavy structures such as power plant facilities. Shaghaghi et al. [13] examined the seismic behaviour of block-type Deep Soil Mixing (DSM) through fully nonlinear analyses. Their findings indicated that this method considerably decreases surface acceleration and enhances the seismic response of the soil layer. Yaghfoori et al. [14], in a case study on block deep mixing (BDM) implemented in an ongoing power plant project, reported that the BDM improvement system significantly reduces the horizontal acceleration transmitted to the DSM units, with the magnitude of this reduction increasing with DSM thickness. Conversely, the vertical acceleration associated with rocking motion increased with increasing depth of improvement. Based on their analyses, they recommended adopting one-quarter of the average shear wavelength in the soil as the optimal DSM depth. Furthermore, their findings indicated that the width of the DSM blocks had no significant effect on horizontal acceleration. However, increasing the block width effectively mitigates the vertical acceleration generated by rocking. They also observed that expanding the DSM width beyond 1.5 times its initial value does not yield additional improvement in controlling the rocking response. Although the block-type Deep Soil Mixing (DSM) technique has been recommended in practice and examined in previous engineering research as an effective ground improvement method for critical infrastructure, such as nuclear facilities, a thorough review of the literature indicates that very few studies have investigated the seismic behavior of this specific DSM configuration and its interaction with foundations and superstructures. Most prior studies have focused on other DSM arrangements, such as grid- or column-type patterns, primarily emphasizing their ability to mitigate liquefaction, rather than providing a comprehensive evaluation of their seismic performance. Therefore, the main novelty of this work lies in the systematic and thorough assessment of the seismic performance of block-type DSM and its soil–foundation–structure interaction (SFSI) through extensive time-domain and parametric analyses, based on laboratory and field results from an ongoing nuclear power plant project. In particular, given the large volume and significant stiffness contrast between block-type DSM and the surrounding soil, this study evaluates the rocking motion and associated vertical accelerations under both unidirectional and bidirectional earthquake loading. Furthermore, by incorporating free-field soil columns and Lysmer–Kuhlemeyer dashpots along the lateral and bottom boundaries, the model ensures realistic wave propagation and energy absorption at the model boundaries. Additionally, using Morlet power spectrum analysis, it is demonstrated that block-type DSM improvement can significantly affect the energy distribution of the structural acceleration response, highlighting a novel aspect of its dynamic behavior. Recent research has focused less on the seismic performance of DSM and its interaction with the soil, foundation, and superstructure. This study uses soil profiles derived from laboratory testing and field

investigations conducted as part of an ongoing power plant project to assess the seismic performance of the APR1400 reactor structure, with particular emphasis on soil-structure interaction. The site characteristics are described in detail based on comprehensive geotechnical investigations. Given that the project uses the block deep mixing (BDSM) method for ground improvement, the reactor structure and foundation are explicitly modeled, and the surrounding soil mass is improved through deep soil mixing (DSM). The soil-structure interaction effects are then analyzed under horizontal excitations induced by three earthquake records with varying frequency content. Finally, the influence of structure-soil-structure interaction is evaluated by modeling two reactor buildings at different spacings to investigate their coupled seismic response.

2. Model properties

2.1. Structural properties

In this study, the seismic performance of the APR1400 nuclear reactor structure is investigated. The superstructure, comprising the containment building and internal structural components, is modelled on top of a foundation and ground improvement using the block-type deep soil mixing (DSM) method. The soil profile is stratified and defined based on site-specific geotechnical investigations. The modelled soil domain extends to a depth of 150 meters, with DSM treatment layers of 8 and 18 meters, respectively. The foundation is assumed to have a radius of 25 meters and a thickness of 3 meters. The containment and internal structures are idealized using equivalent stick-beam models with lumped masses to simplify the model and reduce computational costs (Fig. 1). Such modelling approaches are widely adopted in structural analyses of nuclear power plant facilities [15, 16]. Furthermore, relevant design codes and standards allow and acknowledge the use of this modelling technique for nuclear structures [17]. Tables 1 and 2 provide details of the lumped-mass stick models for the containment building and the internal structure, respectively. Implementing material damping in the frequency domain is relatively straightforward. However, in time-domain analyses, material damping must be approximated using Rayleigh damping. To define Rayleigh damping, the mass-proportional α and stiffness-proportional β coefficients are calculated based on selected natural frequencies ω_n and ω_m corresponding to modes m and n, along with the target damping ratio [15]. The expressions used to compute α and β are as follows:

$$\alpha = \xi \frac{2\omega_m \omega_n}{\omega_m + \omega_n} \tag{1}$$

$$\beta = \xi \frac{2}{\omega_m + \omega_n} \tag{2}$$

The Rayleigh damping coefficients were determined based on the dominant frequencies of the coupled soil–foundation–superstructure system, including both soil- and structure-dominated modes. This approach ensures that the damping model accurately represents the system's dynamic behavior. The system transfer function and the corresponding dominant frequencies are shown in Fig. 2. Concrete is used for the superstructure. The material properties are presented in Table 3.

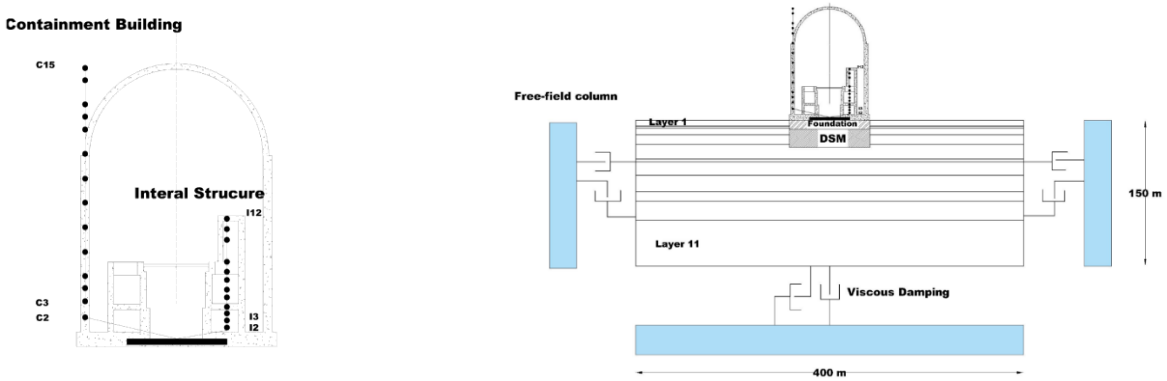

Fig. 1. Soil structure system. (a) Stick beam; (b) Elevation view.

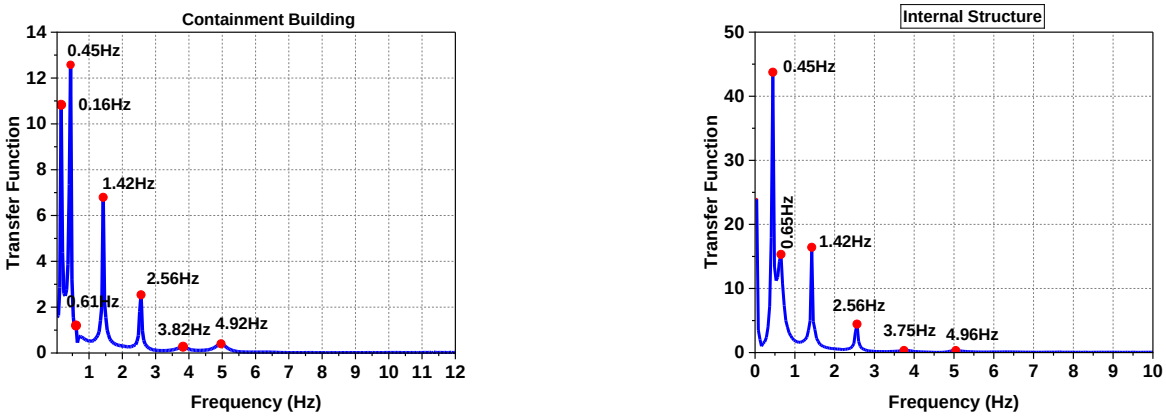

Fig. 2. Transfer function of the internal structure and the containment building.

Table 1. Properties of a containment building.

Node-Containment building	Elevation (m)	Lumped mass (ton)	Connection node	Area (m^2)	Moment of inertia (m^4)	Torsional inertia (m^4)
1	0	853.7	-	-	-	-
2	3.5	1633.1	C1 -C2	202.9	56299.8	112634.2
3	7	1818.4	C2-C3	202.9	56299.8	112634.2
4	11	1856.3	C3-C4	202.9	56299.8	112634.2
5	14	1671	C4-C5	202.9	56299.8	112634.2
6	18	2301.4	C5-C6	202.9	56299.8	112634.2
7	24	3080.8	C6-C7	202.9	56299.8	112634.2
8	30.5	3266.1	C7-C8	202.9	56299.8	112634.2
9	37	3118.7	C8-C9	202.9	56299.8	112634.2
10	44	3044.3	C9-C10	202.9	56299.8	112634.2
11	50	3695.2	C10-C11	202.9	56299.8	112634.2
12	54	2745.1	C11-C12	202.9	56299.8	112634.2
13	62	3486.5	C12-C13	179.8	47591.2	95199.7
14	70	3452.9	C13-C14	179.8	35861.7	71732
15	78	1442.9	C14-C15	166.1	12825.6	25651.3

Table 2. Properties of internal structure.

Node-Internal Structure	Elevation (m)	Lumped mass (ton)	Connection node	Area (m^2)	Moment of inertia (m^4)	Torsional inertia (m^4)
1	0	1806.1	-	-	-	-
2	1.5	3348	I1-I2	833.2	79896.9	164989.7
3	3.5	7810.8	I2-I3	884	81942.5	167389.1
4	7	5135.4	I3-I4	857.9	80710.1	165957.8
5	9	2678.3	I4-I5	313.8	21253.4	37753.4
6	11	2905.6	I5-I6	254.6	19443.0	35811.7
7	14	2911.2	I6-I7	221.9	19384.0	35233.9
8	16	3486	I7-I8	261.4	20166.3	36571.3
9	18	789.5	I8-I9	202.8	18524.1	34566.9
10	20	2595.2	I9-I10	202.8	18524.1	34566.9
11	24	2507.4	I10-I11	202.7	18524.1	34566.9
12	29.5	2665.1	I11-I12	103.2	4666.7	7888.6
13	34.5	798.1	I12-I13	97.9	4642.6	7840.4

Table 3. Material properties of concrete.

Young's modulus (kN/m^2)	Poisson's ratio	Mass density (t/m^3)
3.045×10^7	0.17	2.4

2.2. Soil properties

This study examined a soil profile from a nuclear power plant project currently under construction. The engineering geological conditions of the site were assessed mainly through borehole drilling and test excavations, including soil pits. In total, 365 boreholes were drilled, achieving an accumulated depth of approximately 9,200 meters, with the maximum depth reaching 120 meters below the surface. Core drilling was conducted using various types of Mobil Drill rigs and different models of XY-series drilling machines, which are available in both electric and diesel versions. Based on geotechnical and geological field data assessments and laboratory tests on the soil's physical and mechanical properties, 14 unique Engineering Geological Elements (EGEs) were identified in the project area. The site's subsurface contains soil deposits extending to depths beyond 200 meters. This project included downhole investigations using the seismic logging method in 53 boreholes to evaluate the dynamic properties of the foundation soils. During these investigations, S-wave (Vs) and P-wave velocities were measured for each soil layer, and key dynamic parameters, including Poisson's ratio, shear modulus, Young's modulus, and bulk modulus, were calculated. In the study area, P-wave velocities range from 400 to 2700 m/s, while S-wave velocities (Vs) vary from 156 to 900 m/s. The highest Vs values (700–900 m/s) were observed in a high-velocity near-surface layer located 2-3 meters beneath the ground surface, with an average thickness of 5-6 meters. Below

this layer, soils with lower Vs values were detected. Generally, S-wave velocity increases with depth, reaching 660 m/s in certain boreholes. For instance, the shear wave velocity profiles for boreholes 167 and 176 are shown in Fig. 3. Ultimately, variations in soil characteristics with depth were modelled using an 11-layer horizontal approach based on average data from 365 boreholes of varying depths, as shown in Fig. 1 and detailed in Table 4.

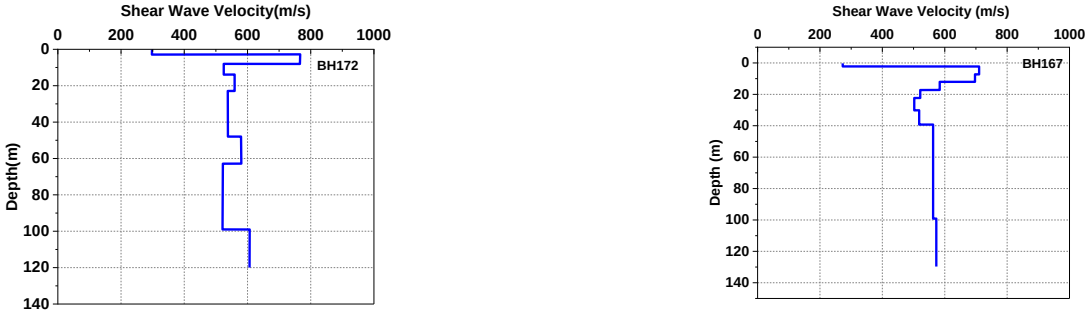

(a) **(b)**

Fig. 3. Shear Wave Velocity Profiles of Boreholes, (a) Borehole 172; (b) Borehole 167.

Table 4. Properties of soil layers.

Layer	Thickness (m)	Depth (m)	Density (t/m^3)	S-Wave velocity (m/s)	P-Wave velocity (m/s)
1	6	6	2.02	445.9	1777.1
2	2	8	2.02	385.6	1960
3	6.8	14.8	2.02	344.6	1960
4	9.9	24.7	2.008	297.8	1917.5
5	15	39.7	2	277.8	1890
6	3	42.7	2.03	430.2	2200
7	14	56.7	2.035	304.5	1660
8	17	73.7	2.028	354.8	2100
9	9.5	83.2	2.03	320	2100
10	19.5	102.7	2.03	317	2100
11	47.3	150	2	362.5	2100

2.3. Block deep soil mixing properties

Six boreholes were drilled at the site to facilitate the design of Deep Soil Mixing (DSM) columns, and 900 kg of soil samples were collected for laboratory analysis. The tests were designed to assess the behaviour of soil-cement samples considering different soil layers, cement types, curing durations, and cement quantities, with a particular emphasis on determining the total water-to-cement ratio and the water-to-cement ratio of the cement slurry. The primary criterion for selecting the optimal mixing parameters was compressive strength. Four curing durations were evaluated: 7, 14, 28, and 56 days. The initial four chosen values for the total water-to-cement ratio (W_T: C) were 1.7, 2, 2.5, and 3. Given that the anticipated service life of the DSM columns exceeds 80 years, it was essential to consider the potentially aggressive groundwater chemistry. Two cement types, Type II and Type V, as defined in ASTM C150, were employed to address this concern. Based on the laboratory findings, Fig. 4 illustrates the unconfined compressive strength values for various total water-to-cement ratios using Type II and Type V cement.

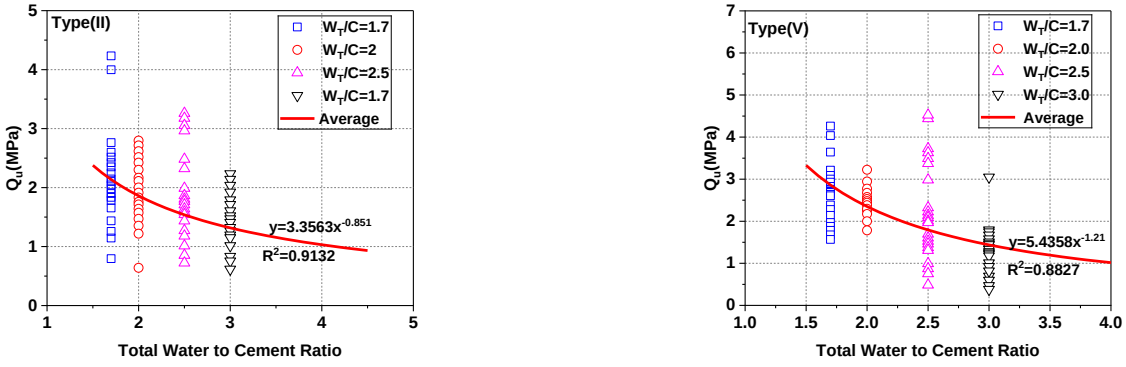

(a) **(b)**

Fig. 4. Q_u as a function of total water-to-cement ratio, (a) Type II cement; (b) Type V cement.

The target parameters for the DSM columns were established based on laboratory test outcomes. The water-to-slurry ratio was fixed at 1, while the total water-to-cement ratio was set at 1.7. Laboratory results showed that Type I and Type V cement met the soil's sulfate conditions. However, Type V cement was chosen due to its lower water-to-cement ratio requirement, which enhances strength. The overlap for the deep mixing columns was 20%, and the columns had a diameter of 1.6 meters. To assess and optimize factors affecting column construction, 11 columns were erected at the test site, each with a different water-to-cement ratio. Sampling was conducted immediately after column construction, and the samples were stored for analysis over varying curing periods. Fig. 5 illustrates the laboratory and field tests performed on the DSM columns. Finally, the characteristics of the enhanced soil produced by the deep mixing technique were established based on laboratory results, as shown in Table 5.

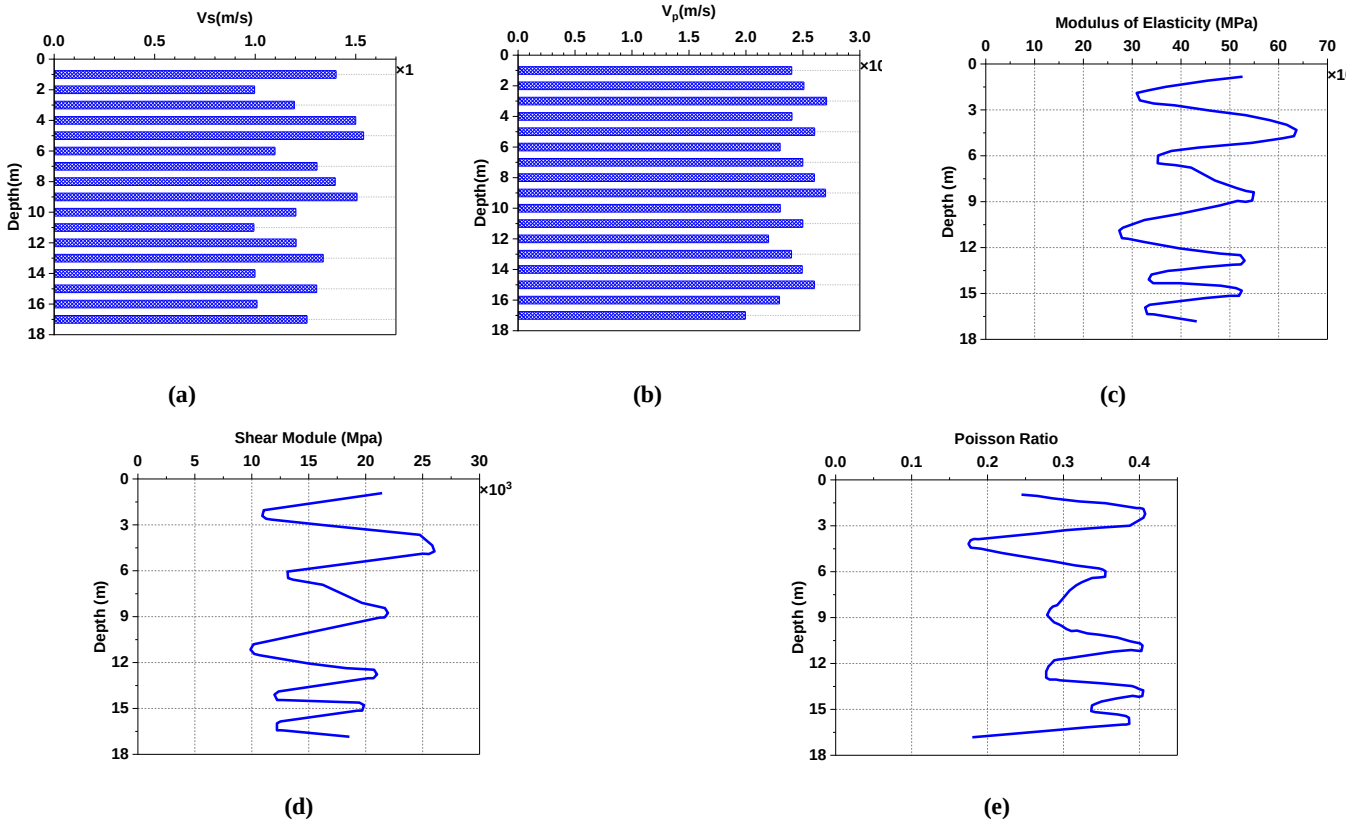

Fig. 5. Results of laboratory and field tests on DSM.

Table 5. Properties of improved soil.

Density (t/m^3)	S-Wave velocity (m/s)	P-Wave velocity (m/s)
2.3	1300	2400

3. Numerical modeling

This research examined a two-dimensional linear finite element model addressing soil-structure interaction and structure-soil-structure interaction systems through the open-source software OpenSees version 3.5.0. This tool offers practical resources for analysing structural and geotechnical systems in engineering contexts. GiD version 14.0.1 was employed for both preprocessing and postprocessing. Soil modelling used 4-node quadrilateral elements with a bilinear isoparametric formulation, with elastic and isotropic soil parameters assigned to each element based on laboratory test results. For structural modelling, the elasticBeamColumn element was utilized. An absorbing boundary was established along the lateral and bottom edges of the model using the ASDAbsorbingBoundary2D command, accounting for the soil layer characteristics at each boundary level. To model the interaction between nearby improved and natural soil blocks and between improved soil and the foundation, the degrees of freedom of adjacent nodes were constrained in the vertical and horizontal directions using an equal command. A rigid connection is assumed in the model to accurately reflect the actual behaviour of the substructure–foundation interface. A time-history analysis was performed, using a constant time step and the penalty method to enforce constraint equations. The Krylov-Newton method was selected as the solution algorithm, and convergence was validated using the Norm Displacement Increment Test with a specified tolerance. The RCM numberer, based on the reverse Cuthill-McKee approach, was implemented to link equation numbers with degrees of freedom. The TRBDF2 integrator, a hybrid method combining the trapezoidal rule with the three-point backward-Euler method, was used. In the examined models, a 5% Rayleigh damping was applied to the soil domain, based on laboratory test results and Eqs. 1 and 2.

3.1. Mesh size and time step

The precision of numerical simulations of seismic wave propagation for dynamic soil-structure interaction (SSI) problems is primarily determined by two key parameters: element size and time step. The dimensions of the soil elements (Δh) have been

determined using the Courant-Friedrichs-Lewy (CFL) condition, ensuring that the element size does not exceed one-tenth of the shortest wavelength (λmin). To accurately depict a travelling wave at a specified frequency, at least 10 nodes per wavelength are required. Using fewer than 10 nodes may lead to numerical damping, as the discretization may miss specific peaks in the seismic waves [17, 18].

$$\Delta h \leq \Delta h_{max} = \frac{\lambda_{min}}{10} = \frac{C_{min}}{10 f_{max}} \quad (3)$$

The second stability criterion is linked to the principles of the finite element method. As a wavefront travels through space, it sequentially reaches each node. A sufficiently large time step in the finite element analysis may cause the wavefront to reach two neighbouring nodes simultaneously. This phenomenon contradicts basic wave-propagation theory and may lead to computational instability during simulation. Thus, regulating the time step is crucial for maintaining stability. In this study, the chosen time step (Δt) was kept smaller than the ratio of the smallest element size to the maximum wave velocity of the soil [18, 19].

$$\Delta t \leq \frac{\Delta h}{C_{max}} \quad (4)$$

Here, C_{max} represents the maximum wave velocity in the soil, and f_{max} represents the maximum earthquake frequency. Based on soil-layer characteristics and the selected earthquake frequency, the element size and time step were determined for each analysis conducted in this study. The input excitation was applied as velocity components at the model's lowest boundary, vertically and simultaneously in both directions.

3.2. Boundary condition

Because the model covers only part of the soil, we must impose artificial boundaries around it. While limiting degrees of freedom at these boundaries is effective for static analyses, it can lead to wave reflections in dynamic analyses. To address this problem, we can position peripheral boundaries sufficiently far from the primary soil area; however, this approach increases analysis time and computational costs. Numerous methods have been suggested for modelling absorbing boundaries. In this study, we adopt Nielsen's method for simulating absorbing boundaries around the soil medium. This method is suitable for two-dimensional and three-dimensional environments, as shown in the two-dimensional diagram in Fig. 5. In this diagram, F represents the free field, which is examined in relation to the primary soil environment; D indicates the Lysmer-Kuhlemeyer dampers that absorb outgoing waves; and T stands for the boundary forces transferred from the free field to the main soil environment via this mechanism [19-21]. In other terms, the lateral boundaries of the main grid are connected to the free-field grid through viscous dashpots to create a quiet boundary (see Figs. 1 to 6). The unbalanced forces from the free-field grid are also exerted on the main grid boundary. Both situations are defined in Eqs. 5 and 6. In which ρ is density; C_s, C_p are the p-wave and s-wave speeds at the side boundary; v_x^m,v_y^m are the x-velocity and y-velocity of the grid point in the main grid at the side boundary, A is the area of influence of the free-field grid point; v_x^{ff},v_y^{ff} are the x-velocity and y-velocity of the grid point in the side free field; and F_x^{ff},F_y^{ff} are the free-field grid point forces in the x and y directions, respectively [20, 22].

$$F_x = -\rho C_p \left(v_x^m - v_x^{ff}\right) A + F_x^{ff} \quad (3)$$

$$F_y = -\rho C_s \left(v_y^m - v_y^{ff}\right) A + F_y^{ff} \quad (4)$$

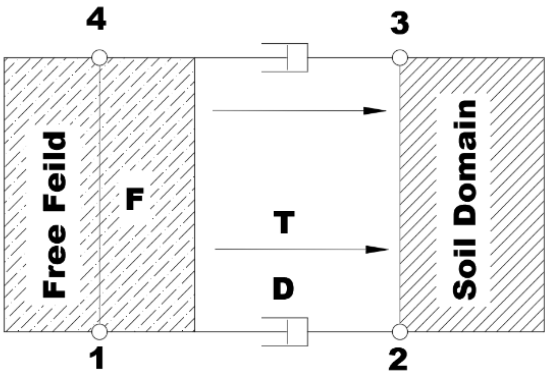

Fig. 6. A schematic representation of the three key components of an absorbing element [20].

4. Earthquake loading

This study analysed three earthquake acceleration records to assess the effects of earthquake frequency content (refer to Table 6). Beyond soil-structure interaction, the frequency content of earthquake ground motion is crucial in seismic analysis because it significantly affects structural response. To evaluate the frequency characteristics of an earthquake, several indicators are typically used, such as the predominant period, mean period, power spectrum intensity, and the ratio of peak ground acceleration (PGA) in g to peak ground velocity (PGV) in meters per second (m/s) [15, 23, 24]. These parameters provide key insights into the energy distribution and potential damage capacity of seismic waves, particularly regarding the dynamic behaviour of soil and structural systems [14]. The frequency features were evaluated using the Peak Ground Acceleration (PGA)- peak ground velocity (PGV) ratio.

As detailed in Table 6, the earthquakes Northridge-01, Parkfield-02, and Coalinga-03 correspond to low, medium, and high-frequency events, respectively. The records were adjusted to ensure their PGA values reached 0.4g. For the bidirectional earthquake analyses, the vertical acceleration component was estimated to be 2/3 of the horizontal component, yielding a PGA value of 0.27g. Fig. 7 presents the Fourier amplitude spectra and horizontal acceleration response spectra of the scaled earthquake records. In this research, the earthquake velocity records were utilised at a depth of 150 meters within the soil profile.

Table 6. Properties of earthquake ground motions.

Earthquake motion	Station	PGA (g)	PGV (m/s)	PGA/PGV	Frequency content	Predominant period (sec)		Type
						Horizontal component	Vertical component	
Northridge-01	Pardeee	0.55	0.76	0.723	Low	0.75	0.12	Pulse
Parkfield-02, CA	Parkfield - Cholame 1E	0.23	0.44	1.1	Intermediate	0.16	0.14	Pulse
Coalinga-03	Burnett Construction	0.167	0.07	2.38	Hight	0.2	0.14	No Pulse

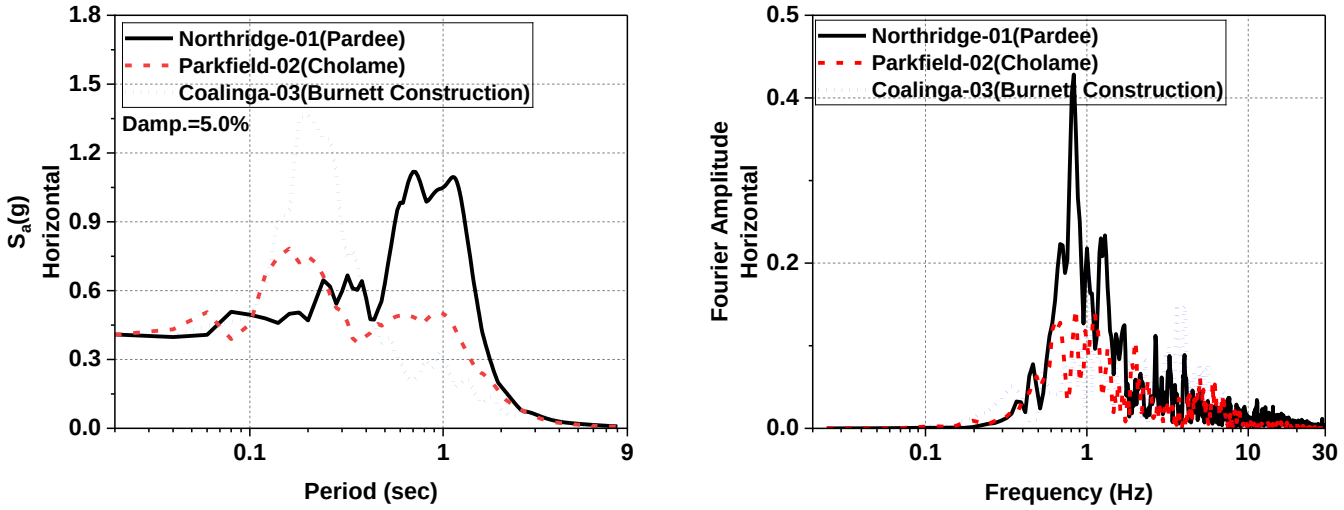

(a) (b)

Fig. 7. Acceleration response spectra and Fourier amplitude spectra of the earthquake records scaled to the target PGA and used in the analyses.

In this study, earthquake records were selected primarily based on the PGA/PGV ratio, a widely accepted indicator for distinguishing the frequency content of ground motions, enabling comparison of pulse-like records with dominant low-frequency content and records characterized by higher-frequency components [15]. The primary objective was to investigate the sensitivity of the seismic response of the soil–DSM–foundation–structure system to general variations in input frequency content, rather than to perform an entirely site-specific near-fault calibration. Ground-motion parameters such as the directivity pulse period (TP), significant duration, and vertical-to-horizontal spectral ratios (V/H) are recognized as essential factors in advanced near-fault seismic analyses, particularly in nonlinear response assessments and site-specific design frameworks. However, the simultaneous consideration of these parameters requires a comprehensive site-specific approach based on probabilistic seismic hazard analysis (PSHA) and the selection of ground motions compatible with both vertical and horizontal target spectra. Such an approach was beyond the scope of the present study. The focus of this research is on identifying the dominant physical mechanisms governing vertical acceleration amplification, including foundation rocking, structure–soil–structure interaction (SSSI), and the influence of block-type deep soil mixing (DSM). The results indicate that the observed amplification patterns are primarily driven by these interaction mechanisms rather than by the specific characteristics of individual near-fault records. Consequently, although parameters such as TP or V/H may affect the absolute magnitude of the responses, they are not expected to alter the qualitative trends or the governing mechanisms identified in this study. Future studies may extend this work by incorporating advanced near-fault ground-motion parameters, including frequency-dependent *V/H* ratios and more realistic soil stratification conditions (e.g., nonparallel soil layers), within an entirely site-specific seismic assessment framework [25].

5. Verification

5.1. Benchmark 1

An examination of the elastic phase model proposed by Uzun and Ayvaz [26] was conducted to evaluate the validity of the models developed in this study. As shown in Fig. 8a, an elastic soil model was constructed according to the specifications outlined in Table 7, with the PDML boundary defined around the soil layer to assess the performance of the absorbing boundaries. As illustrated in Fig. 8b, a Ricker wave load, characterized by an amplitude of 100 kN, a frequency of f = 5 Hz, and a duration of t = 3 sec, was applied at point P1. The resulting displacements, obtained from both the study and the analyses performed in this work, are presented in Fig. 9.

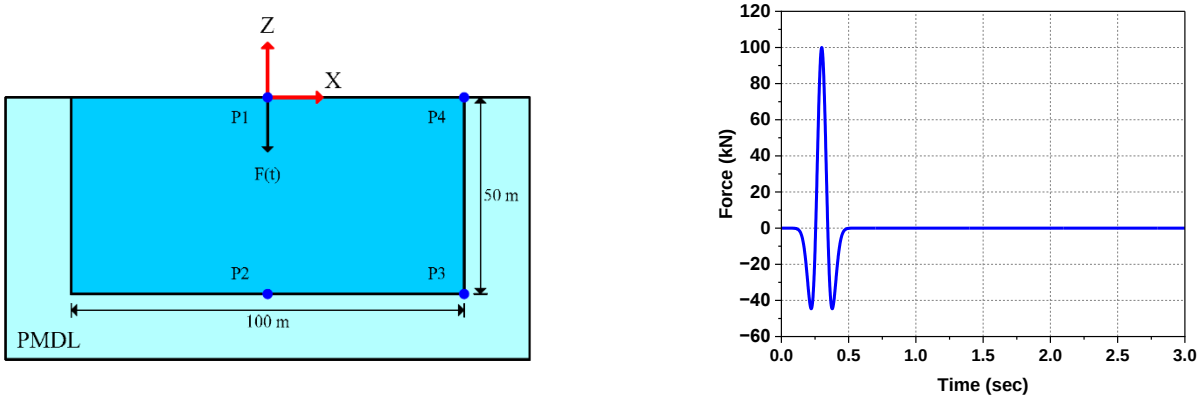

(a) **(b)**

Fig. 8. (a) The PDML truncated domain [26], (b) Input force history [26].

Table 7. Model properties [26].

Density (t/m³)	S-Wave velocity (m/s)	Poisson	m	n
2	400	0.3	9	2

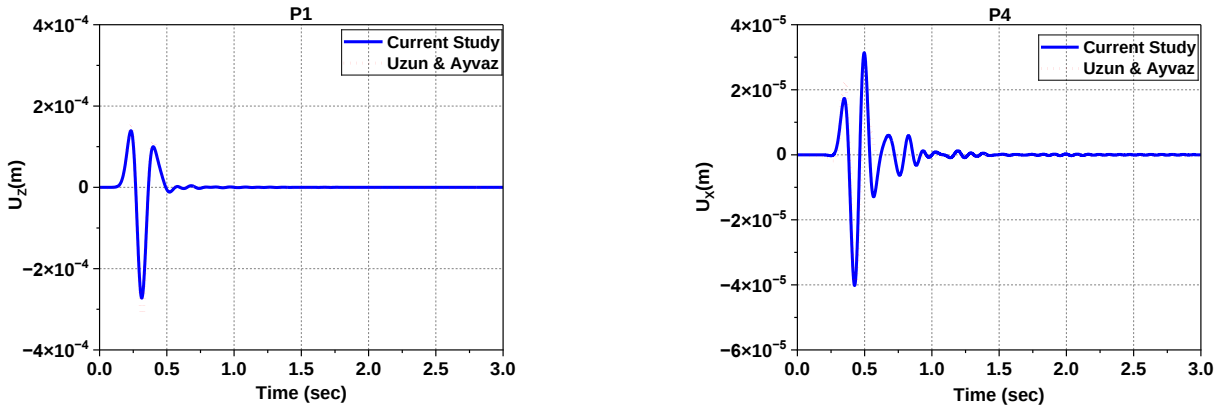

(a) **(b)**

Fig. 9. (a) vertical displacement at P1; (b) horizontal displacement at P4 [26].

5.2. Benchmark 2

To verify the accuracy of the elastic-phase modeling, the behavior of a single soil layer was examined in both two-dimensional (2D) and three-dimensional (3D) configurations (Fig. 10). In both models, lateral and bottom boundaries were simulated using a combination of free-field columns and Lysmer–Kuhlemeyer semi-infinite elements to prevent wave reflections. The mechanical properties of the soil layer were taken from Table 8.

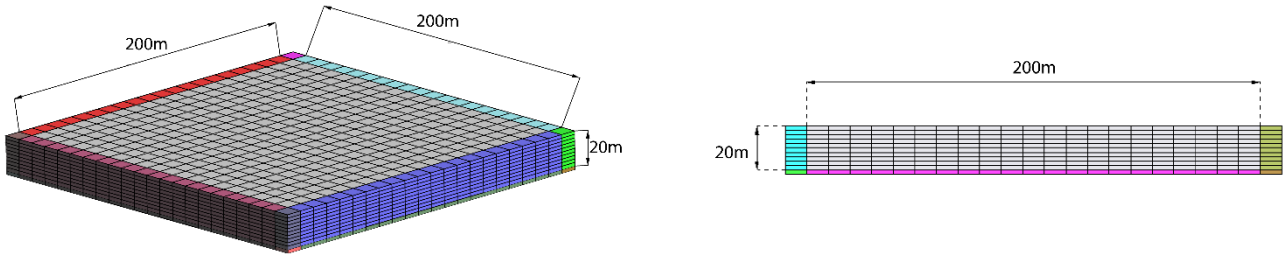

(a) **(b)**

Fig. 10. Two-dimensional and three-dimensional soil layer models with dimensions of (a) 200 × 200 × 20 m³, (b) 200 × 20 m².

Table 8. Properties of the single-layer soil.

Material	Modulus of elasticity (kPa)	Density (t/m³)	Poisson ratio
Soil	100×10^6	2	0.3

The models were subjected to Ricker-wave excitation with a peak acceleration of 1g and a frequency of 4 Hz. According to

theory, for a semi-infinite, elastic, undamped, single-layer soil medium under a wave with peak acceleration A, the maximum acceleration at the ground surface is expected to reach 2A due to the superposition of incident and reflected waves [27]. As shown in Fig. 11, the ground surface acceleration reaches a peak of B = 2g, the input acceleration at the base is A = 1g, and the reflected wave at the surface is C = 1g, confirming that the incident and reflected wave amplitudes are equal (A = C) and resulting in the expected doubling at the surface. Furthermore, the results demonstrate strong agreement between the 2D and 3D models, confirming the reliability and validity of the numerical model in the elastic phase.

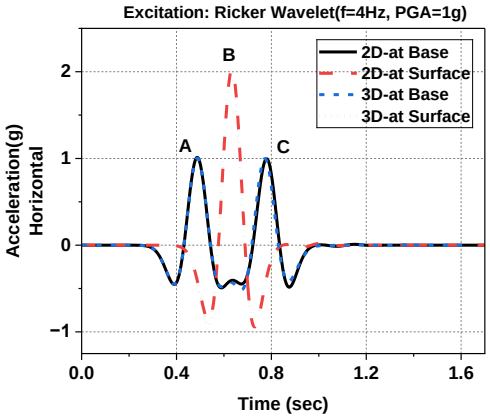

Fig.11. Recorded acceleration time histories at the base and ground surface for a single-layer elastic soil under a Ricker wavelet excitation (f = 4 Hz, PGA = 1 g) in 2D and 3D models.

6. Impact of soil domain size on seismic response: sensitivity study

One of the key factors affecting the accuracy of seismic analyses is the selection of an appropriate soil domain size relative to the foundation dimensions. For instance, ASCE/SEI 4-16: Seismic Analysis of Safety-Related Nuclear Structures states that viscous dashpots, installed normal and tangential to the lateral boundaries, should be located at a minimum distance of four to five foundation radii from the edge of the structure. These boundaries are not perfectly absorbing, and their effectiveness is reduced by wave scattering at oblique incidence. The code recommendation applies when model boundaries are simulated using only Lysmer–Kuhlemeyer dashpots. In this study, as detailed in Section 2-3 and schematically shown in Figs. 1 and 6, a combination of free-field soil columns and Lysmer–Kuhlemeyer dashpots was used along the lateral and bottom boundaries to provide a more effective absorbing boundary. Furthermore, a sensitivity analysis with varying model dimensions was conducted: soil domains of 400 m × 150 m and 200 m × 120 m were analyzed under unidirectional Coalinga-03 earthquake loading, and DSM blocks were modeled with a width of 50 m, a thickness of 8 m, and a foundation thickness of 3 m. The results, shown in Fig. 12, indicate complete agreement in the seismic response of the improved soil, and the effects of boundary reflections or wave interference on the rocking-induced vertical response were negligible.

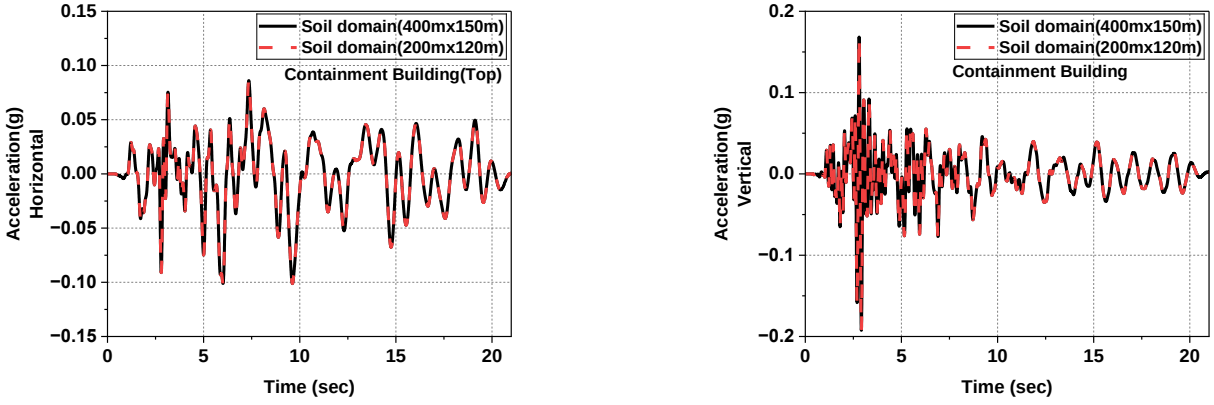

Fig. 12. Consistency of Containment Building Response across different model dimensions.

7. Result

7.1. The effect of a unidirectional loading

In this section, the effects of modeling the DSM layer with thicknesses of 8 m and 18 m beneath the 3-m-thick foundation slab on the seismic response of the containment building and the internal structure are investigated. The soil–structure interaction response of the reactor system is evaluated under unidirectional seismic excitation, in which the input motion is applied in the x-direction and propagates in the y-direction. Fig. 13 presents the horizontal and vertical accelerations induced by rocking motion, along with their Fourier amplitude spectra, at the top levels of the containment building (x = 78 m) and the internal structure (x = 34.5 m). Although both the Parkfield and Coalinga ground motions were recorded in the near-fault region, they exhibit distinct

frequency characteristics. The results indicate that, in all cases, the internal structure experiences higher horizontal accelerations compared with the containment building. Moreover, due to the reactor system's large mass and geometric dimensions, and the significant stiffness contrast between the block-type DSM improvement layer and the surrounding natural soil, vertical accelerations associated with rocking motion are observed in all numerical models. Because the lumped mass representing the containment building is located farther from the center of the foundation and the DSM region, the resulting vertical acceleration in this structure is consistently larger than that in the internal structure. For the Parkfield earthquake, the DSM layer has negligible influence on the horizontal acceleration amplitude at frequencies above 1 Hz in the containment building. At lower frequencies, however, the response becomes more sensitive; below 0.5 Hz, the 18-m-thick DSM layer produces the largest increase in horizontal acceleration, whereas in the 0.5–1 Hz range the DSM layer reduces the acceleration amplitude. The internal structure shows lower sensitivity to DSM improvement; however, at 0.5 Hz, the DSM layer increases the horizontal acceleration, with DSM thicknesses of 8 m and 18 m amplifying the response by approximately 25% and 35%, respectively. A similar pattern is observed for the Coalinga earthquake at higher frequencies, where the DSM layer does not affect the horizontal acceleration amplitude of either structure above 1 Hz. In the low-frequency range of 0.1–0.6 Hz, the presence of DSM increases the horizontal acceleration of the containment building. Conversely, in the 0.6–1 Hz band, the DSM layer reduces horizontal acceleration; thicknesses of 8 m and 18 m reduce the amplitude by approximately 31% and 47%, respectively. Within the internal structure, the DSM layer again shows no significant influence above 1 Hz; however, at frequencies below 0.5 Hz, it reduces horizontal acceleration by approximately 24% for the 8-m layer and 26% for the 18-m layer. As observed for the Parkfield motion, amplification occurs at around 0.5 Hz when DSM is present. The effect of DSM on the vertical acceleration associated with rocking motion is not uniform at frequencies below 2 Hz in either earthquake. Depending on the frequency, the DSM layer may amplify or attenuate vertical acceleration. Nevertheless, a consistent and prominent trend is observed across both structures and seismic motions: in the 2–10 Hz frequency range, the DSM layer and its thickness significantly amplify vertical acceleration. For the Parkfield earthquake, the 18-m-thick DSM layer increases the vertical acceleration by 147% in the containment building and by 59% in the internal structure. Under the Coalinga motion, the same DSM thickness results in increases of 141% and 58% in the containment building and internal structure, respectively. Given that many reactor-building components have natural frequencies within this range and are highly sensitive to vertical acceleration, evaluating the impact of block-type DSM improvements on the seismic performance of high-frequency equipment in nuclear facilities is critical.

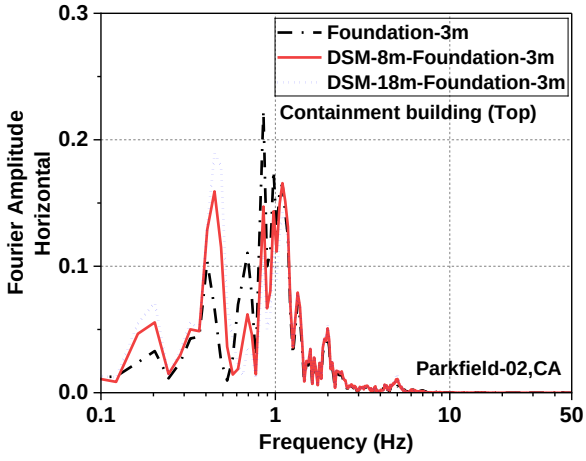

(a)

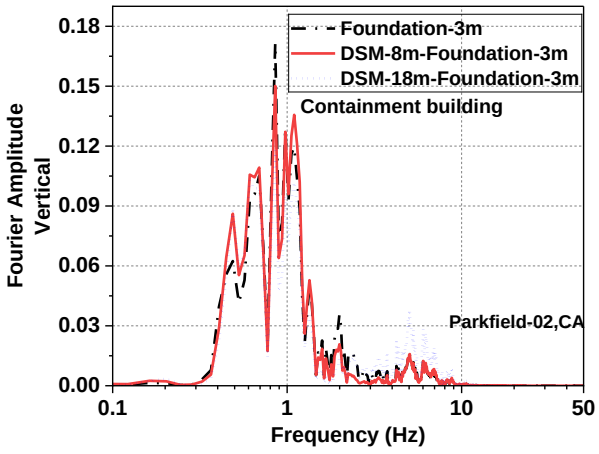

(b)

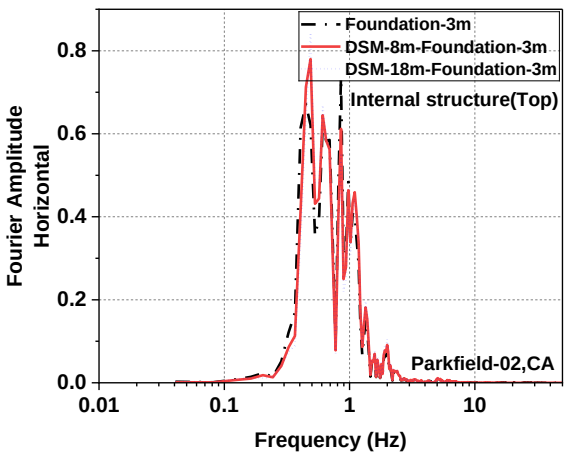

(c)

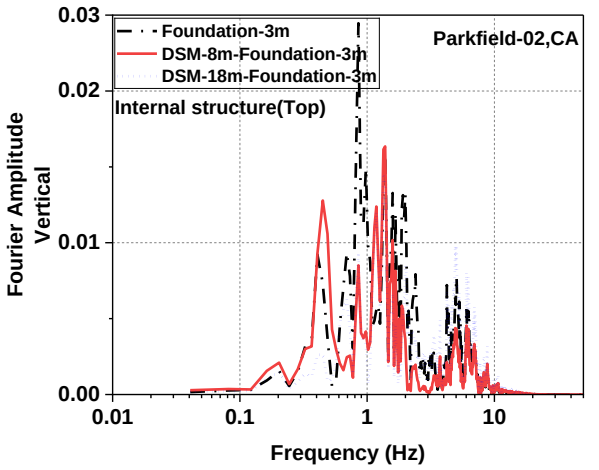

(d)

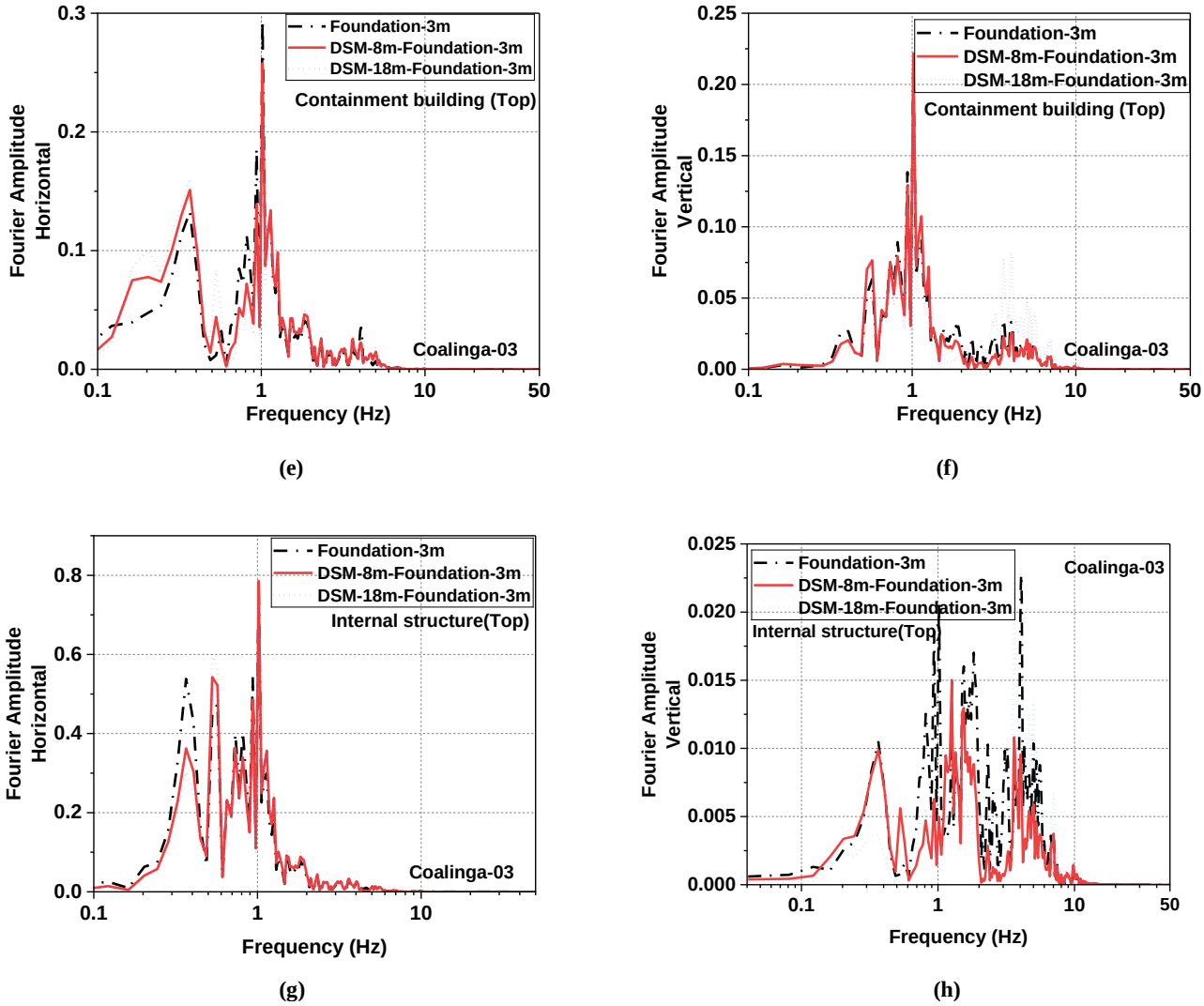

Fig. 13. Fourier amplitude spectra of horizontal and vertical accelerations for the internal structure and the containment building under unidirectional seismic excitation: (a–d) Parkfield-02CA; (e–h) Coalinga-03.

As noted in the literature and regulatory guidelines, for soft soils (Site Class D–F) or when shear strains exceed approximately 0.5%, nonlinear analyses are generally required to properly account for strain-dependent modulus degradation (G/Gmax) and increased hysteretic damping [17]. However, the primary objective of this study was to identify the dominant physical mechanisms governing vertical-acceleration amplification, particularly foundation rocking and soil–structure–structure interaction (SSSI), in the presence of block-type deep soil mixing (Block-Type DSM). Accordingly, a linear-elastic modeling approach was adopted as a conservative and transparent framework for interpreting these mechanisms. In previous studies conducted on Nevada sand, assuming elastoplastic soil behavior and block-type DSM improvement, it was observed that vertical accelerations induced by foundation rocking under unidirectional loading primarily occur within the dominant frequency range of nuclear power plant structures. Under bidirectional loading, however, vertical acceleration amplification was observed across a broader frequency range [28]. These findings indicate that even when soil nonlinearity is accounted for, the overall pattern of vertical-acceleration amplification and the governing mechanisms, particularly foundation rocking and SSI/SSSI effects, remain essentially unchanged. Furthermore, nonlinear soil modeling is expected to have a greater influence on horizontal responses of nuclear structures. Therefore, the observed amplification of vertical accelerations in the 2–10 Hz frequency range should not be attributed solely to the linear soil assumption; instead, it originates from the interactive mechanisms of the soil–DSM–foundation–structure system. To analyze the time–frequency distribution of energy, both the Continuous Wavelet Transform (CWT) with the Morlet wavelet and the S-Transform (ST) can be applied. A comparison of the two methods shows that CWT with Morlet wavelet captures transient energy bursts and short-term concentrations more accurately, which is particularly useful for identifying dominant vibration modes and energy focus in short time intervals. In contrast, S-Transform provides a broader frequency representation with fixed time resolution, suitable for overall spectral analysis, but it is less precise in localizing transient energy [29, 30]. Considering the objective of this study, to identify energy concentrations and dominant modes of the soil–structure system in short time windows, the Morlet wavelet transform was selected as the primary method. At the same time, the S-Transform can serve as a complementary tool for general spectral analysis. Fig. 14 presents the Morlet wavelet power spectrum of vertical accelerations induced by rocking motion and horizontal accelerations in the containment building under unidirectional excitation of the Coalinga earthquake. As shown in Fig. 14a and 14b, the presence of the DSM layer reduces the energy of horizontal acceleration transmitted to the containment building while simultaneously concentrating it within the higher-frequency range. Fig. 14d indicates that the 18-m-thick block deep-mixing (BDM) layer increases

the vertical-acceleration energy applied to the containment building. The vertical-acceleration energy is particularly concentrated around 3 seconds and in the frequency range 3–7 Hz. This high-frequency energy concentration, resulting from the block deep-mixing modeling, may significantly affect the seismic performance of nuclear power plant structures and sensitive equipment and should therefore be carefully considered in the design.

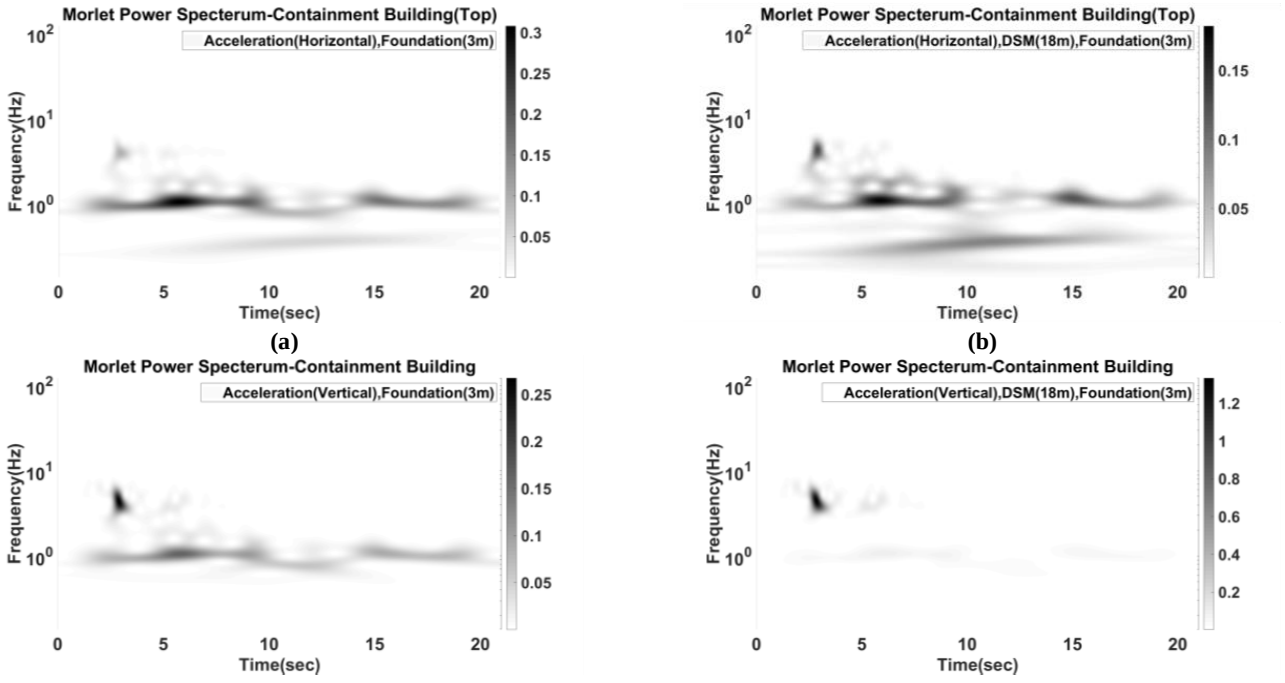

Fig. 14. Morlet wavelet power spectrum of vertical accelerations induced by rocking motion and horizontal accelerations in the containment building under unidirectional excitation of the Coalinga earthquake.

The substantial amplification of vertical accelerations observed in the presence of DSM layers may result from multiple physical mechanisms. In this study, the focus was primarily on evaluating the relative contribution of foundation rocking-induced soil–structure interaction (SSI) and the effect of DSM itself. Our results indicate that the effectiveness of block-type deep soil mixing in mitigating horizontal accelerations becomes significant only when there is a considerable dynamic impedance contrast between the DSM-improved soil and the surrounding natural soil. Yaghfoori et al. [14, 28] showed that the influence of this impedance contrast on horizontal and rocking-induced vertical accelerations was systematically investigated. This study included a parametric assessment of DSM stiffness, based on laboratory results from the ongoing nuclear power plant project, considering variations in the water-to-cement ratio of the DSM grout (ranging from 1.7 to 3). The findings demonstrated that achieving acceptable DSM performance in controlling horizontal accelerations requires a substantial stiffness difference between the improved zone and the surrounding soil. Furthermore, variations in the water-to-cement ratio within the tested range had minimal impact on vertical accelerations induced by foundation rocking. This indicates that rocking motion is the dominant mechanism driving vertical-acceleration amplification, whereas the impedance contrast primarily facilitates its occurrence. The reduction of horizontal accelerations recorded at the ground surface in the vicinity of zones improved by the block-type deep soil mixing (DSM) method can be primarily attributed to the substantial increase in stiffness and dynamic impedance of the treated soil relative to the surrounding natural ground. This impedance contrast leads to partial reflection, scattering, and redirection of seismic waves with dominant horizontal components at the boundaries of the DSM block, thereby limiting the effective transmission of horizontal ground motion to the surface in the near-field region of the improved zone. Moreover, the presence of a stiff, relatively massive DSM block alters the kinematic soil–structure interaction mechanism, thereby intensifying the coupling between translational and rocking motions of the foundation. As a result, a portion of the incoming horizontal seismic energy is redistributed from translational modes into rotational (rocking) modes, which may, in turn, increase vertical accelerations associated with rocking behavior. This redistribution of seismic energy plays a significant role in reducing the amplitude of horizontal ground surface accelerations in the vicinity of the DSM block. In addition, the DSM block may act as a frequency-dependent filter, particularly attenuating the higher-frequency components of the input ground motion. This filtering effect is directly related to increased stiffness and modified wave-propagation conditions within the improved soil mass. Furthermore, it reduces horizontal accelerations near the treated area. It should be emphasized that this reduction in horizontal acceleration is inherently spatial and distance-dependent. At locations farther from the DSM block, phenomena such as wave diffraction, refraction, and re-concentration of seismic energy may amplify horizontal accelerations. This observation indicates that the influence of block-type deep soil mixing on the seismic response of the ground surface and adjacent structures is strongly dependent on the geometry of the DSM block, the spacing between structures, the soil's dynamic properties, and the frequency content of the input earthquake motion. Consequently, a general conclusion cannot be drawn; case-specific, project-oriented evaluations are required. Accordingly, it can be concluded that block-type deep soil mixing should not be regarded merely as a soil improvement technique, but rather as a modification to the seismic wave propagation path, whose effects on horizontal ground surface accelerations are governed by dynamic impedance contrast, wave scattering mechanisms, and rocking-induced soil–structure interaction phenomena.

7.2. The effect of a bidirectional loading

Near-fault earthquakes, characterized by distinct dynamic features such as velocity pulses and high-frequency content, can significantly affect the seismic response of structures [12, 31]. A notable characteristic of these motions is the strong high-frequency vertical component, which may in some cases exceed the horizontal component. This phenomenon is particularly critical for nuclear reactor buildings, where internal equipment typically has high natural frequencies and is highly sensitive to vertical accelerations. Mechanical and electrical systems, as well as piping networks, are therefore highly vulnerable to damage or malfunction caused by vertical vibration. The presence of a strong vertical component can also increase axial forces in columns, reduce connection capacities, and promote brittle failure mechanisms. Consequently, the seismic design of nuclear facilities in high-hazard, near-fault regions requires careful consideration of vertical excitation effects, detailed frequency-domain analyses, and realistic soil–structure interaction modeling. In this study, the seismic behavior of the APR1400 reactor structure (Fig. 1) is evaluated under bidirectional near-fault ground motions, including the Northridge earthquake recorded at the Pardee station and the Coalinga earthquake (Table 6). As previously noted, the horizontal component is scaled to 0.4g and the vertical component to two-thirds of that value (0.27g). In the analytical models developed in this section, the reactor structure is modeled on a 3-m-thick foundation slab underlain by an 18-m-thick block deep-mixing (BDM) improvement layer. Fig. 15 presents the Fourier amplitude spectra of horizontal and vertical accelerations in both the containment building and internal structure under unidirectional and bidirectional loading. The results show that bidirectional loading has little influence on horizontal acceleration but substantially amplifies vertical acceleration. For the Northridge record, vertical components above 1 Hz show average amplification factors of 17 (containment building) and 46 (internal structure). For the Coalinga record, vertical components between 0.1 and 10 Hz increase by factors of 6 and 25, respectively. Given that many nuclear plant components have natural frequencies within this range, evaluating seismic response under two- and three-directional excitations is essential, particularly in near-fault regions.

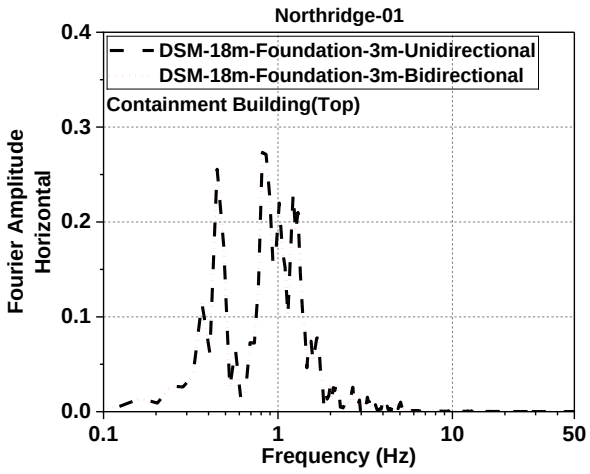

(a)

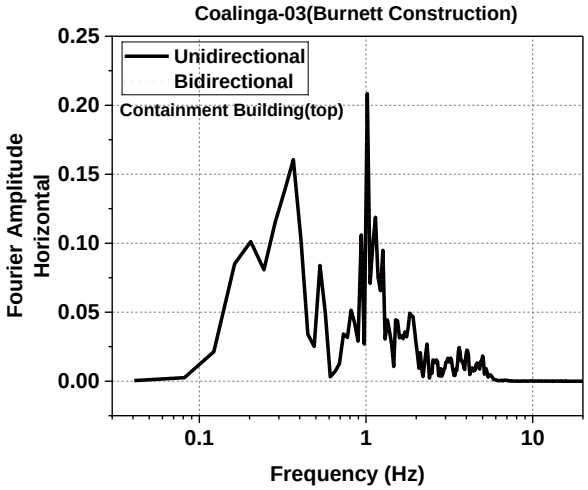

(e)

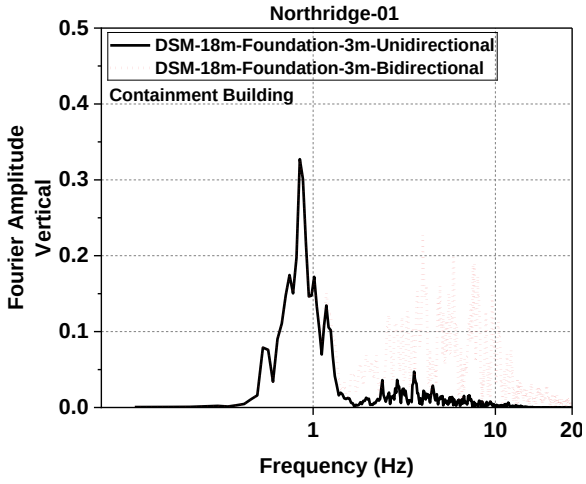

(b)

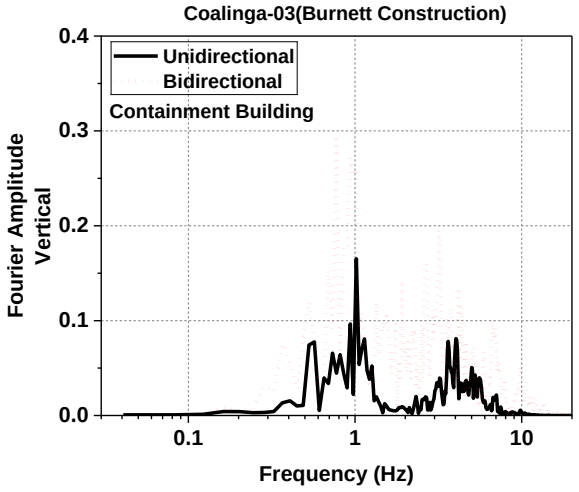

(f)

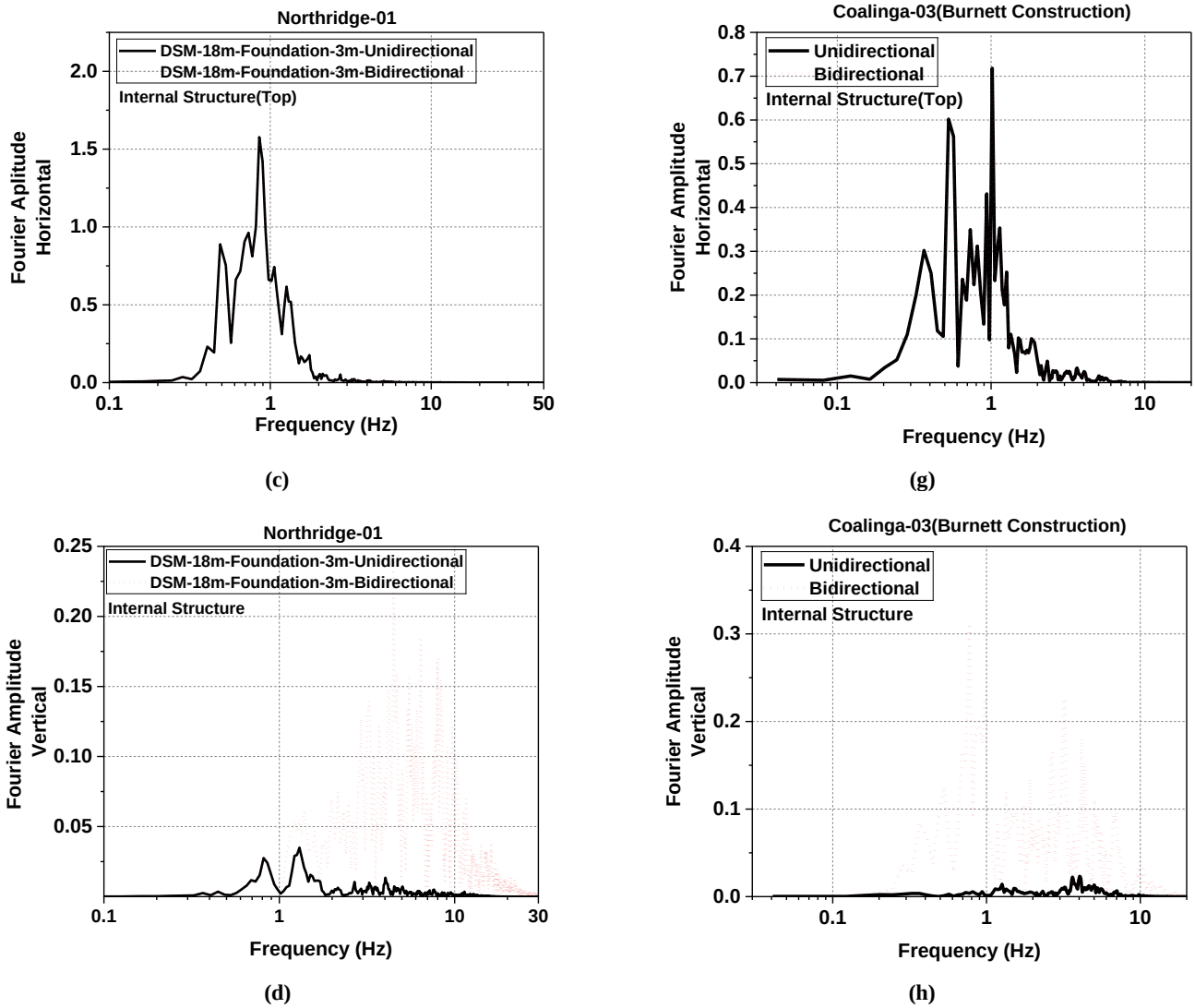

Fig. 15. Fourier amplitude spectra of horizontal and vertical accelerations for the containment building and the internal structure under unidirectional and bidirectional seismic excitations.

Fig. 16 presents the Fourier amplitude spectra of horizontal and vertical accelerations in the containment building and the internal structure under bidirectional excitation of the high-frequency Coalinga earthquake. As shown in Fig. 16a, the difference in horizontal acceleration at the upper levels of the two structures is significant. For frequencies below 0.3 Hz, the horizontal acceleration amplitude in the containment building is, on average, 45% higher than that of the internal structure. However, within the frequency range of 0.3–4 Hz, the average horizontal acceleration amplitude of the containment building is 196% lower than that of the internal structure. For frequencies above 4 Hz, the acceleration amplitudes in both structures are nearly equal. These variations in horizontal acceleration response may affect the performance of connections between the internal structure and the containment building and should therefore be considered in the design. The Fourier amplitude spectra of vertical acceleration in Fig. 16b show that the differences in vertical acceleration between the two structures are smaller than those in the horizontal component. In specific frequency ranges, the internal structure exhibits higher vertical acceleration amplitudes, whereas in other ranges the containment building exhibits larger vertical acceleration amplitudes.

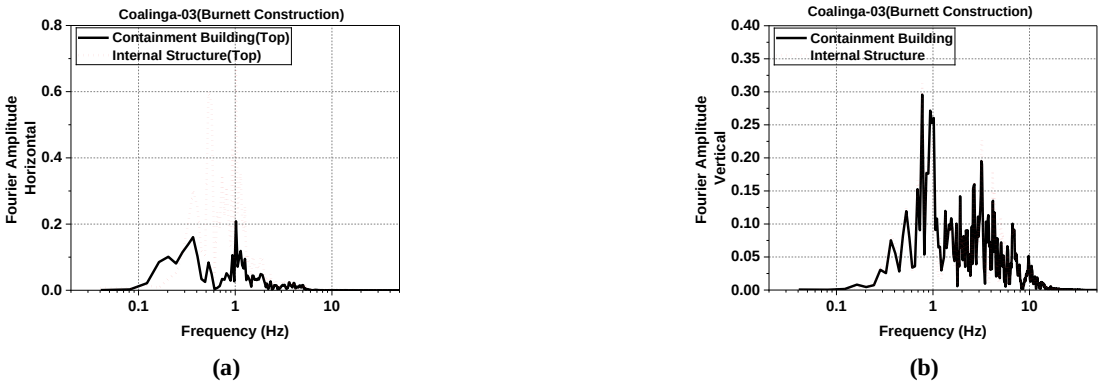

Fig. 16. Fourier amplitude spectra of horizontal and vertical accelerations in the containment building and the internal structure under bidirectional excitation of the Coalinga earthquake.

Fig. 17 presents the Morlet wavelet power spectrum of horizontal and vertical accelerations in the containment building under unidirectional and bidirectional excitation of the Coalinga earthquake. As observed, bidirectional loading does not significantly affect the energy of horizontal acceleration transmitted to the containment building. Still, it increases the energy of vertical acceleration and concentrates it at higher frequencies. This high-frequency energy concentration likely results from the combined effects of multiple-directional motion and the complex interaction between the structure and the DSM improvement layer. The amplification of vertical acceleration, particularly at higher frequencies, may significantly influence the seismic performance of the structure and sensitive equipment within the containment building, and should be carefully considered in seismic design and safety assessments.

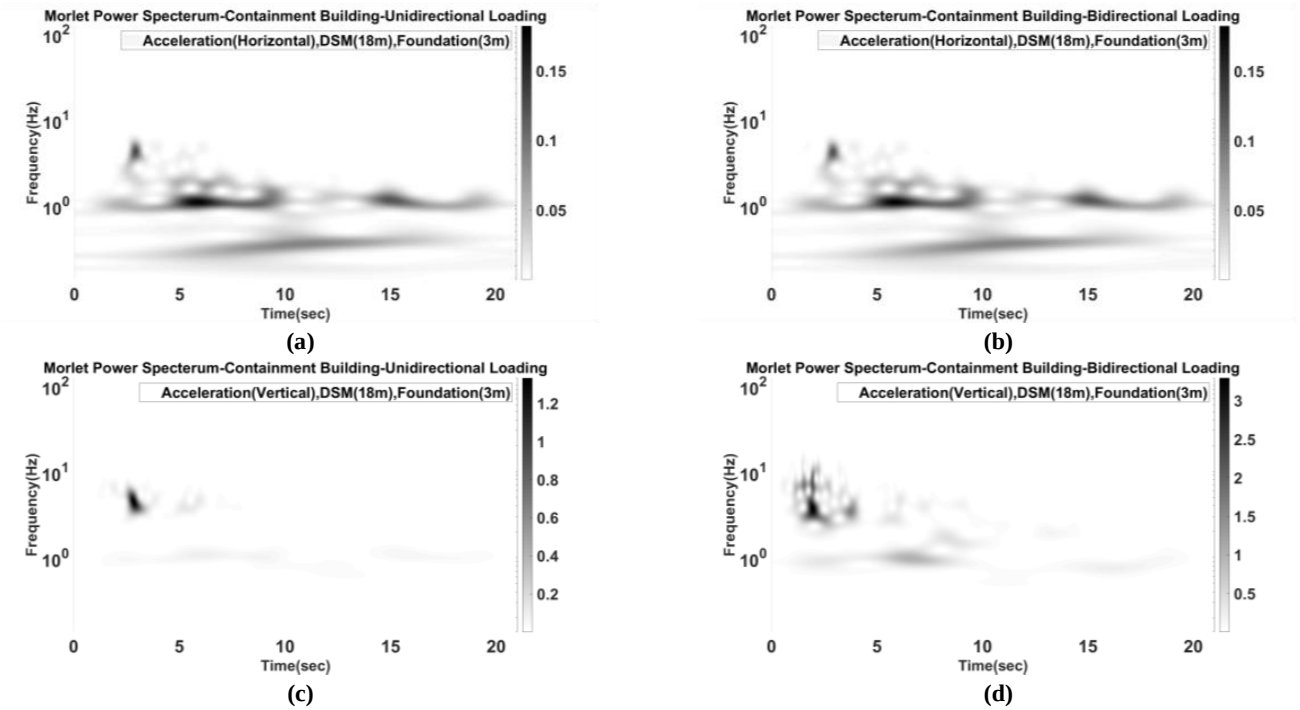

Fig. 17. Morlet wavelet power spectrum of horizontal and vertical accelerations in the containment building under unidirectional and bidirectional excitation of the Coalinga earthquake.

Clause C2.5.3 of ASCE 4-16 (Seismic Analysis of Safety-Related Nuclear Structures) states that the vertical-to-horizontal acceleration ratio (V/H) depends on earthquake frequency, source-to-site distance, local soil conditions, and, to a lesser extent, earthquake magnitude and faulting style. This ratio is typically determined through a site-specific probabilistic seismic hazard analysis (PSHA). If PSHA does not provide a V/H value, the analyst should select an appropriate and well-justified value. For near-fault sites (within 15 km), Holocene soils, or locations with thick soil layers, the V/H ratio should be explicitly calculated. For all other conditions, a conservative value of 2/3 is recommended for all frequencies. Studies by Bozorgnia and Campbell [32] have shown that the natural period, local soil conditions, and source-to-site distance strongly influence the V/H ratio. At the same time, its dependence on earthquake magnitude, faulting mechanism, and sediment depth is weaker. Near the fault, this ratio can reach 1.8 for short periods. However, for near-fault regions, code-specified values require a site-specific PSHA; for other conditions, a value of 2/3 is considered conservative and appropriate. Considering that the primary objective of this study was to assess the overall seismic behavior of the APR1400 reactor on DSM-improved soil, the simplified assumption of the minimum value recommended by ASCE 4-16, i.e., a vertical-to-horizontal acceleration ratio of 2/3, was adopted as the basis for the analyses. The results of Tyapin's [33] study indicate that the weight of the DSM-improved soil blocks and structure is only one of the factors influencing vertical accelerations under bidirectional loading, and its effect is negligible. Given the high-frequency content of the vertical component of ground motion, vertical accelerations are transmitted directly to the ground surface with minimal attenuation. In this study, by assuming elastic behavior for both soil and structure, this direct transmission of vertical accelerations has been confirmed. Therefore, even if the vertical-to-horizontal acceleration ratio exceeds 2/3, the overall pattern of vertical acceleration amplification and the dominant mechanism (foundation rocking and SSSI) remain unchanged, although the numerical values of vertical accelerations increase proportionally with the input ratio.

7.3. The effect of Structure -Soil-Structure interaction

In densely built-up areas, such as power plant islands where reactors, turbines, and other vital facilities are located in close proximity, vibrations from one structure can induce secondary motions in nearby buildings. This can lead to operational issues or even structural damage. This section evaluates the seismic response of the two adjacent structures of the APR1400 reactor, which were modeled simultaneously in the numerical analysis. To assess the effects of structure–soil–structure interaction (SSSI), as shown in Fig. 18, two APR1400 reactor buildings, spaced 30 m and 70 m apart, were modeled on a shared soil medium and subjected to horizontal ground shaking using the Northridge-01 near-fault earthquake record (see Table 6).

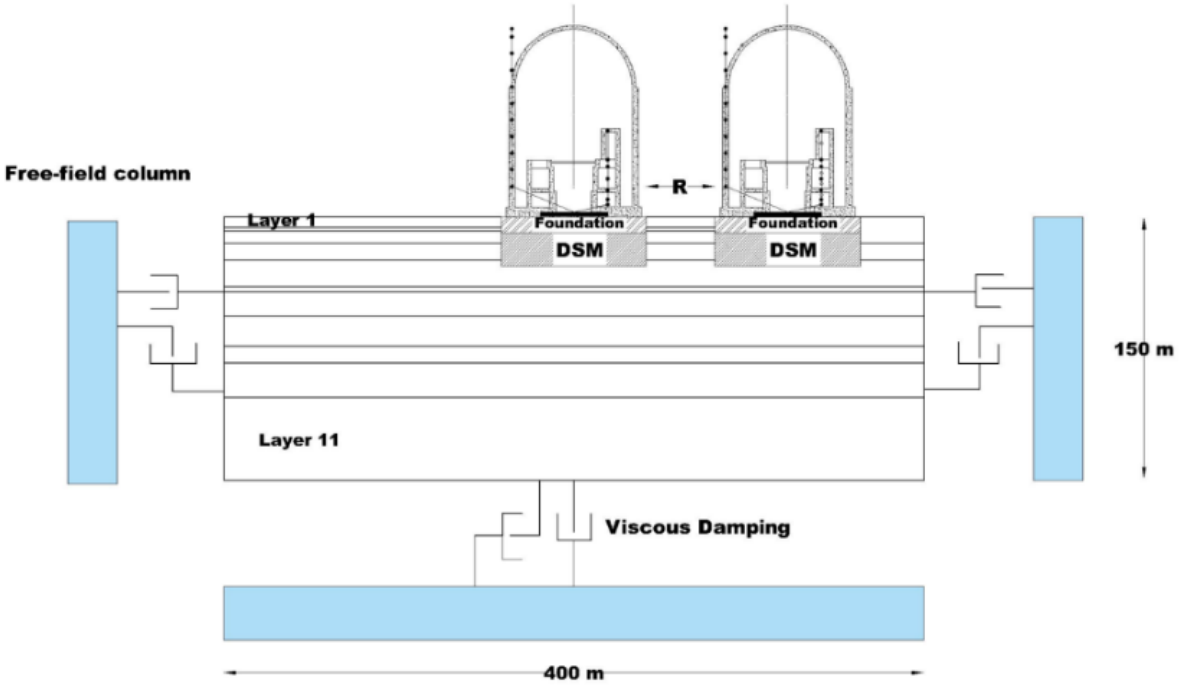

Fig. 18. SSSI models of the reactor pairs separated by distance R.

Fig. 19 illustrates the Fourier amplitude spectra of the horizontal acceleration at the upper levels of the internal structure and the containment building, as well as the vertical acceleration induced by rocking motion, under the unidirectional excitation of the Coalinga earthquake while accounting for structure–soil–structure interaction (SSSI). The results indicate that the influence of SSSI on the vertical acceleration component is considerably more pronounced than on the horizontal component in both structures. For the horizontal component, the presence of the adjacent structure results in only a slight reduction in acceleration amplitude, which is more pronounced for the second-reactor model at 30 m. For the containment building, SSSI reduces the vertical-acceleration amplitude at frequencies below 1.5 Hz, with average reductions of approximately 52% and 30% for the second-reactor model at separation distances of 30 m and 70 m, respectively. However, in the 1.5–10 Hz frequency range, SSSI increases vertical acceleration, with amplification of about 39% at 30 m and 5% at 70 m. In the internal structure, SSSI consistently amplifies the vertical acceleration across all frequencies. At frequencies below 1.5 Hz, the largest vertical acceleration occurs for the second-reactor model at 30 m, whereas in the 1.5–10 Hz range, the maximum amplitudes correspond to 70 m. This behavior suggests that the effect of SSSI is strongly dependent on both the separation distance between the structures and the frequency content of the input motion, resulting in distinct patterns of amplification or attenuation. Overall, the findings show that SSSI predominantly amplifies the vertical acceleration in the higher-frequency range. This is particularly critical for nuclear power plant facilities, as many safety-related components and equipment possess high natural frequencies and are highly sensitive to vertical excitation. Neglecting SSSI may therefore lead to an underestimation of vertical acceleration demands, potentially compromising the seismic safety of high-frequency systems. Consequently, accurate assessment of SSSI effects is essential in the seismic design of closely spaced structures within the nuclear power plant island.

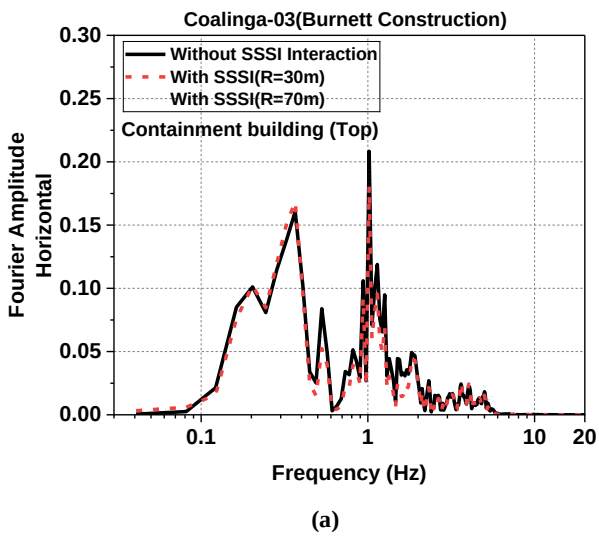

(a)

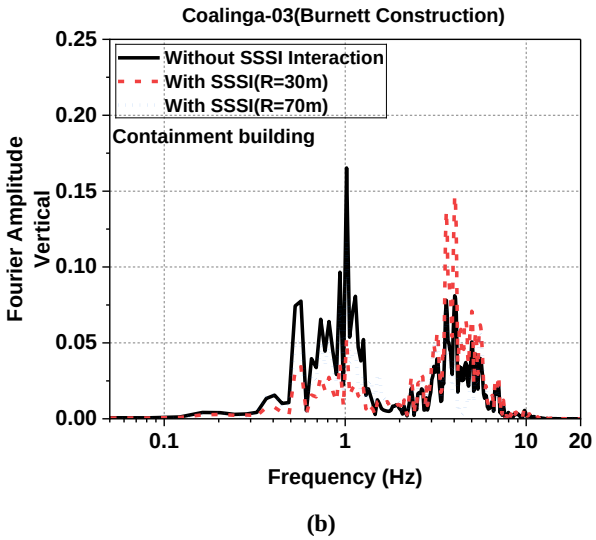

(b)

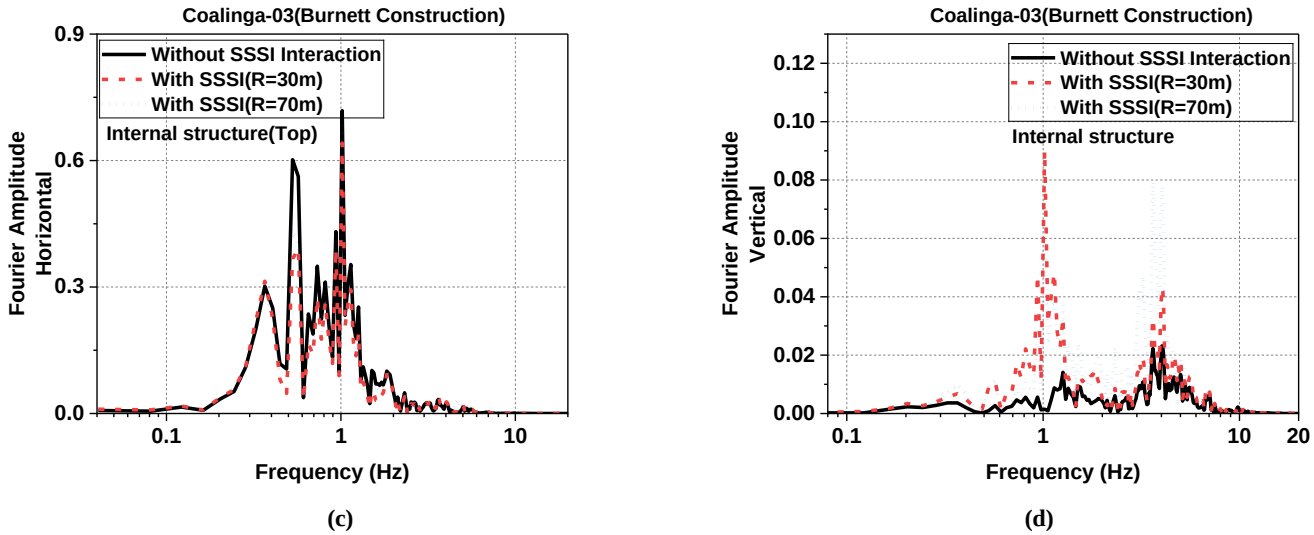

Fig. 19. Effect of structure–soil–structure interaction (SSSI) on horizontal and vertical acceleration Fourier amplitude spectra for the containment building (a–b) and the internal structure (c–d) under unidirectional excitation of the Coalinga-03 earthquake.

Figs. 20 and 21 illustrates the Morlet wavelet power spectra of the vertical acceleration induced by rocking motion and the horizontal acceleration at the top levels of the containment building and the internal structure, accounting for structure–soil–structure interaction (SSSI). The results indicate that SSSI does not significantly affect the time or frequency distribution of energy concentration. In the horizontal component, SSSI reduces the acceleration energy at the top of the containment building, with total energy reductions of approximately 19% and 15% for the secondary reactor modeled at 30 m and 70 m separation distances, respectively. Similarly, the horizontal-acceleration energy within the internal structure decreases by about 34% at 30 m and 26% at 70 m. Therefore, the effect of SSSI on reducing horizontal acceleration is more pronounced in the internal structure, particularly at the 30 m separation. In the vertical component, the impact of SSSI on the containment building varies across frequency ranges: for a 30 m separation, vertical acceleration energy increases by approximately 63%, whereas for a 70 m separation, vertical acceleration energy decreases by approximately 33%. Within the internal structure, vertical acceleration energy under SSSI increases by approximately 3.2 times at 30 m separation and 8 times at 70 m separation. Overall, the influence of SSSI on vertical acceleration due to rocking motion is significantly greater in the internal structure than in the containment building. The increase in vertical-acceleration energy indicates higher dynamic loading on the structure and sensitive equipment, which may lead to damage or degraded performance of structural components and systems. One of the complex and influential mechanisms affecting the seismic behavior of structures on a nuclear power plant island is the occurrence of in-phase or out-of-phase rocking. This phenomenon can significantly alter the vertical and horizontal accelerations of adjacent structures. The occurrence of in-phase or out-of-phase rocking depends on the mass and dynamic characteristics of the structures, the intensity and frequency content of the input earthquake motion, and the properties of the site soil layers [12, 34, 35]. In projects where the block-type deep soil mixing (DSM) method is employed, the simultaneous increase in mass and stiffness of the improved soil, and consequently the significant change in its dynamic impedance relative to the surrounding ground, can modify wave scattering patterns and the rocking behavior of foundations. As a result, the in-phase or out-of-phase rocking interaction between adjacent nuclear power plant structures becomes more complex. Yaghfoori et al. [14] investigated the effect of the rocking motion of the improved soil block on the surrounding ground. They demonstrated that the presence of DSM can markedly alter the distribution of vertical and horizontal accelerations. Specifically, horizontal accelerations decrease in the vicinity of the DSM block, whereas they increase farther from the improved zone. The extent of these regions and the magnitude of acceleration changes depend on the dimensions of the DSM block, the soil's dynamic properties, and the frequency content of the input ground motion. Accordingly, the spacing between adjacent structures and the relative position of each structure with respect to acceleration amplification or attenuation zones are additional key factors influencing the occurrence of in-phase or out-of-phase rocking motion in structure–soil–structure interaction (SSSI) systems. These dependencies make it difficult to draw general conclusions, underscoring the need for case-specific evaluations of SSSI effects based on each project's conditions. In the present study, the results indicate that, for both investigated spacings of 30 m and 70 m between the two nuclear power plant structures, the dominant rocking behavior is nearly out of phase. This rocking asynchrony results in only a limited reduction in horizontal accelerations in the inner structure and the containment building, while simultaneously increasing vertical accelerations in the inner structure across the entire investigated frequency range and increasing vertical accelerations in the containment building at frequencies above 2 Hz.

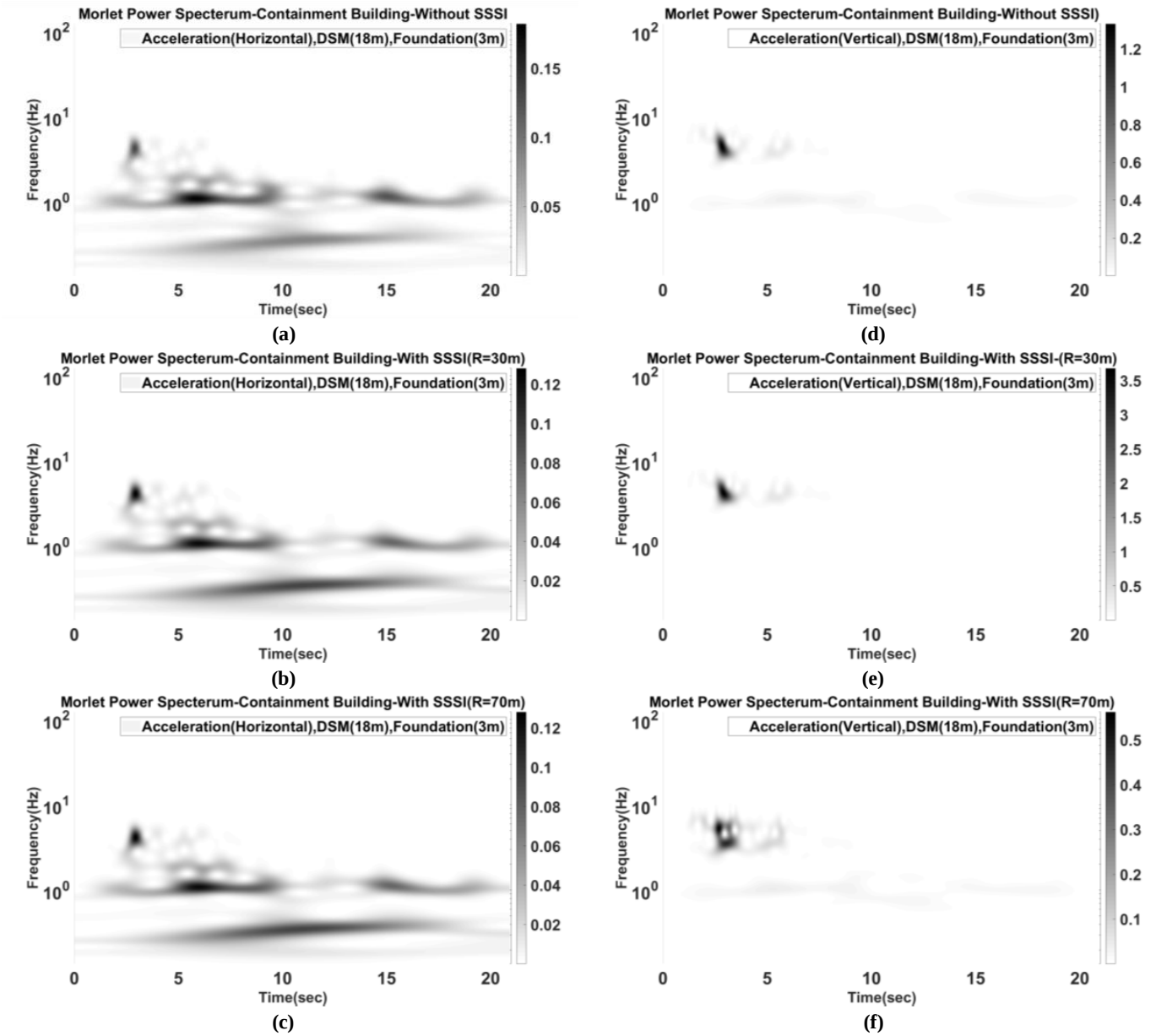

Fig. 20. Morlet wavelet power spectrum of horizontal acceleration at the top level of the structures and vertical acceleration induced by rocking motion in the containment building, considering structure–soil–structure interaction (SSSI).

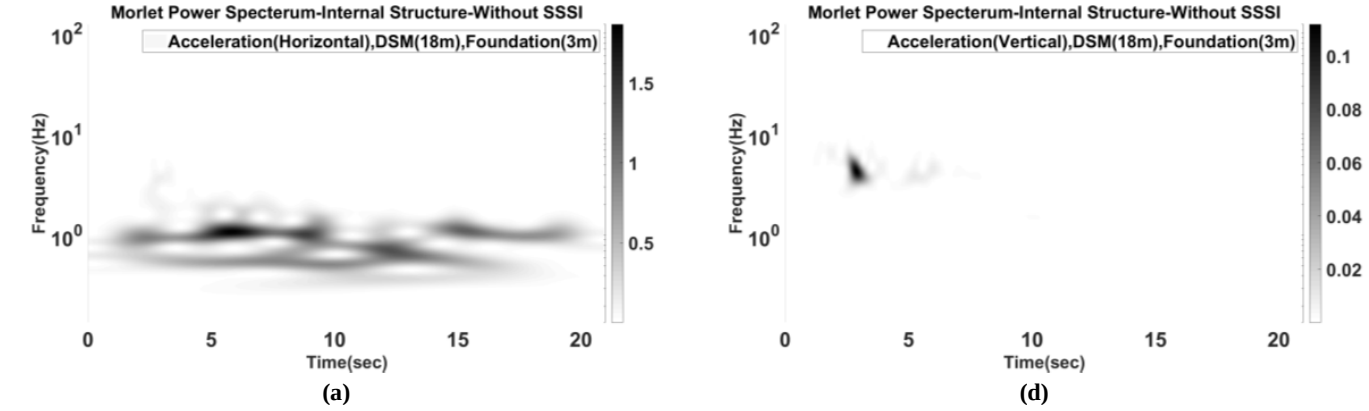

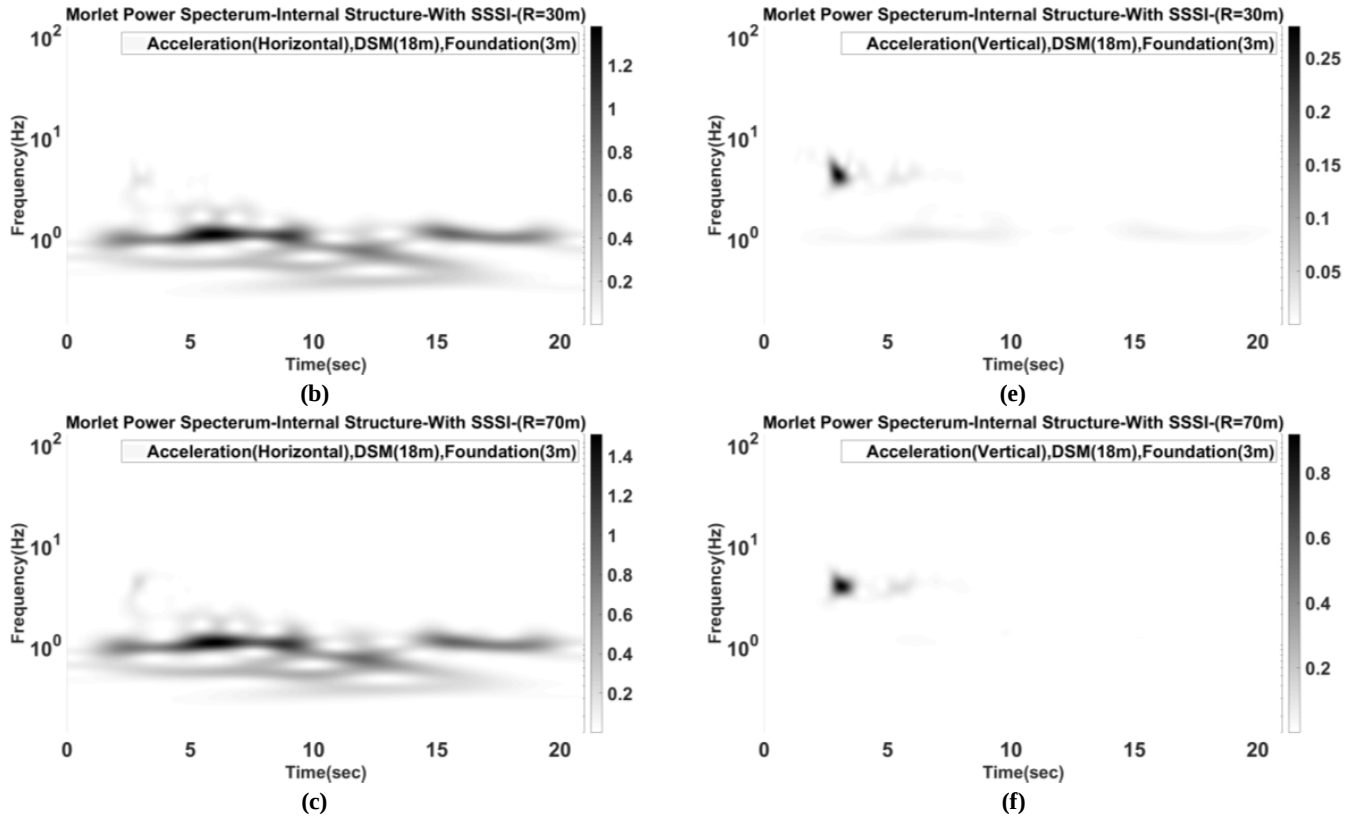

Fig. 21. Morlet wavelet power spectrum of horizontal acceleration at the top level of the structures and vertical acceleration induced by rocking motion in the Internal Structure, considering structure–soil–structure interaction (SSSI).

The results indicate that vertical accelerations can be significantly amplified by rocking motion under unidirectional and bidirectional loading, as well as under structure–soil–structure interaction (SSSI). This has direct implications for the Safe Shutdown Earthquake (SSE) assessment of nuclear power plants. From a regulatory and engineering perspective, the increased demand for vertical acceleration can directly affect the seismic qualification of safety-related and shutdown equipment, which is typically designed and evaluated based on vertical SSE response spectra with predefined safety margins. Amplified vertical accelerations can lead to higher axial forces, increased demands on support and anchorage systems, and local uplift at foundations and equipment bases, potentially challenging the assumed safety margins in equipment qualification. The findings of this study indicate that neglecting rocking motion, bidirectional excitation, and SSSI effects may result in a non-conservative underestimation of vertical SSE demand at both the structural and equipment levels. Consequently, the vertical acceleration transmitted to safety-critical components, including shutdown systems, may exceed design assumptions. Accordingly, this study underscores the need to explicitly account for vertical-acceleration amplification, foundation rocking, and soil–structure interaction in SSE-based seismic safety assessments, particularly for nuclear facilities on block-type DSM-improved sites. Underscores the need to explicitly account for vertical-acceleration amplification, foundation rocking, and soil–structure interaction effects in SSE-based seismic safety assessments, particularly for nuclear facilities constructed on block-type DSM-improved sites.

8. Limitations of the current study

The present study is subject to several modeling limitations that must be considered when interpreting the results. Due to computational constraints, the numerical analyses were performed within a two-dimensional framework; therefore, additional dynamic mechanisms, such as the torsional motion of the DSM block, which can be captured in three-dimensional models, were not considered. A lumped-mass model was used for the structural components, as permitted by ASCE 4-16 [17]. Nguyen et al. [36] also demonstrated that using a lumped-mass model provides reasonably good agreement with other reactor structural modeling approaches. Studies and technical guidelines indicate that the effects of soil–structure interaction (SSI) can differ significantly between linear and nonlinear conditions, particularly in large, stiff structures such as nuclear power plants, which exhibit multiple sources of geometric and material nonlinearity [16, 37-39]. Previous research has shown that nonlinear SSI generally reduces horizontal acceleration responses and the damping of high-frequency acceleration components due to soil plasticity [12, 15]. The primary objective of this study was to identify and interpret the dominant mechanisms of vertical acceleration amplification, particularly the roles of foundation rocking, soil–structure–structure interaction (SSSI), and block-type DSM ground improvement. For this purpose, linear elastic modeling was selected as a transparent and conservative analytical framework, allowing clear differentiation and interpretation of these mechanisms without entanglement with effects arising from material nonlinearity. Independent analyses conducted by the authors on Nevada sand, assuming elastoplastic soil behavior and block-type DSM improvement, indicate that vertical acceleration amplification due to rocking motion of the foundation is observed under both unidirectional and bidirectional loading across the predominant frequency range of the structures [28]. This suggests that the overall pattern of vertical-acceleration amplification and the governing mechanisms, particularly foundation rocking and SSI/SSSI effects, do not fundamentally change when soil nonlinearity is accounted for, although numerical response values may be adjusted.

Therefore, the reported increase in vertical accelerations within the 2–10 Hz frequency range is not solely due to the linear soil simplification but reflects the dynamic interaction of the soil–DSM–foundation–structure system. Nevertheless, for soft soils (Site Class D–F) or for conditions in which shear strains exceed approximately 0.5%, nonlinear analyses are necessary to obtain a more accurate evaluation of responses. The modeling of DSM blocks and the soil–foundation interface was also specifically addressed. DSM blocks were modeled using four-node quadrilateral elements under plane strain and with linear-elastic behavior, consistent with standard practice in the literature, in which DSM columns are typically modeled as a continuous domain with simplified material behavior [13]. The soil–structure interface is crucial for accurately modeling real-world soil–structure interaction (SSI) effects, since the foundation interacts directly with the surrounding soil at this boundary. Two main types of interfaces used in nuclear power plant analyses are tied/bonded and nonlinear/unbonded. The tied interface is the simplest, with no separation or gaps, ensuring the foundation and soil behave synchronously during dynamic events. Conversely, nonlinear interface models realistic seismic soil behavior, allowing sliding and small gaps between the foundation and the soil. This feature enables modeling of rocking motion in shallow foundations, which is essential for estimating seismic response in SSI [1]. Although nonlinear interfaces are generally believed to decrease structural seismic responses, this is not always the case. Incorrect interface specifications can lead to inaccurate seismic demand estimates, potentially compromising the safety of critical structures such as NPPs [12]. Previous research has shown that the interface's impact on structural acceleration and displacement varies with soil type and earthquake frequency. Van Nguyen et al. [15] showed that, apart from very stiff soils (S1), roof acceleration remains largely unaffected whether a fully bonded or nonlinear interface is assumed. Therefore, in most cases, nonlinear interface behavior can be ignored. However, during low- to medium-frequency earthquakes across all soil types, a sliding interface can result in greater displacements than a fully bonded interface. Sextos et al. [40] reported that containment buildings on soft soil are more susceptible to uplift and to combined nonlinear phenomena, such as sliding and rocking, particularly in response to seismic pulses in the 0.5–1.0 Hz frequency range. Saxena et al. [41, 42] further showed that sliding and gapping at the interface increase structural stresses, with the magnitude of these effects depending on the friction coefficient and the foundation embedment depth. Increasing the foundation depth can mitigate the effects of sliding and gapping. In a 3D reactor model of a 34.5 m-thick layered soil, Kanellopoulos et al. [12] demonstrated that gapping mechanisms can generate higher-frequency excitations that adversely affect internal structural components, such as the reactor containment. Therefore, the DSM–soil interface, a pivotal aspect of this study, may affect the structure's seismic response. This impact is contingent on project-specific conditions or finite-element modeling choices. However, a more robust implementation of the DSM can help alleviate these effects. Given the FE modeling conditions, substantial foundation embedment, and the DSM application, which previous studies indicate can mitigate sliding and gapping at the soil–foundation interface, along with OpenSees software limitations in the pre-processing stage, all interface nodes were tied in all directions in this study to facilitate comprehensive analyses. This study does not aim to provide a general analytical methodology covering all aspects of DSM-Soil interaction; instead, it emphasizes the importance of DSM-Soil interaction and examines the overall effect of block-type deep soil mixing, which is generally applicable.

9. Conclusion

This study assesses the impact of soil-structure interaction (SSI) and structure-soil-structure interaction (SSSI) on the APR1400 reactor structure, which is built on a foundation and ground enhanced through deep mixing, using laboratory results and ongoing field investigations from a power plant project. Numerical models were analyzed using three earthquake records with different frequency contents under unidirectional and bidirectional seismic excitations. The findings revealed that:

- The assessment of soil-structure interaction during unidirectional seismic events revealed that the internal structure experiences greater horizontal acceleration than the containment building. Notably, rocking in the containment causes significant vertical acceleration. The effectiveness of Deep Soil Mixing (DSM) and its interaction with both the structure and surrounding soil depend on the earthquake’s frequency content, soil dynamic properties, and DSM depth. This underscores the need for customized seismic evaluations of sensitive reactor equipment tailored to each project's specific features. Results indicate that DSM enhancements beneath the reactor foundation cause minimal changes in horizontal accelerations at high frequencies but greatly affect low-frequency responses. A key finding is the notable increase in vertical accelerations within the 2–10 Hz range, critical for many reactor components. The 18-m DSM layer increases vertical acceleration by more than 140% in the containment building and nearly 60% in the internal structure during near-fault earthquakes. These results underscore the importance of carefully evaluating DSM-improved foundations, given their substantial impact on high-frequency vertical motions.

- Analysis of the Morlet wavelet power spectra shows that the DSM layer reduces the horizontal-acceleration energy transmitted to the containment building but shifts and concentrates this energy into higher frequencies. In contrast, the 18-m BDM layer significantly amplifies vertical-acceleration energy, particularly within the 3–7 Hz frequency range, where many reactor components are most sensitive. This high-frequency concentration of vertical motion highlights the potential for increased seismic demand on nuclear structures and equipment, underscoring the need to account for DSM-induced effects in design and safety evaluations carefully.

- Near-fault ground motions notably increase vertical accelerations in both the containment building and internal structure of the APR1400 reactor, while having little impact on horizontal response. During bidirectional excitation, vertical acceleration can rise by 17–46 times for the Northridge earthquake and 6–25 times for the Coalinga earthquake, depending on the structure. These results emphasize the need to account for vertical and multidirectional excitations, as well as realistic soil–structure interaction, in the seismic design of near-fault nuclear facilities.

- The Morlet power spectrum results indicate that structure–soil–structure interaction (SSSI) does not alter the timing or

frequency bands of energy concentration but significantly affects the energy content of structural accelerations. In the horizontal component, SSSI reduces energy in both structures. For modeling the second reactor at 30 m, the reductions in the containment building and internal structure are approximately 19% and 34%, respectively, and at 70 m, 15% and 26%. In the vertical component, the influence of SSSI, particularly on the internal structure, is substantial; the vertical acceleration energy increases by about 3.2 times at 30 m and by about 8 times at 70 m. These findings highlight that SSSI can significantly amplify rocking-induced vertical demands, potentially affecting the performance and safety of structural components and sensitive equipment.

- The analysis results indicate that the vertical component of near-fault earthquakes, which typically contains high energy at high frequencies, can significantly impact the dynamic response of nuclear power plant structures. Notably, an increase in the Fourier amplitude of acceleration was observed in both the internal structure and the containment building at frequencies above 1 Hz. This becomes particularly critical, given that many mechanical and electrical equipment in such facilities exhibit high natural frequencies and are highly sensitive to excessive vertical accelerations, which may lead to functional disruption or damage. Moreover, the amplification of vertical acceleration at specific frequencies can increase axial forces in vertical members and reduce the safety margin of structural connections, thereby raising the risk of brittle failure. Relying solely on unidirectional analysis or ignoring the vertical component in seismic design can lead to inaccurate structural assessments and increased vulnerability under severe near-fault ground motions.

- The results of this study indicate that the seismic response of soil–foundation–structure systems improved with block-type DSM is highly site-specific and dependent on earthquake characteristics and structural properties; therefore, the numerical results cannot be directly generalized. Nevertheless, by focusing on the underlying physical mechanisms, the study demonstrates that factors such as the stiffness contrast between the DSM block and surrounding soil, foundation rocking, bidirectional seismic excitation, and structure–soil–structure interaction can lead to vertical acceleration amplification and redistribution of seismic energy. Although the magnitude of these effects varies by site, the mechanisms themselves are expected to be relevant to other facilities employing block-type DSM ground improvement. Accordingly, site-specific, SSI-based seismic assessments that explicitly account for DSM modeling, rocking behavior, and SSSI effects are essential for Safe Shutdown Earthquake evaluations.

Statements & Declarations

Author contributions

Ali Yaghfoori: Conceptualization, Methodology, Software, Validation, Formal analysis, Investigation, Writing original draft, Preparation, Visualization.

Iradj Mahmoudzadeh Kani: Conceptualization, Methodology, Writing—review and editing, Supervision, Project administration.

Hassan Yousefi: Conceptualization, Methodology, Writing—review and editing, Visualization, Supervision, Project administration.

Funding

The authors received no financial support for the research, authorship, and/or publication of this article.

Data availability

The data presented in this study will be available on interested request from the corresponding author.

Declarations

The authors declare no conflict of interest.

References

[1] Islam, M. R., Turja, S. D., Van Nguyen, D., Forcellini, D., Kim, D. Seismic soil-structure interaction in nuclear power plants: An extensive review. Results in Engineering, 2024; 23: 102694. doi:10.1016/j.rineng.2024.102694.

[2] Dezhkam, B., Yaghfoori, A. Soil foundation effect on the vibration response of concrete foundations using mathematical model. Computers and Concrete, 2018; 22: 221-225. doi:10.12989/cac.2018.22.2.221.

[3] Kitada, Y., Hirotani, T., Iguchi, M. Models test on dynamic structure–structure interaction of nuclear power plant buildings. Nuclear Engineering and Design, 1999; 192: 205-216. doi:10.1016/S0029-5493(99)00109-0.

[4] Yano, T., Kitada, Y., Iguchi, M., Hirotani, T., Yoshida, K. Model test on dynamic cross interaction of adjacent buildings in nuclear power plants. In: 12th world conference on earthquake engineering; 2000 30 Jan-4 Feb; Auckland, New Zealand. p. 1-8.

[5] Yano, T., Naito, Y., Iwamoto, K., Kitada, Y., Iguchi, M. Model Test on Dynamic Cross Interaction of Adjacent Building Nuclear Power Plants - Overall Evaluation on Field Test. In: Transactions of the 17th International Conference on Structural Mechanics in Reactor Technology (SMiRT 17); 2003 Aug 17–22; Prague, Czech Republic. p. 1-8.

[6] Clouteau, D., Broc, D., Devésa, G., Guyonvarh, V., Massin, P. Calculation methods of Structure–Soil–Structure Interaction (3SI) for embedded buildings: Application to NUPEC tests. Soil Dynamics and Earthquake Engineering, 2012; 32: 129-142. doi:10.1016/j.soildyn.2011.08.005.

[7] Roy, C., Bolourchi, S., Eggers, D. Significance of structure–soil–structure interaction for closely spaced structures. Nuclear Engineering and Design, 2015; 295: 680-687. doi:10.1016/j.nucengdes.2015.07.067.

[8] Lee, T. H., Wesley, D. A. Soil-structure interaction of nuclear reactor structures considering through-soil coupling between adjacent structures. Nuclear Engineering and Design, 1973; 24: 374-387. doi:10.1016/0029-5493(73)90007-1.

[9] Bolisetti, C., Whittaker, A. Seismic structure–soil–structure interaction in nuclear power plant structures. In: 21st International Conference on Structural Mechanics in Reactor Technology (SMiRT 21); 2011 Nov 6-11; New Delhi, India. p. 6-11.

[10] Yue, D., Ghiocel, D. M., Fuyama, H., Ogata, T., Stark, G. Structure-soil-structure interaction effects for two heavy NPP buildings with large-size embedded foundations. In: 22nd International Conference on Structural Mechanics in Reactor Technology (SMiRT22); 2013 Aug 18-23; San Francisco, California. p. 18-23.

[11] Anderson, L. M., Carey, S., Amin, J. Effect of Structure, Soil, and Ground Motion Parameters on Structure-Soil-Structure Interaction of Large Scale Nuclear Structures. Structures Congress, 2012; 2862-2873. doi:10.1061/41171(401)249.

[12] Kanellopoulos, C., Rangelow, P., Jeremic, B., Anastasopoulos, I., Stojadinovic, B. Dynamic structure-soil-structure interaction for nuclear power plants. Soil Dynamics and Earthquake Engineering, 2024; 181: 108631. doi:10.1016/j.soildyn.2024.108631.

[13] Shaghaghi, M. M., Kani, I. M., Yousefi, H. The Seismic Behavior of Block Type Deep Soil Mixing. Latin American Journal of Solids and Structures, 2021; 18: 1-17. doi:10.1590/1679-78256439.

[14] Yaghfoori, A., Mahmoudzadeh Kani, I., Yousefi, H. Seismic performance and optimization of deep soil mixing (DSM) for response mitigation at power plant sites. Engineering Computations, 2025; 1-42. doi:10.1108/EC-05-2025-0508.

[15] Van Nguyen, D., Kim, D., Duy Nguyen, D. Nonlinear seismic soil-structure interaction analysis of nuclear reactor building considering the effect of earthquake frequency content. Structures, 2020; 26: 901-914. doi:10.1016/j.istruc.2020.05.013.

[16] Bolisetti, C., Whittaker, A. S., Coleman, J. L. Linear and nonlinear soil-structure interaction analysis of buildings and safety-related nuclear structures. Soil Dynamics and Earthquake Engineering, 2018; 107: 218-233. doi:10.1016/j.soildyn.2018.01.026.

[17] (ASCE), A. S. o. C. E. Seismic analysis of safety-related nuclear structures. 1st ed. Reston (VA): American Society of Civil Engineers (ASCE); 2017. doi:10.1061/9780784413937.

[18] Jeremić, B., Jie, G., Preisig, M., Tafazzoli, N. Time domain simulation of soil–foundation–structure interaction in non-uniform soils. Earthquake Engineering & Structural Dynamics, 2009; 38: 699-718. doi:10.1002/eqe.896.

[19] Amalu, P. A., Jayalekshmi, B. R. Study on seismic response of unconnected piled raft with rubber mixed soil. Materials Today: Proceedings, 2023; doi:10.1016/j.matpr.2023.10.018.

[20] Çetindemir, O., Zülfikar, A. C. Numerical validation of fully coupled nonlinear seismic soil–pile–structure interaction. Buildings, 2024; 14: 1502. doi:10.3390/buildings14061502.

[21] Cruz, L., Todorovska, M. I., Chen, M., Trifunac, M. D., Aihemaiti, A., Lin, G., Cui, J. The role of the foundation flexibility on the seismic response of a modern tall building: Vertically incident plane waves. Soil Dynamics and Earthquake Engineering, 2024; 184: 108819. doi:10.1016/j.soildyn.2024.108819.

[22] Nielsen, A. H. Absorbing boundary conditions for seismic analysis in ABAQUS. In: ABAQUS users' conference; 2006 May 23-25; Cambridge, Massachusetts. p. 359-376.

[23] Rathje, E. M., Faraj, F., Russell, S., Bray, J. D. Empirical relationships for frequency content parameters of earthquake ground motions. Earthquake Spectra, 2004; 20: 119-144. doi:10.1193/1.1643356.

[24] Tso, W. K., Zhu, T. J., Heidebrecht, A. C. Engineering implication of ground motion A/V ratio. Soil Dynamics and Earthquake Engineering, 1992; 11: 133-144. doi:10.1016/0267-7261(92)90027-B.

[25] Patrício, J. D., Gusmão, A. D., Ferreira, S. R. M., Silva, F. A. N., Kafshgarkolaei, H. J., Azevedo, A. C., Delgado, J. M. P. Q. Settlement Analysis of Concrete-Walled Buildings Using Soil–Structure Interactions and Finite Element Modeling. Buildings, 2024; 14: 746. doi:10.3390/buildings14030746.

[26] Uzun, S., Ayvaz, Y. Implementation of PMDL and DRM in OpenSees for Soil-Structure Interaction Analysis. Applied Sciences, 2024; 14: 8519. doi:10.3390/app14188519.

[27] Towhata, I. Geotechnical earthquake engineering: Damage mechanism observed. 1st ed. Berlin (DE): Springer International Publishing;; 2015. doi:10.1007/978-3-642-35344-4_2.

[28] Yaghfoori, A., Mahmoudzadeh Kani, I., Yousefi, H. Seismic behavior of dry sandy soils improved with Block-Type Deep Soil Mixing in near-fault regions. AUT Journal of Civil Engineering, 2025; doi:10.22060/ajce.2025.24157.5923.

[29] Asgari, A., Ranjbar, F., Bagheri, M. Seismic resilience of pile groups to lateral spreading in liquefiable soils: 3D parallel finite element modeling. Structures, 2025; 74: 108578. doi:10.1016/j.istruc.2025.108578.

[30] Asgari, A., Sorkhi, S. F. A. Wind turbine performance under multi-hazard loads: Wave, wind, and earthquake effects on liquefiable soil. Results in Engineering, 2025; 26: 104647. doi:10.1016/j.rineng.2025.104647.

[31] Chopra, A. K., Chintanapakdee, C. Comparing response of SDF systems to near-fault and far-fault earthquake motions in the context of spectral regions. Earthquake Engineering & Structural Dynamics, 2001; 30: 1769-1789. doi:10.1002/eqe.92.

[32] Bozorgnia, Y., Campbell, K. W. The vertical-to-horizontal response spectral ratio and tentative procedures for developing simplified V/H and vertical design spectra. Journal of Earthquake Engineering, 2004; 8: 175-207. doi:10.1080/13632460409350486.

[33] Tyapin, A. Effect of soil improvement on seismic response. In: 24th International Conference on Structural Mechanics in Reactor Technology (SMiRT 24); 2017 Aug 20-25; Busan, Korea. p. 1-10.

[34] Lu, X., Jing, L., Ma, Y., Yang, J., Qi, W. Shaking table test for seismic response of nuclear power plant on non-rock site. Sustainability, 2023; 15: 10366. doi:10.3390/su151310366.

[35] Anagnostopoulos, S. A., Spiliopoulos, K. V. An investigation of earthquake induced pounding between adjacent buildings. Earthquake Engineering & Structural Dynamics, 1992; 21: 289-302. doi:10.1002/eqe.4290210402.

[36] Nguyen, D.-D., Thusa, B., Park, H., Azad, M. S., Lee, T.-H. Efficiency of various structural modeling schemes on evaluating seismic performance and fragility of APR1400 containment building. Nuclear Engineering and Technology, 2021; 53: 2696-2707. doi:10.1016/j.net.2021.02.006.

[37] Lee, J. H. Practical Numerical Approach for Nonlinear Soil-Structure Interaction Analysis of a NPP Containment Building. In: Transactions of the Korean Nuclear Society Spring Meeting; 2018 May 17-18; Jeju, Korea. p. 1-2.

[38] Kabanda, J., Kwon, O.-S., Kwon, G. Time and frequency domain analyses of the Hualien Large-Scale Seismic Test. Nuclear Engineering and Design, 2015; 295: 261-275. doi:10.1016/j.nucengdes.2015.10.011.

[39] Asgari, A. Effect of Deep Soil Mixing Grid on the Reduction Coefficient in the Liquefiable Soil: 3D Nonlinear Modeling. Journal of Civil and Environmental Engineering, 2025; 55: 89-98. doi:10.22034/ceej.2025.63522.2381.

[40] Sextos, A. G., Manolis, G. D., Athanasiou, A., Ioannidis, N. Seismically induced uplift effects on nuclear power plants. Part 1: Containment building rocking spectra. Nuclear Engineering and Design, 2017; 318: 276-287. doi:10.1016/j.nucengdes.2016.12.035.

[41] Saxena, N., Paul, D., Kumar, R. Effects of slip and separation on seismic SSI response of nuclear reactor building. Nuclear Engineering and Design, 2011; 241: 12-17. doi:10.1016/j.nucengdes.2010.10.011.

[42] Saxena, N., Paul, D. K. Effects of embedment including slip and separation on seismic SSI response of a nuclear reactor building. Nuclear Engineering and Design, 2012; 247: 23-33. doi:10.1016/j.nucengdes.2012.02.010.

Civil Engineering and Applied Solutions

Research Article

journal homepage: ceas.journals.umz.ac.ir

CEAS Civil Engineering and Applied Solutions

Parametric Study of Settlement in Shallow Foundations of Adjacent Buildings on Sandy Soil: A Finite Element Parametric Study

Vali Ghaseminejad [a], Seyed Mojtaba Moosavi [b*], Taher Zargar Herijani [a]

[a] *Department of Civil Engineering, Noswhahr Branch, Islamic Azad University, Nowshahr, Iran*

[b] *Geotechnical Engineering Research Center, International Institute of Earthquake Engineering and Seismology (IIEES), Tehran, Iran*

ARTICLE INFO

Keywords:
Settlement
Adjacent buildings
Sandy soils
Finite element analysis
Soil–structure interaction
PLAXIS

Article history:
Received 04 November 2025
Accepted 06 February 2026
Available online 01 July 2026

ABSTRACT

Urban densification and limited availability of suitable land often necessitate the construction of high-rise buildings in close proximity. Such developments can lead to seismic-induced settlements not only beneath the new structures but also in neighboring existing buildings. This study employs a finite element approach using PLAXIS to evaluate the settlement interaction of adjacent shallow foundations on sandy soils under seismic loading. A parametric investigation was conducted to assess the effects of building height (number of stories), foundation width, and spacing between adjacent buildings. Results indicate that the spacing between buildings is the most influential parameter in controlling induced settlement in existing structures, followed by the number of stories of the newly constructed building. In contrast, foundation width showed only a marginal impact on induced settlement. The findings emphasize the importance of soil–structure interaction in urban environments and provide practical insights for mitigating seismic risks and ensuring the safety of adjacent structures.

1. Introduction

In most cases, the loads transferred through shallow foundations vary significantly, leading to differential settlements that can cause considerable damage to the superstructure. Settlement of foundations under surcharge-induced stresses has long been a major concern in geotechnical engineering. When the magnitude of total or, more critically, differential settlement exceeds the allowable limits prescribed by design codes, structural and nonstructural damages may occur, including cracks in walls, distortion of doors and windows, and failures in utility systems such as water and sewage pipelines. The problem becomes more pronounced when two buildings are constructed adjacent to each other on similar subsoil conditions. In such cases, additional stress concentrations may develop beneath the existing foundation, resulting in increased total and differential settlements that can compromise structural integrity. From a geotechnical perspective, the construction of a new building beside an existing one introduces two primary risks: (a) soil failure or lateral movement adjacent to the existing foundation due to excavation for the new footing, which may cause wall collapse or lateral displacement of the excavation face; and (b) non-uniform settlement of the existing foundation arising from the stress increase imposed by the new structure. In the latter case, the side of the existing building closest to the new construction experiences larger vertical stress increments, leading to higher settlement and potential tilting of the entire structure.

In many urban areas, regulatory authorities have established comprehensive guidelines to control excavation activities and to mitigate potential damage to existing buildings located adjacent to construction sites. However, no specific regulations are typically enforced regarding the control of differential settlements in existing structures caused by stress increments from newly constructed buildings. As a result, numerous old buildings have experienced non-uniform settlements due to adjacent construction, leading to cracks in walls, distortions in ceilings, and in severe cases, structural deterioration.

* Corresponding author.
E-mail addresses: Iran.moosavi@iiees.ac.ir (S.M. Mosavi).

https://doi.org/10.22080/ceas.2026.30450.1053
ISSN: 3092-7749/
How to cite this article: Ghaseminejad, V., Moosavi, S.M., Zargar Herijani, T. Parametric Study of Settlement in Shallow Foundations of Adjacent Buildings on Sandy Soil: A Finite Element Parametric Study. Civil Engineering and Applied Solutions. 2026; 2(3): 73-84. doi:10.22080/ceas.2026.30450.1053.

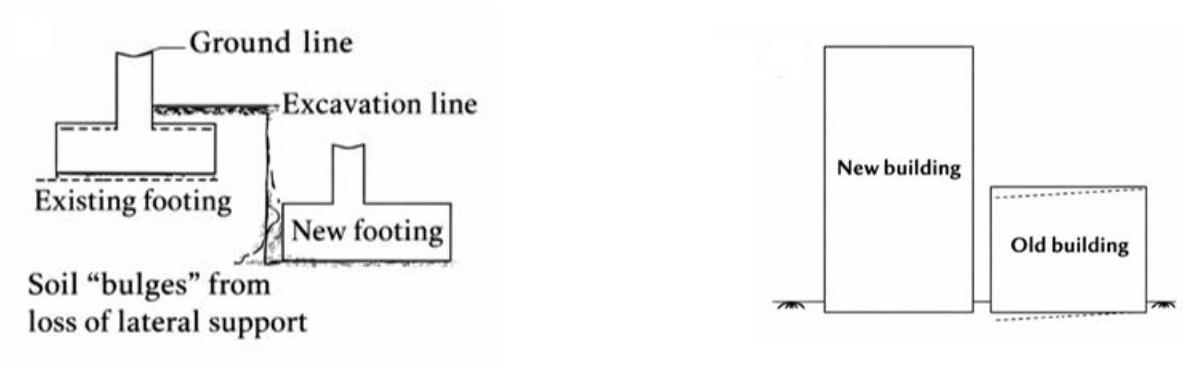

(a) **(b)**

Fig. 1. Effect of new foundation construction on the performance of an existing footing: (a) soil failure and lateral displacement due to excavation; (b) non-uniform settlement of the existing foundation induced by adjacent building construction.

Fig. 2 illustrates an example of structural damage in an old building caused by differential settlement induced by adjacent foundation loading.

Fig. 2. Example of wall cracking and structural damage in an existing building caused by differential settlement due to adjacent construction.

The interaction between adjacent foundations has been the subject of extensive research. Das and Larbi-Cherif [1] showed through physical model tests on sand that settlements increase significantly when center-to-center spacing is less than 4.5 times the foundation width. Similarly, Amer and Romi [2] demonstrated that for clay soils, settlement and tilting of flexible strip footings increase as spacing decreases, with tilting directed toward the system center and influenced by both applied load and spacing.

Numerical studies by Jao et al. [3] for reinforced concrete strip footings on cohesive soil provided equations linking settlement interference to relative spacing. Physical modeling studies by Kumar and Saran [4] highlighted the mitigating effect of geogrid reinforcement on tilting, while Kumar and Bhoi [5] reported that settlement at ultimate load increases with decreasing spacing and higher soil friction angles. Ghosh and Sharma [6] further demonstrated that settlement of interacting footings on layered soils can be reduced by improving the weaker layer. Kusakabe et al. [7] demonstrated that the growing availability of spatial data and advances in computational science have enabled large-scale three-dimensional analyses of soil–structure interaction for evaluating soil liquefaction. However, the highly nonlinear and multi-physical nature of such models leads to significant computational challenges. In this regard, they proposed an efficient finite element approach that integrates several high-performance computing techniques to conduct large-scale 3D liquefaction simulations, demonstrating its effectiveness in analyzing grid-form ground improvement systems.

Hwang et al. [8] investigated the effects of seismic structure–soil–structure interaction (SSSI) between adjacent shallow-founded buildings on liquefiable soils through dynamic centrifuge tests and 3D numerical simulations. Their results highlighted that foundation spacing, relative building height and mass, and the geometry of the neighboring structures significantly influence system performance. SSSI was found to slightly reduce settlement but increase tilt, especially when the spacing between buildings was smaller than their width. The study emphasized that SSSI can notably affect key seismic demand parameters even at relatively large separations, underscoring the need to consider these interactions in the seismic design and liquefaction assessment of urban structures.

Tian et al. [9] examined the city-scale effects of tall buildings on the seismic responses of nearby shorter structures in the Shanghai Central Business District using nonlinear time-history analyses. Their results showed that due to the large mass and long fundamental periods of tall buildings, seismic perturbations can influence a wide surrounding area, altering ground motion energy and increasing the seismic demands and potential damage of adjacent shorter buildings. The study emphasized the necessity of accounting for these large-scale interactions when assessing the seismic safety of densely built urban areas.

Hwang et al. [10] investigated the effectiveness of stiff in-ground structural walls as a countermeasure against liquefaction-induced deformations using 3D fully coupled nonlinear finite-element analyses validated by centrifuge tests. The study revealed that while structural walls can reduce foundation settlement in many cases, they may also increase residual tilt or amplify settlement under certain soil conditions, such as thick dense crust or uniform dense sand layers. The wall penetration depth and flexural stiffness were key factors influencing mitigation performance, with the crust thickness being the most critical parameter overall. The results emphasized that the design of such walls must carefully consider the coupled soil–foundation–structure interaction and site-specific ground motion characteristics.

Kassas et al. [11] examined the effects of structure–soil–structure interaction (SSSI) on adjacent shallow-founded buildings over liquefiable sand using fully coupled hydromechanical analyses with the PM4Sand model. Their results, validated against centrifuge experiments, showed that while SSSI can reduce settlement, it significantly increases foundation rotation, especially when the spacing between buildings is small. The severity of this effect depends on the liquefiable layer depth and the gap between structures. The study highlighted that SSSI can have both beneficial and detrimental impacts on seismic performance, underscoring the need to consider these interactions in the seismic design of closely spaced buildings on liquefiable soils.

Barrios et al. [12] conducted geotechnical centrifuge experiments at JNIOSH in Tokyo to investigate the seismic behavior of stand-alone and closely spaced shallow foundations on saturated sand. Using harmonic excitations in a laminar box, the study compared foundation–soil responses with free-field conditions. Results showed that adjacent footings exhibited inward tilting and reduced soil dilation beneath the foundations compared to isolated ones. Settlement was primarily caused by footing penetration into the supporting sand, and acceleration attenuation in the near-surface soil was smaller in the presence of foundations. The findings highlighted the significant influence of foundation proximity on the dynamic soil–foundation–structure interaction.

Hwang et al. [13] investigated the effects of ground densification on the seismic performance of isolated and adjacent buildings on liquefiable soils using 3D fully coupled nonlinear finite-element analyses validated by centrifuge tests. The study showed that while ground densification effectively reduces settlement when extending through the full depth of the critical layer, it may also increase foundation tilt and structural deformation, especially in asymmetric or closely spaced configurations. The influence of densification on structure–soil–structure interaction (SSSI) was found to depend strongly on treatment geometry, building spacing, and structural properties. These findings highlight the need for careful design of densification geometry and placement in urban environments with neighboring buildings.

Bagheri et al. [14] evaluated the seismic performance of two adjacent 30-story high-rise buildings, one with a conventional moment-resisting frame (MF) and the other with a dual system incorporating shear walls (MFSW), considering soil–structure interaction (SSI) using a hybrid piled raft foundation. Nonlinear dynamic analyses under multiple ground motions showed that the MFSW system significantly reduced fundamental periods, interstory drifts, and soil shear strains, enhancing overall resilience. The study also highlighted critical effects of seismic-induced soil–pile–structure interaction (SSPSI) on displacement amplification and emphasized that optimized hybrid pile configurations improve foundation performance. These findings underscore the importance of integrating superstructure design and foundation–soil interaction in the seismic assessment of high-rise buildings.

Accordingly, the present study aims to address these gaps by integrating numerical modeling [14-23] and experimental investigations [24, 25], as presented herein.

Despite these insights, a systematic investigation of factors affecting settlement due to the construction of a new structure adjacent to an existing one remains limited. The present study addresses this gap using PLAXIS, a finite element-based software, to examine the influence of the number of stories, spacing between foundations, and foundation width on settlement behavior.

2. Validation

As noted in previous sections, PLAXIS (version 8.5), a two-dimensional finite element software capable of simulating and solving geotechnical problems, was employed in this study to evaluate the effects of adjacent buildings on the settlement of existing structures. Since numerical results are highly dependent on the quality of input parameters, the outputs generated by such software may deviate significantly from reality. Therefore, prior to application, the software must be validated or calibrated to ensure the reliability of its predictions. Various calibration methods are reported in the literature, with the most reliable approach being the use of field-measured data from instrumented geotechnical projects.

In this study, geotechnical monitoring data from the Esfandiar Tunnel in northern Tehran were used for validation. This tunnel, excavated within soil deposits, provides comprehensive instrumentation data, including surface settlement measurements recorded during construction, which were utilized in this research. The ultimate goal of software validation is to confirm both the proper functioning of the numerical model and the accuracy of its outputs. In cases where the discrepancy between the validation model and the actual measurements is less than 15%, the software is considered reliable. The section of the tunnel under study is approximately 520 m long, featuring two traffic lanes and a maximum height of 6.5 m. The geological and geotechnical profile of the tunnel alignment, shown in Fig. 3, includes a range of soil types from coarse sandy alluvium to finer clay layers. Accurate modeling of any civil engineering project requires precise knowledge of the geotechnical properties of the constituent soils. Extensive investigations, including exploratory boreholes, laboratory tests, and in-situ tests, were conducted for the Esfandiar Tunnel to characterize the soil layers. Table 1 summarizes the basic properties and main geotechnical parameters of the different soil strata, which were used as input data for software validation.

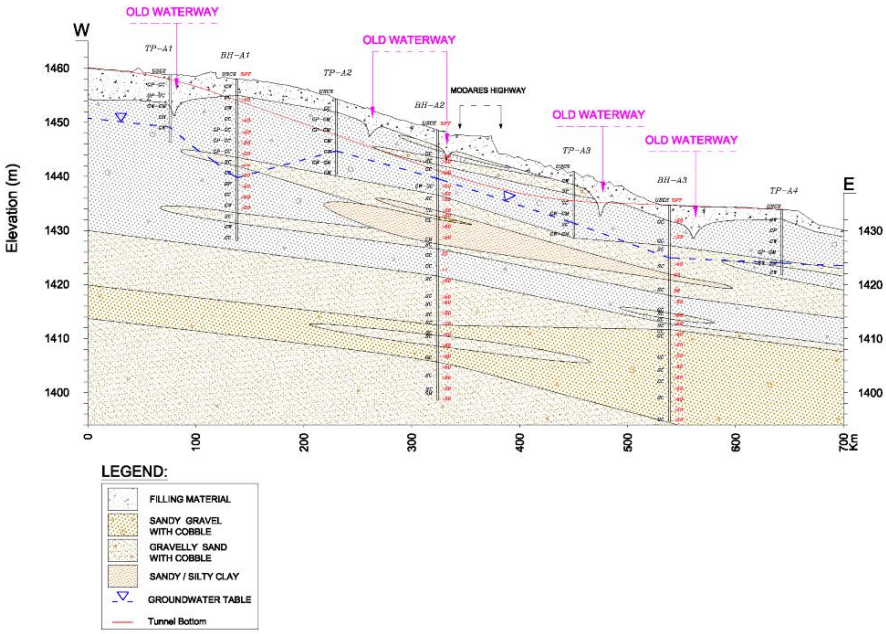

Fig. 3. Geological and geotechnical profile of the studied tunnel section.

Table 1. Summary of the main geotechnical soil parameters for the studied section.

Geotechnical parameters of the sand layer (GC, GM)	
Internal friction angle	$\varphi = 34 \sim 38$
Cohesion	$X = 0.15 \sim 0.3$ kg/cm^2
Wet density	$\gamma = 1.90$ g/cm^3
Poisson's ratio	$\nu = 0.30$
Deformation modules	$E = 600 \sim 900$ kg/cm^2
Permeability	$K = 5E-5 \sim 5E-4$ cm/s
Geotechnical parameters of the sand layer (SC, SM)	
Internal friction angle	$\varphi = 32 \sim 34$
Cohesion	$C = 0.2 \sim 0.4$ kg/cm^2
Wet density	$\gamma = 1.85$ g/cm^3
Poisson's ratio	$\nu = 0.32$
Deformation modules	$E = 500 \sim 700$ kg/cm^2
Permeability	$K = 1E-5 \sim 1E-4$ cm/s
Geotechnical parameters of the fine-grained layer (CL)	
Internal friction angle	$\varphi = 22 \sim 24$
Cohesion	$C = 0.3 \sim 0.5$ kg/cm^2
Wet density	$\gamma = 1.98$ g/cm^3
Poisson's ratio	$\nu = 0.4$
Deformation modules	$E = 300 \sim 500$ kg/cm^2
Permeability	$K = 1E-6 \sim 1E-8$ cm/s

In the Esfandiar Tunnel project, surface settlements were precisely recorded over different time intervals along the studied section. An illustration of these measurements is presented in Fig. 4. As indicated by the monitoring data, the surface settlement ranged between 30 and 60 mm within the study area. Subsequently, the tunnel section was numerically simulated using PLAXIS, and the surface settlements predicted by the software were compared with the field-measured values. The results of this comparison are presented in Fig. 5.

Since multiple sections with recorded surface settlements exist along the studied tunnel, only three representative sections were selected for comparison with the numerical results to avoid data complexity. The surface settlement results for these three sections, along with the predictions from PLAXIS, are presented in Fig. 5. The first observation from these graphs is that the surface settlement patterns predicted by the software closely match the field-measured settlement profiles, which represent the actual ground behavior.

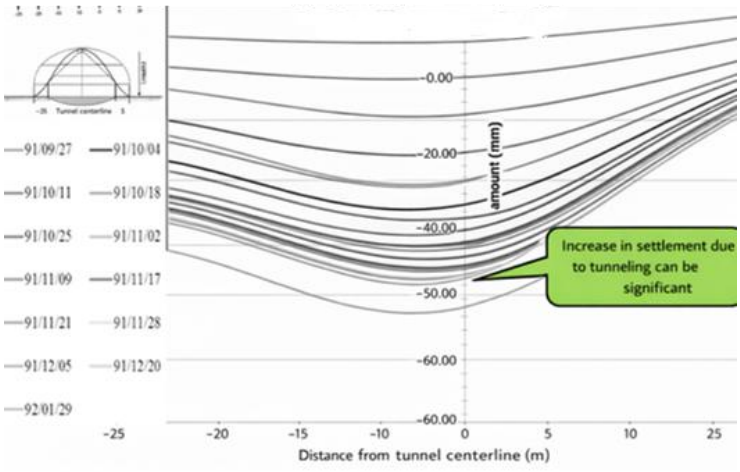

Fig. 4. Surface settlements recorded at different time intervals along the validated section.

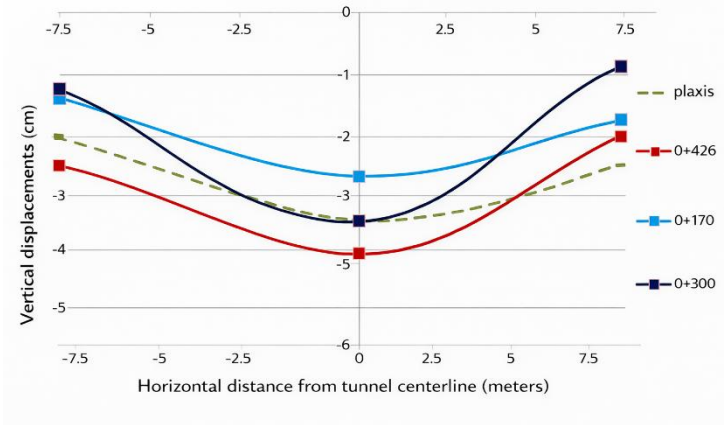

Fig. 5. Comparison of surface settlements between the studied section and the developed numerical model.

In other words, the shape of the ground settlement observed in reality is well reproduced by the numerical model, showing a characteristic bell-shaped profile in both cases. Furthermore, the maximum settlements predicted by the software are very close to the measurements recorded at different sections. The minor discrepancies can be attributed to geological variations and the inherent uncertainty in determining precise geotechnical parameters of the different soil layers. Therefore, this comparison confirms the reliability and accuracy of the software, allowing confident use of its outputs for subsequent analyses.

3. Numerical modeling of the problem

The assessment of the effects and performance of new structures on pre-existing buildings has long been recognized in civil engineering literature as a complex and ambiguous issue. The construction of a new structure adjacent to existing buildings can induce various effects, with settlement being the most critical factor, as it can significantly influence the deformations and settlements imposed on the pre-existing structures. Accordingly, this study investigates the various aspects of constructing a new building and its effects on the induced deformations and settlements of existing structures.

For numerical and parametric analyses of the influence of new structures on existing ones, it is first necessary to define the problem and represent it within a numerical environment. Moreover, to enable comparison of outputs across different models, the modeling conditions must be consistent. In this study, all numerical models are formulated based on plane strain assumptions. Fifteen-node triangular elements were used for the soil domain, while five-node elements were employed for structural components such as building foundations.

Although this study is parametric in nature and does not require actual field data, the most precise soil parameters available within the software were used for the soil elements. Another important aspect of numerical model development is the constitutive model of the soil. In this study, the soil behavior is represented using the Elastic–Perfectly Plastic Mohr–Coulomb model, which has been widely applied in both scientific research and practical projects. Further details regarding the constitutive model used will be provided in subsequent sections.

The Mohr–Coulomb (MC) model was adopted based on the objectives and strain levels relevant to this study. The applied seismic loading is represented through quasi-static equivalent lateral forces rather than full dynamic time histories; therefore, the analysis does not aim to simulate cyclic pore-pressure generation, stiffness degradation, or liquefaction mechanisms for which advanced cyclic constitutive models (e.g., PM4Sand, UBCSAND) are required.

The soil profile consists of non-liquefiable, medium-dense sand subjected to low-to-moderate shear strain levels. Under such conditions, the MC model has been shown to provide sufficiently accurate predictions of global deformation and settlement

behavior. Since the focus of the research is on evaluating seismic-induced settlement interaction, not on reproducing cyclic stress–strain loops or hysteretic soil response, the use of a more sophisticated model was not essential for the intended performance metrics.

Boundary conditions for all numerical models were defined such that lateral displacements along the left and right boundaries (X-direction) were restricted, while vertical displacements (Y-direction) were allowed. The bottom boundary was fixed in both X and Y directions.

Rayleigh damping with small-strain damping ratios of 2–5% was adopted to represent material damping under quasi-static loading conditions. Standard visco-elastic absorbing boundaries provided by PLAXIS 2D were applied along the model sides to minimize artificial reflections and boundary effects. These modeling details are included here to ensure transparency of the numerical setup.

4. Parametric studies

As is well known, a parametric study involves the evaluation of influencing factors on a given subject individually. In this study, various factors arising from the construction of a new structure adjacent to an existing building were investigated. The effects of each factor on the displacements and settlements of the pre-existing structure were examined, and the parameters considered are listed as follows:

- Number of stories of the new structure
- Width of the new foundation
- Horizontal distance between the new and existing structures

For each modeling scenario, the numerical model must have well-defined boundary conditions to control nodal displacements and rotations during analysis, ensuring accurate stress distribution and displacement patterns. PLAXIS provides robust tools to define such boundary conditions. In most geotechnical numerical models involving foundations and subgrades, it is essential to geometrically define the foundation layer so that stresses and displacements in various directions can be accurately calculated. Accordingly, the boundaries around the foundation layer must be defined, and horizontal and vertical displacements along the edges must be specified.

It is important to ensure that the model boundaries are sufficiently far from the load application area so that boundary effects do not influence the studied structure. PLAXIS includes a standard fixity tool that allows straightforward generation of appropriate boundary conditions for most numerical modeling problems. In all models developed in this study, the weight of each story was considered as one ton per square meter, equivalent to approximately 10 kN, in accordance with commonly used codes such as ABA and ASTM. To monitor settlement in the numerical model, three points were selected for comparison: one at the center of the new structure, one at the center of the existing structure, and one at the edge of the foundation nearest to the new building, as shown in Fig. 6. For consistency in comparing different models, all output data were recorded at these three points.

In this study, shear modulus variation due to strain-dependent soil softening was not considered because the analysis does not involve seismic or cyclic loading conditions. The numerical framework is limited to quasi-static settlement behavior of adjacent shallow foundations, where small-strain stiffness assumptions are generally adequate. Accordingly, the Mohr–Coulomb constitutive model in PLAXIS, which employs a constant small-strain shear modulus, was adopted. This limitation has now been explicitly acknowledged to ensure that readers do not interpret the analysis as representing dynamic or strain-dependent degradation mechanisms.

Although the use of a 2D plane-strain model provides a reasonable approximation for long-building configurations where strip footings extend considerably in the out-of-plane direction, it inherently neglects three-dimensional effects. In real conditions, 3D load distribution, edge effects, and spatial stress paths may either amplify or reduce settlement interaction between adjacent foundations. Therefore, the results presented in this study should be interpreted as representative of idealized long-strip footing behavior, and future research employing full 3D numerical modeling is recommended to more comprehensively capture these spatial effects.

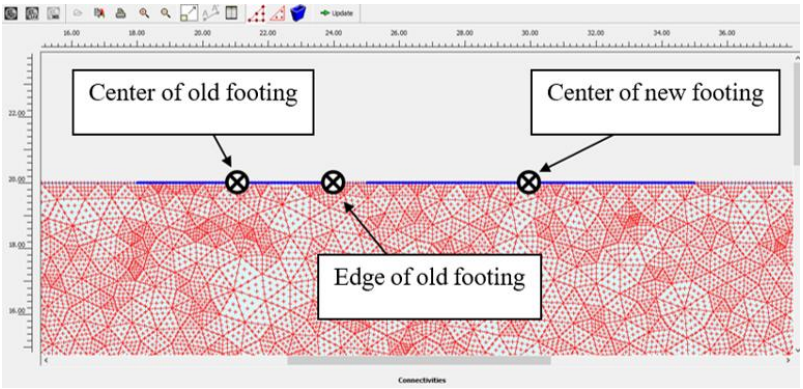

Fig. 6. Selected points for plotting settlement diagrams.

4.1. Effect of the number of stories of the new structure

One of the primary factors influencing surface displacements and deformations is the load imposed by the number of stories of a building. To examine the effect of the number of stories on the settlement of adjacent structures, buildings with varying numbers of stories, 2, 4, 6, and 8, were considered in this study. The selection of these story numbers is based on the fact that such buildings are more prevalent in the study area.

For simulating the building loads, the distributed load option in PLAXIS was used, with two separate loading systems, A and B, defined for the existing and the new structures. Each loading system in PLAXIS can be activated or deactivated at different stages of the simulation as required. It should be noted that in each parametric study, only the factor under investigation is varied while all other model properties remain constant. Accordingly, to evaluate the effect of the number of stories of the new building on the settlement of the existing structure, the horizontal distance between the two buildings was fixed at 1 m, the foundation width of the new building was set to 10 m, and that of the existing building to 6 m. The subsoil was assumed to be sandy. The results of the analysis regarding the influence of the number of stories on the settlement of the existing structure are presented in the following figures.

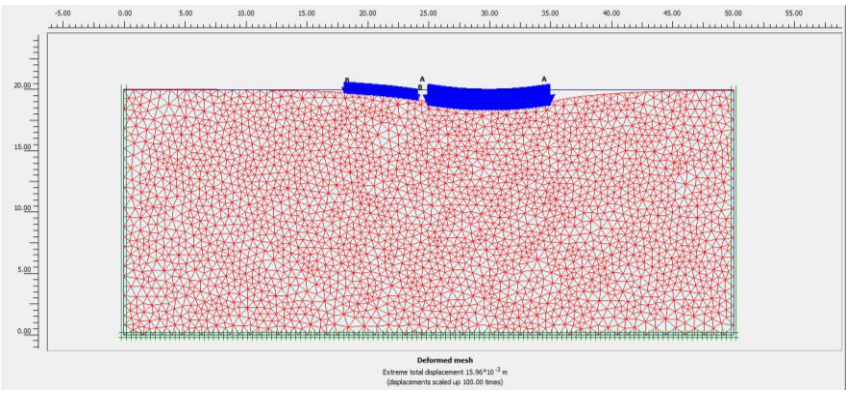

Fig. 7. Example of the deformed mesh after loading (displacements magnified 100 times).

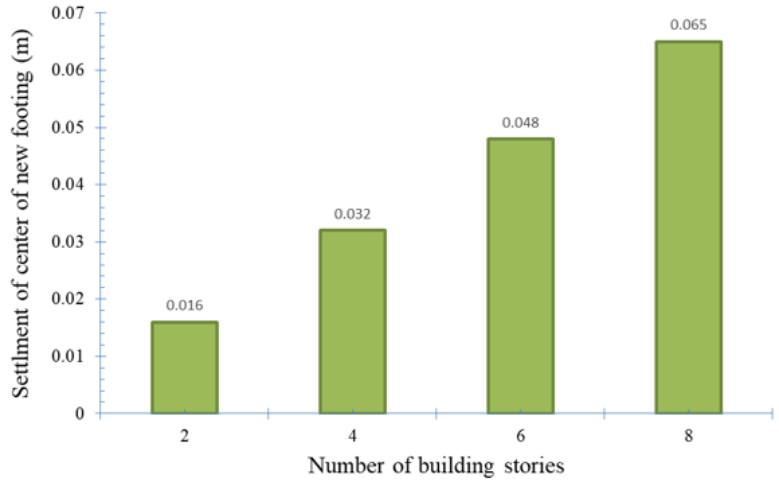

Fig. 8. Final settlement at the center of the new building foundation versus the number of stories.

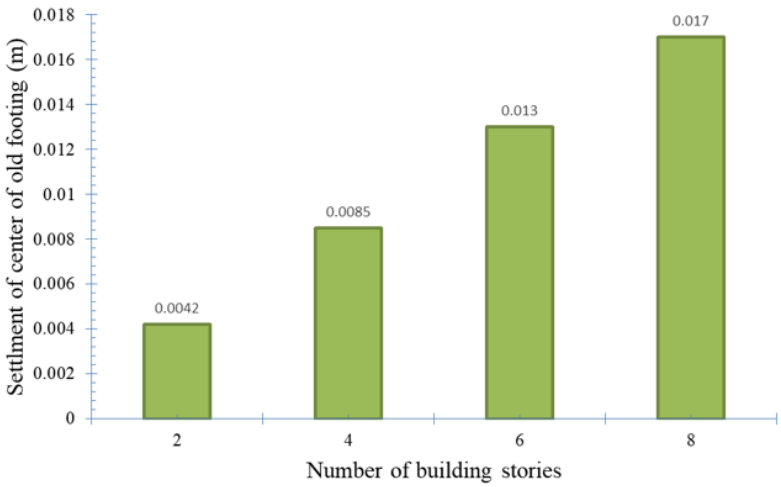

Fig. 9. Final settlement at the center of the existing building foundation versus the number of stories.

The first notable observation from both graphs is that, as expected, settlement increases with the number of stories. According to Fig. 8, the settlement at the center of the new building foundation was calculated as 16 mm for the 2-story case, 32 mm for 4 stories, 48 mm for 6 stories, and 65 mm for 8 stories. In contrast, Fig. 9 shows that the center of the existing building foundation experienced settlements of approximately 4 mm, 8.5 mm, 13 mm, and 17 mm corresponding to the construction of 2-, 4-, 6-, and 8-story new buildings, respectively. A key point from comparing these two graphs is that the settlement of the adjacent existing building is noticeably smaller than that of the new building. However, even a 2-story new building induces nearly 5 mm of settlement in the existing structure. These results indicate that if the new building is 8 stories high and the foundations are spaced 2 m apart, approximately 17 mm of settlement may occur in the pre-existing structure, which could potentially lead to cracking and architectural damage.

4.2. Effect of the new foundation width

Another important factor influencing surface deformations is the loaded area; in other words, the foundation width of the new building is one of the main factors causing settlement in adjacent structures. In this section, to investigate the effect of the new foundation width on the deformation and settlement of the existing building, all other model parameters were kept constant while only the foundation width of the new building was varied. The widths considered, 6, 8, 10, and 12 m, represent the majority of buildings in the study area. Since the objective of this parametric study is to examine the effect of the new foundation width on the settlement of the existing structure, all other influential factors were kept constant across all models. Accordingly, the horizontal distance between the two foundations was fixed at 1 m, the width of the existing foundation was set to 6 m, and the height of the new building was 6 stories for all models.

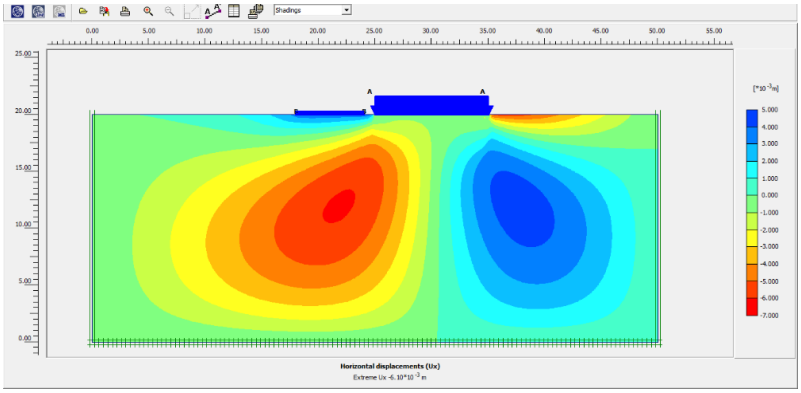

Fig. 10. Example of the horizontal displacement pattern for a 6-story building with a 10 m foundation width and 1 m foundation spacing.

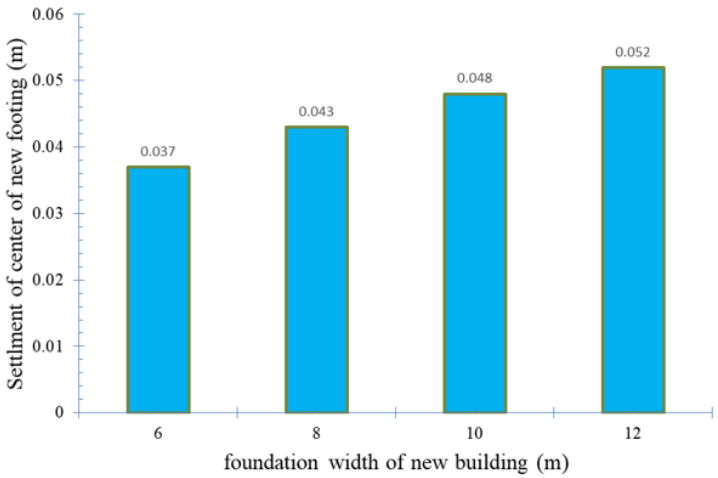

Fig. 11. Final settlement at the center of the new building foundation versus foundation width.

As clearly observed in these figures, increasing the foundation width from 6 m to 12 m leads to higher settlement at the center of the new building. This is due to the increased loading area in the numerical model. Additionally, as is known, a wider foundation exhibits greater flexibility, resulting in larger displacements at its center. According to the literature, increasing the foundation length can also enhance its bending, which contributes to the increased settlement at the foundation center. For the 6-story building, the settlement at the new foundation center was calculated as 37 mm for a 6 m width, 43 mm for 8 m, 48 mm for 10 m, and 52 mm for 12 m. Overall, this indicates that, for a building with a fixed number of stories, increasing the foundation width does not cause a significant change in settlement magnitude.

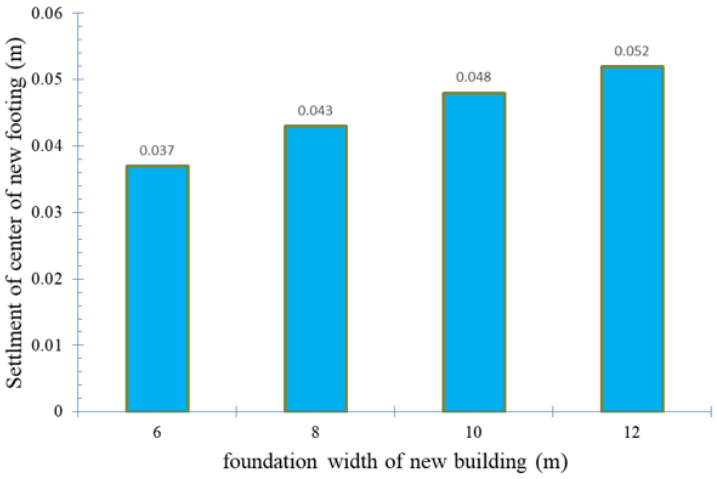

Fig. 12. Final settlement at the center of the existing building foundation versus foundation width.

Based on the data in Fig. 12, if the new foundation width is 6 m, the settlement at the center of the existing building foundation is 10 mm. Increasing the new foundation width to 8 m raises the settlement to 12 mm. Further increases to 10 m and 12 m result in 13 mm settlement, showing that increasing the foundation width beyond 10 m has little effect on the settlement of the existing structure.

4.2. Effect of the distance between structures

Due to the limited availability of suitable land in urban environments and the increasing economic value of existing plots, constructing buildings in close proximity has become inevitable. When adjacent structures are constructed within overlapping stress fields, they can exert various effects on each other. Therefore, the distance between a new building and an existing structure is a critical factor influencing deformations and settlements in the pre-existing building. This section investigates the effect of the distance between the new and existing structures on induced settlements and displacements.

To evaluate the effect of foundation spacing, all other parameters, including the number of stories, foundation widths of both the new and existing structures, and geomechanical properties of the subsoil, were kept constant, while the distance between the foundations was varied. Four spacing scenarios were considered: nearly touching foundations, 1 m spacing, 3 m spacing (equivalent to half of the existing foundation width, *B*/2), and 6 m spacing (equivalent to one full width, B). For this study, the new foundation width was set to 10 m, the existing foundation width to 6 m, and the new building height to 6 stories.

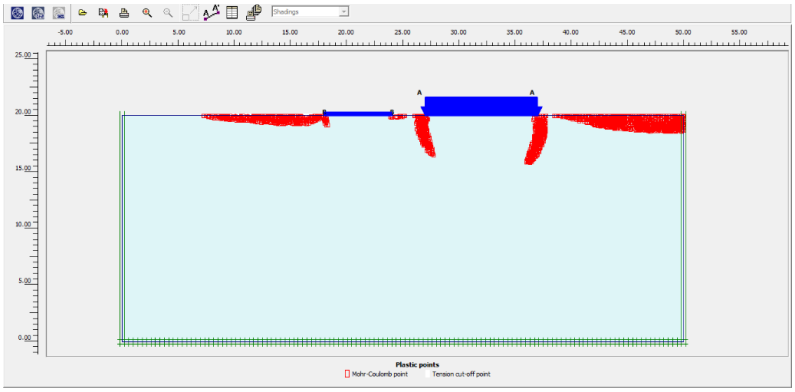

Fig. 13. Example of plastic points formation for a 6-story building with a 10 m foundation width and 3 m spacing; plastic points indicate nodes where the stress has reached a level causing plastic deformations.

As expected, increasing the distance between the new and existing structures reduces the induced settlement at the center of the existing foundation. According to the results shown in Fig. 15, when the foundations are nearly touching, the settlement at the center of the existing building is approximately 16 mm. Increasing the distance to 1 m reduces the settlement to 13 mm. When the spacing is further increased to 3 m (equivalent to half of the existing foundation width, 0.5 B), the induced settlement decreases to about 8 mm. Finally, with a spacing of 6 m (equivalent to the full foundation width, 1 B), the settlement at the center of the existing structure reduces to 4 mm. These results clearly indicate that the distance between adjacent foundations has a significant influence on induced settlements and displacements. The calculations show that increasing the spacing by 0.5 B reduces the induced settlement at the existing building center by approximately 50 %. Increasing the spacing to 1 B further decreases the induced settlement from 16 mm to around 4 mm, corresponding to a 75 % reduction.

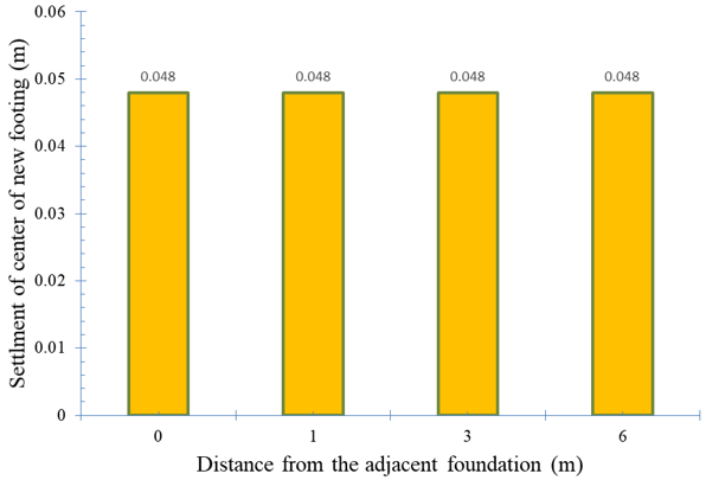

Fig. 14. Final settlement at the center of the new building foundation versus distance from the adjacent foundation.

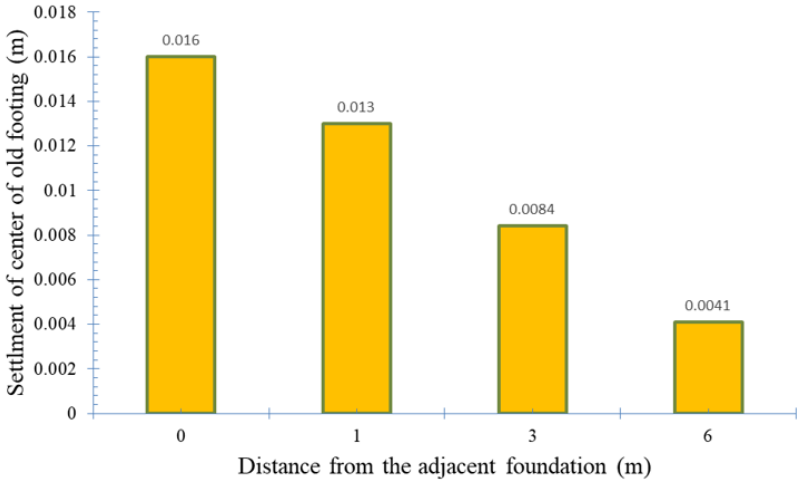

Fig. 15. Final settlement at the center of the existing building foundation versus distance from the adjacent foundation.

5. Conclusion

As is well known, multiple factors influence the settlement of existing structures due to the construction of new buildings. In this study, the main factors examined in a parametric analysis included the number of stories of the new building, the width of its foundation, and the horizontal distance between the new and existing structures. The subsoil in this study was assumed to be sandy.

Buildings and structural elements were modeled in PLAXIS using plate elements. Foundations were represented as structural elements, and the number of stories was simulated as distributed loads. According to applicable codes, a load of 10 kN per story was assigned in the model. The main findings from the numerical analyses are summarized as follows:

1. Number of Stories: One of the most influential factors on the settlement of existing structures is the number of stories of the new building. As expected, increasing the number of stories increased settlement at both the center of the new and existing foundations. While settlements in the new building were significantly higher than in the existing structure, the effect on the pre-existing building was still notable; for example, adding two stories to the new building induced approximately 5 mm of settlement at the center of the existing foundation.

2. Foundation Width: Another influential factor is the foundation width of the new building. The results indicate that, in general, changing the foundation width, while keeping other parameters such as loading, number of stories, and subsoil properties constant, has little effect on settlement of the adjacent structure. Specifically, increasing the new foundation width from 6 m to 12 m resulted in only a 3 mm increase in settlement of the existing building, which is negligible.

3. Distance between Structures: The horizontal distance between adjacent buildings was also investigated. The results showed that increasing the spacing between buildings has a significant effect on reducing induced settlements in the existing structure. For instance, increasing the distance to 3 m (equivalent to half the existing foundation width) reduced the induced settlement by approximately 50 %.

6. Engineering implications

The findings of this study provide several practical insights for urban geotechnical and structural engineering. One of the most influential factors affecting settlement of existing structures is the number of stories of the new building. As expected, increasing the number of stories increases settlement at both the new and existing foundations. For example, adding two stories to the new

building induced approximately 5 mm of settlement at the center of the existing foundation, which, while smaller than the settlement in the new building, is still notable for design considerations. The foundation width of the new building has a relatively minor effect on adjacent settlements. Increasing the foundation width from 6 m to 12 m, while keeping other parameters constant, resulted in only a 3 mm increase in settlement of the existing structure, which can generally be considered negligible. The spacing between adjacent buildings was found to have the most significant influence. Increasing the distance to 3 m (about half the foundation width) reduced induced settlement in the existing structure by approximately 50 %, highlighting the importance of maintaining sufficient separation between buildings in densely built areas.

Overall, these results emphasize that careful consideration of building height, spacing, and to a lesser extent foundation width, combined with proper soil–foundation interaction assessment, is essential for minimizing settlement risks. The study provides guidance for design strategies that enhance the safety and resilience of adjacent structures, contributing to more effective urban densification planning and mitigation of settlement-induced damage.

Statements & Declarations

Author contributions

Vali Ghaseminejad: Conceptualization, Investigation, Methodology, Formal analysis, Resources, Writing - Original Draft, Writing - Review & Editing.

Seyed Mojtaba Moosavi: Conceptualization, Methodology, Formal analysis, Project administration, Supervision, Writing - Review & Editing.

Taher Zargar Herijani: Investigation, Visualization, Validation, Formal analysis, Resources, Writing - Original Draft, Writing - Review & Editing.

Funding

The authors received no financial support for the research, authorship, and/or publication of this article.

Data availability

The data presented in this study will be available on interested request from the corresponding author.

Declarations

The authors declare no conflict of interest.

References

[1] Das, B. M., Larbi-Cherif, S. Bearing Capacity of Two Closely-Spaced Shallow Foundations on Sand. Soils and Foundations, 1983; 23: 1-7. doi:10.3208/sandf1972.23.1.

[2] Amer, E. A. A., Romi, M. E. A. Settlement and tilt of two interfering footings on clay. In: Proceedings of the First Palestinian Convention in Civil Engineering; 1993 Dec 6-10; Palestinian. p. 89-98.

[3] Jao, M., Wang, M., Chou, H., Lin, C. Behavior of interacting parallel strip footings. Electronic Journal of Geotechnical Engineering, 2002; 7: 1-10.

[4] Kumar, A., Saran, S. Closely Spaced Footings on Geogrid-Reinforced Sand. Journal of Geotechnical and Geoenvironmental Engineering, 2003; 129: 660-664. doi:10.1061/(ASCE)1090-0241(2003)129:7(660).

[5] Kumar, J., Bhoi, M. K. Interference of Multiple Strip Footings on Sand Using Small Scale Model Tests. Geotechnical and Geological Engineering, 2008; 26: 469-477. doi:10.1007/s10706-008-9175-6.

[6] Ghosh, P., Sharma, A. Interference effect of two nearby strip footings on layered soil: theory of elasticity approach. Acta Geotechnica, 2010; 5: 189-198. doi:10.1007/s11440-010-0123-2.

[7] Kusakabe, R., Ichimura, T., Fujita, K., Hori, M., Wijerathne, L. A finite element analysis method for simulating seismic soil liquefaction based on a large-scale 3D soil structure model. Soil Dynamics and Earthquake Engineering, 2019; 123: 64-74. doi:10.1016/j.soildyn.2019.04.021.

[8] Hwang, Y.-W., Ramirez, J., Dashti, S., Kirkwood, P., Liel, A., Camata, G., Petracca, M. Seismic Interaction of Adjacent Structures on Liquefiable Soils: Insight from Centrifuge and Numerical Modeling. Journal of Geotechnical and Geoenvironmental Engineering, 2021; 147: 04021063. doi:10.1061/(ASCE)GT.1943-5606.0002546.

[9] Tian, Y., Chen, S., Liu, S., Lu, X. Influence of tall buildings on city-scale seismic response analysis: A case study of Shanghai CBD. Soil Dynamics and Earthquake Engineering, 2023; 173: 108063. doi:10.1016/j.soildyn.2023.108063.

[10] Hwang, Y.-W., Dashti, S., Bessette, C. Mitigation of Liquefaction Damage to Shallow-Founded Structures with In-Ground Structural Walls. Journal of Geotechnical and Geoenvironmental Engineering, 2025; 151: 04024158. doi:10.1061/JGGEFK.GTENG-12498.

[11] Kassas, K., Adamidis, O., Anastasopoulos, I. Structure–soil–structure interaction (SSSI) of adjacent buildings with shallow foundations on liquefiable soil. Earthquake Engineering & Structural Dynamics, 2022; 51: 2315-2334. doi:10.1002/eqe.3665.

[12] Barrios, G., Uemura, K., Kikkawa, N., Itoh, K., Larkin, T., Orense, R., Chouw, N. Dynamic response of stand-alone and adjacent footing on saturated sand. Soil Dynamics and Earthquake Engineering, 2021; 143: 106584. doi:10.1016/j.soildyn.2021.106584.

[13] Hwang, Y.-W., Dashti, S., Kirkwood, P. Impact of Ground Densification on the Response of Urban Liquefiable Sites and Structures. Journal of Geotechnical and Geoenvironmental Engineering, 2022; 148: 04021175. doi:10.1061/(ASCE)GT.1943-5606.0002710.

[14] Bagheri, M., Ranjbar Malidarreh, N., Ghaseminejad, V., Asgari, A. Seismic resilience assessment of RC superstructures on long–short combined piled raft foundations: 3D SSI modeling with pounding effects. Structures, 2025; 81: 110176. doi:10.1016/j.istruc.2025.110176.

[15] Asgari, A., Ahmadtabar Sorkhi, S. F. Wind turbine performance under multi-hazard loads: Wave, wind, and earthquake effects on liquefiable soil. Results in Engineering, 2025; 26: 104647. doi:10.1016/j.rineng.2025.104647.

[16] Ibsen Lars, B., Asgari, A., Bagheri, M., Barari, A. Response of Monopiles in Sand Subjected to One-Way and Transient Cyclic Lateral Loading. In: editors. Advances in Soil Dynamics and Foundation Engineering. 2014. p. 312-322. doi:10.1061/9780784413425.032.

[17] Jahangiri, V., Naeim, B., Akbarzadeh, M. R., Asgari, A. Optimal intensity measures for resilience-oriented probabilistic seismic demand models of elevated steel tanks. Structures, 2025; 82: 110576. doi:10.1016/j.istruc.2025.110576.

[18] Asgari, A., Ranjbar, F., Bagheri, M. Seismic resilience of pile groups to lateral spreading in liquefiable soils: 3D parallel finite element modeling. Structures, 2025; 74: 108578. doi:10.1016/j.istruc.2025.108578.

[19] Asgari, A., Bagheripour, M. H. Earthquake Response Analysis of Soil Layers Using HFTD Approach. In: editors. Soil Dynamics and Earthquake Engineering. 2012. p. 320-325. doi:10.1061/41102(375)39.

[20] Akbarzadeh, M. R., Naeim, B., Asgari, A., Estekanchi, H. E. Framework for multi-hazard parameterized fragility based uncertainty quantification and sensitivity analysis of offshore wind turbines. Soil Dynamics and Earthquake Engineering, 2026; 201: 109963. doi:10.1016/j.soildyn.2025.109963.

[21] Akbarzadeh, M. R., Jahangiri, V., Naeim, B., Asgari, A. Advanced computational framework for fragility analysis of elevated steel tanks using hybrid and ensemble machine learning techniques. Structures, 2025; 81: 110205. doi:10.1016/j.istruc.2025.110205.

[22] Patrício, J. D., Gusmão, A. D., Ferreira, S. R. M., Silva, F. A. N., Kafshgarkolaei, H. J., Azevedo, A. C., Delgado, J. M. P. Q. Settlement Analysis of Concrete-Walled Buildings Using Soil–Structure Interactions and Finite Element Modeling. Buildings, 2024; 14: 746. doi:10.3390/buildings14030746.

[23] Bagheri, M., Jamkhaneh Mehdi, E., Samali, B. Effect of Seismic Soil–Pile–Structure Interaction on Mid- and High-Rise Steel Buildings Resting on a Group of Pile Foundations. International Journal of Geomechanics, 2018; 18: 04018103. doi:10.1061/(ASCE)GM.1943-5622.0001222.

[24] Asgari, A., Arjomand, M. A., Bagheri, M., Ebadi-Jamkhaneh, M., Mostafaei, Y. Assessment of Experimental Data and Analytical Method of Helical Pile Capacity Under Tension and Compressive Loading in Dense Sand. Buildings, 2025; 15: 2683. doi:10.3390/buildings15152683.

[25] Ebadi-Jamkhaneh, M., Arjomand, M. A., Bagheri, M., Asgari, A., Nouhi Hefzabad, P., Salahi, S., Mostafaei, Y. Experimental Study on the Pullout Behavior of Helical Piles in Geogrid-Reinforced Dense Shahriyar Sand. Buildings, 2025; 15: 2963. doi:10.3390/buildings15162963.

Civil Engineering and Applied Solutions

Research Article

journal homepage: ceas.journals.umz.ac.ir

CEAS Civil Engineering and Applied Solutions

Seismic Behavior and Practical Local Buckling Assessment of Composite Steel Plate Shear Walls

Mehdi Ebadi-Jamkhaneh [a*]

[a] *Department of Civil Engineering, School of Engineering, Damghan University, Damghan, Iran, P.O.BOX: 36716-45667*

ARTICLE INFO

Keywords:
Composite steel plate shear wall
Nonlinear analysis
Earthquake
Shear stud
Concrete panel

Article history:
Received 29 November 2025
Accepted 26 December 2025
Available online 01 July 2026

ABSTRACT

This study investigates the seismic performance of 4- and 6-story composite steel plate shear walls (CSPSWs) using advanced finite element models developed in ABAQUS. The numerical model, rigorously validated against experimental data, was subjected to nonlinear time history analysis under a suite of seven scaled ground motions. The results demonstrate that the design shear strength prescribed by AISC 341-10 is conservative, underestimating the peak dynamic base shear by 28% to 37% for the studied frames. This significant discrepancy is primarily attributed to the substantial shear force resisted by the boundary frame elements and the reinforced concrete panel, contributions not accounted for in the code's simplified methodology. Boundary columns were found to carry up to 26% of the total base shear. Furthermore, the study presents a practical assessment of local buckling in the steel web, proposing a methodological approach for determining shear stud spacing. The analysis confirms that a stud spacing of 300 mm provides a safety margin of 1.7 against buckling before yielding, ensuring the desired energy dissipation mechanism. The research underscores the enhanced seismic resilience of CSPSWs and provides quantitative insights to inform more efficient design practices.

1. Introduction

Composite Steel Plate Shear Walls (CSPSWs) have proven to be an extremely effective lateral force-resisting system, particularly for high-rise buildings in seismic-prone areas. These systems ingeniously combine the advantages of both steel and concrete, overcoming the limitations of using each material individually. A typical CSPSW consists of a steel plate wall that is connected to reinforced concrete panels or infilled with concrete to produce a synergistic system in which the steel plate provides high tensile strength and ductility, while the concrete component prevents or delays the global buckling of the steel plate, thereby enhancing the wall's stiffness and compressive strength [1, 2].

Through seminal experimental work conducted by Zhao and Astaneh-Asl [3], early achievements in validating the cyclic capabilities of composite shear walls were provided through their test work on 3-story half-scale specimens composed of a reinforced concrete wall bolted to a steel plate shear wall. The test series demonstrated high deformation capacity and stable cyclic post-yielding behaviour with the 33 cycles of cyclic shear and drift displacement that the specimens underwent. This maximum drift had a percentage increase of 5%, which was also a crucial finding in the study. The study also highlighted that the function of connectors was to brace the steel plates by providing a composite action, which prevented the steel from buckling as a whole and thus developed a composite effect of the shear wall and reinforced concrete wall combination to develop the highest shear capacity that these systems could develop. The development of inelasticity (localised buckling of the steel plate between the connector bolts) developed during the last cycles of testing and serves to support the principle that composite action is essential to allowing full development of the ductility and high shear capacity that these systems exhibit.

* Corresponding author.
E-mail addresses: m.ebadi@du.ac.ir (M. Ebadi-Jamkhaneh).

https://doi.org/10.22080/ceas.2025.30655.1056
ISSN: 3092-7749/
How to cite this article: Ebadi-Jamkhaneh, M. Seismic Behavior and Practical Local Buckling Assessment of Composite Steel Plate Shear Walls. Civil Engineering and Applied Solutions. 2026; 2(3): 85–95. doi:10.22080/ceas.2025.30655.1056.

In-depth research has advanced several configurations of CSPWS and studied the factors that influence them. Mo et al. [4] conducted a general review of these factors and provided several conclusions. Mo et al. [4] concluded that CFCSWs' performance is impacted by many variables, including axial load ratio, ratio of steel plate reinforcements, and shear connector spacing. They also indicated that an increased axial load will produce a more rapid loss of stiffness and strength than that of lower axial loads, while the presence of a higher steel plate ratio increases ductility and axial resistance. They also noted that if the spacing of shear connectors is too large, local buckling of the steel plates may occur in the elastic stage, negating the benefits of the composite system. These findings point to the need for careful detailing in connection design.

The ability to allow for innovative configurations has been researched by tampering with composite wall panels with L-shaped tooling for a composite wall edge region [5]. Results of cyclic testing have shown that composite walls were more effective than conventional reinforced concrete walls in dissipating energy and providing rigidity, among other structural properties. A second example of doing something a little different is the work of Xiao et al. [6], who studied embedded steel plate high-strength concrete (HSC) walls. Their 20-subject testing had conclusive evidence that the HSC walls improved the load, deformation, and energy dissipation capacities of normal RC walls. The optimum thresholds for design presented in the conclusion of the paper suggest that a control range for the steel ratio and maximum axial compression ratio of 0.5 should be maintained to ensure optimum seismic performance. Significant progress has been made toward developing accurate models for predicting the cyclic behavior of Composite Plate Shear Walls (C-PSW) and Concrete-Filled (CF) walls using numerical modeling techniques. Shafaei et al. [7] have produced results showing that it is both effective and efficient to develop simplified 2D FEM and fibre-based models using phenomenological effective stress-strain relationships to model C-PSW for the above-mentioned shapes. These simplified models will provide engineers with much-needed tools to easily and accurately simulate the earthquake response of C-PSW and CF walls.

Recent research has pushed the boundaries by incorporating advanced materials and investigating non-planar wall sections. Yang et al. [8] proposed a novel CSPSW where conventional concrete panels were replaced with Engineered Cementitious Composite (ECC) panels. Their nonlinear finite element analysis demonstrated that ECC panels, with their high tensile ductility and damage tolerance, provided superior restraint to the steel plate. The resulting system exhibited larger lateral stiffness and shear capacity than ordinary CSPSWs, with significantly reduced damage in both the steel plate and the cover panels.

For core-wall structures in high-rise buildings, C-shaped CSPSWs are critical. Kenarangi et al. [9] experimentally investigated the cyclic inelastic flexural behavior of large-scale C-shaped C-PSW/CF walls. Their findings were highly positive, demonstrating that the walls could develop their calculated plastic moment capacity and exhibited satisfactory cyclic performance under combined axial and lateral loads. This research provides vital validation for using C-PSW/CF as a primary lateral force-resisting system in complex, high-rise core-wall buildings.

A contemporary trend is the integration of high-strength materials to enhance economic efficiency and structural performance. Lou et al. [10] studied the seismic performance of shear walls using high-strength steel. Their pseudo-static tests revealed a nuanced trade-off: while increasing steel grade boosted bearing capacity and deformation capacity, it concurrently led to a reduction in ductility and energy dissipation capacity. This underscores the need for balanced design, potentially involving limits on steel ratio and axial compression ratio when utilizing high-strength steels to ensure adequate ductile performance under seismic demands.

The integration of Machine Learning (ML) and Artificial Neural Networks (ANN) offers a transformative paradigm shift for research on CSPSWs and other advanced structural systems. The validated high-fidelity finite element models (FEM) developed in the present study for CSPSW seismic analysis represent an excellent foundation for generating the extensive, high-quality datasets required to train such data-driven surrogate models. This approach directly addresses a critical challenge in computational structural engineering, where detailed nonlinear time-history or pushover analyses are accurate but prohibitively expensive for rapid design iteration or large-scale parametric studies. Machine learning models, including various ensemble and gradient boosting algorithms optimized with metaheuristic techniques, have demonstrated exceptional performance (with R^2 values often exceeding 0.95) in efficiently predicting complex structural responses such as the maximum inter-story drift ratio of steel diagrid systems, hysteretic curves of composite walls, and the flexural capacity of composite shear walls. Beyond mere prediction, advanced ML frameworks incorporate explainability tools like SHapley Additive exPlanations (SHAP), which provide vital insights into the relative importance and interactions of key design parameters, such as geometric dimensions, material strengths, and connector spacing, in determining structural behavior. This methodology creates a powerful synergy: the physical principles embedded in detailed FEMs ensure the data's fidelity, while the trained ML models offer engineers a rapid and reliable tool for performance assessment and design optimization. The pioneering work of researchers like Naeim et al. [11], Akbarzadeh et al. [12], and Jahangiri et al. [13] clearly demonstrates the pathway toward such integrated frameworks, which promise to significantly enhance the efficiency and scalability of performance-based seismic design for modern composite structural systems.

This research investigates the seismic behavior of steel-concrete composite shear walls under various earthquake records. A key focus is on optimizing the design by conducting a parametric study to determine the optimal spacing of shear connectors and the thickness of the concrete panel. The study aims to identify configurations that maximize energy dissipation and ductility while preventing premature local buckling of the steel plate, thereby establishing practical design guidelines for enhanced seismic performance.

2. Methodology

The numerical modeling section consists of four parts. Section 2.1 describes the constitutive models of the concrete and steel materials used in the numerical models. Section 2.2 presents the elements used, and Section 2.3 explains the contact interactions

between different parts and the applied loading. In Section 2.4, the validation of the numerical model against an experimental specimen is performed.

2.1. Material constitutive behavioral model

2.1.1. Concrete

The concrete damaged plasticity (CDP) model in ABAQUS was utilized to simulate the inelastic behavior of concrete under both compressive and tensile stresses. For the compressive response, the modified Hognestad model was employed to define the uniaxial stress-strain relationship. This model provides a robust representation of the concrete's nonlinear ascending branch and the post-peak strain-softening behavior. In the tensile regime, the stress-strain curve is linear up to the tensile strength. After cracking, the descending branch of the curve is modeled with a strain-softening response that gradually reduces the stress-carrying capacity to zero at the ultimate tensile strain. This study specifically uses a stress-crack width relationship to define the post-cracking behavior. By converting the crack width to an equivalent strain, a uniaxial stress-strain law for tension is derived and implemented in the model.

The plasticity parameters of the CDP model were carefully calibrated. The flow potential function, which governs the direction of plastic flow, was defined using the Drucker-Prager hyperbolic function. The dilation angle, which controls the volume change under plastic deformation, was set to 40°. Furthermore, other key parameters were specified as follows: the eccentricity of the plastic potential surface was 0.1, the ratio of the biaxial to uniaxial compressive strength (f_{b0}/f_{c0}) was 1.16, and the shape factor for the yield surface (K_c) was 0.667. These parameters collectively ensure an accurate representation of the concrete's pressure-dependent yielding and failure [14, 15].

To mitigate convergence difficulties associated with strain-softening material models, a viscosity parameter was incorporated. This parameter introduces a slight rate-dependence into the constitutive equations, which helps regularize the problem and improves the convergence rate of the implicit analysis. For this model, a viscosity coefficient of 0.01 was adopted. This value provides sufficient numerical stabilization without significantly compromising the quasi-static nature of the study, thereby ensuring a robust and efficient solution process for simulating the complex fracture and crushing of concrete [16-20].

2.1.2. Steel plate, rebar, and shear stud

To accurately simulate the hysteretic behavior of the steel reinforcement under cyclic loading, a combined isotropic-kinematic hardening model was implemented in ABAQUS. This model accounts for both the Bauschinger effect and the evolution of the yield surface size. The kinematic hardening component, which governs the translation of the yield surface, was defined using three backstress components in the Chaboche formulation with the following specific parameters: the first backstress (α_1) had an initial modulus C_1 = 20,000 MPa and a saturation rate γ_1 = 500; the second backstress (α_2) was defined with C_2 = 1,500 MPa and γ_2 = 50; and the third backstress (α_3) with C_3 = 100 MPa and γ_3 = 5. Concurrently, the isotropic hardening component, which controls the expansion of the yield surface, was specified such that the initial yield stress of 240 MPa saturated to a maximum of 370 MPa, modeled with an exponential law defined by a hardening modulus $Q\infty$ = 150 MPa and a saturation exponent b = 5. This combined formulation enabled the model to replicate key cyclic phenomena, including a reduced compressive yield stress of approximately 200 MPa following initial tensile yielding and the progressive shifting of hysteresis loops, which was crucial for the seismic assessment performed in this study.

2.2. Elements

The structural components of the shear wall system were discretized using element formulations appropriate to their geometric and mechanical characteristics. The steel components, namely the shear wall plate and the boundary elements, were modeled with S4R shell elements. This element type is a 4-node, reduced-integration finite membrane-strain shell element that is highly effective for simulating thin-walled steel sections. Its formulation accounts for both bending and membrane stresses and can capture large-rotation behavior and the potential for buckling, making it an optimal choice for modeling the complex response of steel plates under in-plane and out-of-plane loads [21-24].

The concrete panel was simulated using C3D8R solid elements, which are 8-node linear bricks with reduced integration. This element is the standard for modeling massive, three-dimensional continuum structures like concrete, as it can accurately represent the state of stress within the volume of the panel. The reinforcement, including both longitudinal and transverse rebars embedded within the concrete panel, as well as the shear connectors, was modeled using T3D2 elements. These are 2-node, 3-dimensional truss elements that resist only axial forces. An embedded constraint technique was employed, whereby the T3D2 truss elements are embedded within the mesh of C3D8R solid elements, ensuring a perfect bond that simulates the composite action between the concrete and the steel reinforcement, while efficiently neglecting the more complex local bond-slip effects for a global structural analysis [25-27]. Fig. 1 illustrates the geometric specifications, boundary conditions, and types of elements employed in the numerical model.

A mesh sensitivity analysis was conducted to ensure the numerical robustness of the results, particularly for phenomena such as local buckling, concrete cracking, and shear stud action, which are known to be mesh-dependent [28]. Three distinct global mesh sizes were investigated for the concrete panel and the steel plate: a coarse mesh of 100 mm, a medium mesh of 50 mm, and a fine mesh of 25 mm. The key seismic performance parameters, including the initial elastic stiffness, the peak load-bearing capacity, and the cumulative energy dissipation under cyclic loading, were compared across these mesh densities. The results, summarized in Table 1, indicate that the differences in response between the medium (50 mm) and fine (25 mm) meshes are negligible, with

variations of less than 2% in peak load and energy dissipation. The coarse mesh (100 mm) showed a more pronounced deviation, especially in predicting the post-peak softening behavior and localized damage patterns. Consequently, the medium mesh size of 50 mm was selected for all subsequent analyses. This size provides an optimal balance between computational efficiency and result accuracy, ensuring that the findings are independent of the discretization choice.

Table 1. Results of the mesh sensitivity analysis.

Mesh size (mm)	Initial stiffness (kN/mm)	Peak load (kN)	Energy dissipation (kJ)
Coarse (100)	84.1	562	42.5
Medium (50)	86.8	571	44.2
Fine (25)	87.1	573	44.3

Note: Values are from a monotonic pushover analysis of the validation specimen. The energy dissipation is calculated up to a top displacement of 40 mm.

2.3. Loading protocol and contact between the components

The numerical model incorporated several constraints and boundary conditions to accurately represent the structural system. The connections between the boundary elements were assumed to be rigid. A tie constraint was defined between the steel shear wall plate and the boundary element to ensure full compatibility and force transfer at their interface. The base of the two boundary elements was fully fixed against translational movement in all three global directions. To prevent out-of-plane buckling and enforce a state of plane stress, the top of the boundary element was restrained in the direction perpendicular to the web of the wall. Both monotonic and cyclic displacement-controlled loading protocols were applied to the top of the boundary element to investigate the system's hysteretic response.

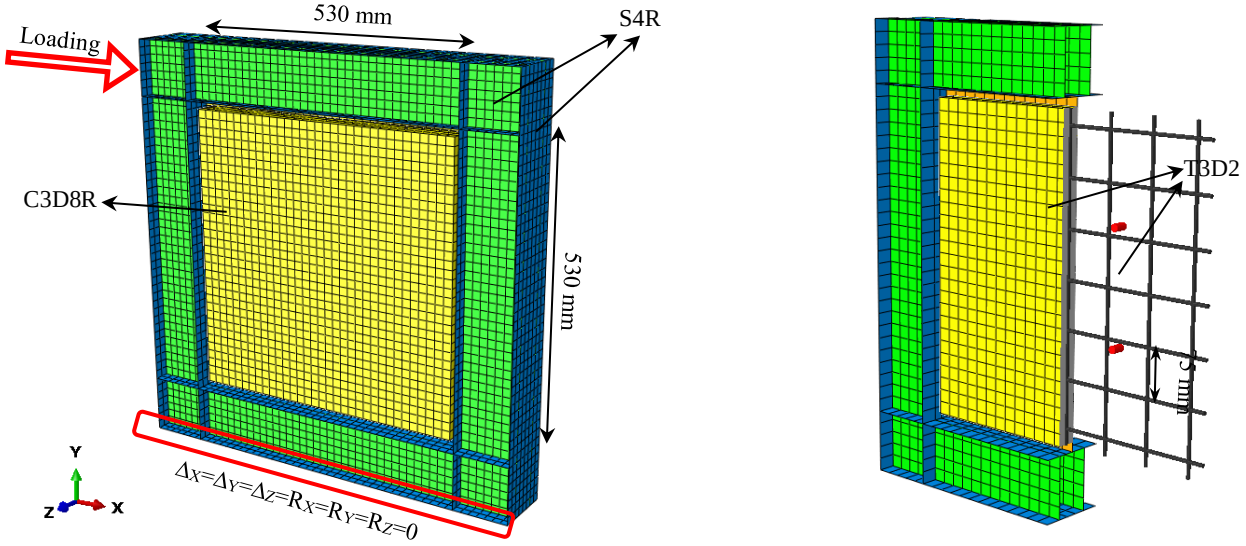

a) Dimensions and elements of the model b) Transverse cut to show the rebars and shear studs

Fig. 1. FE model detail.

2.4. Validation of the numerical model

In the present study, to validate the numerical model, the experimental investigation conducted by Arabzadeh et al. [29] was used in 2011. The CS specimen was considered among the experimental specimens. The beam and column elements were of type 2IPE100, and the steel plate infill had a thickness of 2 mm. The reinforcing bars inside the concrete panel had a diameter of 3 mm and were spaced 50 mm apart. The thickness of the concrete panel was 30 mm, and the concrete cover on the rebars was considered 15 mm. The yield stresses of the steel materials used in the column and beam were 361 MPa and 510 MPa, respectively. The yield stress and ultimate stress of the steel infill plate material were 268 MPa and 415 MPa, respectively.

Fig. 2 presents a comparison between the results of the laboratory specimen and the finite element model. The initial elastic stiffness of the experimental specimen was 85 kN/mm, while the value of this parameter in the numerical model was obtained as 87 kN/mm. Furthermore, the maximum load-bearing capacity in the experimental specimen was 585 kN, which was approximately 3% higher than that of the finite element model. In general, the behavior, failure mode, and seismic performance parameters of the experimental specimen and the numerical model show good agreement. Consequently, the employed material models, boundary conditions, and contact definitions between the various components of the system can be generalized for use in the numerical model.

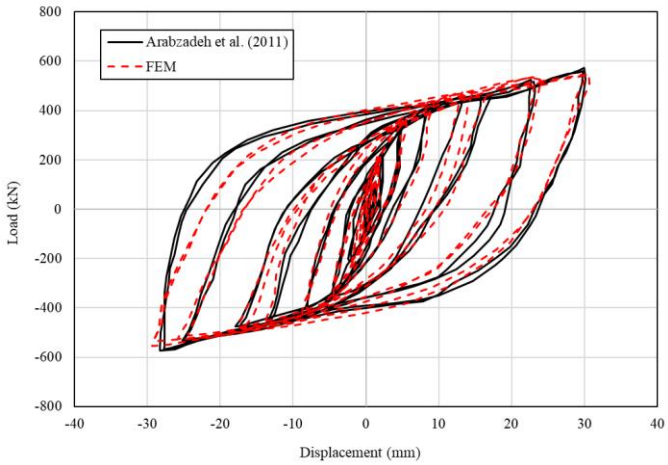

a) Load-displacement curves

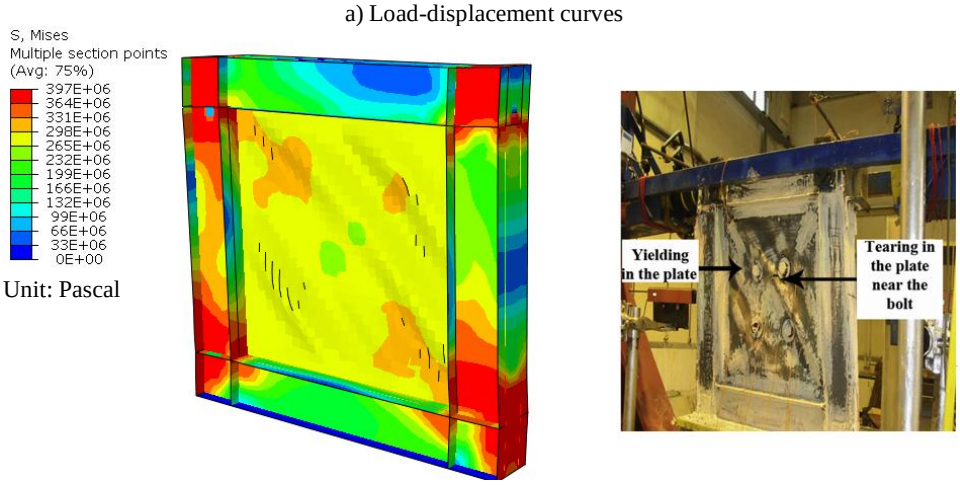

b) Failure mode of the test specimen [29] and the FE model

Fig. 2. Load-displacement curves and failure mode of the models.

3. Model definition

The design of the CSPSW followed a capacity-based methodology, as specific guidelines are codified in the Canadian standard [30]. The overarching principle was to concentrate inelastic deformation and energy dissipation in the steel infill plates, while ensuring the boundary beams and columns possess sufficient strength to remain essentially elastic under forces generated by the yielding infills. The concrete panel was detailed according to AISC 341-10 [31], with a specified thickness of 200 mm and a minimum reinforcement ratio of 0.0025, with bar spacing not exceeding 450 mm. The boundary members were specifically designed to withstand the full development of the tension field yield force in the steel plates. This tension field action, as described by Astaneh-Asl [32], becomes fully active after the concrete panel disintegrates under severe loading, a key behavioral aspect of C-PSWs where the concrete initially provides buckling restraint to the steel infill.

To investigate the behavior of the composite steel plate shear wall, two models-a four-story and a six-story structure-were utilized. The vertical boundary elements for the four-story and six-story frames were selected as IPB350 and IPB550 sections, respectively. The horizontal boundary elements in both frames were of type IPB250. A steel infill plate with a thickness of 5 mm was used. The concrete panel had a thickness of 200 mm and was reinforced with a grid of 6 mm diameter bars spaced at 300 mm. A 50 mm gap was provided between the concrete panel and the boundary elements. The compressive strength of the concrete panel was designated as 40 MPa.

To ensure a consistent and code-compliant seismic assessment, a set of seven ground motion records was selected (Table 2). These records were scaled independently for the four-story and six-story frames to account for their distinct dynamic characteristics. The scaling procedure adhered to the principles outlined in ASCE 7-16 [33]. For each frame, the individual records were scaled such that the average value of their 5% damped response spectra does not fall below 1.0 times the target spectrum, which was defined based on the site-specific seismic hazard, over a period range of 0.2T to 1.5T, where T represents the fundamental period of the respective frame (Fig. 3) [34]. This period-based scaling ensures that the input ground motions impose a consistent and appropriate level of seismic demand, tailored to the dynamic properties of each structure, thereby facilitating a meaningful comparison of their seismic performance. The scaling was performed to enable the calculation of the mean structural response from the suite of records, as this approach provides a more robust and reliable estimate of the expected seismic behavior than using a single record.

Table 2. Features of ground motions.

Earthquake	Abbreviation	Magnitude	Station	PGA (g)	PGV (cm/s)	Scaling factor (4-story)	Scaling factor (6-story)
Imperial Valley-06, 1979	IV	6.53	El Centro Array #3	0.27	47.99	0.77	0.79
Loma Prieta, 1989	LP	6.93	APEEL 2 - Redwood City	0.27	53.62	0.86	0.93
Kocaeli, Turkey, 1999	KT	7.51	Ambarli	0.25	36.52	1.32	1.54
Chi-Chi, Taiwan, 1999	CT	7.62	CHY047	0.18	26.63	1.50	1.76
Tottori, Japan, 2000	TJ	6.61	SMN002	0.18	21.95	0.91	1.16
Darfield, New Zealand, 2010	DN	7.0	Christchurch Resthaven	0.26	62.18	0.67	0.84
Christchurch, New Zealand, 2011	CN	6.2	Christchurch Resthaven	0.37	48.27	0.88	1.08

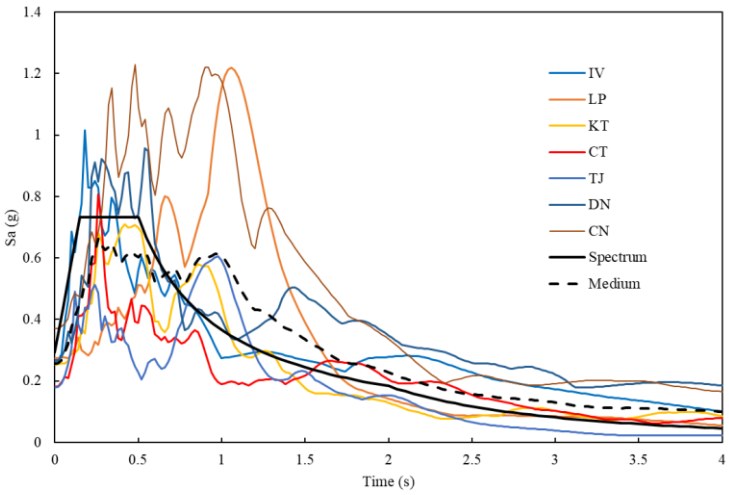

Fig. 3. Elastic spectra of seismic records.

4. Results and discussions

According to Fig. 4, non-linear time history analyses performed in ABAQUS for the 4-story CSPSW recorded maximum base reactions of 5152 kN, 4267 kN, 4912 kN, 4767 kN, 5237 kN, 4613 kN, and 4870 kN under the IV, LP, KT, CT, TJ, DN, and CN earthquakes, respectively. In comparison, the corresponding reactions for the 6-story CSPSW were 4762 kN, 4937 kN, 6054 kN, 5832 kN, 4812 kN, 5026 kN, and 5967 kN. The non-linear time history analyses revealed that the nominal shear strength of 3768 kN, calculated per AISC 341-10, significantly underestimated the actual dynamic response. For the 4-story and 6-story CSPSWs, the nominal strength was 28 and 37% lower than the peak dynamic base shears of 5237 kN and 6054 kN, respectively. This discrepancy is attributed to the load-sharing contributions of structural elements not considered in the code's simplified equation. The boundary steel columns provided a substantial portion of the system's shear resistance, with peak contributions of 25-26% and average contributions of 22 and 18% for the 4-story and 6-story frames, respectively. Furthermore, the reinforced concrete (RC) panels made a significant contribution to the overall strength, with their influence being most pronounced at the first story and diminishing progressively at higher levels. These findings demonstrate that the current design methodology, which ignores the capacity of boundary columns and RC panels, results in a conservative estimate of the system's true lateral strength.

According to Figs. 5 and 6, the analysis of axial forces and bending moments in the boundary column of the 4-and 6-story CSPSW under various earthquake records reveals a consistent internal force distribution pattern, albeit with significant variation in magnitude. Axial forces demonstrate a predictable accumulation from the top to the base, with the maximum compressive force reaching 15,993.6 kN under the IV ground motion, indicating the substantial global overturning moment demand on the column. Conversely, bending moments do not exhibit a monotonic increase and are often most severe at the column base, peaking at 1,114.83 kN-m under the DN earthquake. This peak moment at the base, coupled with the high concurrent axial force, defines the critical design scenario for the column. The significant scatter in both axial and moment values across different earthquakes, such as the notably lower forces under the CN record, underscores the critical influence of ground motion characteristics on the inelastic demand and highlights the necessity of a multi-record analysis to capture the full range of structural responses.

Preliminary parametric analyses indicate that increasing steel plate thickness or enlarging beam and column sections increases the share of lateral load resisted by the steel plate and boundary elements, whereas thickening the concrete panel primarily enhances local buckling restraint without significantly affecting global shear distribution. These trends clarify the sensitivity of component-level load sharing to geometric and material variations and provide practical insight for CSPSW design optimization.

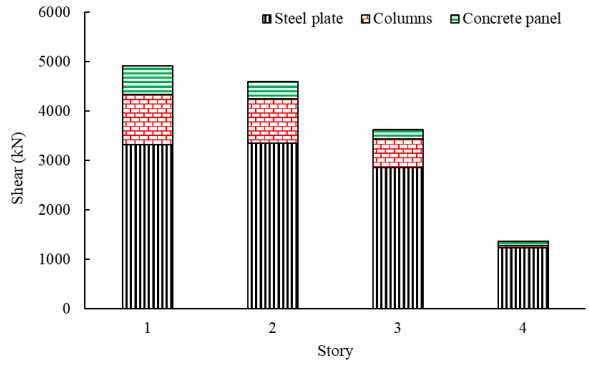

a) 4-story under KT record

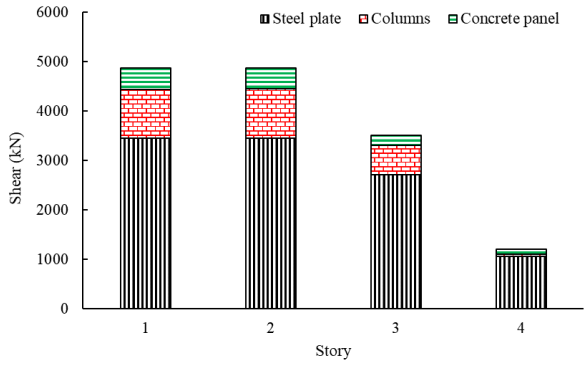

b) 4-story under CN record

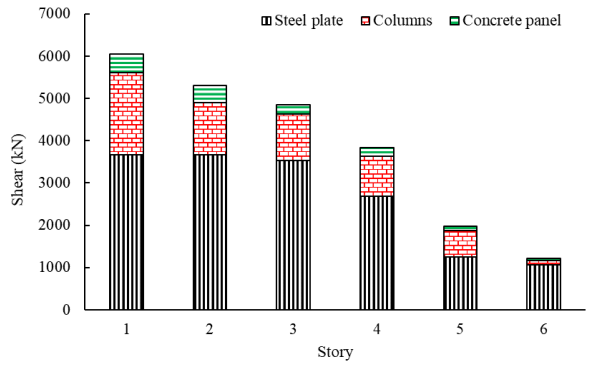

c) 6-story under KT record

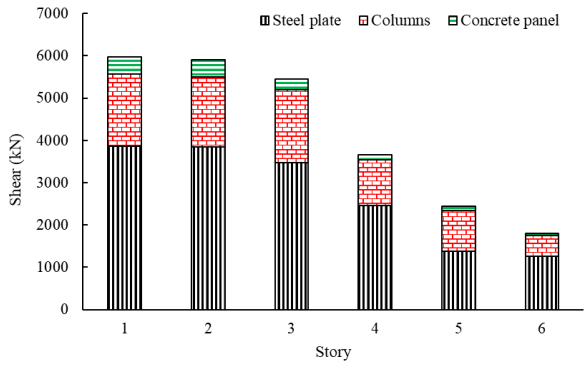

d) 6-story under CN record

Fig. 4. Peak story shear contribution for different components of 4- and 6-story.

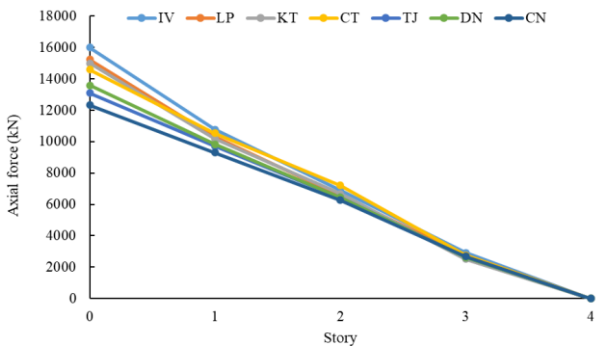

a) Axial force distribution

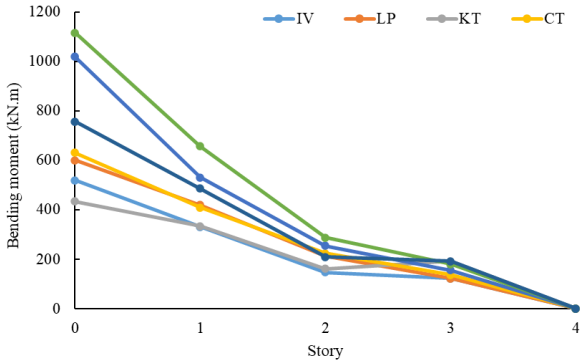

b) Bending moment distribution

Fig. 5. Axial force and bending moment at the column in the 4-story model.

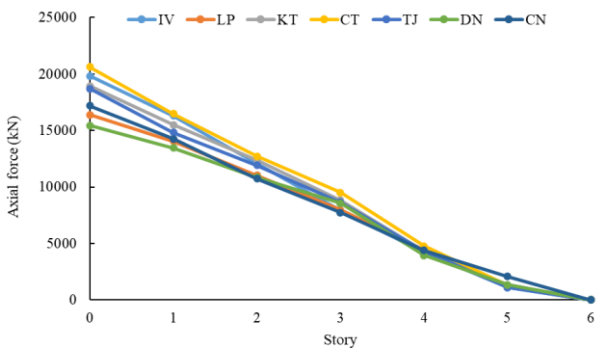

a) Axial force distribution

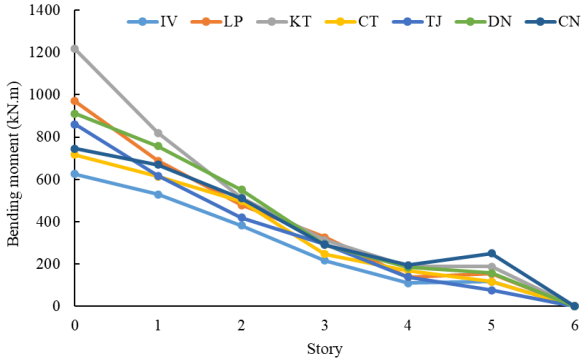

b) Bending moment distribution

Fig. 6. Axial force and bending moment at the column in the 6-story model.

Fig. 7 depicts the story displacement envelopes, recorded at the occurrence of maximum top-story displacement, illustrating the lateral deformation patterns induced by the selected suite of ground motions. The displacement profiles show a consistent increase along the height, confirming the expected flexural behavior. However, the significant scatter in values, particularly at the roof level (e.g., 68.4 mm vs. 119.6 mm for the 4-story frame), underscores the strong influence of ground motion frequency content on the structural response and the necessity for a multi-record design approach.

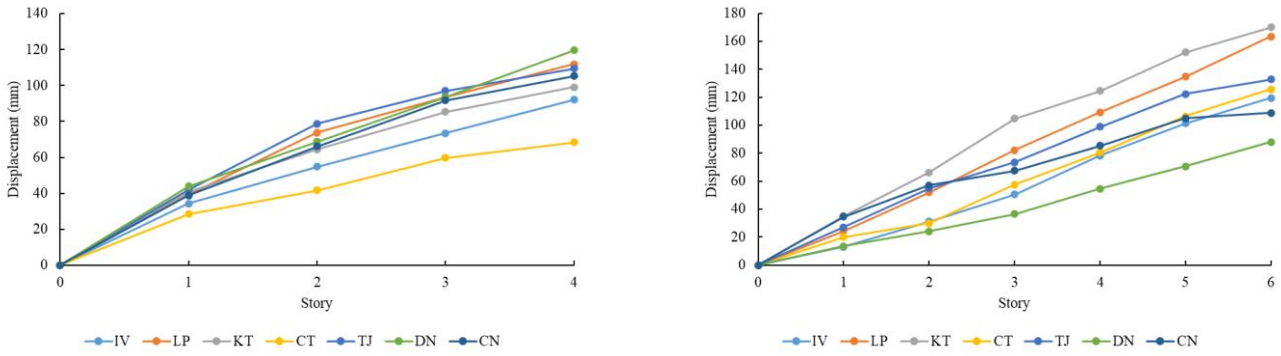

a) 4-story b) 6-story

Fig. 7. Distribution of displacement at the height of the models.

It should be noted that the observed underestimation of dynamic shear strength by AISC 341-10, quantified as 28–37% in this study, is strictly associated with the specific composite steel plate shear wall configurations examined herein, namely the 4-story and 6-story frames with fixed plate thickness, aspect ratio, and boundary member stiffness. The magnitude of conservativeness in simplified design provisions is known to be influenced by key parameters such as wall height, steel plate slenderness, and the relative stiffness of boundary elements. Therefore, the findings of this study should not be interpreted as a generalized limitation of the AISC provisions, but rather as evidence that, for the investigated configurations, the load-sharing contributions of boundary columns and reinforced concrete panels can be significant and are not explicitly accounted for in the current design formulation. Further parametric investigations are required to assess the extent of this behavior across a broader range of geometric and structural characteristics.

5. Determining the optimum shear stud spacing

To prevent local shear buckling of the steel plate before it yields, the elastic critical buckling stress must exceed the material's shear yield stress. For a composite plate shear wall, the concrete infill acts as a series of vertical and horizontal stiffeners at the shear stud lines, creating smaller subpanels. The refined elastic critical shear buckling stress for composite panel subpanels accounts for rotational stiffness at boundaries and concrete confinement effects:

$$\tau_{crl}^{*} = \eta_c \eta_s \frac{K_{sl}^{*} \pi^2 E}{12(1-\nu^2)} \left(\frac{t}{c}\right)^2 \tag{1}$$

Where $K_{sl}^{*} = 8.98 + \frac{5.61}{\alpha^2} + \Delta K_{sl}(\beta_r)$ is the enhanced buckling coefficient, $\eta_c = 1 + 0.25\sqrt{f_c'/E_s}$ is the concrete confinement factor, $\eta_s = 0.9 + 0.1log(\beta_r)$ is the rotational stiffness factor. β_r is the rotational stiffness parameter, which is $\frac{k_{\theta c} 12(1-\nu^2)}{Et^3}$.

The refined spacing requirement ensures optimal performance:

$$c \leq \frac{t}{\sigma_y} \sqrt{\frac{K_{sl}^{*} \pi^2 E \eta_s \eta_c}{12(1-\nu^2)\sqrt{3} \times 1.1}} \tag{2}$$

For typical construction steel (E = 200,000 MPa, ν = 0.3):

$$c \leq 1855 \eta_s \eta_c \gamma_{sh} \tag{3}$$

For the studied CSPSWs (t = 5 mm, σ_y = 350 MPa, f'_c = 30 MPa):

The design calculations yielded a base allowable stud spacing of 495 mm to prevent local buckling. After applying corrections for concrete confinement ($\eta_c = 1.08$, increasing spacing to 535 mm) and boundary stiffness ($\eta_s = 0.95$, refining it to 508 mm), the final permissible spacing was established at approximately 510 mm. The implemented 300 mm spacing, therefore, provides a substantial safety margin of 1.7, confirming a design that is both robust against buckling and maintains economic efficiency.

From a practical design perspective, the proposed buckling-based formulation can be directly used to establish rational shear stud spacing limits for composite steel plate shear walls. For typical mid-rise CSPSWs with steel plate thicknesses of 4–6 mm and normal-strength concrete panels, the analytical results indicate that stud spacing in the range of approximately 300–500 mm is sufficient to ensure that elastic local buckling of the steel plate occurs after yielding. The lower bound of this range, as adopted in the present study, provides a clear safety margin against premature buckling while remaining compatible with common construction

practices, welding accessibility, and cost considerations. Compared with existing code-based spacing limits, which are often conservative and do not explicitly account for concrete confinement and boundary rotational stiffness, the proposed formulation enables designers to quantitatively assess the influence of material properties and detailing on buckling resistance, thereby supporting more transparent and efficient CSPSW design.

6. Conclusion

This study comprehensively investigated the seismic performance of composite steel plate shear walls through detailed numerical analysis.

- The current AISC 341-10 design methodology is conservative, underestimating the actual dynamic shear strength by 28-37%. This discrepancy arises because the code ignores the significant load-sharing contributions of the boundary columns and the reinforced concrete panel.
- Boundary columns provide substantial shear resistance, with peak contributions of 25-26% of the total base shear, highlighting their crucial role in the system's lateral load-resisting mechanism.
- The seismic response is highly sensitive to ground motion characteristics. A multi-record analysis is essential to capture the full range of structural demands, including the critical combination of high axial force and bending moment at the column base.
- A refined and scientifically rigorous methodology was developed to determine the maximum shear stud spacing, preventing local buckling before steel yielding. The implemented 300 mm spacing provides a safety margin of 1.7, confirming a robust and economical design.
- The validated finite element model demonstrates that CSPSWs exhibit excellent seismic performance through effective composite action, offering a reliable and efficient structural system for seismic regions.

Statements & Declarations

Author contributions

Mehdi Ebadi-Jamkhaneh: Conceptualization, Methodology, Formal analysis, Resources, Writing - Original Draft.

Funding

The authors received no financial support for the research, authorship, and/or publication of this article.

Data availability

The data presented in this study will be available on interested request from the corresponding author.

Declarations

The authors declare no conflict of interest.

References

[1] Ebadi Jamkhaneh, M., Ahmadi, M. Numerical and parametrical investigations of the behavior of composite steel plate shear walls with opening. Sharif Journal of Civil Engineering, 2021; 37.2: 13-23. doi:10.24200/j30.2020.54966.2689.

[2] Katrangi, M., Khanmohammadi, M. Seismic behavior of composite encased steel plate shear wall using experimental and numerical methods. Journal of Building Engineering, 2025; 114: 114477. doi:10.1016/j.jobe.2025.114477.

[3] Zhao, Q., Astaneh-Asl, A. Cyclic Behavior of Traditional and Innovative Composite Shear Walls. Journal of Structural Engineering, 2004; 130: 271-284. doi:10.1061/(ASCE)0733-9445(2004)130:2(271).

[4] Mo, J., Uy, B., Li, D., Thai, H.-T., Tran, H. A review of the behaviour and design of steel–concrete composite shear walls. Structures, 2021; 31: 1230-1253. doi:10.1016/j.istruc.2021.02.041.

[5] Kisa, M. H., Yuksel, S. B., Caglar, N. Experimental study on hysteric behavior of composite shear walls with steel sheets. Journal of Building Engineering, 2021; 33: 101570. doi:10.1016/j.jobe.2020.101570.

[6] Xiao, C., Zhu, A., Li, J., Li, Y. Experimental study on seismic performance of embedded steel plate-HSC composite shear walls. Journal of Building Engineering, 2021; 34: 101909. doi:10.1016/j.jobe.2020.101909.

[7] Shafaei, S., Varma, A. H., Broberg, M., Klemencic, R. Modeling the cyclic behavior of composite plate shear walls/concrete filled (C-PSW/ CF). Journal of Constructional Steel Research, 2021; 184: 106810. doi:10.1016/j.jcsr.2021.106810.

[8] Yang, X., Xu, L., Pan, J. Mechanical behavior of full-scale composite steel plate shear wall restrained by ECC panels. Journal of Building Engineering, 2021; 44: 102864. doi:10.1016/j.jobe.2021.102864.

[9] Kenarangi, H., Kizilarslan, E., Bruneau, M. Cyclic behavior of c-shaped composite plate shear walls – Concrete filled. Engineering Structures, 2021; 226: 111306. doi:10.1016/j.engstruct.2020.111306.

[10] Lou, G.-B., Chen, P.-X., Zheng, J.-H. Seismic performance of high-strength steel plate-concrete composite shear walls. Journal of Building Engineering, 2024; 82: 108258. doi:10.1016/j.jobe.2023.108258.

[11] Naeim, B., Javadzade Khiavi, A., Khajavi, E., Taghavi Khanghah, A. R., Asgari, A., Taghipour, R., Bagheri, M. Machine Learning Approaches for Fatigue Life Prediction of Steel and Feature Importance Analyses. Infrastructures, 2025; 10: 295. doi:10.3390/infrastructures10110295.

[12] Akbarzadeh, M. R., Naeim, B., Asgari, A., Estekanchi, H. E. Framework for multi-hazard parameterized fragility based uncertainty quantification and sensitivity analysis of offshore wind turbines. Soil Dynamics and Earthquake Engineering, 2026; 201: 109963. doi:10.1016/j.soildyn.2025.109963.

[13] Jahangiri, V., Akbarzadeh, M. R., Shahamat, S. A., Asgari, A., Naeim, B., Ranjbar, F. Machine learning-based prediction of seismic response of steel diagrid systems. Structures, 2025; 80: 109791. doi:10.1016/j.istruc.2025.109791.

[14] Ghassemieh, M., Rezapour, M. Finite Element Modeling of SMA-Confined Concrete: Influence of Winding Pitch and Temperature on Strength and Energy Dissipation. Civil Engineering and Applied Solutions, 2026; 2: 33-45. doi:10.22080/ceas.2025.30055.1042.

[15] Rezapour, M., Ghassemieh, M. Numerical Investigation of Fe-SMA Strengthened Masonry Walls under Lateral Loading. Civil Engineering and Applied Solutions, 2025; 1: 1-15. doi:10.22080/ceas.2025.29594.1022.

[16] Ebadi Jamkhaneh, M., Kafi, M. A., Kheyroddin, A., Shokri Amiri, M. Progressive collapse resistance of a composite steel and concrete structural frame. Proceedings of the Institution of Civil Engineers - Structures and Buildings, 2018; 172: 197-213. doi:10.1680/jstbu.17.00149.

[17] Ebadi Jamkhaneh, M., Ahmadi, M., Sadeghian, P. Simplified relations for confinement factors of partially and highly confined areas of concrete in partially encased composite columns. Engineering Structures, 2020; 208: 110303. doi:10.1016/j.engstruct.2020.110303.

[18] Ebadi-Jamkhaneh, M., Homaioon-Ebrahimi, A., N. Kontoni, D.-P. Numerical finite element study of strengthening of damaged reinforced concrete members with carbon and glass FRP wraps. Computers and Concrete, 2021; 28: 137-147. doi:10.12989/cac.2021.28.2.137.

[19] Ebadi-Jamkhaneh, M., Kontoni, D.-P. N., Homaioon Ebrahimi, A. Assessment of Different Methods for Enhancing Progressive Collapse Resistance of Irregular Reinforced Concrete Buildings Using Pushdown Analysis. Arabian Journal for Science and Engineering, 2024; 49: 13861-13883. doi:10.1007/s13369-024-08847-4.

[20] Ebadi-Jamkhaneh, M. Determining minimum non-connected concrete panel thickness and concrete type impact on seismic behavior of CSPSW. Structural Engineering and Mechanics, 2024; 91: 607-626. doi:10.12989/sem.2024.91.6.607.

[21] Ebadi Jamkhaneh, M., Ebrahimi, A. H., Shokri Amiri, M. Experimental and Numerical Investigation of Steel Moment Resisting Frame with U-Shaped Metallic Yielding Damper. International Journal of Steel Structures, 2019; 19: 806-818. doi:10.1007/s13296-018-0166-z.

[22] Koloo, F. A., Badakhshan, A., Fallahnejad, H., Jamkhaneh, M. E., Ahmadi, M. Investigation of Proposed Concrete Filled Steel Tube Connections under Reversed Cyclic Loading. International Journal of Steel Structures, 2018; 18: 163-177. doi:10.1007/s13296-018-0313-6.

[23] Ebadi Jamkhaneh, M., Homaioon Ebrahimi, A., Shokri Amiri, M. Investigation of the Seismic Behavior of Brace Frames with New Corrugated All-Steel Buckling Restrained Brace. International Journal of Steel Structures, 2019; 19: 1225-1236. doi:10.1007/s13296-018-00202-2.

[24] Homaioon Ebrahimi, A., Ebadi Jamkhaneh, M., Shokri Amiri, M. 3D Finite-Element Analysis of Steel Moment Frames Including Long-Span Entrance by Strengthening Steel Cables and Diagonal Concentrically Braced Frames under Progressive Collapse. Practice Periodical on Structural Design and Construction, 2018; 23: 04018025. doi:10.1061/(ASCE)SC.1943-5576.0000388.

[25] Azarbara, M., Madandoust, R. Numerical Investigation of Trapezoidally Corrugated Steel Shear Walls with Openings: Effects of Stiffeners and Corrugation Orientation. Civil Engineering and Applied Solutions, 2026; 2: 60-70. doi:10.22080/ceas.2025.29967.1041.

[26] Rahimi, M., Bargi, K., Rezapour, M. Balancing Cost and Seismic Performance: Rectangular vs. T-shaped Shear Walls in Steel Frame Tall Buildings. Civil Engineering and Applied Solutions, 2026; 2: 12-21. doi:10.22080/ceas.2025.30091.1043.

[27] Rahimi, M., Bargi, K. Comparative Evaluation of Seismic Behavior of T-Shaped versus Rectangular Concrete Shear Walls in High-Rise Buildings. Civil Engineering and Applied Solutions, 2025; 1: 16-26. doi:10.22080/ceas.2025.29715.1029.

[28] Asgari, A., Ranjbar, F., Bagheri, M. Seismic resilience of pile groups to lateral spreading in liquefiable soils: 3D parallel finite element modeling. Structures, 2025; 74: 108578. doi:10.1016/j.istruc.2025.108578.

[29] Arabzadeh, A., Soltani, M., Ayazi, A. Experimental investigation of composite shear walls under shear loadings. Thin-Walled Structures, 2011; 49: 842-854. doi:10.1016/j.tws.2011.02.009.

[30] Canadian Standards Association (CSA). CAN/CSA-S16-09: Limit states design of steel structures. Longueuil (QC): CSA; 2009.

[31] American Institute of Steel Construction (AISC). AISC 341-10: Seismic Provisions for Structural Steel Buildings. Farmington Hills (MI): AISC; 2010.

[32] Astaneh-Asl, A. Seismic Behavior and Design of Composite Steel Plate Shear Walls. 1st ed. Berkeley (CL): Structural Steel Educational Council (SSEC); 2002.

[33] Engineers, A. S. o. C. Minimum Design Loads and Associated Criteria for Buildings and Other Structures. 1st ed. Farmington Hills (MI): American Society of Civil Engineers (ASCE); doi:10.1061/9780784414248.

[34] Jahangiri, V., Naeim, B., Akbarzadeh, M. R., Asgari, A. Optimal intensity measures for resilience-oriented probabilistic seismic demand models of elevated steel tanks. Structures, 2025; 82: 110576. doi:10.1016/j.istruc.2025.110576.